Structural performance of complex core systems for FRP-balsa composite sandwich bridge decks

PAR

Michael OSEI-ANTWI

EPFL

ÉCOLE POLYTECHNIQUE
FÉDÉRALE DE LAUSANNE

Suisse
2014

To my wife Gloria

Preface

Bridge deck slabs offer favorable opportunities for the application of fiber-reinforced polymer (FRP) composite materials. The slabs are resistant to corrosion, lightweight and allow the rapid installation of new and widening or upgrading of existing bridges by replacing heavy concrete decks. There are two basic concepts of GFRP decks: orthotropic slabs composed of adhesively-bonded pultruded shapes and sandwich constructions. Sandwich slabs frequently exhibit significant technical advantages over pultruded decks, such as greater geometrical flexibility resulting in the conception of larger spans or skew shapes. They are composed of GFRP face sheets and honeycomb or foam cores. In the latter case, additional GFRP webs are normally required to provide sufficient shear capacity of the core. However, the honeycomb structure or the internal GFRP webs in the foam core configuration result in a support of non-uniform stiffness for the upper face sheet, which – under frequent wheel loads – may lead to the debonding of the latter from the core. To overcome this drawback, i.e. to provide a core of sufficient shear capacity without internal webs and uniform support for the upper face layer, the use of balsa wood is evaluated in this thesis. Since the mechanical properties of the balsa depend on its density, combinations of balsa of different densities – tailored to the structural requirements – and even with timber inserts are conceivable.

The main aim of this thesis is therefore to understand and model the mechanical behavior of complex core systems composed of layered balsa core structures with different densities and timber inserts. This work also contributed to the construction of the first GFRP-balsa sandwich road bridge in 2012, the Avançon Bridge in Bex, Switzerland.

Prof. Dr. Thomas Keller

Abstract

Based on current fiber-reinforced polymer (FRP) composite construction principles, FRP decks fall into two categories: pultruded decks and sandwich decks. Sandwich decks comprise face sheets and either honeycombs or foams reinforced with internal FRP webs for shear resistance. The honeycomb structure and the webs cause debonding between the upper face sheets and the core due to the uneven support of the former. An alternative material that has high shear capacity and can provide uniform support for the upper face sheet is balsa. Balsa panels have therefore been proposed as the core material for sandwich decks in this research work. Balsa panels are produced by adhesively bonding dissimilar balsa blocks, resulting in a non-homogenous and anisotropic material. These inherent characteristics are not taken into account in the current shear behavior of balsa, thus making it unreliable. Balsa also exhibits high ductility when subjected to compressive loads, however, the shear ductility required by engineers to design safe sandwich structures is lacking. Furthermore, currently existing GFRP-balsa sandwich bridge concepts can only be applied to short-span bridges due to high cost and manufacturing challenges in the case of sandwich slab bridges. In hybrid sandwich deck-steel girder bridges, low bending stiffness in the bridge direction and low composite action in the deck have been the drawbacks. The purpose of this research is to develop novel concepts for lightweight, stiffer and stronger sandwich decks, using balsa cores, which can be fabricated with fewer manufacturing challenges and offer longer spans than existing decks.

Balsa panels were experimentally investigated to establish their shear properties and shear ductility at the three orthotropic shear planes. The influence of shear plane, balsa density and adhesive joints on the shear properties was quantified.

Two new GFRP-balsa sandwich bridge concepts (complex core systems) have been proposed for long-span bridges. In the first concept, the sandwich core comprises high- and low-density balsa cores and an FRP arch reinforced at the core interface. Sandwich beams based on this concept were experimentally investigated to evaluate their structural performance. The beams demonstrated high bending stiffness and strength and were lightweight. Crack initiation and propagation in the balsa blocks of the complex balsa core could finally be explained. A new analytical model to predict the bending behavior of the new sandwich beams was developed.

The second bridge concept involves integrating timber inserts into the balsa core of a sandwich deck. GFRP-balsa sandwich beams, with timber inserts, were numerically investigated to evaluate their structural performance. High stress concentrations occurred in

the face sheets and cores at the balsa/timber core joints which were eliminated by changing the core joints from butt to scarf. An optimum angle of termination of scarf joints, based on low stress concentrations at the joints, low costs and manufacturing challenges, was recommended in the design of GFRP-balsa sandwich decks. An existing analytical model for predicting axial stress concentrations in face sheets at butt core joints was extended to scarf joints and a new analytical model was developed to predict shear stress concentrations in the cores at both butt and scarf joints.

Finally, the results obtained from the experimental work, the new models and the two proposed sandwich bridge concepts were implemented in the design of new GFRP-balsa sandwich slab bridges and decks. The structural limits of the new bridges were established and the potential of the new GFRP-balsa sandwich deck to replace a reinforced concrete deck was explored. Taking manufacturing limits into account (800-mm slab thickness) and using the proposed complex core system, sandwich bridge slabs of up to approximately 19 m can be constructed. Furthermore, GFRP-balsa sandwich decks bonded on steel girders can reach spans of up to 30 m. The findings of this research work therefore establish that deteriorated reinforced concrete decks with long spans of even up to 30 m can be replaced by GFRP-balsa sandwich decks. Also, based on this work, in the future, existing reinforced concrete decks can be widened using the proposed sandwich decks due to their lightweight, which has been extensively demonstrated. This will lead to cost saving since the bridge substructure will no longer need to be reconstructed.

Résumé

Les tabliers de ponts en FRP (polymères renforcés par des fibres) offrent de nombreux avantages tels qu'une haute résistance et rigidité spécifique et une bonne résistance à la corrosion. Deux systèmes sont actuellement utilisés : les tabliers pultrudés et les tabliers sandwich. Ces derniers sont composés de deux faces et d'un noyau en nid d'abeille ou en mousse renforcé par des âmes internes permettant d'augmenter la résistance à l'effort tranchant. Les nids d'abeille et les âmes internes engendrent un appui discontinu de la face supérieure ce qui entraîne son décollement du noyau à long terme sous les charges ponctuelles de trafic. L'utilisation d'un noyau en balsa garantissant une résistance à l'effort tranchant élevée et un appui uniforme de la face supérieure est une alternative présentée et évaluée dans cette thèse. Les panneaux en balsa sont constitués de différents blocs assemblés par collage et résultent en un matériau non homogène et anisotrope. Ces propriétés ne sont actuellement pas prises en considération dans la caractérisation du comportement à l'effort tranchant des panneaux. Le comportement ductile du balsa en cisaillement n'a non plus été examiné jusque là. En outre, les conceptions actuelles de ponts-dalles en sandwich à base de GFRP (FRP-verre) et balsa limitent leur utilisation à de faibles portées en raison des difficultés liées à la fabrication et aux coûts élevés. Quant aux ponts mixtes constitués d'un tablier en sandwich et de poutres maîtresses en acier, leurs rigidités longitudinales sont faibles et leurs comportements mixtes (avec une liaison parfaite) limités. L'objectif de cette thèse est de développer de nouveaux concepts de structures en sandwich légères, rigides et résistantes à base de noyaux en balsa garantissant de plus grandes portées que les ponts existants.

Une campagne expérimentale a permis d'établir le comportement mécanique en cisaillement des panneaux de balsa selon les trois plans orthotropes. L'influence de la densité des blocs de balsa ainsi que l'effet des joints collés ont été quantifiés.

Deux nouveaux concepts de sandwich à base de GFRP et de balsa (systèmes de noyaux complexes) sont proposés pour réaliser des ponts de plus grandes portées. Le premier concept comprend des panneaux de balsa à haute et à basse densité et l'intégration d'un arc en FRP à l'interface. Les études expérimentales menées sur des poutres sandwich basées sur ce concept ont permis d'évaluer leurs performances et de démontrer leur grande rigidité et résistance tout en restant légères. Les modes de rupture de poutres à noyaux complexes, spécialement du noyau en balsa composé de blocs de différentes densités et l'influence des joints collés ont été analysés. Des modèles analytiques ont été développées permettant de calculer les rigidités

à la flexion et à l'effort tranchant des poutres à noyaux complexes ainsi que les contraintes axiales et de cisaillement dans les faces et les divers composants du noyau.

Le deuxième concept consiste en intégrer des renforts en bois dans le noyau en balsa de tabliers en sandwich. Des études numériques menées sur de poutres sandwich en GFRP et balsa avec des renforts en bois ont permis d'évaluer leurs performances. L'apparition de concentrations de contraintes sur les faces et le noyau au droit des joints entre le balsa et le bois sont éliminés en remplaçant les joints verticaux par des joints en biais. Un angle optimal pour les joints en biais a été défini réduisant les concentrations de contraintes et intégrant les aspects de fabrications et de coûts. Un modèle analytique existant permettant de calculer les concentrations de contraintes axiales dans les faces au droit des joints verticaux a été étendu au cas de joints biais et un nouveau modèle a été établi pour estimer les concentrations de contraintes de cisaillement dans le noyau au droit des joints verticaux ou biais.

Par la suite, l'application des systèmes de noyaux complexes développés dans le domaine des ponts est évalué et les limites d'utilisations définies. Des ponts-dalles en sandwich à base de GFRP et de systèmes de noyaux complexes, d'une épaisseur limitée à 800 mm pour des raisons de fabrication, peuvent atteindre 19 m de portée. Des ponts mixtes constitués d'un tablier sandwich en GFRP-balsa et de poutres maîtresses en acier (avec une liaison parfaite) peuvent atteindre 30 m de portée par la mise en place de renforts en bois au dessus de ces dernières. Le remplacement de tabliers en béton de ponts existants et endommagés par des tabliers en sandwich est possible jusqu'à des portées de 30 m. D'après ces résultats, l'élargissement de tabliers de ponts existants par le système de noyau complexe proposé serait aussi envisageable dans le futur. Ceci limiterait l'augmentation des charges permanentes sur l'infrastructure et donc en réduirait ou éventuellement éviterait les travaux de renforcement ou de reconstruction.

Mots-clés : Tablier de ponts, ponts en matériaux composites, bois de balsa, panneaux sandwich, polymères renforcés par des fibres, poutre multicouche sandwich, joint au noyau, renfort en bois, remplacement de tableur en béton.

Acknowledgements

In the course of my doctoral research, I have been fortunate enough to receive a lot of encouragement and support from my family, colleagues and friends. In addition, many others have contributed to different parts of my work, providing their professional expertise that has proved extremely useful.

First, I would like to express my sincere gratitude to my thesis directors: Prof. Dr. Thomas Keller for providing me with such a priceless opportunity to further my scientific education and also for his guidance and support during our fruitful discussions. A lot of appreciation goes to Dr. Julia de Castro for her regular supervision advice and technical writing guidance, particularly during the difficult times of my research and also for the conversion of my abstract from English to French. I will also not forget Dr. Anastasios P. Vassilopoulos for his co-supervision role and discussion on analytical and numerical modeling aspect of my research.

I would also like to acknowledge the partners of this project, 3A Composite Sins, Switzerland, for the generous funding of this project, without which the project would not have reached this prime stage. A special appreciation goes to the bridge team, Mr. Markus Spieler, Mr. Sebastien Lavanchy, Dr. Ing. Jan Rothe and Dirk Wilde for their time, support and presence regularly at the up-date meetings and their contributions to the practical applications of the research work in bridge construction.

I would like to express my deepest thanks to the thesis defense committee for the time and effort they devoted to reading and evaluating the thesis as well as their contributions to improving the manuscript, thanks to their expert suggestions: Prof. Dr. Eugen Brühwiler, Director, Structural Maintenance and Safety Laboratory (MCS), EPFL, Switzerland; Prof. John Nairn, Professor and Richardson Chair, Department of Wood Science and Engineering, Oregon State University, Corvallis, Oregon, USA; Dr. Wendel Sebastian, Reader, Department of Civil Engineering, University of Bristol, UK and Prof. Dr. Ian Smith, Director, Applied Computing and Mechanics (IMAC), EPFL, Switzerland, President of the jury.

I also appreciate the sound support from the incredible team working in the laboratory (IIC-EPFL), Sylvain Demierre for his technical coordination and contribution to experimental set-ups; François Perrin for the precise and high quality work provided, Gilles Guignet for his useful help with experimental set-ups, Patrice Gallay, Gérald Rouge and Léa Frédérique Dubugnon for their unfailing help and support.

Table of contents

1.
Introduction

New Avancon Bridge, Bex, Switzerland installed in October, 2012, comprising GFRP-balsa sandwich deck bonded onto steel, longitudinal girders

1.1   Context and motivations

Civil infrastructure relating to bridges worldwide, which was developed and rapidly expanded in the middle of the last century, is now reaching a critical age with widespread signs of deterioration and inadequate functionality. In the USA for instance, at the turn of the century, about 35% of the over 580,000 bridges were considered structurally deficient [1]. Deficiencies commonly identified, by Karbhari [2] among others, have been 1) deck deterioration due to wear, deicing salt, temperature gradient, etc., 2) corrosion of steel members, 3) corrosion of concrete steel reinforcements and 4) ageing and deterioration of concrete. An innovative, cost-effective and technologically driven solution to these challenges is the use of FRP composites.

Typical advantages of FRP that have made it a promising construction solution in recent times are high stiffness and strength per unit weight, excellent corrosion resistance, and high fatigue performance [2]. Thanks to these advantages, the application of FRPs in bridge decks has resulted in dead load reduction and subsequent increase in live load ratings, possibility of widening bridges without imposing additional dead loads on the substructure, faster installation reducing costs and traffic congestion and enhanced service life even in harsh environments.

The first application of FRP in bridge construction was proposed by Meier [3] in the late 1980s and was limited to the strengthening of existing reinforced concrete bridges. Based on his design, CFRP laminates were used for the strengthening of the Ibachbrucke Bridge in Lucerne, Switzerland. Later in the early 90s, Meier's strengthening method was extended to piers to resist earthquake damage [4] and prestressed systems by replacing corroded steel tendons [5]. In 1992, the first all-composite footbridge was constructed in Aberfeldy, Scotland [6]. The Aberfeldy Bridge is cable-stayed and all its components, including cables, pylons, beams, bridge decks, and railings, were manufactured from FRPs as well as the connections, which were adhesively bonded. Since then, other composite footbridges have been constructed, including the 40.3-m-span cable-stayed Kolding Footbridge in Denmark in 1997 [7] and later that same year, the 12.5-m-span Pontresina Bridge [8] in Switzerland. At the end of 2000, 16 of the 36 fully functional FRP bridges were all–composite bridges constructed for both pedestrian and vehicular traffic [9].

Parallel to FRP bridge construction, numerical and experimental investigations were performed to evaluate the structural performance of several bridge decks for an efficient and cost-effective deck configuration [10]. The decks involved had spans between 2.1-2.3 m, as

shown in Fig. 1.1 [11-14]. All the decks were modeled using finite element methods (FEM) as beams in the bridge direction and as trusses in the transverse direction. The deflection limit and not the strength was concluded to be the critical requirement in the design of FRP decks. The type II decks in Figs. 1.1a and 1.1c and type III deck in Fig. 1.1d were the most efficient since their inclined truss members exhibited the lowest deflections.
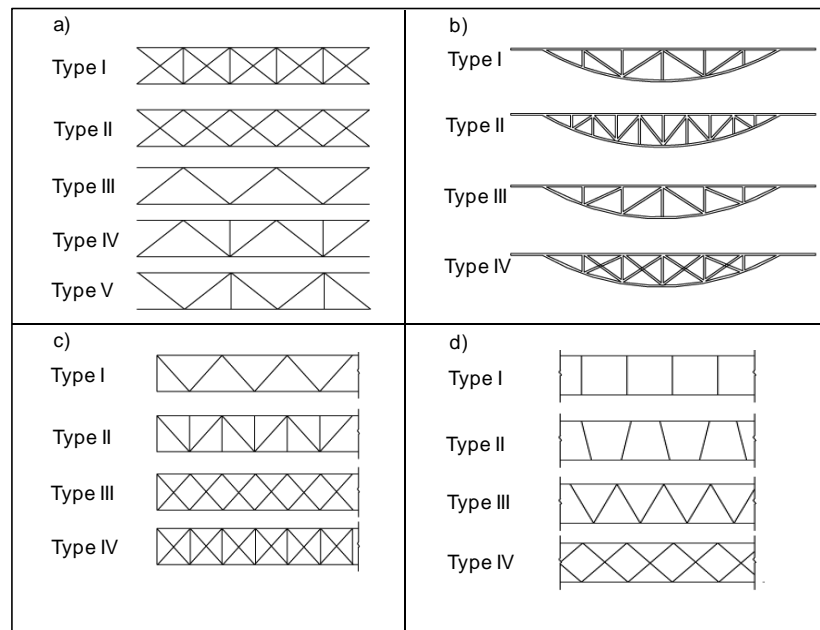
Figure 1.1: FRP deck configurations in transverse direction [10]

Further research on the above concepts resulted in the development of some commercial FRP decks manufactured from adhesively-bonded pultruded profiles. Typical commercial decks are DuraSpan [15] (see Fig. 1.2a), Asset [16] (see Fig. 1.2b), EZ-Span Harik et al. [17] and Strongwell Systems' Composite Advantage deck [18]. The application of these decks has so far been hindered mainly by their span limitation of less than 3 m [9]. Consequently, much research and most current developments have been focused into new design systems, particularly sandwich structures [9, 14], since they exhibit flexible thickness and can thus be used for longer bridge spans.
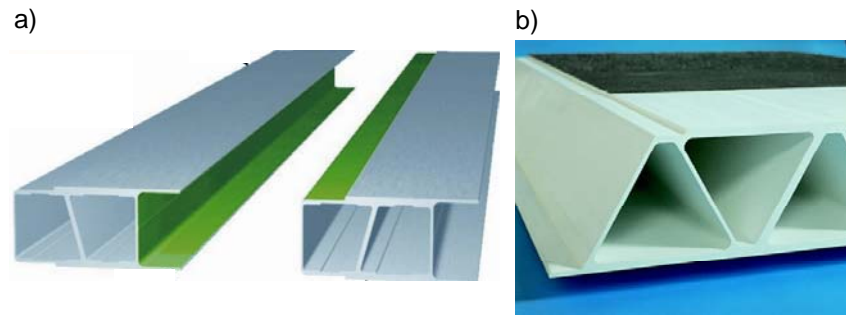
Figure 1.2: a) DuraSpan deck (Martin Marietta Composites) and b) ASSET deck (Fiberline Composites)

Sandwich decks are composed of GFRP face sheets and honeycomb or foam cores, as shown in Fig. 1.3. In the latter case, additional internal GFRP webs are normally required to provide sufficient shear resistance. These decks unfortunately do not have the adequate capacity to withstand extensive vehicular traffic loads, which may lead to indentation and also debonding between the upper face sheet and the core [19-21] as shown in Fig. 1.4. The debonding problems have been attributed to uneven support of the upper face sheet caused by the stiff webs and the flexible core or honeycomb walls and the space in between.

Figure 1.3: Sandwich decks with (a) honeycomb core (Kansas Structural Composites) and (b) foam core with internal GFRP webs (Hardcore Composites)
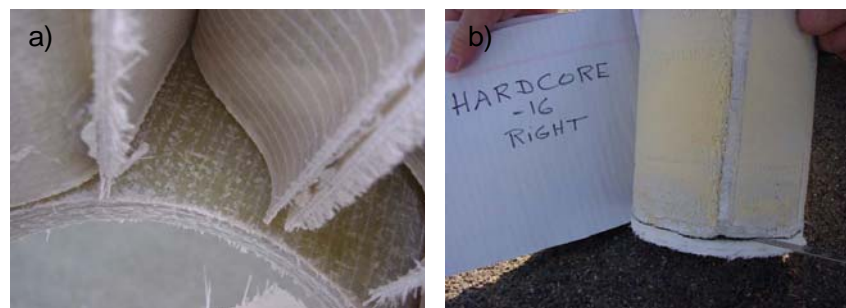
Figure 1.4: Salem Avenue Bridge, Dayton, Ohio, USA, (a) debonded face sheets from honeycomb core (Infrastructure Composite deck) and (b) debonded face sheets from web (Hardcore Composite)

In order to eliminate these drawbacks and provide a core with sufficient capacity and uniform support for the upper face sheet, a hybrid FRP-concrete sandwich bridge deck has already been proposed by Keller et al. [22]. An alternative core material able to fulfill the shear requirements and provide uniform support for the upper face sheet as well as indentation resistance is balsa [23-25], when applied in the end-grain configuration, with fibers perpendicular to the face sheets (in line with the wheel load direction). Balsa panels, however, are produced from adhesively-bonded balsa blocks [26], and although the adhesive joints may influence their shear performance, this effect has not yet been investigated. Earlier applications of balsa in sandwich decks were for secondary purposes, usually as part of the upper deck or sandwich girder components [27-29]. Recently in 2012, balsa was used as the primary core element in the Avançon Bridge deck in Bex, Switzerland [30] as shown in Fig. 1.5. The 11.45-m-span lightweight bridge is composed of a 285-mm-deep GFRP-balsa bridge deck adhesively bonded onto two steel girders. Compared to a reinforced concrete deck, this sandwich deck exhibits relatively lower bending stiffness in the bridge direction and low composite action in the deck core, due to relatively lower in-plane shear stiffness.

Figure 1.5: Installation of Avançon Bridge in Bex, Switzerland, 2012, semi-integrated balsa-GFRP sandwich deck adhesively bonded to steel main girders [30]

The purpose of this research was to improve on the core performance of the Avançon Bridge which comprises a uniform high-density balsa core, in terms of structural efficiency and deck weight in order to achieve longer bridge spans. One effective way is to use a complex core assembly. A complex core system comprising a thin FRP laminate with an arch shape that separates the core into an upper high-density balsa and a lower low-density balsa seems advantageous. The high-density balsa is required to prevent indentation and wrinkling of the upper face sheet and provides sufficient shear stiffness and strength in the deck's

support region. In the less-stressed lower zone between the supports, the low-density balsa is used to minimize the deck weight. The arch shape is an excellent choice since it starts at the supports and rises towards the mid-span maintaining a thin layer of the high-density balsa between the upper face sheet and arch interface to prevent indentation. The FRP arch can reduce the compressive load borne by the upper face sheet at the mid-span and the vertical component of its arch force can also reduce the shear load borne by the balsa core.

Furthermore, a solution for increasing the longitudinal bending stiffness and composite action between the upper and lower face sheets of the Avançon Bridge deck while maintaining the deck weight, may involve inserting a stiffer lightweight core into the balsa core above the steel girders. A timber insert with its fibers oriented in the bridge direction seems advantageous.

1.2   Objectives

The aim of this research is to develop structural concepts that can provide improved structural performance of the existing GFRP-balsa sandwich decks while maintaining an overall lightweight structure, so that longer bridge spans can be constructed, which can also replace reinforced concrete decks. In order to achieve this, the following objectives have been defined:

- Characterize the shear mechanical behavior of balsa panels to be used as core material in sandwich decks;
- Develop and understand how complex core systems work in sandwich beams and how they can be extended to sandwich decks;
- Develop models to predict the bending behavior of complex core systems;
- Implement the developed complex core systems in GFRP-balsa sandwich decks, establish the decks' structural limits and explore their potential to replace long-span reinforced concrete decks.

1.3   Methodology

To achieve these objectives, the following methodology was adopted:

- Experimental investigation of balsa panels to obtain their shear modulus and strength, including the influence of shear plane, balsa density, adhesives between balsa blocks and ductility if subjected to shear loads;

- Experimental investigation of the bending behavior of FRP sandwich beams with complex core system of high- and low-density balsa cores and integrated FRP arch (complex core system 1);

- Analysis of failure in complex balsa core of the proposed sandwich beams, using fracture mechanics;

- Development of new analytical models to predict the bending behavior of complex core systems;

- Numerical investigation of a complex core system that involves timber inserts in a balsa sandwich deck (complex core system 2) to obtain an optimum angle of termination to solve the problem of stress concentrations at balsa/timber joints and development of analytical models to predict these stress concentrations for butt and scarf core joints;

- Designing of examples to demonstrate the applicability of complex core systems in sandwich slabs and decks, with special attention paid to their span limits and potential to replace reinforced concrete decks.

1.4   Thesis organization

The research work presented in this thesis is divided into three main parts: shear characterization of balsa panel as core material of sandwich deck, development of complex core systems and application of complex core systems in sandwich bridge construction.

In the first part, balsa panels were characterized as core materials for sandwich decks. This characterization focused on their shear properties since the balsa core is subjected to shear loads in sandwich decks. A shear experimental investigation was performed on balsa panels to obtain its shear response at its three orthotropic shear planes. The main aims were to obtain the shear stiffness and strength and shear ductility of the balsa core as well as quantify the influence of shear plane, density and adhesive joints.

The second part is concerned with the development of complex core systems to be implemented in long-span sandwich decks. Two complex core systems were proposed. The first concept involves bonded high- and low-density balsa and an FRP arch integrated at the interface (complex core system 1). Sandwich beams of 2-m spans (representing a scale factor of 5 of the targeted 10-15-m bridge spans) using this concept were manufactured and examined under four-point and asymmetric three-point bending experiments to compare their bending behavior to that of a reference case of uniform high-density balsa sandwich beam.

The axial and shear strain distributions were measured and based on the material properties of balsa (from first part) and FRP laminates, the corresponding stress distributions were determined. The main aims were to evaluate the superiority of the new sandwich beams in terms of bending stiffness, strength and weight as well as quantify the shear contribution of the FRP arch. An in-depth failure analysis was also performed using the experimentally determined stresses and fracture mechanics. The main aims were to understand the crack initiation and propagation in the complex balsa core and explain the influence of block arrangement, balsa block density and adhesive bonds on the crack paths. A new multilayer model was developed to predict the deflections and stress distributions in the complex sandwich beams (complex core system 1). The results of the four-point bending experiment were used to validate the new multilayer model.

The second proposed bridge concept involves integrating timber inserts into sandwich decks (complex core system 2). Numerical investigations were performed on sandwich beams with weak/stiff core joints to evaluate their structural performance. Both butt and scarf joints were investigated. The main aims were to estimate stress concentrations that occur in face sheets and cores at the core joints and find an optimum angle of termination that can eliminate this local effect. Lap joints, which are intermediate core joints between butt and scarf joints, were developed to simulate the latter. An existing analytical model for butt joints was extended to predict the axial stress concentrations in the face sheets at the scarf joints and a new analytical model, based on lap joints, was developed to predict the shear stress concentrations in the cores at both butt and scarf joints. Numerical results, based on FEM, were used to validate the new analytical models.

The final part deals with the application of the developed complex core systems in sandwich bridge construction. The two proposed bridge concepts were implemented in two design case studies: a GFRP-balsa sandwich slab bridge based on complex core assembly (from complex core system 1) and a hybrid GFRP balsa sandwich deck-steel girder bridge based on sandwich deck with timber inserts (from complex core system 2). The balsa material properties (from first part) were implemented in the designs. The multilayer model (from second part) was used to determine deflections and stresses in the sandwich bridge slab for SLS and ULS verifications respectively. The recommended angle of termination (from second part) was used to select the core joint in the GFRP-balsa sandwich deck and the lap joint model was used to estimate the local stresses in the face sheets and timber at the balsa/timber joints, for ULS verification. The structural limits of the new GFRP-balsa sandwich bridges

were evaluated and the potential of the new sandwich deck to replace a reinforced concrete deck was finally demonstrated. The general organization of the thesis is shown in Fig. 1.4.

The following is a summary of the chapter contents:

Chapter 2: An extensive experimental investigation to establish the shear stiffness and strength and shear ductility of balsa at the three shear planes is presented. A quantification of the influence of shear plane, density and adhesive joints on the shear properties of balsa is also established. This chapter is concerned with **Paper 1** in the list of publications in Section 1.5 below.

Chapter 3: An extensive experimental investigation performed based on four-point and three-point bending methods to evaluate the bending behavior of sandwich beams with complex core of bonded high- and low-density balsa and integrated FRP arch (complex core system 1), is presented. The superiority of the new sandwich beams over existing beams with uniform high-density balsa cores in terms of stiffness, strength and weight is demonstrated as well as the quantification of the FRP arch contribution to shear resistance. This chapter is concerned with **Paper 2** in the list of publications in Section 1.5 below.

Chapter 4: An extensive failure analysis of the complex balsa core in the sandwich beams with complex core system examined in Chapter 3 is presented. The influence of balsa block arrangement, block density and adhesive joints on crack initiation and propagation is investigated. This chapter is concerned with **Paper 4** in the list of publications in Section 1.5 below.

Chapter 5: The structure of the sandwich beam proposed in Chapter 4 results in a multilayer beam system. A new analytical model, based on classical sandwich theory, to predict the axial and shear stresses in multilayer beams is presented. A validation of the model by FEM and experimental results from Chapter 3 is also presented. This chapter is concerned with **Paper 5** in the list of publications in Section 1.5 below.

Chapter 6: An extensive numerical investigation of stress concentrations at butt, lap and scarf joints in a GFRP-balsa sandwich beam with timber inserts (complex core system 2) is presented. Stress concentrations in the face sheets and cores at the butt joints and the solution to this problem by the use of scarf joints are demonstrated. An existing analytical model extended to predict axial stress concentrations in face sheets at scarf joints and a new analytical model to predict shear stress concentrations in cores at both butt and scarf joints

and their validation by numerical results are presented. This chapter is concerned with **Paper 6** in the list of publications in Section 1.5 below.

Chapter 7: The application of the complex core systems (Chapter 3 and Chapter 6) in the design of new GFRP-balsa sandwich slabs and decks is presented. The structural limits of the new decks are established and the potential of replacing a reinforced concrete deck with the new GFRP-balsa sandwich deck is demonstrated. This chapter is concerned with **Paper 7** in the list of publications in Section 1.5 below.

Chapter 8: General conclusions concerning this research are presented with emphasis on the contributions to the scientific and industrial communities. Furthermore, suggestions for future research areas in this field are given.
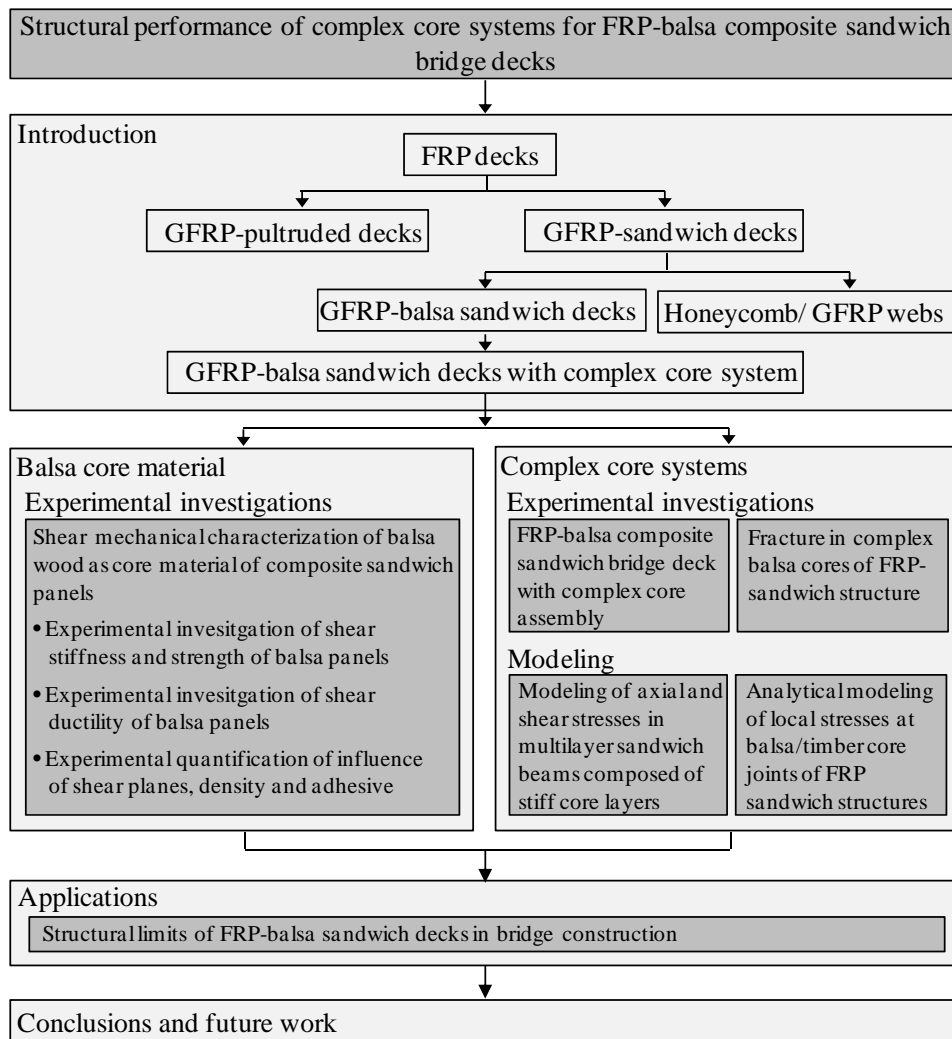

Figure 1.4: Thesis organization and methodology

1.5   List of publications

Paper 1. Osei-Antwi M, de Castro J, Vassilopoulos AP, Keller T. Shear mechanical characterization of balsa wood as core material of composite sandwich panels. Journal of Construction and Building Materials 2013; 41: 231-238.
http://dx.doi.org/10.1016/j.conbuildmat.2012.11.009

Paper 2. Osei-Antwi M, de Castro J, Vassilopoulos AP, Keller T. FRP-balsa composite sandwich bridge deck with complex core assembly. J Compos Constr 2013; 17(6); 04013011:1-9. http://dx.doi.org/10.1061/(ASCE)CC.1943-5614.0000435

Paper 3. Keller T, Rothe J, de Castro J, Osei-Antwi M. GFRP-balsa sandwich bridge deck – concept, design and experimental validation. J Compos Constr 2014
http://dx.doi.org/10.1061/(ASCE)CC.1943-5614.0000423

Paper 4. Osei-Antwi M, de Castro J, Vassilopoulos AP, Keller T. Fracture in complex balsa cores of fiber-reinforced polymer sandwich structures. Submitted to J Compos Constr, in February 2014.

Paper 5. Osei-Antwi M, de Castro J, Vassilopoulos AP, Keller T. Modeling of axial and shear stresses in multilayer sandwich beams with stiff cores. Submitted to Composite Structures, in February 2014.

Paper 6. Osei-Antwi M, de Castro J, Vassilopoulos AP, Keller T. Analytical modeling of local stresses at balsa/timber core joints of FRP sandwich structures. Submitted to Composites Structures, in February 2014.

Paper 7. Osei-Antwi M, de Castro J, Vassilopoulos AP, Keller T. Structural limits of FRP-balsa sandwich decks in bridge construction. Submitted to Composites: B, in February 2014.

References

[1] Alampalli S, O'Connor J, Arthur PY. Fiber-reinforced polymer composites for the superstructure of short-span rural bridge. Composite Structures 2002; 58(1): 21-27.

[2] Karbhari VM, Zhao L. Use of composites for 21st century civil infrastructure. Comput Methods of Appl Mech Engrg 2000; 185: 433-454.

[3] Meier U. Bruckensanierung mit Hochleistungs-Faserverbundwerk-stoffffen.Material und Technik 1987; 15: 125-128.

[4] Haf-Elsafi O, Lund R, Alampalli S. Strengthening of a bridge pier capbeam using bonded FRP composite plates Composite Structures 2002; 57: 393-403.

[5] Dorton RA, Reel R. Methods of increasing live load capacity of existing highway bridges. Transportation research board 1997; ISBN 0-309-06105-9.

[6] Burgoyne C, Head P. Aberfedly Bridge-an advanced textile reinforced footbridge. In: TechTextil symposium Frankfurt 1993; 418.

[7] Braestrup MB. Footbridge constructed from glass-fiber reinforced profiles. Struct Engrg Int 1999; 4; 256-258.

[8] Strehler B, Kunzle O. Static and dynamic testing of fiber-reinforced bridge girders. Struct Engrg Int 1999; 4; 300-301.

[9] Keller T. Recent all-composite and hybrid fibre-reinforced polymer bridges and buildings. Prog Struct Eng and Mater 2001; 3(2): 132-140.

[10] Bakeri B, Sunder SS. Concepts for hybrid FRP bridge deck system. Proceedings of 1st Materials Engineering Congress, *ASCE*, Denver, CO. 1990;1006-1014.

[11] Zihong L. Testing and analysis of a fiber reinforced polymer deck. Virginia Polytechnic Institute and State University, PhD 2007.

[12] Zureick A. Fiber-reinforced polymeric bridge decks, Proceedings of the National Seminar on Advanced Composite Material Bridges, FHWA 1997.

[13] McGhee KK, Barton FW, Mckeel WT. Optimum design of composite bridge deck panels. Adv Compos Mater Civil Engrg Struct, Proceedings of the Specialty Conference, A.S.C.E., Las Vegas, Nevada 1991; 360-370.

[14] Henry J. Deck girders system for highway bridges using fiber reinforced plastics. MS thesis, North Carolina State Univ., Raleigh, NC. 1985.

[15] Harik I, Alagusundaramoorthy P, Siddiqui R, Lopez-Anido R, Morton S, Dutta P, Shahrooz B. Static testing on FRP bridge deck panels, Proceedings of the 44th International Sampe Symposium and Exhibition, Long Beach, California, US; 1643-1654.

[16] Composites Technology. Building bridges to bridge and building rehab markets. 2008.

[17] Cassity P. Advanced composites for bridge infrastructure Renewal-Phase II DARPA. Adv Compos Tech, Transfer/Bridge Infrastructure Renewal Consortium, Vol. IV, Task 16; 2000.

[18] Luke S, Canning L, Collins S, Knudsen E, Brown P, Taljstern B, Olofsson I. Advanced composite bridge decking system. In: Struct Eng Int 2 , Adv Mater 2002; 76-79.

[19] Reising RMW, Shahrooz BM, Hunt VJ, Newmann AR Helmicki AJ, Hastak M. Close look at construction issues and performance of four fiber-reinforced polymer composites bridge decks. J Compos Constr 2004; 8(1): 33-42.

[20] Telang NM, Dumlao C, Mehrabi A, Ciolko AT, Gutierrez J. Field inspection of in-service FRP bridge decks. NCHRP (TRB)-4 report 2006; 564-Appendix 4

[21] Triandafilou LN, O'Connor JS. Field issues associated with the use of fiber reinforced polymer composite bridge decks and superstructures in harsh environments. Struct Eng Int 2010; 20(4): 409-415.

[22] Keller T, Schaumann E, Vallée T. Flexural behavior of a hybrid FRP and lightweight concrete sandwich bridge deck. Composites Part A 2007; 38(3): 879-889.

[23] Chevalier JL. Creeps and fatigue properties of end-grain balsa and other typical sandwich cores. Sandwich Constructions 2, Proc., 2nd Int. Conf. on Sandwich Constructions, Gainesville, Fl 1992; 519-539.

[24] Dai J, Hahn HT. Flexural behavior of sandwich beams fabricated by vacuum-assisted resin transfer molding. Compo Struct 2003; 61(3): 247-253.

[25] Bekisli B, Grenestedt KL. Experimental evaluation of a balsa sandwich core with improved shear properties. Compos Sci Technol 2004; 64(5): 667-674.

[26] Alcan Baltek Corporation. Data sheet. Mechanical properties vs. density and grain orientation for balsa wood, Northvale, NJ; 2001.

[27] Kosmatka JB. Structural testing of DARPA/BIR composite army bridge treadway. Compos Struct 1999; 4: 99-115.

[28] Fireco. 'Bascule FRP composite footbridge.'

(http://www.fireco.no/references/Gangbru%20Vesterelven.pdf) (Jun. 12, 2013)

[29] Verheus A. The Utrecht bridge: a 100% composite box beam design FRP bridges, Proc, Int Conf on FRP bridges London 2012; 154-165.

[30] Keller T, Rothe J, de Castro J, Osei-Antwi M. GFRP-balsa sandwich bridge deck – concept, design and experimental validation. J Compos Constr 2014.

http://dx.doi.org/10.1061/(ASCE)CC.1943-5614.0000423

2.

Experimental investigation on shear behavior of balsa panels

Balsa panel composed of balsa blocks joined by PVAc base adhesive making it a non homogenous and anisotropic material with three orthotropic shear planes

2.1 Overview

Excellent strength-to-weight and stiffness-to-weight ratios make balsa wood a preferred material for cores of sandwich structures. Sandwich panels produced with balsa core are found in major load-bearing applications such as hulls of ships and aircrafts, as reported in [1] and [2]. In bridge construction, the first attempts are underway to replace honeycomb and foam materials by the better performing balsa wood as core material for composite bridge decks, e.g. for the 56-m-span Bascule Footbridge in Norway [3]. In all cases, as core material, the balsa wood is subjected primarily to shear stresses.

In an earlier work [4], the shear properties of balsa wood were investigated using the shear lap test method according to ASTM C273 [5]. The results demonstrated the anisotropic nature of balsa wood by 14.5 % and 8 % increases in shear stiffness and strength for the longitudinal-radial (LR) plane compared to the longitudinal-transverse (LT) plane. According to Dinwoodie [6], this anisotropy of balsa wood is primarily based on the longitudinal arrangement of cells and the orientation of the microfibrils in the second layer (S_2) of the secondary wall which is an integral part of the tracheid cell wall. Similar shear properties for the LR and LT planes were obtained in [7], also employing the ASTM C273 [5] shear test method. However, lower values were observed for the radial-transverse (RT) plane. Using a shear-compression biaxial testing machine, 35 % higher strength and 100 % higher stiffness for the LR plane compared to the LT plane were found in [8].

Unlike balsa wood, which is obtained from the trunk of the tree, balsa panel production involves the adhesive joining of selected smaller cubic blocks of balsa with the fiber direction perpendicular to the panel plane as shown in Fig. 2.1. In this way, end grain balsa panels of relatively uniform density can be produced. In such panels, the relevant planes of shear stiffness and strength are the shear plane parallel to the end grain of the balsa (designated Eg plane, showing average properties of the LT and LR planes of wood), the shear plane transverse to the fiber direction (designated Fg/T and corresponding to the RT plane), and the shear plane parallel to the fiber directions (Fg/P, corresponding to the radial-longitudinal (RL) plane). Furthermore, the presence of the polyvinyl acetate (PVAc)-based adhesive joints between the lumber blocks may influence the shear response of the panels. However, till now, this effect had not been quantified.
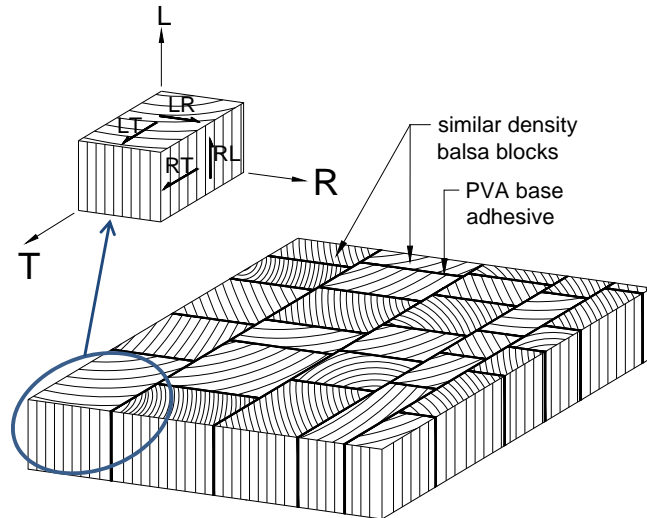
Figure 2.1: Panel composed of balsa blocks joined by PVAc base adhesive and definition of shear planes of wood

Balsa wood also exhibits a significant energy absorption capacity when subjected to compression in the fiber direction, which is attributed to the cellular/porous microstructure of the cells [8, 9]. A corresponding behavior if subjected to shear has not yet been evaluated.

As demonstrated above, experimental shear properties depend on the testing method used. Modeling the ASTM C273 [5] set-up by finite element analysis resulted in high stress concentrations at the re-entrant corners between loading plates and specimen due to bending of the loading plates [10]. In [11], it was shown that by preventing the local crushing of wood at the loading points, the Iosipescu (v-notch) method according to ASTM D5379 [12] is the best method for determining the shear properties of wood. Furthermore, comparing a torsion test method using a torsion-twist device and the Iosipescu method in [13] showed that, whilst the latter resulted in a direct shear/strain relationship, the former resulted in an indirect and complicated relationship. In addition, the shear-compression biaxial testing machine presented in [14] to examine the shear stiffness and strength of balsa wood was used in [8]. This method, however, also produced edge effects and non-uniform stresses in the specimen. Recently, a single cube apparatus for shear testing to improve the Iosipescu and other shear methods was presented in [15]. Although, this study highlighted some disadvantages of the Iosipescu method such as effects of strain gage usage on strain measurements and a complex fixture, the latter drawback has been corrected by the use of the video extensometer in this chapter.

The primary objective of this chapter is to experimentally characterize the shear stiffness and strength of end grain balsa panels as a function of density with respect to the

three shear planes: plane parallel to the end grain, Eg, plane parallel to flat grain, Fg/P, and plane transverse to flat grain, Fg/T. Furthermore, the existing knowledge gaps mentioned above are filled, such as quantification of the effect of adhesive joints on shear behavior as well as characterization of the material in terms of ductility if subjected to shear. Based on the above discussion, the Iosipescu (v-notch) method was adopted for this study and a video extensometer was used instead of strain gages for strain measurements.

2.2 Balsa wood microstructure

Balsa wood is composed of different types of cells such as tracheids (arranged longitudinally, 80-90% by vol.), parenchyma (arranged radially, 8-15% by vol.) and sap channels [8]. Tracheids are long tubular structures with in most cases irregular hexagonal cross sections. They mainly consist of cellulose, hemicelluloses and lignin, which together form the elementary fibrils [15]. The latter, aggregated into larger units by hydrogen bonds, constitute the microfibrils which are the basic elements of the cell wall layers. The tracheid cells consist of primary wall (P) and secondary wall (S) layers, as shown in Fig. 2.2 [6, 8, 16]. The secondary wall is further sub-divided into the S_1, S_2 and S_3 layers whereof the S_2 layer (of approx. 2-µm thickness) accounts for roughly 85% of the secondary wall thickness. The much thinner S_1 and S_3 layers comprise microfibrils oriented at off-axis angles of 50 to 90° while the S_2 layer has a microfibril orientation of 10 to 30° to the longitudinal axis and therefore forms the main structural layer of the whole tracheid cell. The tracheid cells are interconnected by a middle lamella, which consists entirely of lignin, a relatively brittle phenolic polymer. The middle lamella together with the primary wall (consisting of approx. 80 % of lignin) form the compound middle lamella according to Bodig and Jayne [16].

The parenchyma rays penetrate the tracheids radially and are responsible for misalignments of the latter along the tree's natural axis [9]. Sap channels, responsible for fluid transport in the tree, have thinner cell walls and are relatively larger in diameter (150 to 250 µm compared to 30 to 40 µm for tracheids). The presence of misalignments in tracheids, the periodic appearance of rays and sap channels and imperfections such as knots contribute to a significant scattering of the mechanical properties of the wood. The mechanical properties also strongly depend on the balsa density, which is mainly determined by the cell wall thickness and much less so by the cell diameter [17]. Variation of density occurs across the trunk due to the different growth of the early/spring wood and late/summer wood in each annual ring [18, 19].
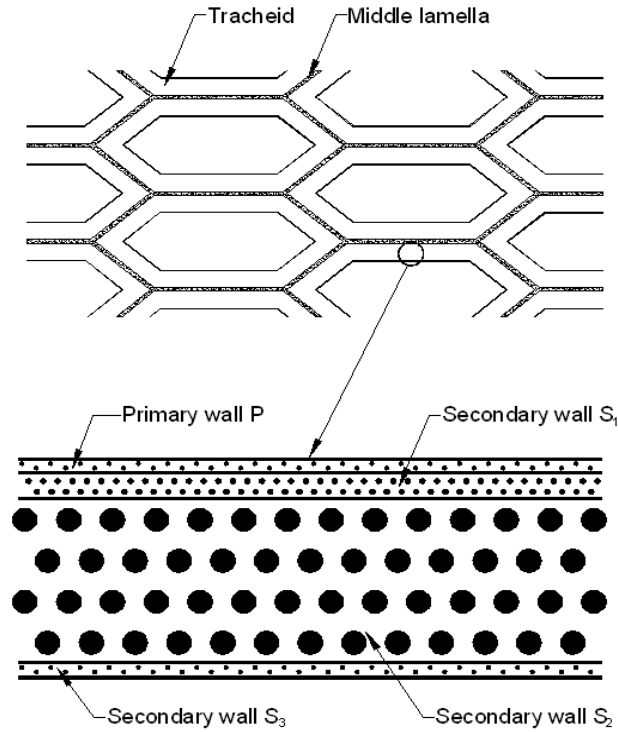
Figure 2.2: Simplified microstructure of balsa wood showing middle lamella and tracheid cells with P, S_1, S_2 and S_3 cell wall layers

2.3   Experimental investigation

2.3.1   Balsa Material

Commercial balsa panels SB 150, produced from Baltek Corporation, USA were used. The 1200 x 600 x 100-mm panels were built up from kiln-dried balsa lumber blocks of approx. 90 x 110-mm cross-sectional size, using a PVA adhesive (elastic and shear modulus of approx. 5 and 1.9 GPa) as shown schematically in Fig. 2.1. The radial and tangential directions were randomly arranged, thereby mixing the LR and LT planes. According to the manufacturer, the average density of SB 150 panels is 291 kg/m^3 with a minimum value of 197 kg/m^3. The moisture content according to ASTM 4442-07 (method A) [20] was approx. 12%.

2.3.2   Specimen description

Iosipescu specimens were cut from the panels according to the three principal shear planes, Eg, Fg/P and Fg/T, as shown in Fig. 2.3 and designated in Table 2.1. The average density of the Iosipescu specimens was 299 ± 65 kg/m^3 (similar to the manufacturer's value given above).

Table 2.1: The v-notch specimen designation and specimen

Designation	Shear plane	Adhesively-bonded joint
Eg	Parallel to end grain	None
Eg_J	Parallel to end grain	Parallel to grain at mid-height
Fg/P	Parallel to flat grain	None
Fg/P_J	Parallel to flat grain	Joining the v-notches
Fg/T	Transverse to flat grain	None
Fg/T_J	Transverse to flat grain	Joining the v-notches

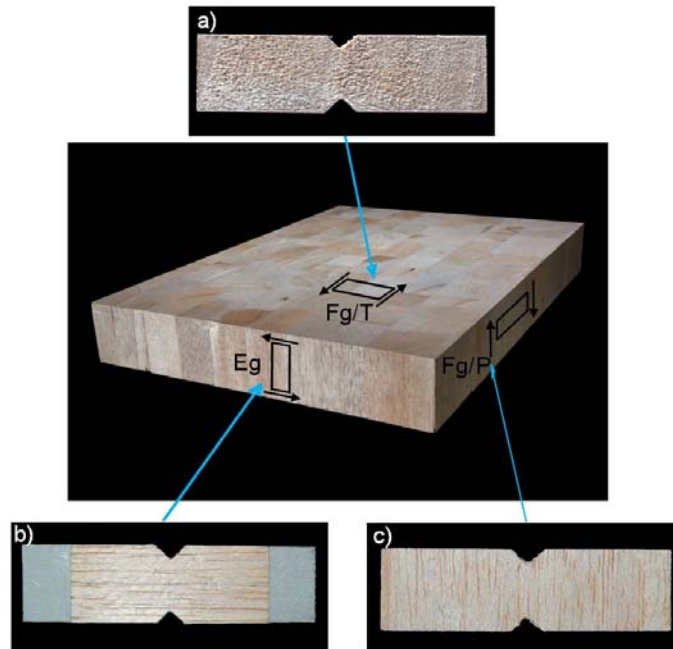*Figure 2.3: Balsa panel showing: a)shear plane transverse to flat grain (Fg/T), b)shear plane parallel to end grain (Eg specimen with tabs), and c)shear plane parallel to flat grain (Fg/P)*

Density variation is mainly caused by changes in the cell wall thickness from the thinner early wood to the thicker late wood of the trunk of the same tree or different cell wall thicknesses from different balsa trees. The specimen shape and dimensions were based on the ASTM D5379 [12], see Fig. 2.4. For each shear plane, specimens were cut with and without PVAc adhesive joints in order to evaluate the effects of the latter on the panel properties. In Eg specimens, the joints were perpendicular to the load axis at mid-height while they were located along the load axis between the two v-notches in Fg/P and Fg/T specimens. To avoid local crushing in Eg specimens (as observed in [11]) aluminum tabs of 1.5-mm thickness were bonded to the end supports, as shown in Fig. 2.3b.

Figure 2.4: Iosipescu (v-notch) specimen according to ASTM-D5379, dimensions in (mm)

2.3.3 Experimental set-up, instrumentation and program

A MTS 25-kN universal testing machine with an integrated load cell adjusted to 25% of its capacity was used. The Iosipescu fixture was mounted, as shown in Fig. 2.5. A video extensometer comprising a 10-bit Sony XCLU100 CCD camera connected to a Fujinon HF35SA-1, 35-mm f 1.4-22 lens with an accuracy of ± 0.005 mm was used to measure the shear deformations. Black target dots at the four corners of two square grids of sizes 6 and 12 mm were marked on the specimens, as shown in Fig. 2.5. The shear strains of the 12-mm grid were 7 % higher than those of the 6-mm grid due to the additional interaction with higher bending effects in the former case. These effects were minimized by taking into account only the results obtained for the 6-mm grid. The movement of the dots was recorded at a frequency of 10 Hz.

Figure 2.5: Experimental set-up, specimen with black dots for video extensometer measurements

The shear strain, γ, was obtained from the deformed shape A´B´C´D´ shown in Fig. 2.6 as follows:

$$\gamma = \alpha + \beta \tag{1}$$

where

$$\alpha = \frac{AA'}{AC} \tag{2}$$

and

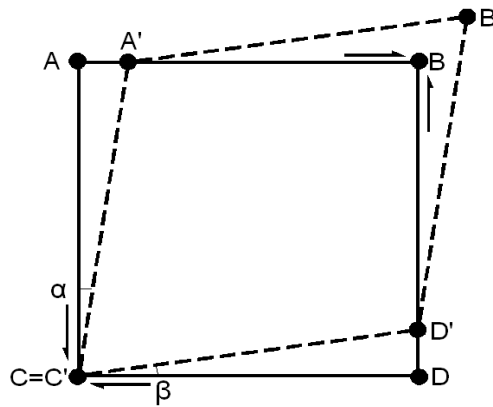$$\beta = \frac{DD'}{CD} \tag{3}$$

Figure 2.6: Angular shear deformation of video extensometer grid

One-cycle quasi-static loading was applied to 48 specimens. Tables 2.2-2.4 give an overview of these specimens (16 per shear plane, half of them with and half without joints) and their denomination (J represents joint). In specimens with joints, the densities on both sides of the joint were different. To evaluate the material ductility, a two-cycle loading was applied to a further 24 specimens (see Tables 2.5-2.7, 2.8 specimens per shear plane, without joints). These specimens were loaded up to 90 % of the estimated ultimate load. After 1 minute, unloading was performed and after another minute (during which full recovery occurred) the specimens were reloaded up to failure. Loading and unloading were performed at a 1-mm/min displacement rate under laboratory conditions (23 ± 5°C and relative humidity of 50 ± 10%).

2.4 Experimental results and discussion

2.4.1 Effect of shear planes on shear responses and failure modes

Selected representative shear stress-strain curves of each shear plane are shown in Fig. 2.7. Shear moduli were determined from the slope of the stress-strain curves over a strain range of 0.004 with the lower strain point being in the range of 0.0015 to 0.0025 (according to ASTM D5379) [12]. Shear strengths were obtained by dividing the ultimate load by the cross section between the v-notches (12 x 5 mm). The resulting shear moduli, G, and shear strengths, τ_u, are summarized in Tables 2.2-2.4 for each shear plane.
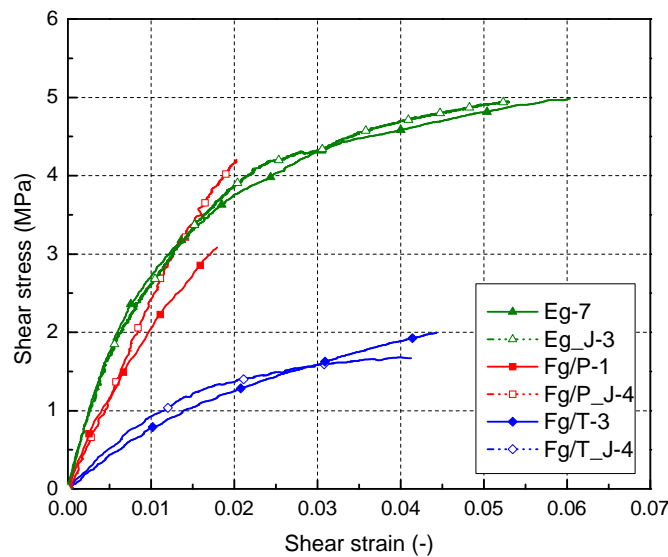

Figure 2.7: Shear stress-strain responses for similar densities (271.6-295.6 kg/m³) for Eg, Fg/P and Fg/T shear planes with and without joints

The Eg specimens showed a non-linear response - which is typical for wood [21] - and exhibited the highest shear stiffness and shear strength for a given density, see Fig. 2.7 and Tables 2.2-2.4. At failure, a first crack suddenly initiated at the root of the top notch and then propagated parallel to the tracheids, as shown in Fig. 2.8a. Initiation of a second crack at the root of the bottom notch led to the ultimate failure, which was accompanied by a loud noise. The superior stiffness and strength can be attributed to the balsa microstructure. The loading led to bending of the tracheids, which are the stiffest and strongest elements of the microstructure. At higher loads plasticization and kinking on the compression side (mechanisms according to [8]) led to a loss in stiffness. At the ultimate load, the bending caused shearing in the middle lamella between the tracheids.
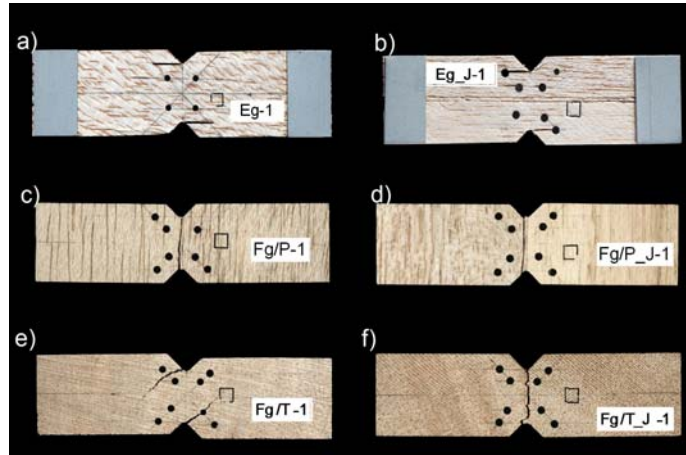
Figure 2.8:Failure mode for specimens: a) Eg-1, b) Eg_J-1, c) Fg/P_1, e) Fg/T-1 and f) Fg/T_J-1

The Fg/T specimens also exhibited a non-linear response, showing, however, the lowest shear stiffness and strength values for the same density (Fig. 2.7 and Table 2.4). Similar to Eg specimens, a first crack initiated at the root of one v-notch and subsequently a second crack developed at the adjacent root, which led to the ultimate failure of the specimens. The cracks, however, propagated at approximately 45° (see Fig. 2.8e), the failure direction in isotropic materials, to which the behavior of this shear plane can be attributed according to Tagarielli et al. [7]. The observed specimen responses can again be explained by the microstructure. Shearing in the Fg/T plane mainly led to transverse bending of the tracheid cell walls. The transverse bending stiffness of the thin cell walls, however, is much lower than the longitudinal stiffness of the tracheid ″tubes″. Similarly, the bending resistance of the cell walls is also lower. The progressive failure of the cell walls gradually decreased the shear stiffness with increasing load.

In contrast to the previous shear planes, Fg/P plane specimens showed a much more linear response and intermediate shear stiffness and strength at the same density (values between Eg and Fg/T). Failure occurred parallel to the tracheids between the roots of the two notches, see Fig. 2.8c. In this case, global shear stiffness and strength were mainly determined by the corresponding values of the middle lamella, which consists of relatively brittle lignin (see above).

Table 2.2: Shear modulus and strength for end grain plane (ρ_1 for less dense and ρ_2 for more dense half of specimens with joints)

End grain

Specimen	ρ_1[kg/m^3]	ρ_2[kg/m^3]	G[MPa]	τ_u[MPa]
Eg-1	180.3		200.5	1.8
Eg-2	187.9		281.2	3.5
Eg-3	210.2		330.2	4.1
Eg-4	229.5		190.1	2.9
Eg-5	257.3		310.7	4.3
Eg-6	289.3		410.3	4.4
Eg-7	295.6		327.1	5.1
Eg-8	379.2		414.0	4.5
Eg_J-1	253.1	261.9	250.1	3.8
Eg_J-2	210.8	399.7	440.5	5.1
Eg_J-3	271.6	273.0	386.3	4.9
Eg_J-4	233.9	436.0	554.7	6.0
Eg_J-5	228.9	400.2	290.2	4.5
Eg_J-6	246.0	330.4	438.0	4.5
Eg_J-7	296.3	334.9	336.2	4.5
Eg_J-8	276.7	436.0	472.4	7.2
Mean (Eg)	253.7		308.0	3.9
Mean (Eg_J)	252.2	359.0	396.1	5.1
SD (Eg)	66.5		83.4	1.1
SD (Eg_J)	28.1	69.1	100.7	1.1
CV (Eg)	26.2		27.1	28
CV (Eg_J)	11.2	19.2	25.0	21

Table 2.3: Shear modulus and strength for plane parallel to flat grain (ρ_1 for less dense and ρ_2 for more dense half of specimens with joints)

Flat grain parallel

Specimen	ρ_1[kg/m^3]	ρ_2[kg/m^3]	G[MPa]	τ_u [MPa]
Fg/P-1	274.2		242.7	3.3
Fg/P-2	281.6		213.6	2.8
Fg/P-3	303.0		232.4	3.5
Fg/P-4	310.4		264.0	4.0
Fg/P-5	311.2		227.8	3.5
Fg/P-6	316.6		252.4	3.5
Fg/P-7	415.1		380.1	6.0
Fg/P-8	424.9		334.6	6.0
Fg/P-J-1	196.4	323.3	148.9	1.7
Fg/P-J-2	212.6	281.2	181.3	2.0
Fg/P-J-3	249.6	375.7	210.2	2.6
Fg/P_J-4	282.1	292.1	271.2	4.1
Fg/P_J-5	275.2	332.1	260.0	4.5
Fg/P_J-6	358.0	390.5	380.1	5.6
Fg/P_J-7	375.3	410.9	446.0	6.1
Fg/P_J-8	417.7	438.8	450.4	6.6
Mean (Fg/P)	329.6		268.5	4.0
Mean (Fg/P_J)	295.9	355.6	293.5	4.2
SD (Fg/P)	57.8		58.2	1.2
SD (Fg/P_J)	79.8	57.0	118.9	1.9
CV (Fg/P)	17.5		22.7	30
CV (Fg/P_J)	27.0	16.0	40.2	46

Table 2.4: Shear modulus and strength for plane
transverse to flat grain (ρ_1 for less dense and ρ_2 for
more dense half of specimens with joints

Flat grain transverse

Specimen	$\rho_1[kg/m^3]$	$\rho_2[kg/m^3]$	G[MPa]	τ_u [MPa]
Fg/T-1	174.0		46.6	0.9
Fg/T-2	186.4		41.1	1.1
Fg/T-3	280.1		86.4	2.1
Fg/T-4	323.5		82.2	2.0
Fg/T-5	328.9		150.5	2.8
Fg/T-6	354.7		153.0	3.5
Fg/T-7	355.6		130.6	3.4
Fg/T-8	374.7		129.1	3.9
Fg/T_J-1	246.3	361.9	133.9	1.5
Fg/T_J-2	253.7	366.1	102.6	1.7
Fg/T_J-3	260.6	368.0	105.1	1.7
Fg/T_J-4	295.2	345.5	119.5	1.5
Fg/T_J-5	296.3	351.6	129.2	1.2
Fg/T_J-6	298.9	337.8	152.0	2.1
Fg/T_J-7	302.6	333.3	126.1	2.1
Fg/T_J-8	310.3	345.0	166.4	1.7
Mean (Fg/T)	297.2		102.4	2.5
Mean (Fg/T_J)	283.0	351.2	129.4	1.7
SD (Fg/T)	77.6		44.6	1.1
SD (Fg/T_J)	25.1	13.0	21.6	0.3
CV (Fg/T)	26.1		43.5	46
CV (Fg/T_J)	8.9	3.7	16.8	17

2.4.2 Effect of density on shear stiffness and strength

The dependence of shear stiffness and strength on the density is shown in Figs. 2.9a and 2.9b for the three shear planes. In the case of specimens with joints, the average density of the balsa on both sides of the joint was selected for shear stiffness while for strength only the lower density was considered (where failure occurred). In both plots, shear properties increase at a similar rate, maintaining the sequence Eg, Fg/P, Fg/T from highest to lowest values along the density axis. In the Eg and Fg/T cases, where both shear properties directly depend on the cell wall stiffness and strength (see previous section), this dependence of density is obvious since the density mainly depends on the cell wall thickness (see above). In the case of Fg/P planes, shear properties are controlled by the compound middle lamella comprising the true

middle lamella and the primary wall, with the latter forming an integral part of the tracheid cell wall, which increases in thickness with an increase in density.

Figure 2.10 shows the shear strength vs. stiffness relationship, normalized by the density - thus eliminating the major effect of the cell wall thickness. The results should in fact be concentrated in a cluster of points for each shear plane. With the exception of the Eg plane (which combines the shear properties of LT and LR planes), this is confirmed by the fairly limited dispersion of the resulting clusters. The properties again follow the order from high to low for Eg, Fg/P and Fg/T planes.
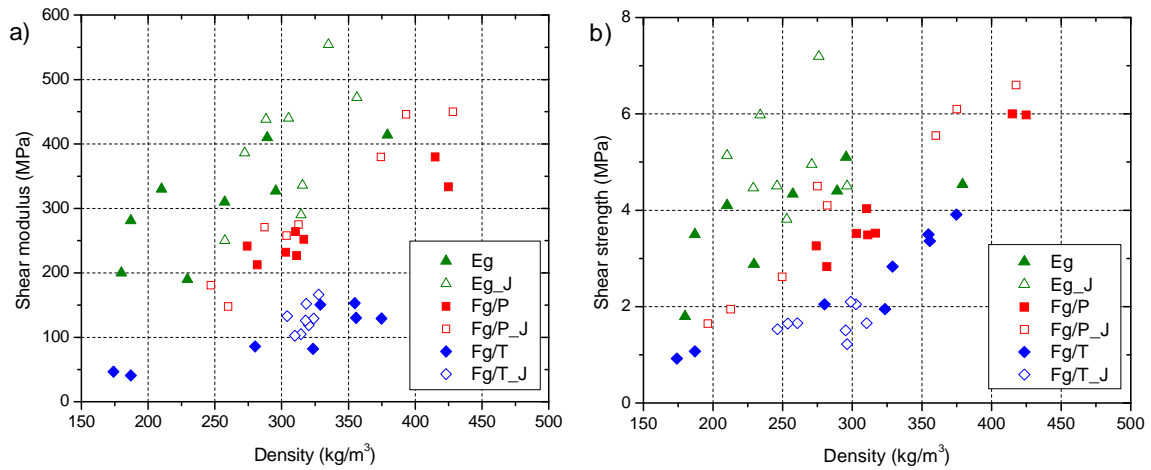
Figure 2.9: a) shear modulus vs. density and b) shear strength vs. density for all shear planes
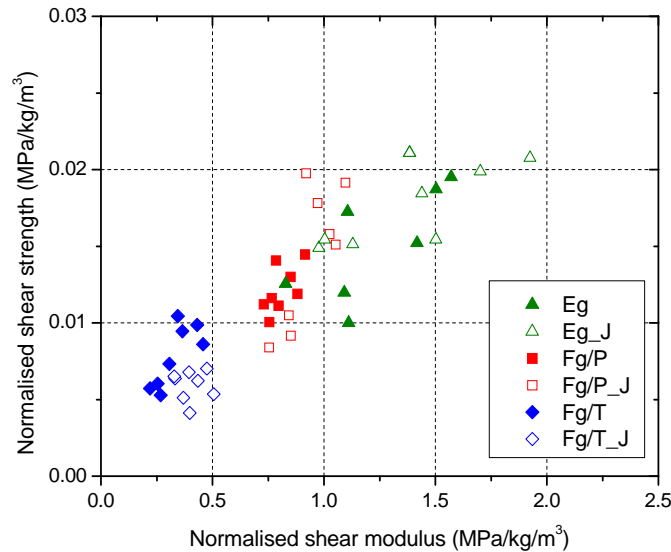
Figure 2.10: Normalised shear strength vs. Shear stiffness for all shear planes

2.4.3 Effect of adhesive joints on shear stiffness and strength

The Eg_J specimens with joints exhibited higher shear stiffness (29 %) and strength (31 %) than specimens without joints, as shown in Figs. 2.9a and 2.9b and Table 2.2. Since the joints in these specimens were located along the horizontal axis between the v-notches, the average value of the upper and lower densities (ρ_1 and ρ_2 in Table 2.2) was taken into account. The dependency of stiffness and strength on the density was the same as without joints. The failure mechanism was not affected by the joints and thus comparable to that without joints, see Fig. 2.8b. However, the first crack always appeared on the lower density side.

The Fg/T_J specimens showed higher shear stiffness (26 %) but lower shear strength (32 %) than Fg/T specimens, again see Figs. 2.9a and 2.9b. The higher shear stiffness could be attributed to the much stiffer adhesive layer in the critical section between the v-notches. The failure mode changed compared to specimens without joints, see Fig. 2.8f. Failure mainly occurred in the interface between the adhesive and lower density balsa between the two v-notches. In fact, in cutting the balsa blocks before they were adhesively bonded together during manufacturing of the balsa panels, the tracheids became truncated and the contact surface was reduced to the cell wall areas in the worst case. This weakening of the adhesive bond resulted in a change of the failure mode and a decrease of the ultimate load compared to specimens without joints. Stiffness and strength also increased with increasing density since both properties depended on the cell wall thickness.
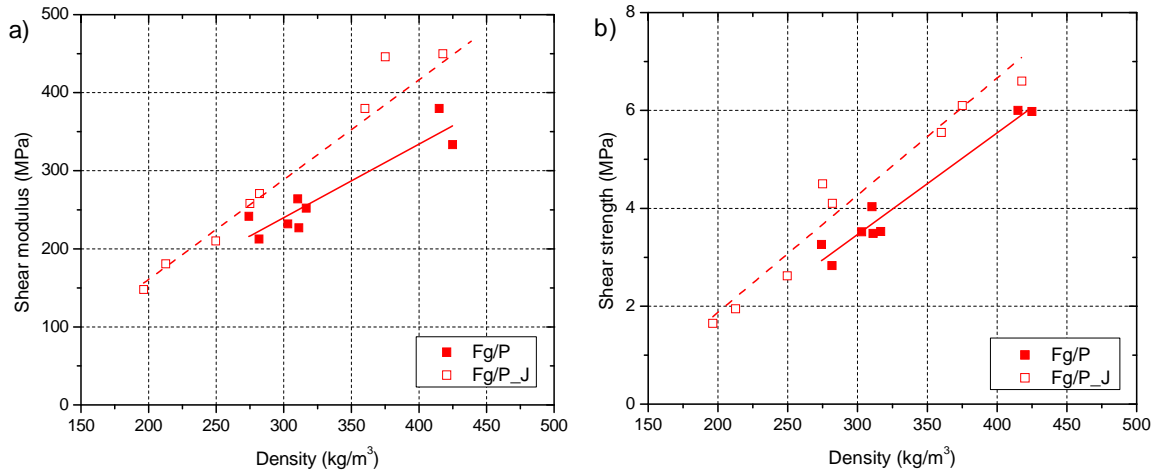

Figure 2.11: a) shear modulus vs. density and b) shear strength vs. density for Fg/P plane with and without joint

Similar to Eg_J specimens, Fg/P_J specimens exhibited slightly higher shear stiffness (9 %) and strength (5 %) compared to Fg/P specimens, as shown in Figs. 2.11a and 2.11b. The higher stiffness could be attributed to the higher adhesive stiffness in the joint between the v-notches (similar to Fg/T_J specimens). The failure mode remained basically the same as without joints, however, the failure plane was shifted away from the v-notch axis (where the adhesive was situated) into the lower-density balsa, see Fig. 2.8d. The shear area was thus slightly increased, which led to a higher ultimate failure load.

2.4.4   Material ductility

Figure 2.12 shows selected and representative shear stress-strain responses of loading-unloading-reloading cycles for all three shear planes. Material ductility is represented by the capacity to dissipate inelastic energy. The dissipated inelastic energy is proportional to the area between the loading and reloading curves computed at 90 % of the ultimate failure load, i.e. 90% of the resulting shear strength, τ_u, shown in Fig. 2.13 [22].
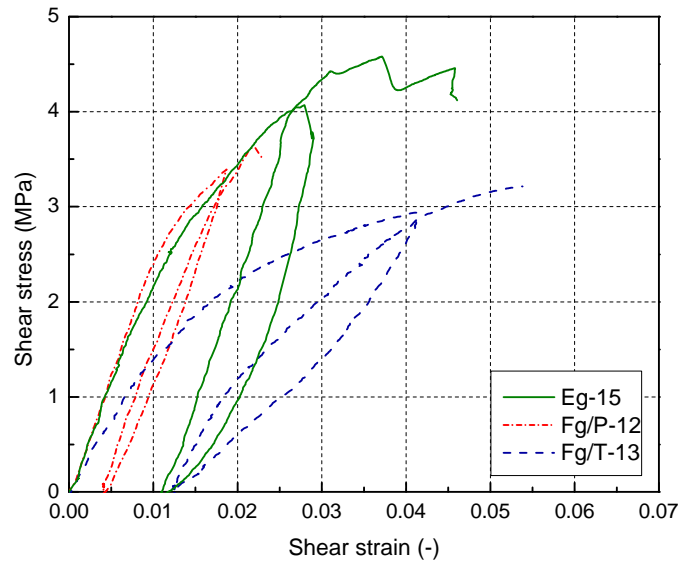
Figure 2.12: Shear stress vs strain loading and unloading cycles for all shear planes
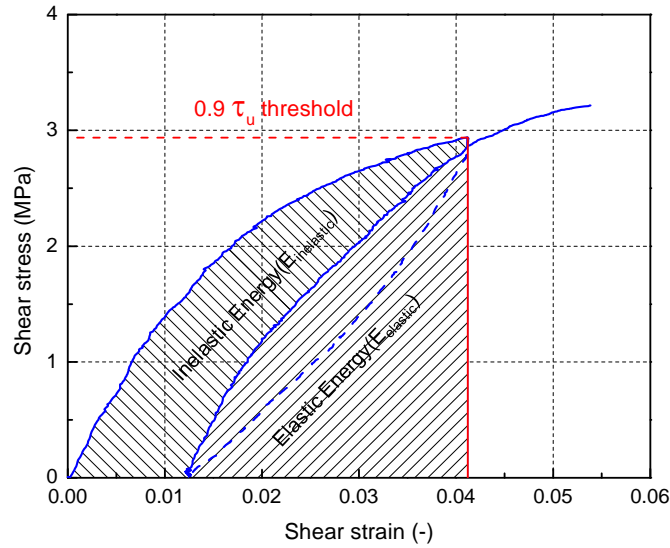
Figure 2.13: Typical shear stress vs strain for loading and unloading cycles showing inelastic and elastic energies

To compare the different planes, the ductility index, μ, according to Naaman and Jeong [23] was calculated as follows:

$$\mu = \frac{1}{2}\left(\frac{E_{total}}{E_{elastic}} + 1\right) \tag{4}$$

where E_{total} is the sum of the elastic energy, $E_{elastic}$, (which is the integration of the area under the reloading curve also up to 90 % of the ultimate failure load) and the inelastic energy, $E_{inelastic}$, as defined in Fig. 2.13. The resulting values are summarized in Tables 2.5-2.7 for the three shear planes. The Eg specimens exhibited the highest ductility index, which can be attributed to the plastic bending and kinking of the tracheids. Fg/P specimens showed the lowest index, which can be attributed to the relatively brittle lignin of the middle lamella (see above). Fg/T specimens were in between. Inelastic energy was dissipated by the plastic transverse bending of the tracheid cell walls.

Figure 2.14 also shows that the ductility indices are almost independent of density, i.e. the cell wall thickness did not change the capacity to dissipate inelastic energy.

Table 2.5: Energy dissipation and ductility index data for end grain plane

End grain					
Specimen	$\rho[kg/m^3]$	E_{total}	$E_{elastic}$	$E_{inelastic}$	μ
Eg-10	207.5	0.043	0.026	0.017	1.33
Eg-11	238.1	0.092	0.050	0.042	1.42
Eg-12	244.7	0.063	0.045	0.018	1.20
Eg-13	257.3	0.069	0.032	0.037	1.58
Eg-14	312.8	0.071	0.058	0.013	1.11
Eg-15	323.4	0.071	0.037	0.034	1.46
Eg-16	357.9	0.137	0.058	0.079	1.68
Eg-17	438.5	0.182	0.106	0.076	1.36
Average	297.5	0.091	0.052	0.040	1.39
SD	76.0	0.046	0.025	0.026	0.19

Table 2.6: Energy dissipation and ductility index data for plane parallel to flat grain

Flat grain parallel					
Specimen	$\rho[kg/m^3]$	E_{total}	$E_{elastic}$	$E_{inelastic}$	μ
Fg/P-10	283.9	0.025	0.018	0.007	1.19
Fg/P-11	302.0	0.036	0.031	0.005	1.08
Fg/P-12	307.5	0.031	0.030	0.001	1.02
Fg/P-13	309.7	0.069	0.059	0.010	1.08
Fg/P-14	310.3	0.022	0.020	0.002	1.05
Fg/P-15	342.6	0.055	0.051	0.004	1.04
Fg/P-16	357.9	0.037	0.035	0.002	1.03
Fg/P-17	415.2	0.087	0.063	0.024	1.19
Average	328.6	0.045	0.038	0.007	1.09
SD	42.1	0.023	0.017	0.008	0.07

Table 2.7: Energy dissipation and ductility index data for plane transverse to flat grain

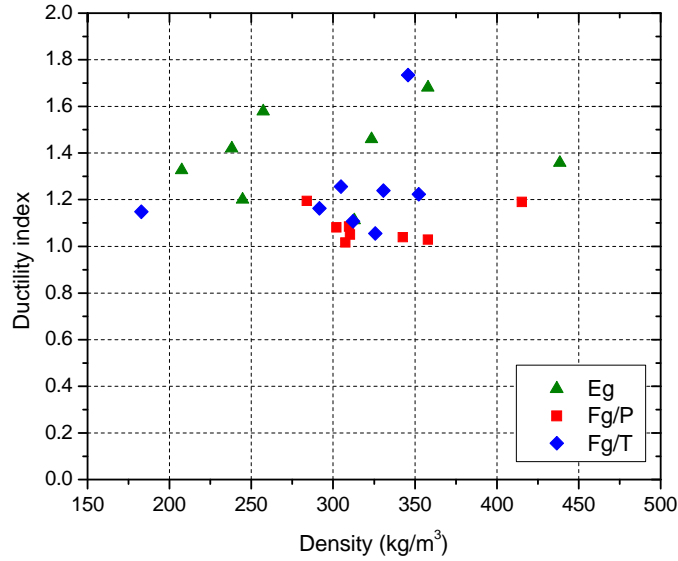| Flat grain transverse					
Specimen	$\rho[kg/m^3]$	E_{total}	$E_{elastic}$	$E_{inelastic}$	μ
Fg/T-10	182.8	0.035	0.027	0.008	1.15
Fg/T-11	291.7	0.061	0.046	0.015	1.16
Fg/T-12	304.8	0.068	0.045	0.023	1.26
Fg/T-13	312.0	0.017	0.014	0.003	1.11
Fg/T-14	325.8	0.040	0.036	0.004	1.06
Fg/T-15	330.7	0.034	0.023	0.011	1.24
Fg/T-16	345.8	0.237	0.096	0.141	1.73
Fg/T-17	352.3	0.081	0.056	0.025	1.22
Average	305.7	0.072	0.043	0.029	1.24
SD	53.6	0.070	0.025	0.046	0.21

Figure 2.14: Ductility index vs. density for all shear planes

2.5 Conclusions

Balsa wood is a lightweight material that is often used as a core material in sandwich structures. In this application the main loading case is shear. Due to the anisotropic nature of the material, the shear stress-strain behavior depends on the shear plane. An experimental study was performed using Iosipescu specimens to evaluate the effects of the shear plane, density and adhesive joints on the shear stiffness and strength of the balsa panels. The observed failure modes and material ductility, which varied depending on the shear plane, were attributed to the balsa microstructure. The following conclusions were drawn:

1) The shear planes exerted a significant effect on shear stiffness and strength. Highest values were obtained for the Eg shear plane (parallel to end grain), intermediate values for the Fg/P plane (parallel to flat grain) and lowest values for the Fg/T plane (transverse to flat grain).

2) Shear stiffness and strength increased with increasing density of the balsa. Since density mainly depends on the tracheid cell wall thickness, this result could be attributed to the microstructure.

3) The thin adhesive joints in the balsa panels between the lumber blocks slightly increased the shear stiffness and strength with one exception: the strength of Fg/T-J specimens was reduced because of a change in the failure mode.

4) Due to plastic deformations in the tracheids, Eg and Fg/T specimens exhibited significant ductility. The ductility of Fg/P specimens was less pronounced because it was affected by the relatively brittle lignin material of the middle lamella.

The results exhibited relatively large variations due to the natural and anisotropic characteristics of the material. In order to obtain reliable fractile values as a basis for design, the database has to be significantly extended.

References

[1] Cantwell WJ, Davies PJ. A study of skin-core adhesion in glass fibre reinforced sandwich materials. Appl Compos Mater 1996; 3: 407-420.

[2] Grenestedt KL Bekisli B. Analysis and preliminary tests of balsa sandwich core with improved shear properties. Int J Mech Sci 2003; 45: 1327-1346.

[3] http://www.fireco.no/references/Gangbru%20Vesterelven.pdf, 2003.

[4] Feichtinger KA. Test methods and performance of structural core materials - 1. static properties. J Reinf Plast Compos 1989; 8: 334-357.

[5] Dinwoodie JM. Timber-a review of the structure-mechanical property relationship. J Microsc 1987; 104 (1) 3-32.

[6] ASTM Standard C 273-94. Standard test method for shear properties of sandwich core materials. American Society of Testing and Materials, 1994.

[7] Tagarielli VL, Dashpande VS, Fleck NA, Chen C. A constitutive model for transversely isotropic foams, and its application to the indentation of balsa woods. Int J Mech Sci 2005; 47 (1): 666-686.

[8] Silva AD, Kyriakides S. Compressive response and failure of balsa wood. Int J Solids and Struct 2007; 44: 8685-8717.

[9] Vural M, Ravichandran G. Dynamic response and energy dissipation characteristics of balsa wood: experiment and analysis. Int J Solids and Struct 2003; 40: 2147-2170.

[10] Soden PD, McLeish RD. Variables affecting the strength of balsa wood. J Strain Anal and Eng Des 1976; 11(4) 225-234.

[11] Yoshihara H, Ohsaki H, Kubojima Y. Applicability of the shear test on the measurement of the shear properties of wood. J Wood Sci 1999; 45: 24-29.

[12] ASTM Standard D 5379/D5379M-05. Test method for shear properties of composite materials by the V-notched beam method. American Society of Testing and Materials, 2005.

[13] Yoshihara H, Ohsaki H, Kubojima Y, Ohta M. Comparisons of shear stress/shear strain relations of wood obtained by Iosipescu and torsion tests. Wood Fiber Sci 2001; 33 (2): 275-283.

[14] Vogler TJ, Kyriakides S. Inelastic behavior of an AS4/PEEK composite under combined transverse compression and shear. Part I: experiments. Int J Plast. 1999b; 15: 783-806.

[15] Hassel BI, Berard P, Moden CS, Berglund LA. The single cube apparatus for shear testing – Full-field strain data and finite element analysis of wood in transverse shear. Compos Sci Technol 2009; 69: 877-882.

[16] Bodig J, Jayne BA. Mechanics of wood and wood composites. Reprint ed. New York: Krieger Publishing Company; 1993.

[17] Easterling KE, Harrysson R, Gibson LJ, Ashby MF. On the mechanics of balsa and other woods. Proc R Soc London Ser A, Math Phys Sci, 1982; 383 (1784): 31-41.

[18] Kahle E, Woodhouse J. The influence of cell geometry on the elasticity of softwood. J Mater Sci 1994; 29 1250-1259.

[19] Panshin A J, de Zeeuw C. Textbook of wood technology. 2nd ed. USA: McGraw-Hill Book Company; 1964.

[20] ASTM Standard D 4442-07, standard test method for direct moisture content measurement of wood and wood base materials. American Society of Testing and Materials, 2007.

[21] Xavier JC, Garrido NM, Oliveira M, Morais JL, Camanho PP, Pierron F. A comparison between the Iosipescu and off-axis shear test methods for the characterization of Pinus Pinaster Ait. Composites Part A 2004; 35: 827-840.

[22] De Castro J, Keller T. Design of robust and ductile FRP structures incorporating ductile adhesive joints. Composites Part B 2010; 41: 148-156.

[23] Naaman AE, Jeong SM. Structural ductility of concrete beams prestressed with FRP tendons. Non-metallic (FRP) Reinforcement for Concrete Structure, Ghent, Belgium: RILEM Symposium (FRPRCS) 1995: 379-386.

3.

Complex core system 1: FRP-balsa sandwich beams-experimental investigation
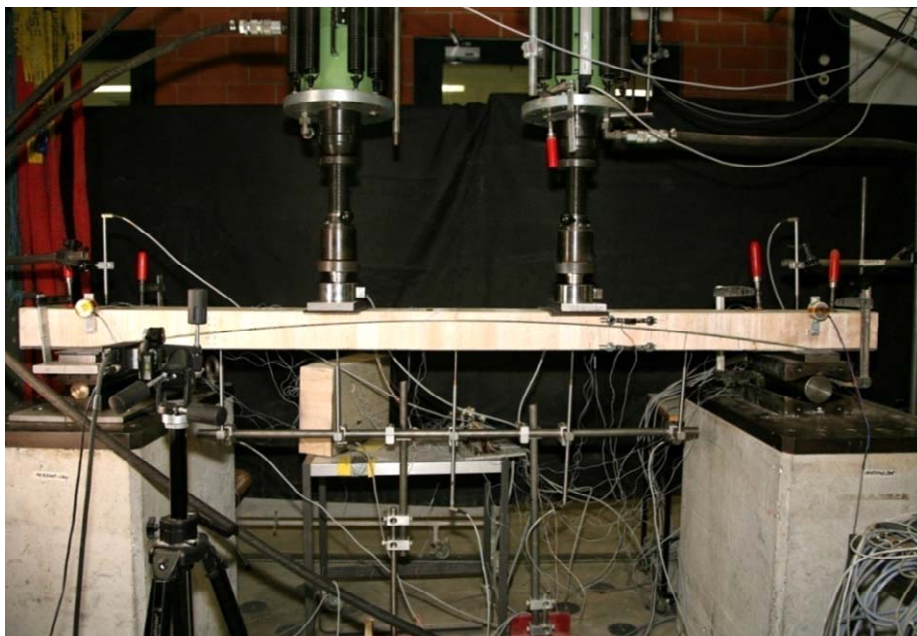
Experimental set-up for sandwich beams with complex core system consisting of upper high-density and lower low-density balsa and a FRP arch inserted into the high/low density interface

3.1 Overview

The construction of highway bridge decks using glass fiber-reinforced polymer (GFRP) materials has increased in recent years due to favorable characteristics such as high strength per unit weight, resistance to corrosion, excellent fatigue performance, increased live load ratings for applications on existing bridges and rapid field installation with minimized traffic disruptions. Based on current construction principles, GFRP decks can be categorized into pultruded and sandwich decks. In the first case, pultruded structured shapes (GFRP profiles) are adhesively bonded together to form orthotropic slabs with the pultrusion direction spanning transversely across the bridge's longitudinal girders [1-5]. Sandwich decks are composed of GFRP face sheets and honeycomb or foam cores. In the latter case, additional GFRP webs are normally required to provide sufficient shear capacity of the core [6-8]. Sandwich decks may exhibit significant technical advantages over pultruded decks such as less orthotropy and variable deck depths to allow longer spans, skew shapes and adaptation to transverse slope requirements. However, the honeycomb structure or the internal GFRP webs in the foam core configuration provide a support of non-uniform stiffness for the upper face sheet, which – under frequent wheel loads – may lead to the debonding of the upper face sheet from the core [9-11].

To overcome this drawback, i.e. to provide a core with sufficient shear capacity and uniform support for the upper face sheet, a hybrid FRP-concrete sandwich bridge deck with a lightweight-concrete core has already been proposed by Ref. [12]. An alternative core material able to fulfill the shear requirements is balsa wood, when applied in the end-grain configuration, i.e. with the wood fibers perpendicular to the upper face sheet (in-line with the wheel load direction, [13-16]. The earliest applications of balsa cores in sandwich bridge decks were for military bridges such as the light weight (43 kN) 12.2-m-long deployable Composite Army Bridge (CAB). Since 1999, the CFRP-balsa bridge deck of the CAB has experienced more than 20'000 military vehicle crossings of weights up to 907 kN [17]. A CFRP-balsa core sandwich has also been used as the deck of the 56-m span bascule footbridge in Arendal, Norway [18]. Furthermore, a 12-m-long and 5-m-wide pedestrian and light vehicular traffic bridge in Utrecht (NL) was assembled from an upper GFRP-balsa sandwich deck and adhesively bonded GFRP girders [19]. More recently, the Avançon Bridge, a 285-mm-deep GFRP-balsa bridge deck has been built in Bex, Switzerland, see Fig. 3.1 [20]. The 7.5-m-wide deck with a skew angle of 65° was adhesively bonded to two steel girders of 11.45-m span and transverse concrete end-beams to form a semi-integral bridge.

Figure 3.1: Installation of Avancon Bridge in Bex, Switzerland, 2012, semi-integrated balsa-GFRP sandwich deck adhesively bonded to steel main girders

Since balsa wood is available in different densities and thus offers different mechanical properties and furthermore can easily be cut into complex shapes by CNC milling, complex core assemblies using balsa of different densities – which can be tailored to the core stress state – can quite easily be fabricated. An end-grain high-density balsa is required to prevent indentation and wrinkling of the upper face sheet and provide sufficient shear strength and stiffness in the support region of the deck. In the less-stressed lower zone between the supports, however, a low-density balsa can be used to also minimize the deck weight. To separate the upper high-density balsa (bonded to the upper face sheet) from the lower low-density balsa (bonded to the lower face sheet) an arch is an advantageous interface shape. The arch shape starts at the supports and rises towards mid-span maintaining a thin layer of high-density balsa between upper face sheet and shell interface in order to prevent indentation of the former. To further reduce the shear load borne by the core, a thin FRP laminate layer can be inserted into the arch interface between the high- and low-density balsa. The vertical components of the FRP arch force thereby reduce the shear load borne by the balsa core.

Based on the Avançon Bridge design with uniform high-density end-grain balsa core, the aim of this work was to investigate to what extent core performance could be improved in terms of structural efficiency and deck weight thanks to a more complex core assembly in order to also be applicable for slab-bridges with spans up to 15 m and slab thicknesses up to 50-70 cm. Quasi-static load-bearing experiments on sandwich arch beams with core assemblies as described above were thus performed. Symmetric four-point and asymmetric three-point loading was applied, the latter representing an unfavorable loading for a

symmetric arch. Reference beams comprising either simple/homogeneous high- or low-density cores were also investigated.

3.2 Detailed beam description

3.2.1 Configuration and dimensions

Five different beam configurations have been investigated, see Fig. 3.2 and Table 3.1. Three beams were fabricated for each configuration – 15 beams in total. Two basic types were conceived: arch-type beams (A-beams in the following) with a circular FRP arch in the high/low-density balsa core interface and presumed predominant arch behavior as well as beam-type beams (B-beams) with predominant beam behavior. The circular arch shape was selected to facilitate manufacturing – from the structural point of view, a parabolic shape would be preferable. In all configurations, the lower face sheet was a 2-mm-thick CFRP (carbon-FRP) layer while a 2-mm-thick GFRP (glass-FRP) layer was applied as upper face sheet. CFRP was selected for the lower face sheet to balance the arch-thrust introduced at the two supports and was then used in all configurations to limit the number of parameters. For the arch laminate, either CFRP (configuration A-C) or GFRP (A-G) was selected.

Table 3.1: Description of different beam configuration

Beam config.	Designation	Balsa core		FRP laminates		
		Top	Bottom	Top	Arch	Bottom
Arch type	A-C	SB150	SB50	GFRP	CFRP	CFRP
Arch type	A-G	SB150	SB50	GFRP	GFRP	CFRP
Beam type	B-H/L	SB150	SB50	GFRP	----	CFRP
Beam type	B-H	SB150	SB150	GFRP	----	CFRP
Beam type	B-L	SB50	SB50	GFRP	----	CFRP
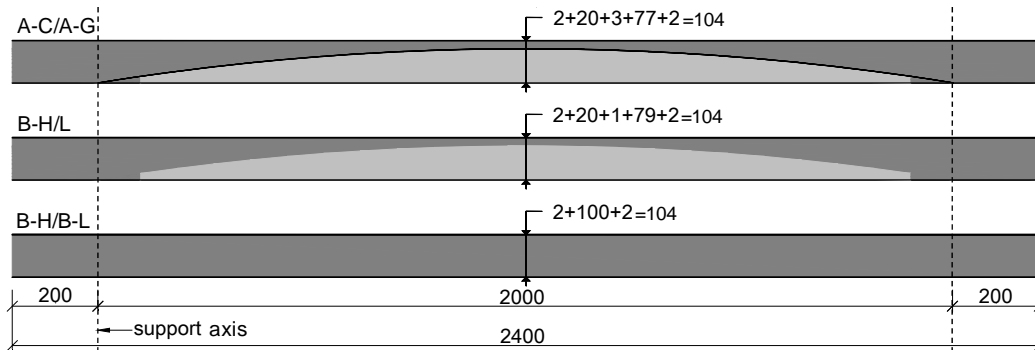
Figure 3.2: Composition/description of A-C, A-G, B-H/L, B-h and B-L beams (in mm)

The beam-type beams had either simply bonded high/low-density interfaces (without FRP, configuration B-H/L) or purely high- or low-density balsa cores (reference beams B-H and B-L). In all configurations, the support region of low-density balsa was replaced by a small, 100-mm-long tapered high-density element, see Fig. 3.3, to avoid support failure.
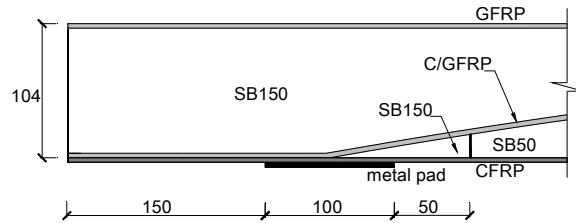
Figure 3.3: Support details showing connection between FRP arch and lower CFRP

The beam length and width were 2400 mm and 180 mm respectively. The total 104-mm beam depth was composed of the balsa core (100 mm) and face sheet thicknesses of 2x2 mm. In the case of the complex core beams, the arch laminate thickness (2 mm) and adhesive thickness (0.4-0.7 mm in B-H/L and A-G beams, 1.0-2.0 mm in A-C beams due to initially less efficient vacuum application) were compensated by the CNC-cutting in the low-density core. The minimum high-density thickness at mid-span was 20 mm.

3.2.2 Material properties

The 2-mm GFRP laminates used for all beams (face sheet and arches) consisted of ten layers of unidirectional (UD) 250-g/m^2 E-glass fabric each from Suter Kunststoffe AG (Swiss-Composite, Switzerland), resulting in a fiber volume fraction of 49%, embedded in an SR1710 inj/SD7820 epoxy resin from Sicomin Epoxy Systems, France. The 2-mm CFRP laminates were composed of nine layers of UD 200-g/m^2 carbon T-700 fabric each (resulting in 52% volume fraction) and the same resin. High- and low-density balsa core materials, designated Baltek SB150 and SB50 respectively, were obtained from 3A Composites, Sins, Switzerland. A Gurit Ampreg 22 epoxy adhesive was used to bond the high- and low-density cores. The densities and mechanical properties of the balsa and FRP laminates are listed in Tables 3.2 and 3.3. Details concerning the shear performance of the balsa materials can also be found in Ref. [21].

Table 3.2: Stiffness properties of Balsa core and FRP laminates (x=longitudinal, y=vertical, z=transverse beam direction)

Properties	Balsa SB150	Balsa SB50	UD GFRP	UD CFRP
Density (kg/m^3)	250	95	2500	1800
Longitudinal elastic modulus, E_x(MPa)	227[a]	75[a]	39000[b]	120000[b]
Out-of-plane elastic modulus, E_y (MPa)	7982[a]	1993[a]	10000[b]	10800[b]
Transverse elastic modulus, E_z (MPa)	227[a]	75[a]	10000[b]	10800[b]
Out-of-plane shear modulus, G_{xy} (MPa)	354[a]	221[a]	2400[b]	7400[b]
In-plane shear modulus, G_{yz} (MPa)	309[a]	106[a]	-	-
In-plane shear modulus, G_{xz} (MPa)	64[a]	35[a]	-	-

[a]mean values according to Ref. [22]

[b]values estimated by rule of mixtures using data sheets from Ref. [23] and Ref. [24]

Table 3.3: Strength properties of Balsa core and FRP laminates (x=longitudinal, y=vertical, z=transverse beam direction)

Properties (MPa)	Balsa SB150	Balsa SB50	UD GFRP	UD CFRP
Longitudinal compressive strength, σ_{cx}	26.3[c]	6.3[c]	290[c]	900[c]
Transverse compressive strength, σ_{cy}	1.2[c]	0.4[c]	141[b]	141[b]
Longitudinal tensile strength, σ_{tx}	23.5[c]	7.4[c]	890[a]	1420[a]
Transverse tensile strength, σ_{ty}	-	-	35[b]	42[b]
Out-of-plane shear strength, τ_{xy}	4.2[b]	1.5[c]	-	-
In-plane shear strength, τ_{yz}	5.1[d]	1.8[e]	-	-
In-plane shear strength, τ_{xz}	1.7[d]	0.4[e]	-	-

[a]estimated values from Ref. [25] and Ref. [26]

[b]values according to Ref. [26]

[c]mean values according to Ref. [22]

[d]values according to Ref. [21]

3.2.3   Beam manufacturing

The beams were manufactured in four stages: balsa core preparation, fabric lay-up, VARTM vacuum infusion and final cutting of the resulting sandwich panels into three beams each. The balsa core components were cut by CNC milling from 8 SB150 and 8 SB50 panels with standard dimensions of 1200 mm length, 600 mm width and 120 mm thickness and subsequently adhesively bonded together (vertical joints at mid-span of all beams and arch-shaped interfaces of B-H/L beams). Furthermore, grooves of about 1-mm depth were cut on the underside of the SB150 top balsa core at the centerline to create space for installing strain gages and their wires on the arches. The FRP arches were fabricated in an intermediate step: the lower balsa core together with the lower face sheet and arch laminate were infused first.

The upper balsa core was then bonded onto the arch laminate and cured under vacuum at 22°C for 12 hours, followed by the final infusion of the top face sheet. The weights, G, of the different beams are listed in Table 3.4.

3.3 Experimental work

3.3.1 Experimental set-up

The beams were loaded in a simple beam set-up, using a roller and a pin support, at 2000-mm span in different loading cycles up to failure, see Fig. 3.4. Two beams of each configuration (beams -1 and -2) were examined under a 4-point and the third beam (beam -3) was loaded under a 3-point asymmetric set-up using hydraulic jacks of 150-kN capacity each. In the 4-point set-up, the loads were applied at the third points of the span, while in the 3-point arrangement the left jack was removed. Displacement control at a rate of 5 mm/min was used for loading and unloading. The first cycle always went up to the serviceability limit state (SLS load, P_{SLS}), corresponding to a mid-span deflection of 4 mm (span/500 ratio). Therefore SLS loads slightly varied according to beam configuration and loading type, see Table 3.4.
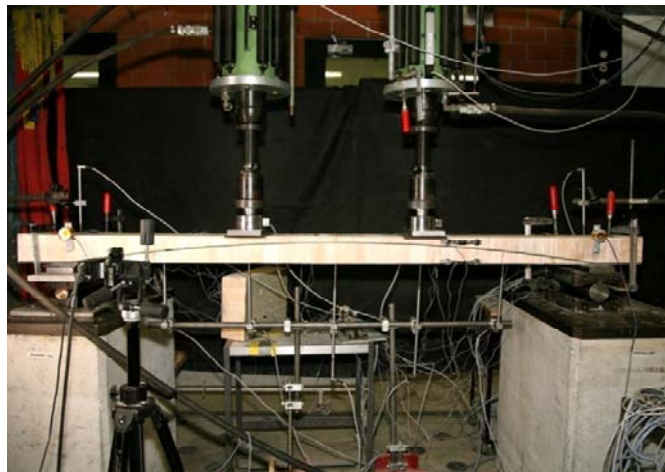
Figure 3.4: Experimental set-up for beam A-G-1 with GFRP arch integrated in balsa core

3.3.2   Instrumentation and measurements

The loads were measured by 50-kN Wagezelle load cells, placed between the jacks and the beam. The deflections were monitored by two WA/100-mm and five WA/50-mm linear voltage displacement transducers (LVDTs) on the underside and on the top of the beams at axes B, E, G, H, I, K and N, see Fig. 3.5.
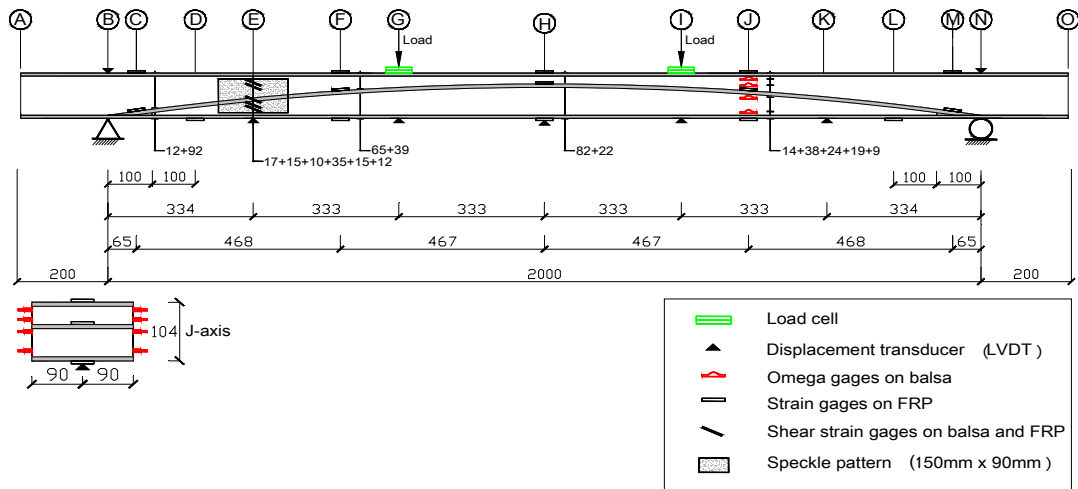
Figure 3.5: Fully instrumented A-G-2 with cross section at J-axis

The axial strains in the face sheets and arch were obtained by ten (in the case of beams B-beams) and fifteen (A-beams) HBM 1-LY11-6/120 strain gages at axes C, D, F, H, J, K, L and M. Axial deformations of the core were measured using four PI-2-100 Omega gages of 100-mm gage length with 350 Ω resistance (manufactured by Tokyo Sokki Kenkyujo), one in the compression zone, one on each side of the arch (in A-beams, and the same locations maintained for B-beams) and another in the tension zone at axis J. A similar set of four omega gages was attached to the back face. Shear deformations through the core depth were measured by five torsional/shear (v-shaped) strain gages (type HBM 1-XY41-6/120) at axis E, see Fig. 3.6a. One of these gages was applied on the arch laminate. All measurements were recorded by a UPM 60 using Labview software. Furthermore, a stereo correlation system, comprised of two AVT Manta G-504B/C cameras, was used to capture the displacements of a 150-mm-wide and 90-mm-deep black speckled pattern applied on the core surface in the E-axis region of beams A-G-2, B-H/L-2 and B-L-2, see Fig. 3.6b.
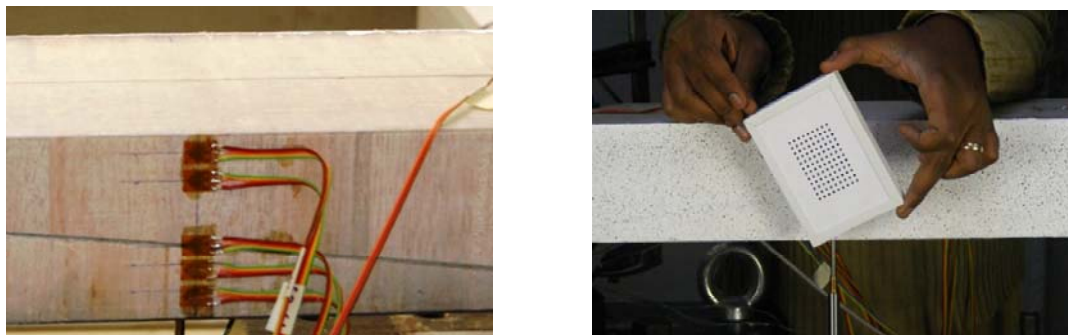
Figure 3.6: a) Shear strain gauges in E-axis and b) speckled pattern during calibration

3.4 Experimental results

3.4.1 Load-deflection responses and failure modes

The cyclic mid-span load-deflection responses of one beam of each configuration (at 4-pointloading) are shown in Fig. 3.7. All curves were linear up to failure while the arch beams exhibited the highest stiffness (sequence from high to low stiffness: A-C, A-G, B-H, B-H/L, B-L). The sequence of ultimate loads was similar with the exception of the B-H ultimate loads, which were lower than those of the B-H/L beams. The arch beams exhibited a load drop after the first failure, a subsequent increase at slightly lower stiffness up to a second, lower peak where the final failure occurred. The ultimate loads, P_u, and mid-span deflections at ultimate load, w_u, are listed in Table 3.4.
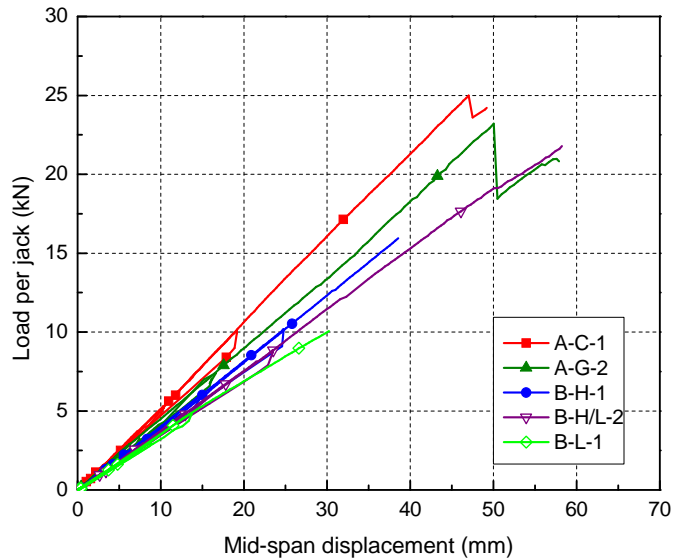
Figure 3.7: Load-deflection responses at mid-span of beams under four-point bending loading

The failure modes were independent of the two loading configurations (3- or 4-point bending). All arch beams failed in the same mode, see Fig. 3.8. Failure was initiated by a vertical shear crack through the low-density core between support and jack (region of highest shear force), accompanied by a first drop in the load. The low-density core then debonded from the arch and lower laminate, starting at the shear crack and progressing towards the jack and support respectively. In this phase, the load increased again up to a second peak, when shear failure also occurred in the high-density core. Failure in the B-H/L beams occurred similarly, first through a vertical crack in the low-density core, which then suddenly propagated through the high-density core however without exhibiting a second peak.

Table 3.4: Weight, SLS and ultimate mid-span deflection, and failure modes of experimental beams

Beam	G (kg)	P_{SLS} (kN)	P_u (kN)	w_u (mm)	P_u/P_{SLS} (-)	P_{SLS}/G (kN/kg)	P_u/G (kN/kg)	Failure mode (1st peak)
A-C-1	16.7	2x2.0	2x22.5	38.0	9.9	0.24	2.69	Shear SB50
A-C-2	17.4	2x2.0	2x25.0	47.0	12.5	0.23	2.87	Shear SB50
A-C-3	16.8	1x4.0	1x37.2	37.2	9.3	0.24	2.21	Shear SB50
A-G-1	16.6	2x1.8	2x24.9	52.1	13.8	0.23	3.00	Shear SB50
A-G-2	16.7	2x1.9	2x24.5	45.9	12.9	0.23	2.93	Shear SB50
A-G-3	17.0	1x3.5	1x35.9	41.1	10.2	0.21	2.11	Shear SB50
B-H-1	19.5	2x1.6	2x15.7	38.6	9.9	0.16	1.61	Compr. GFRP
B-H-2	19.2	2x1.6	2x16.9	40.8	10.6	0.17	1.76	Compr. GFRP
B-H-3	19.6	1x3.1	1x30.1	40.7	9.7	0.16	1.54	Compr. GFRP
B-H/L-1	12.5	2x1.5	2x19.0	58.2	14.5	0.24	3.04	Shear SB50
B-H/L-2	13.8	2x1.5	2x21.0	53.8	14.0	0.22	3.04	Shear SB50
B-H/L-3	13.8	1x2.8	1x31.3	44.0	11.2	0.20	2.27	Shear SB50
B-L-1	7.6	2x1.4	2x9.9	30.6	7.1	0.37	2.61	Compr. GFRP
B-L-2	7.7	2x1.4	2x12.1	37.7	9.1	0.36	3.14	Compr. GFRP
B-L-3	7.9	1x2.6	1x26.5	39.2	10.2	0.33	3.35	Compr. GFRP

All reference beams B-H and B-L failed through a compression failure of the upper GFRP face sheet between the jacks, see Fig. 3.9, followed by a local debonding of the laminate from the balsa core and local crushing of the latter. In the highest moment region, the axial stresses remained below the wrinkling strength (see Table 3.5).
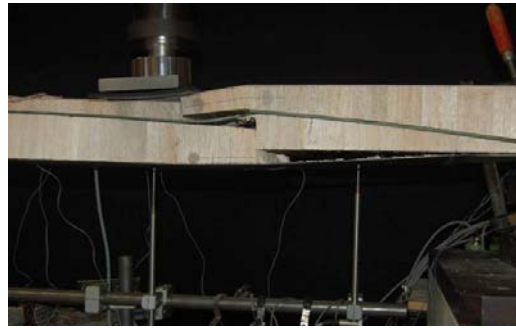
Figure 3.8: Typical failure mode of arch beams (beam A-G-2 is shown)
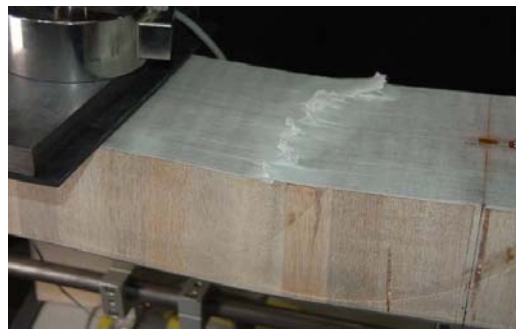
Figure 3.9: Typical failure of B-H and B-L beams (beam B-H-3 is shown)

Table 3.5: Mid-span axial stresses of FRP laminates at ultimate loads (beams under 4-point bending)

Beam	Top, compression (MPa)	Arch, compression (MPa)	Bottom, tension (MPa)
A-C-1	173	241	496
A-C-2	207	263	595
A-G-1	286	166	510
A-G-2	276	157	533
B-H-1	261	-	307
B-H-2	293	-	344
B-H/L-1	379	-	439
B-H/L-2	356	-	416
B-L-1	325	-	233
B-L-2	325	-	239
Strength[a]	290	290	1420
Wrinkling[b]	696 (B-H) 435 (B-L)	435 (B-L)	-

[a]estimated values from Ref. [25] and Ref. [26]

[b]estimated values according to Ref. [27]

3.4.2   Axial strain distributions

The axial strain distributions through the depth of the beams at axis J (see Fig. 3.5), measured by strain gages on the face sheet and arch laminate mid-axes and Omega gages on the balsa surface, are shown in Fig. 3.10 for beams A-G-1, B-H/L-1 and B-L-1 at their ultimate loads (see Table 3.4).
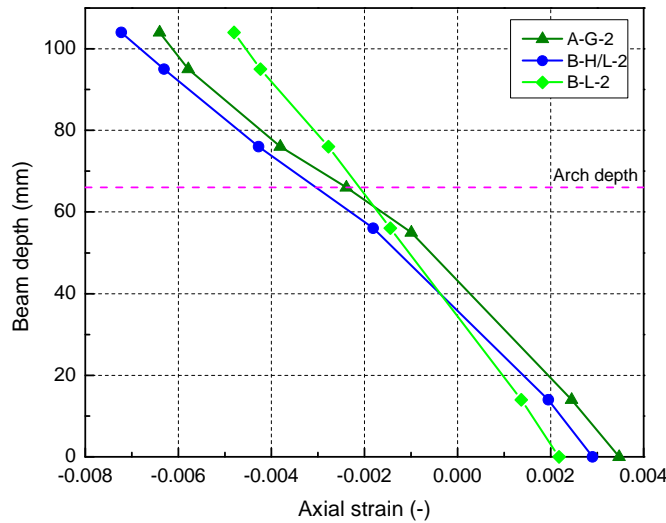
Figure 3.10: Axial strain distribution at J-axis for beams A-G-2, B-H/L-2 and B-L-2 at their ultimate loads

Due to the much stiffer lower CFRP face sheet, the neutral axis shifted downwards from the mid-depth. The strain distribution in all B-beams remained plane up to the ultimate load. The A- and B-H/L beams, however, exhibited a slightly strain non-linearity at the depth of the arch. The strains in the upper GFRP face sheets of the A-beams were generally lower than those of the B-beams at the same load level.

3.4.3 Out-of-plane shear strain and stress distributions

Out-of-plane shear strain distributions through the depth of the balsa core (and in the arch laminate), at E-axis for beams A-G-2, B-H/L-2 and B-L-2 at their SLS and ultimate loads, are shown in Fig. 3.11. The curves were obtained from the speckled pattern measurements while the dots resulted from the strain gages. Both measurements agreed well. The beams with uniform core exhibited a more or less constant strain through the depth. In contrast, the strains in the upper high-density balsa of the other beams were significantly lower than those in the lower low-density balsa. The FRP arches, however, did not exhibit any strain discontinuity.

The corresponding shear stress distributions are shown in Fig. 3.12. Since the ratio of the upper and lower shear strains corresponded approximately to the ratio of the G-moduli (354/221=1.6), the shear stresses were almost constant through the high- and low-density parts. Only the FRP arches exhibited a much higher shear stress (caused by arch bending, see next section) according to their much higher G-modulus.
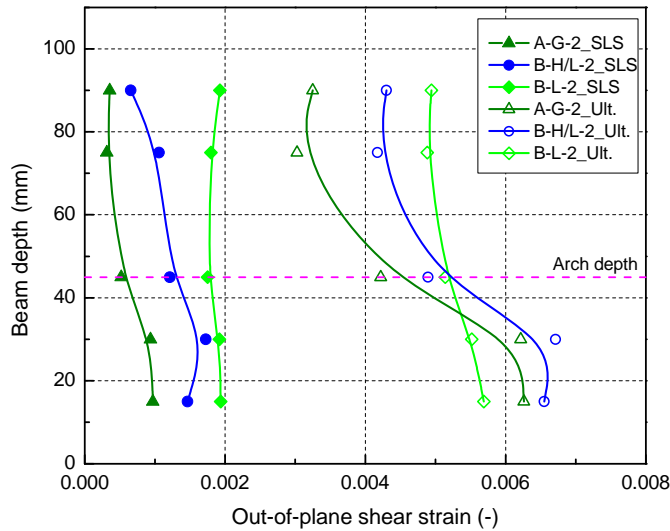
Figure 3.11: Out-of-plane shear strain distributions in balsa core and FRP arch at E-axis for beams A-G-2, B-H/L-2, and B-L-2 at their SLS and ultimate loads (dots from shear gauges, curves from speckled pattern measurements)
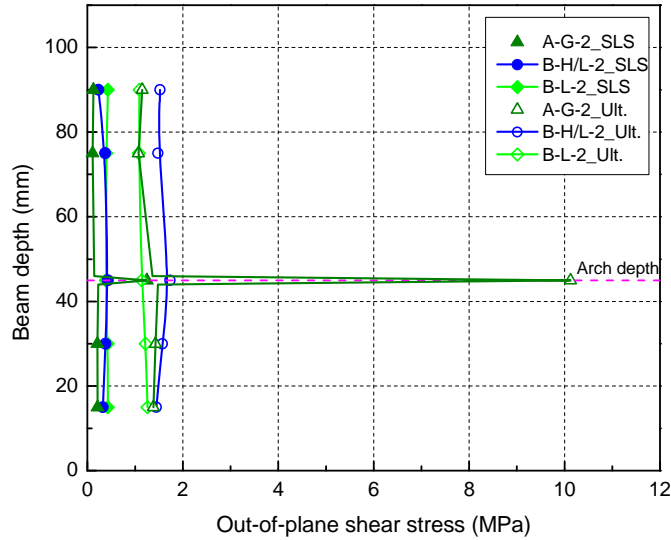
Figure 3.12: Out-of-plane shear stress distributions in balsa core and FRP arch at E-axis for beams A-G-2, B-H/L-2, and B-L-2 at their SLS and ultimate loads

3.5 Discussion

3.5.1 Shear contribution of arches

The FRP arches contributed to the shear resistance in the regions between loads and supports. This contribution consisted of two parts: the shear force due to arch bending and, more significantly, the vertical component of the axial force in the arch. The arch bending mainly resulted from the circular arch form, which was not geometrically tailored to the two- or one-axis loading. The vertical components of the axial forces in the arch were maximum in the fourth points of the span, see Fig. 3.13, and – due to co-action of arch and beam mechanisms – decreased towards the support, which represented a disadvantage of this concept. In the case of a pure arch mechanism (not influenced by the bending mechanism), the arch forces and their vertical components would not decrease towards the supports. On the other hand, the depth of the high-density balsa was maximum close to the support and thus compensated for this decrease of the arch contribution. In fact, shear failure never occurred in this region of reduced arch contribution but rather in the middle of the lateral spans where the arch contribution was maximum.
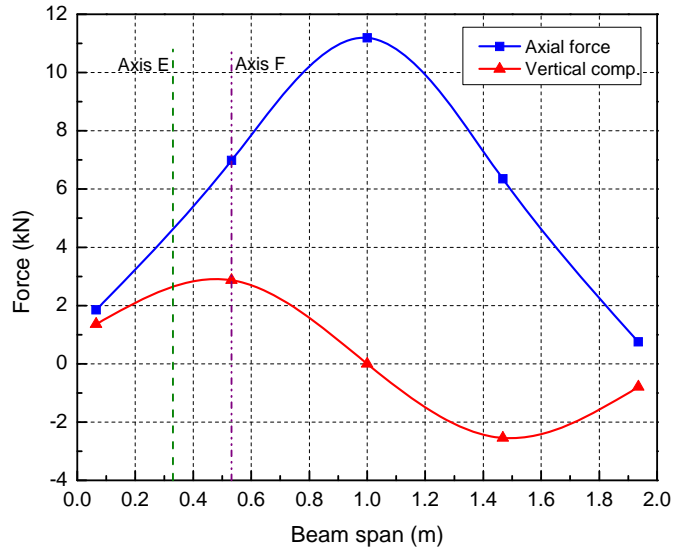
Figure 3.13: Axial arch force (derived from strain measurements) at ultimate load and its vertical component that contributes to shear resistance (A-G-1 beams)

From the shear strain measurements in axis E, the shear contributions of the high- and low-density balsa and the arch (sum of axial and bending component) could be estimated (in E-axis) for the symmetric and asymmetric loading, see Fig. 3.14. In the symmetric cases, up to the first peak, the contributions were approximately 32% from low-, 49% from high-density balsa and 19% from the arch (whereof 14% were due to the axial force and 5% due to bending).
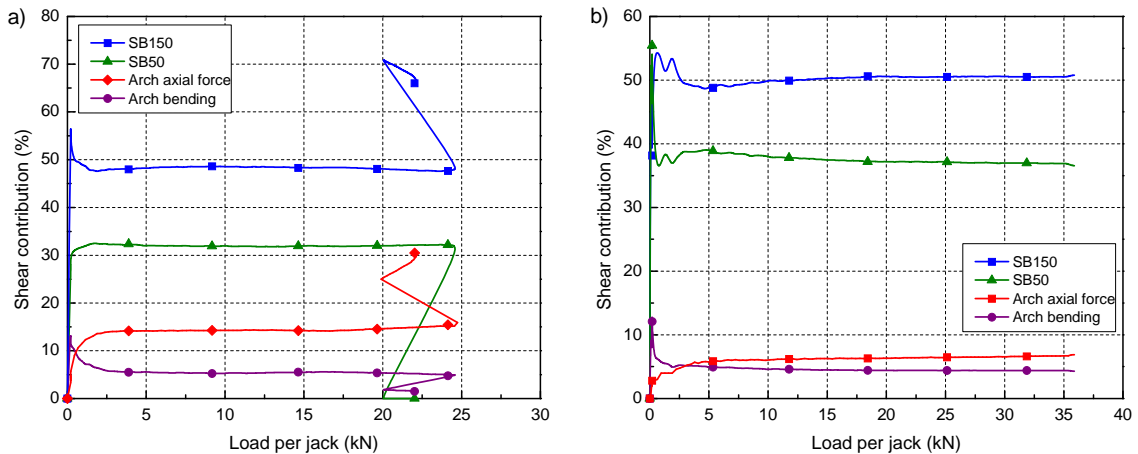
Figure 3.14: Contributions of core components to shear resistance at E-axis under a) four-point bending (A-G-3), b) three-point bending (A-G-3)

In the asymmetric case, the total and the axial arch contributions were reduced to 12 and 7% respectively. The shear contribution of the low-density and high-density balsa cores increased to 38 and 50% accordingly. The decreasing contributions of the total and axial arch contributions in the asymmetric case resulted from the fact that the arch shape was not tailored to asymmetric loading. The individual contributions remained approximately constant during the loading up to failure (in A-beams up to the first peak). The maximum total arch contribution was close to axis F, see Fig. 3.13, and increased to approximately 20% of the total shear force in the symmetric case. From Fig. 3.14a) it can further be derived that, in the symmetric case, after the initial shear failure in the low-density balsa (first peak), the arch contribution could increase significantly to approximately 30% of the remaining shear load at the second peak (without however increasing the load capacity beyond the first peak).

The arch efficiency thereby strongly depends on its depth. The maximum depth (which ideally is the core thickness) is reduced by the required high-density layer above the arch in order to prevent indentation. The effect of this thin layer on the maximum arch depth, however, reduces with increasing span and thus increasing sandwich thickness. For longer spans, the efficiency of the arch therefore will be much higher than in these beams.

3.5.2   Failure modes and ultimate loads

In addition to the shear resistance contribution in the lateral spans, the FRP arches also reduced the compression forces in the upper face sheet in the maximum moment region between the jacks, where the arch approached the upper face sheet, see Table 3.5. Compression failure of the upper face sheet was therefore prevented in the arch beams, unlike in the reference beams, and the load could thus be increased up to shear failure in the low-density core. The reason why the B-H/L beams did not fail in the upper face sheet (as the other B-beams did) could not be explicitly correlated to the measurements. The shear stresses developed in those beams at shear failure were similar to the low-density balsa shear strength of 1.5 MPa, see Fig. 3.12, and therefore explained the shear failure, although the axial compression stresses in the upper face sheet exceeded the estimated strength (see Table 3.5). The ultimate loads for the two failure modes were apparently similar for all beams: A-G beams also approached an upper face sheet failure (see Table 3.5) while B-L beams were close to core shear failure (see Fig. 3.12).

Fig. 3.14a) further shows that a redistribution of forces occurred after the first peak in the arch beams. Subsequent to failure of the low-density core below the arch, the arch

mechanism was further activated and the remaining structure was still able to bear loads up to the second lower peak when shear failure also occurred in the upper core.

3.5.3 Efficiency of configurations

The aim of this work was to investigate to what extent structural efficiency could be improved and deck weight further decreased thanks to a more complex core assembly, compared to a homogeneous high-density core. In particular, the performance of an FRP arch integrated into the balsa core was of interest.

In a first step, the structural efficiency was evaluated by the SLS and ultimate loads obtained (P_{SLS} and P_u). The SLS load directly depends on beam deformation and thus beam stiffness. The ultimate loads depend on the structural configuration and material strength. The ratio P_u/P_{SLS} can be assumed as a total safety factor, which in all cases was very high (7.1-14.0, see Table 3.4). The effect of the beam weight, G, can be taken into account by normalizing the SLS and ultimate loads by the beam weight. The corresponding results are shown in Fig. 3.15 (P_{SLS} vs. P_u), Fig. 3.16 (P_{SLS}/G vs. P_u/G) and Table 3.4.
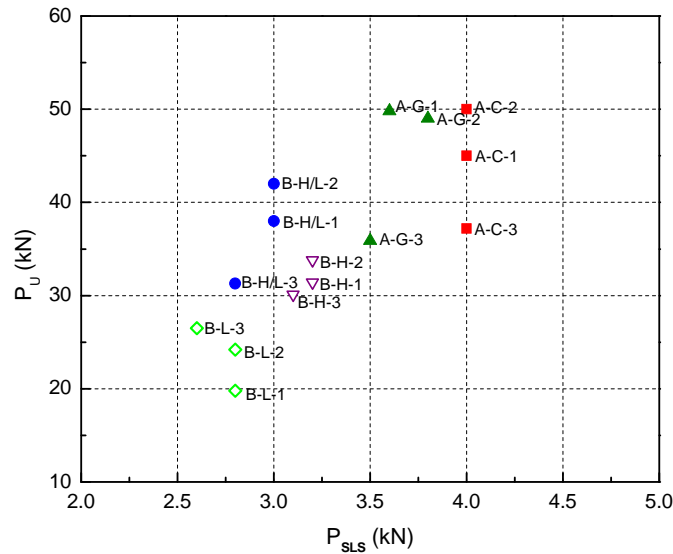
Figure 3.15: Ultimate load, P_u, versus SLS load, P_{SLS}, of all beams
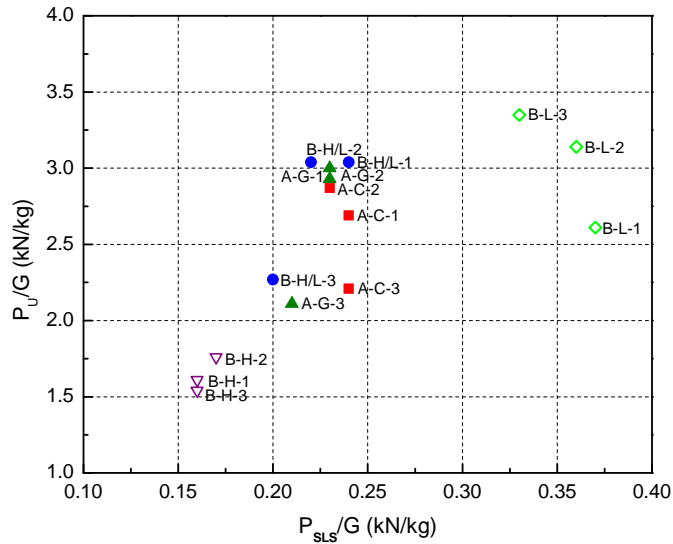
Figure 3.16: Ultimate load, Pu, versus SLS, PSLS, normalized by beam weight, G, of all beams

In terms of structural performance, the arch beams were superior to all other configurations, see Fig. 3.15 (highest P_{SLS} and P_u values), in particular compared to the B-H beams (homogeneous high-density core). A marginal difference between GFRP and CFRP arches was only seen in the slightly higher SLS loads borne by the latter; however, the ultimate loads were similar. This small difference does not seem to justify the much higher cost of CFRP compared to GFRP materials.

If, in a second step, the beam weight is also taken into account, the B-L beams with homogenous low-density balsa core exhibited the best performance, see Fig. 3.16. However, the SLS and ultimate loads were the lowest of all configurations (see Fig. 3.15) and, due to the relatively low compressive strength in the end-grain direction (see Table 3.3), this configuration is sensitive to indentation. The arch beams exhibited approximately the same performance as the B-H/L beams; however, the performance of both types was better than that of the B-H beams. Taking all these factors into account, the arch beams with GFRP arch between the upper high-density and lower low-density balsa core (A-G beams) exhibited the best overall performance.

Other criteria such as fatigue behavior may obviously contribute to structural efficiency. The fatigue performance of beams similar to B-H beam type was investigated for the Avançon Bridge. Results showed no degradation of the GFRP-balsa sandwich structure [20].

3.5.4   Size effect

The experimental results obtained and discussed so far are based on a beam span of 2.4 m. The question thus arises whether a size effect can reduce the performance if the span is increased to the aimed span of 15 m. However, since the design is stiffness driven and large safety factors exist, a significant size effect that could reduce the performance is not expected, because normally only strength and much less stiffness are sensitive to size effects.

Nevertheless, concerning strength, several results are available to discuss a potential size effect on the shear strength of the balsa core. Figure 3.17 shows the balsa shear strength as a function of the specimen thickness and balsa density obtained from small scale Iosipescu shear experiments [21], four-point bending experiments on the SB50 A-beams and six four-point bending experiments on similar large-scale sandwich beams with 2.0 m span, 389 mm width, and 200 mm core thickness. The Iosipescu SB150 balsa specimens had 40 mm span, 5 mm width and 12 mm thickness between the notches and densities of 296 ± 79 kg/m^3. The SB150 balsa cores of the six large scale beams had densities of 291 ± 94 kg/m^3. The results allow comparing the shear strength of the 12 mm and 200 mm thick specimens that have a similar density of around 290 kg/m^3. The strength of the approximately 17 times thicker core decreased by 50%. The size effect on the shear strength of the balsa core thus is significant. However, this reduction is still much smaller than the safety factors that existed in the beams (7.1-14.0 at balsa core failure, see Table 3.4)
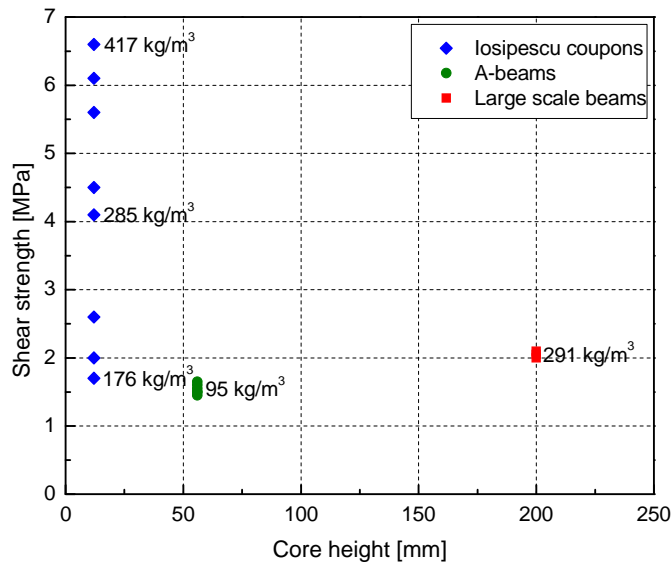
Figure 3.17: Influence of specimen thickness and density on shear strength of balsa core

3.6 Conclusions

Fifteen FRP-balsa sandwich beams were investigated under four-point and asymmetric three-point bending to evaluate structural efficiency and beam weight for different complex core assemblies in view of an application for slab-bridges of up to 15-m span. The complex sandwich cores consisted of high-density and low-density balsa and a GFRP or CFRP arch adhesively bonded in the high-/low-density balsa interface. Their behavior was compared to two reference cases with uniform, either only high-density or low-density, balsa core. The following conclusions were drawn from this work:

1) The FRP arch had three beneficial effects: a) it reduced the forces in the upper face sheet in the mid-span region and thus prevented compression failure of the latter which led to a higher ultimate load at shear failure in the core; b) it contributed to the shear resistance in the shear loaded regions between loads and supports; c) it increased the beam stiffness.

2) The shear resistance of the FRP arch contribution consisted of two parts: a) the shear force due to arch bending and b) the vertical component of the arch axial force. The maximum shear resistance contribution was 20% for symmetric loading.

3) The FRP arch did not lead to any shear strain discontinuity in the out-of-plane direction. The axial strains, however, slightly deviated from the plain stress distribution at ultimate load.

4) The overall best performance in terms of stiffness, strength and weight resulted from the core configuration with a GFRP arch between an upper high-density and lower low-density core. This performance was much better than that of the beams with uniform high-density core.

References

[1] Zureick A. Fiber reinforced polymer bridge decks. Proc., National Seminar on Advanced Composite Material Bridges, FHWA 1997.

[2] Keller T. Recent all-composite and hybrid fibre-reinforced polymer bridges and buildings. Prog Struct Eng and Mater 2001; 3(2): 132-140.

[3] Bakis CE, Bank LC, Brown VL, Cosenza E, Davalos JF, Lesko JJ, Machida A, Rizkalla SH, Triantafillou TC. Fiber-reinforced polymer composite for construction – state-of-the-art review. J Compos Constr 2002; 6(2): 73-87.

[4] Keller T, Schollmayer M. Plate bending behavior of pultruded GFRP bridge deck system. Compos Struct 2004; 64(3-4): 285-295.

[5] Zihong L. Testing and analysis of a fiber reinforced polymer deck. Ph.D. thesis, Virginia Polytechnic Institute and State Univ., Blacksburg, VA. 2007

[6] Zi G, Kim MB, Hwang KY, Lee HY. The static behavior of modular foam-filled GFRP bridge deck with a strong web-flange joint. Compos Struct 2008; 85(2): 155-163.

[7] Robinson, MJ, Kosmatka JB. Lightweight fiber-reinforced polymer composite deck panels for extreme applications. J Compos Constr 2008; 12(3): 344-354.

[8] Kos E, Stoll F. Engineered sandwich cores: vehicular bridge deck applications. SAMPE J 2008; 44 (4): 36-42.

[9] Reising RMW, Shahrooz BM, Hunt VJ, Newmann AR Helmicki AJ, Hastak M. Close look at construction issues and performance of four fiber-reinforced polymer composites bridge decks. J Compos Constr 2004; 8(1): 33-42.

[10] Telang NM, Dumlao C, Mehrabi A, Ciolko AT, Gutierrez J. Field inspection of in-service FRP bridge decks. NCHRP (TRB)-4 report 2006; 564-Appendix 4

[11] Triandafilou LN, O'Connor JS. Field issues associated with the use of fiber reinforced polymer composite bridge decks and superstructures in harsh environments. Struct Eng Int 2010; 20(4): 409-415.

[12] Keller T, Schaumann E, Vallée T. Flexural behavior of a hybrid FRP and lightweight concrete sandwich bridge deck. Composites Part A 2007; 38(3): 879-889..

[13] Chevalier JL. Creeps and fatigue properties of end-grain balsa and other typical sandwich cores. Sandwich Constructions 2, Proc., 2nd Int. Conf. on Sandwich Constructions, Gainesville, Fl 1992; 519-539.

[14] Dai J, Hahn HT. Flexural behavior of sandwich beams fabricated by vacuum-assisted resin transfer molding. Compo Struct 2003; 61(3): 247-253.

[15] Bekisli B, Grenestedt KL. Experimental evaluation of a balsa sandwich core with improved shear properties. Compos Sci Technol 2004; 64(5): 667-674.

[16] Kepler JA. Simple stiffness tailoring of balsa sandwich core material. Compos Sci Technol 2011; 71(1): 46-51.

[17] Kosmatka JB. Structural testing of DARPA/BIR composite army bridge treadway. Compos Struct 1999; 4: 99-115.

[18] Fireco. 'Bascule FRP composite footbridge.'
(http://www.fireco.no/references/Gangbru%20Vesterelven.pdf) (Jun. 12, 2013)

[19] Verheus A. The Utrecht bridge: a 100% composite box beam design FRP bridges, Proc, Int Conf on FRP bridges London 2012; 154-165.

[20] Keller T, Rothe J, de Castro J, Osei-Antwi M. GFRP-balsa sandwich bridge deck – concept, design and experimental validation. J Compos Constr 2014

http://dx.doi.org/10.1061/(ASCE)CC.1943-5614.0000423

[21] Osei-Antwi M, de Castro J, Vassilopoulos AP, Keller T. Shear mechanical characterization of balsa wood as core for composite sandwich panels. Constr Build Mater 2013; 41: 231-238.

[22] Alcan Baltek Corporation. Data sheet, Mechanical properties vs. density and grain orientation for balsa wood, Northvale, NJ. 2001.

[23] Sicomin Epoxy Systems. Data sheet. SR 1710 inj/SD 78720, France 2004; 1-4.

[24] Swiss Composites Suter Kunststoffe AG . Data sheet. Basalt-, glass and carbon fibers and fabric, Switzerland 2010; 1-5.

[25] Manshadi B, Mahmudi H, Abedian A, Mahmudi R. A novel method for materials selection in mechanical design: combination of non-linear normalization and a modified digital logic method. Mater Des 2007; 28(1): 8-15.

[26] Gay D, Hoa SV. Composite materials: design and applications. 2nd ed. CRC Press, Boca raton, Fl 2007.

[27] Zenkert D. An introduction to sandwich construction. Failure modes, EMAS Publishing, London, UK 1995; 107-114.

4.

Complex core system 1: Failure analysis
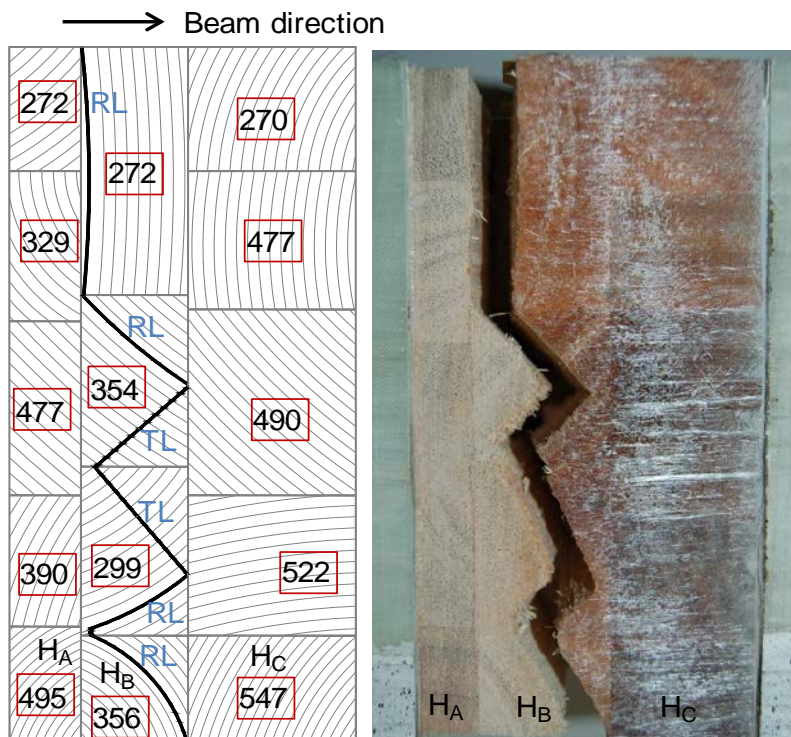
Crack paths in lowest density balsa blocks of complex balsa core restricted from penetrating the adhesive layers between the blocks (values in kg/m^3)

4.1 Overview

Fiber-reinforced polymer (FRP) sandwich structures are composed of FRP face sheets and honeycomb, foam or balsa cores [1]. Basically, the face sheets bear the bending and the core the shear loads. Depending on the span-to-depth ratio and constituent material properties, several distinct failure modes may occur in sandwich structures when loaded in bending: compressive and tensile face sheet failure, face sheet wrinkling, core shear failure, core indentation failure or compressive or tensile core failure [2]. Wrinkling or compressive face sheet failure normally occurs in long sandwich beams while short span beams are sensitive to core shear failure [3]. Corresponding failure mode maps have been developed for foam and honeycomb cores [4-5]. Meanwhile, end-grain balsa cores, which comprise balsa wood fibers orientated perpendicularly to the face sheets, are increasingly used as core materials in sandwich structures due to their superior out-of-plane properties. The lightweight 11.45-m FRP-balsa sandwich bridge deck of the new Avançon Bridge in Switzerland [6], for instance, allowed widening of the bridge from one to two lanes without additionally loading the substructure of the former concrete bridge that it replaced.

End-grain balsa panels are non-homogenous materials composed of similar sized blocks with a cross section of approximately 90 x 110-mm, as shown in Fig. 4.1, which are selected within a limited density range [7]. The balsa blocks of both higher and lower density are randomly assembled to avoid concentrations of softer blocks in the final panel. Assembly is performed by adhesive bonding frequently using the thermoplastic polyvinyl acetate adhesive PVAc.

Figure 4.1: Balsa panel composed of adhesively-bonded balsa blocks (dimensions 1200 x1200 x 60mm)

Furthermore, inside a balsa block, density may vary due to the cyclical changes of early and late wood as a result of which density may increase from early to late wood by up to about 92% according to [8]. Nevertheless, most of the few available studies on failure analysis of these materials assume the material as being homogenous [9-10]. The effects of the balsa block composition of the panels on the location, initiation and propagation of the cracks were not taken into account. Other studies considered the block structure to some extent. In [11], the location of the shear failure was assumed to occur in the low-density balsa blocks, without experimental evidence however. In [12], crack propagation was observed at less dense and hence less stiff locations in the balsa core, where peak shear strain measurements varied between 0.15% and 0.5%; the crack propagation mechanisms, however, were not investigated. In [13], crack initiation in an FRP-balsa sandwich core interface bond was observed. The crack subsequently propagated in the balsa-adhesive interface and then deviated into the balsa and interface parallel to the adhesive block joint. This was exclusively attributed to the low tensile strength of balsa in the transverse direction to the fibers and contributions of potential flaws to the interface failure at the adhesive block joint were not investigated.

In this chapter, the effects of assemblies of blocks of different densities and orientations and adhesive bonding between the blocks on the crack propagation and failure mode of balsa panels are investigated. The failure modes in the core of GFRP-balsa sandwich beams with complex core assemblies are analyzed. The investigation of this type of beams was performed with a view to further optimization of the GFRP-balsa sandwich bridge deck used in the Avançon Bridge described above.

4.2 Crack initiation and propagation in balsa sandwich cores

The relevant crack planes in end-grain balsa sandwich cores under flexural loads, i.e. if core shear failure is dominant, are the radial-longitudinal (RL) and tangential-longitudinal (TL) planes, see Fig. 4.2 (first and second letters indicate the direction normal to the crack plane and the direction of the crack respectively). Cracks in the longitudinal-radial (LR) or longitudinal-tangential (LT) planes are rare in practice since this would require fracture of the fibers [14]. In Mode I, the fracture toughness in RL fracture is lower than in TL fracture (e.g. for balsa of 260 kg/m^3 density, K_{Ic}(RL)=0.14 MPa m$^{1/2}$ while K_{Ic}(TL)=0.20 MPa m$^{1/2}$ [14]), because cracks propagate in the former case only in the early wood (see Fig. 4.2) while in the latter case, they propagate in both the early and the tougher late wood, where fiber bridging

occurs [15]. In Mode II, toughness is similar in both RL and TL fracture (for the same balsa of 260 kg/m^3 density, K_{IIc}(RL)≈K_{IIc}(TL)=0.26 MPa m$^{1/2}$ [14]) since no fiber bridging occurs in either fracture plane.
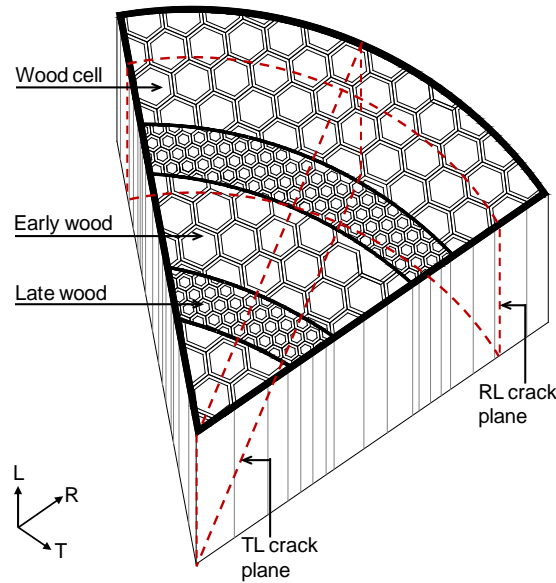
Figure 4.2: Relevant planes of crack propagation in balsa wood

Interface failure (IF) in block joints, i.e. debonding between the balsa and the adhesive, is another prevalent failure type which is caused by voids in the adhesive layer or flaws at the wood-adhesive interface due to non-uniform or low penetration of the adhesive into the wood cells [16]. The crack propagating in the interface may then deviate into the balsa, but in most cases is not able to penetrate the adhesive layer since the Mode I fracture toughness, K_{Ic}, of PVAc is between 3.1 and 3.4 MPa m$^{1/2}$ [17] and thus much higher than that of balsa (see values above).

The fracture toughness in balsa fracture is mainly influenced by the wood density and fiber bridging. The fracture toughness vs. wood density shows a linear relationship in log-scale, as shown in Fig. 4.3, which summarizes data from different references [14, 18-20]. Fracture energy values (G_{Ic}) in [14] were converted into fracture toughness (K_{Ic}) using $K_{1c} = \sqrt{G_{1c}E_z/(1-v^2)}$ according to [21], where E_z is the Young's modulus of wood in the transverse direction to the fibers and v is the Poisson ratio of wood. A fracture toughness-density relationship was established in [20] for Mode I fracture as $K_{Ic}=D\,(\rho/\rho_s)^{3/2}$, with D=2.00 MPa m$^{1/2}$ for crack propagation normal to the wood fibers (in the LR-plane), and D=0.18 MPa m$^{1/2}$ for propagation along the wood fibers (in the RL-plane), where ρ is the

wood density and ρ_s is the density of the wood cell wall (assumed as being 1500 kg/m^3). In [22], Mode II fracture toughness was obtained as $K_{IIc}= 2.5K_{Ic}$.
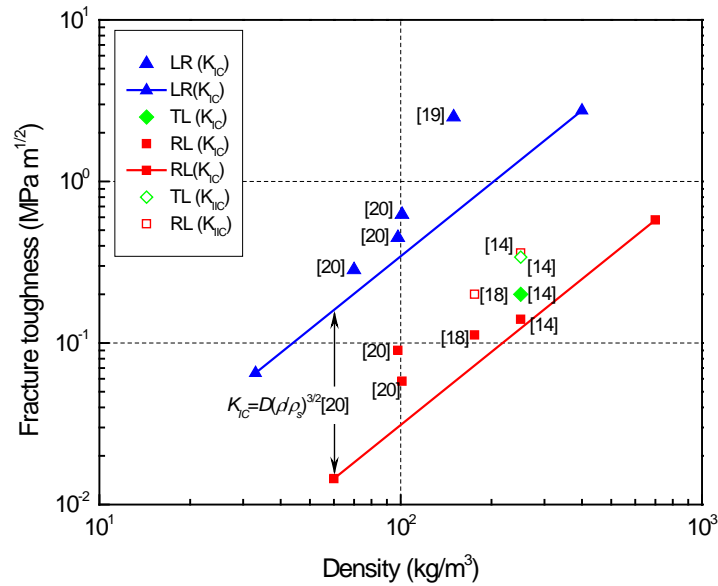
Figure 4.3: Fracture toughness, K_c, as a function of failure plane and mode, vs. density of balsa wood

Fiber bridging develops at the crack tip of the process zone during crack propagation. In [23], fiber bridging was quantified using a digital image correlation method. The results showed an increase in fiber bridging and thus fracture toughness with increasing balsa density. At the microstructure level, fracture toughness is influenced by the cell wall thickness, which determines the density of the wood. This was demonstrated in [20] where crack propagation in balsa cell walls of different thicknesses was analyzed using a three-point bending jig in a scanning electron microscope. The results showed that Mode I crack propagation in balsa wood occurs due to the cell wall breaking when the fracture energy of the cell wall is exceeded. The strain energy release rate, *G,* depended on the elastic modulus transverse to the fibers, which in turn depended on the thickness of the cell walls.

4.3 Crack initiation in complex balsa core

4.3.1 Experimental set-up and material properties

Two types of GFRP-balsa sandwich beams with complex balsa cores were investigated under four-point bending in [24], see Figs. 4.4 and 4.5. In both configurations, the lower face sheets consisted of a 2-mm-thick CFRP layer, while a 2-mm-thick GFRP layer was applied on top. The core of beams B-H/L was composed of an upper high-density balsa (SB150) and lower

low-density balsa (SB50) layer, separated by a circular adhesively-bonded interface. In beams A-G, an additional circular GFRP arch was placed in the high/low-density balsa layer interface to improve the shear resistance of the core. The end-grain balsa cores were cut from panels, as shown in Fig. 4.1, into complex shapes by Computer Numerical Control (CNC) milling. The beams had a length, span, width and total height of 2400 mm, 2000 mm, 180 mm and 104 mm respectively and were fabricated by Vacuum-Assisted Resin Transfer Molding (VARTM). Three beams per configuration were examined.
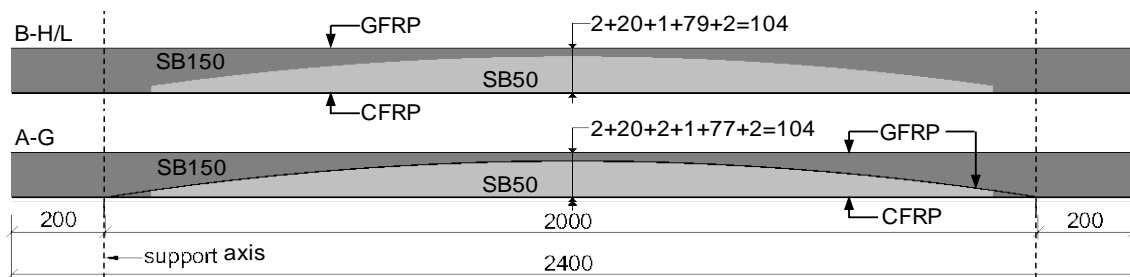
Figure 4.4: Composition of B-H/L and A-G beams with complex balsa-GFRP cores (dimensions in mm)
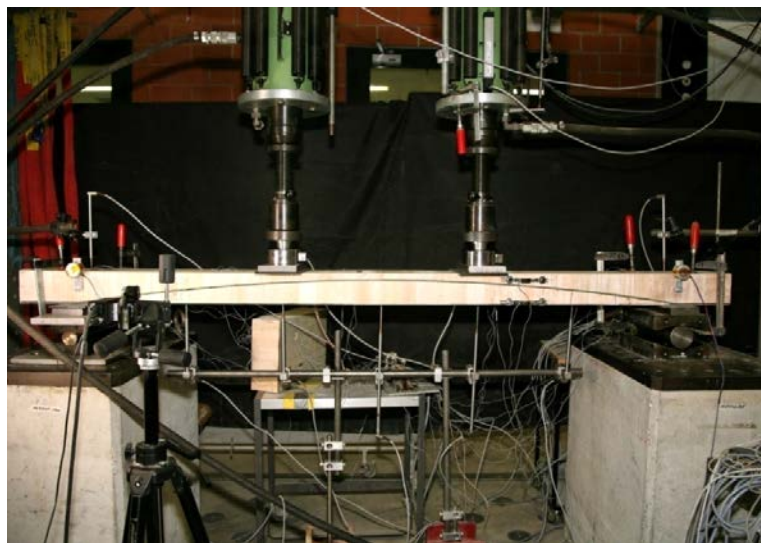
Figure 4.5: Experimental set-up for A-G-2 beam with GFRP arch integrated at interface of upper high-density (SB150) and lower low-density (SB50) balsa core

The loads were applied using two hydraulic jacks of 150-kN capacity. To obtain the axial and out-of-plane shear strain distributions in the core, a stereo correlation system was used (amongst others) to measure the displacements of a 150-mm-wide and 90-mm-deep black speckled pattern applied on the core surface, at 335 mm from the left support of one beam of each type, as shown in Fig. 4.6.
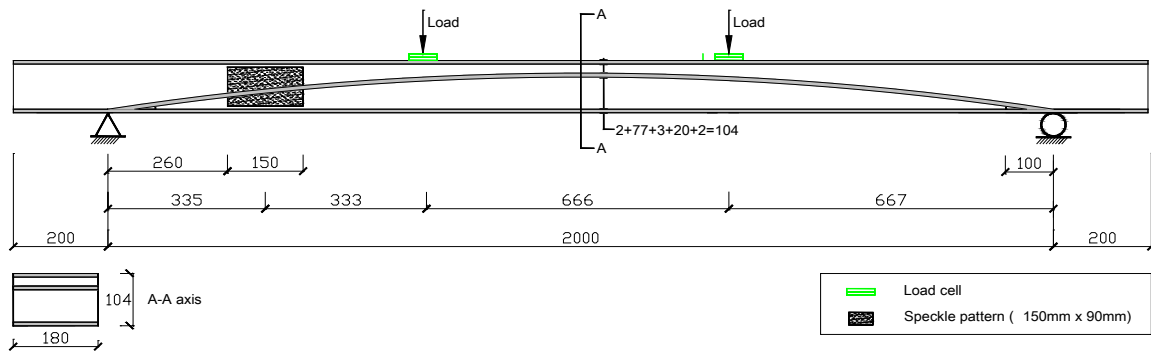
Figure 4.6: A-G-2 beam set-up and location of speckle pattern area (dimensions in [mm])
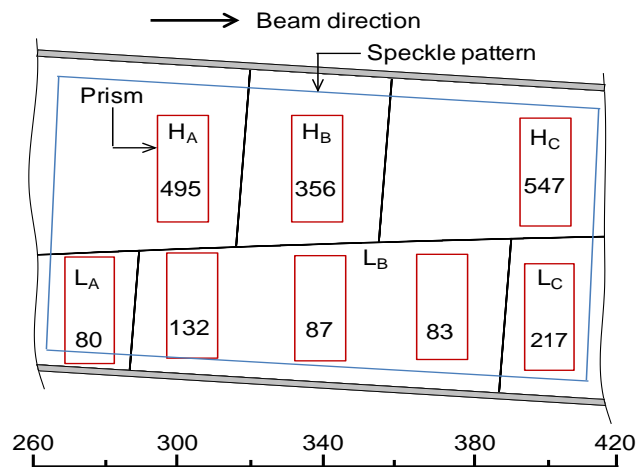
Figure 4.7: Speckle pattern area on B-H/L-2 beam showing covered balsa blocks, prisms and their densities, ruler indicates distance from left support in (mm)

The pattern surface covered three trapezoidal blocks of the SB150 layer, H_A, H_B and H_C, and three blocks of the SB50 layer, L_A, L_B and L_C, as shown in Fig. 4.7. The L_C block was a repair element that replaced part of the original block as shown in Fig. 4.8; this is usually done at locations with defects such as knots [25].
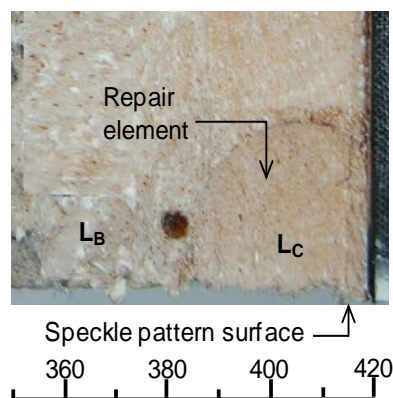
Figure 4.8: Repaired balsa core of B-H/L-2 beam

66

The repair element is not bonded but just inserted. During post-failure analysis, smaller prisms of size 35x15x10 mm were cut from each block to measure the density; the exact locations of the prisms are shown in Fig. 4.7. From the measured densities, the mechanical properties of each prism were estimated using density-mechanical property relationships according to [26] (e.g. $G_{xy}=0.880\rho+137$ and $\tau_{xy}=0.013\rho+0.330$ for the out-of-plane shear stiffness and strength, ρ is the density in (kg/m^3)). These relationships were established by fitting regression curves to the experimentally obtained stiffness and strength data of balsa wood, of a density between 64 and 300 kg/m^3.

Table 4.1: Density and stiffness properties of balsa blocks (estimated based on density acc. to [26], x=longitudinal, y=vertical, z= transverse beam axis)

Properties	SB 150 blocks			SB 50 blocks				
	H_A	H_B	H_C	L_A	L_B			L_C
Density (kg/m^3)	495	356	547	80	83	87	132	217
Longitudinal elastic modulus, E_x (MPa)	500	343	502	62	65	68	111	197
Out-of-plane elastic modulus, E_y (MPa)	21911	13538	22013	1573	1660	1777	3243	6679
Transverse elastic modulus, E_z (MPa)	500	343	502	62	65	68	111	197
Out-of-plane shear modulus, G_{xy} (MPa)	602	451	704	208	98	101	138	329
In-plane shear modulus, G_{yz} (MPa)	574	450	576	96	211	214	254	270
In-plane shear modulus, G_{xz} (MPa)	85	75	86	29	31	32	45	60

Table 4.2: Strength properties of balsa blocks (estimated based on density acc. to [26])

Properties	SB 150 blocks			SB 50 blocks				
	H_A	H_B	H_C	L_A	L_B			L_C
Longitudinal compressive strength, σ_{cx} (MPa)	73.8	45.2	85.4	5.4	5.2	5.6	10.4	21.9
Transverse compressive strength, σ_{cz} (MPa)	2.8	2.0	3.0	0.4	0.4	0.4	0.7	1.2
Longitudinal tensile strength, σ_{tx} (MPa)	54.4	36.6	61.3	6.5	6.5	6.7	11.1	20.3
Transverse tensile strength, σ_{tz} (MPa)	2.7	1.9	2.9	0.4	0.3	0.3	0.6	1.1
Out-of-plane shear strength, τ_{xy} (MPa)	6.4	4.7	7.1	1.4	1.4	1.4	2.0	3.0
In-plane shear strength, τ_{yz} (MPa)	10.1	7.2	11.2	1.6	1.6	1.7	2.6	4.3
In-plane shear strength, τ_{xz} (MPa)	3.2	2.2	3.6	0.4	0.3	0.4	6.7	1.3

The resulting densities and mechanical properties of the balsa blocks are listed in Tables 4.1 and 4.2. A significant variability of densities and hence mechanical properties existed amongst the H- and L-blocks, even within the individual blocks (see L_B where three prisms were examined). This was attributed to the presence of early and late woods in the balsa blocks. Further details concerning the beam experiments are presented in [24].

4.3.2 Experimental results and analysis

4.3.2.1 Longitudinal strain distributions in balsa blocks

The longitudinal strain field measured by the stereo correlation system on the core surface of beam B-H/L-2, at its ultimate load (2x21 kN), is shown in Fig. 4.9a, while Fig. 4.9b shows the axial strain distribution at a 6-mm distance from the top and bottom face sheets along the pattern length as well as the corresponding densities of the prisms.
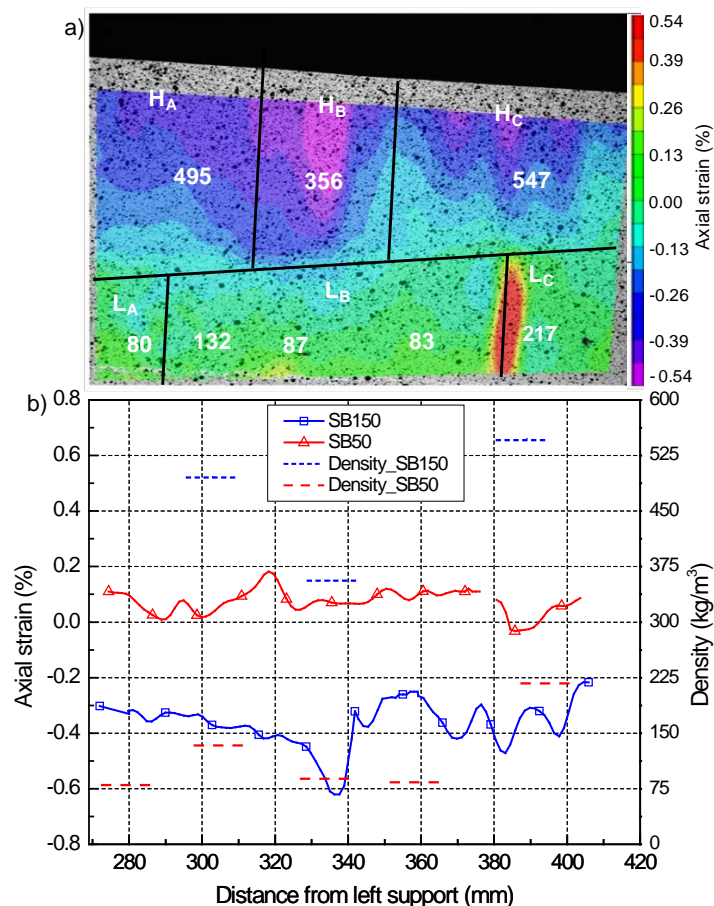
Figure 4.9: B-H/L-2 beam at ultimate load, a) longitudinal strain field and schematic of balsa blocks with corresponding densities (kg/m³), b) axial strain curves at 6-mm distance from top and bottom face sheets and densities

The strain field varied inversely proportional to the densities of the balsa blocks along the beam length and similarly within the single blocks, depending on the early and late wood contents. The maximum strains were measured in the L_B and H_B blocks. Between the repair element, L_C, and the adjacent block, L_B, a large strain was measured across the non-bonded gap (see Fig. 4.9a), which did not however represent a material strain, and as a result the corresponding peak was thus ignored in Fig. 4.9b (and in all the following figures).
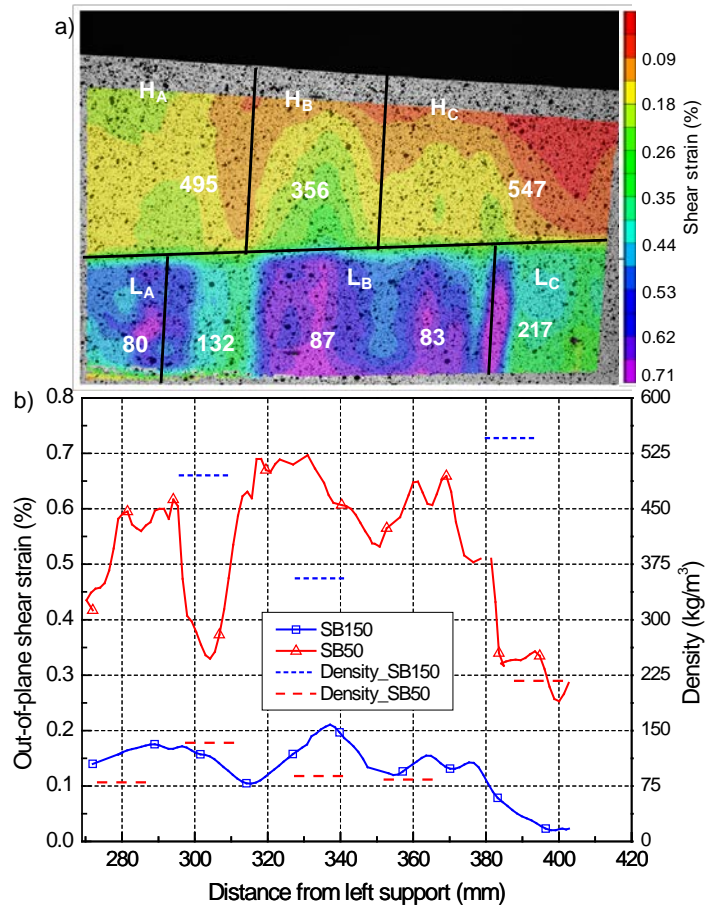
Figure 4.10: B-H/L-2 beam at ultimate load, a) out-of-plane shear strain field and schematic of balsa blocks with corresponding densities (kg/m³), b) out-of-plane shear strain curves at 6-mm distance from top and bottom face sheets and densities

Similarly to Fig. 4.9, the out-of-plane shear strain field is shown in Fig. 4.10a and the strain curves at a 6-mm distance from the face sheets and the densities are shown in Fig. 4.10b. The shear strains again varied inversely proportional to the balsa density and were generally higher in the lower low-density layer. As an example, the average shear strain ratio of the L_B and H_B blocks, between 325-340 mm, is 4.2 ($\approx 0.0062/0.0015$), similar to their inverse shear stiffness ratio of 4.5 ($\approx 1/(101/451)$). Maximum shear strains occurred in the less dense L_B block.

4.3.2.2 Stress distributions in balsa blocks

The longitudinal stresses at a 6-mm distance from the face sheets along the length, together with the prism densities and strengths and the location of the block joints are shown in Fig. 4.11a. The stresses were determined from the strain measurements and stiffness properties of the balsa prisms (see Table 4.1). A maximum compressive axial stress of -2.6 MPa was obtained in the H_C block, which was lower than the estimated transverse compressive strength of -3.0 MPa. However, the stresses in the H_B block (-2.0 MPa) reached the strength of this block. The maximum axial tensile stresses were almost constant at 0.1 MPa and thus much lower than the minimum tensile strength (0.3 MPa).
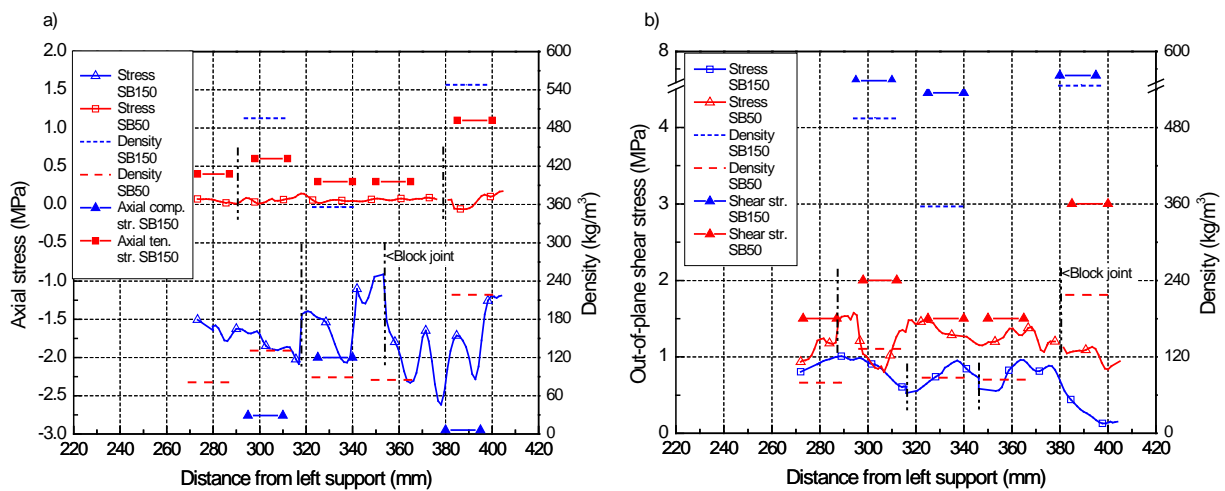
Figure 4.11: B-H/L-2 beam at ultimate load, a) longitudinal stress distribution and b) out-of-plane shear stress at 6-mm distance from top and bottom face sheets; also shown are block joints and prism densities and strengths

The same data as in Fig. 4.11a but for the out-of-plane shear stress is shown in Fig. 4.11b. In this case, the maximum shear stresses in the upper high-density blocks (1.0 MPa) were much lower than the shear strengths (minimum: 4.7 MPa). In the lower low-density core, the maximum shear stress values (1.5MPa) reached the shear strengths (1.4 MPa) at several locations in the L_A and L_B blocks.

4.3.2.3 Failure criterion

As shown in Fig. 4.11, relatively high longitudinal and out-of-plane shear stresses can occur at the same location. In order to see how stresses and failure locations were correlated, a stress interaction failure criterion, the Tsai-Wu criterion, was thus applied. This criterion is suitable for orthotropic materials with linear elastic behavior such as balsa wood [27]. Assuming an orthotropic plane strain condition, the criterion is as follows:

70

$$f = \left(\frac{1}{\sigma_{tx}} - \frac{1}{\sigma_{cx}} \right) \sigma_x + \frac{1}{\sigma_{tx}\sigma_{cx}} \sigma_x{}^2 + \frac{1}{\tau_{xy}} \tau_s{}^2 \leq 1.0 \tag{1}$$

where σ_{tx}, σ_{cx}, σ_x, τ_{xy} and τ_s represent the transverse tensile strength, transverse compressive strength, longitudinal stress, out-of-plane shear stress and out-of-plane shear strength of the balsa core respectively. The criterion function, f, for the individual balsa blocks is shown in Fig. 4.12. In the upper high-density layer, f-values above unity were predicted in the H_B block at 337 mm from the support. The interaction between the axial stresses and the low axial compressive strength (first two terms in Eq. 1) contributed 92% of the f-function value at this location. In the low-density layer, values of the f-function above unity occurred at two locations in the L_B block, at 295 mm and 318 mm from the left support. According to Eq. (1), the interaction between the shear stress and strength (third term in Eq. 1) contributed 69% and 72% of the f-function values at these locations.
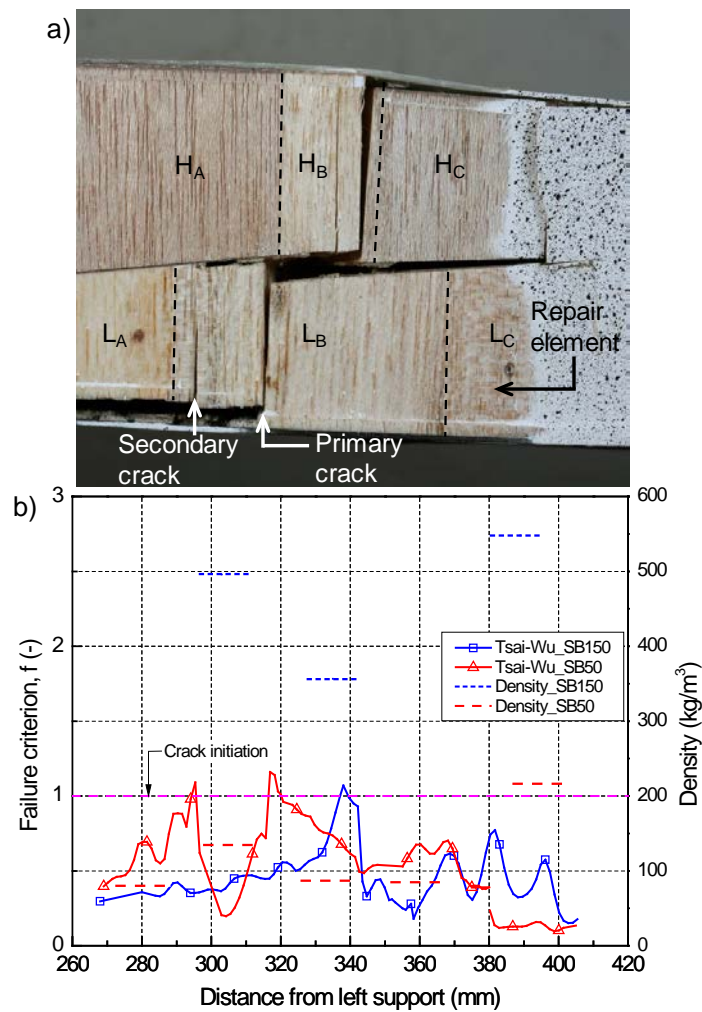
Figure 4.12: B-H/L-2 beam, Tsai-Wu failure functions and corresponding locations of cracks

71

4.3.2.4 Failure modes

The cyclic mid-span load-deflection responses of one beam of each configuration are shown in Fig. 4.13. Both curves were almost linear up to failure. Failure in the B-H/L-2 beam was sudden and occurred simultaneously in both core layers. In the lower low-density layer, two cracks occurred through the thickness of the L_B block, a primary larger crack at 318 mm and a secondary crack at 295 mm from the left support, as shown in Fig. 4.12a, exactly at the locations where the failure function exceeded unity. In the upper high-density layer, a similar crack formed in the lighter H_B block at 337 mm from the left support, again at the location indicated by the failure criterion. These cracks caused debonding between the two balsa layers and both the lower CFRP and upper GFRP face sheets, and propagated towards the left support and in the opposite direction towards the jack. The remaining two beams exhibited the same failure mode.
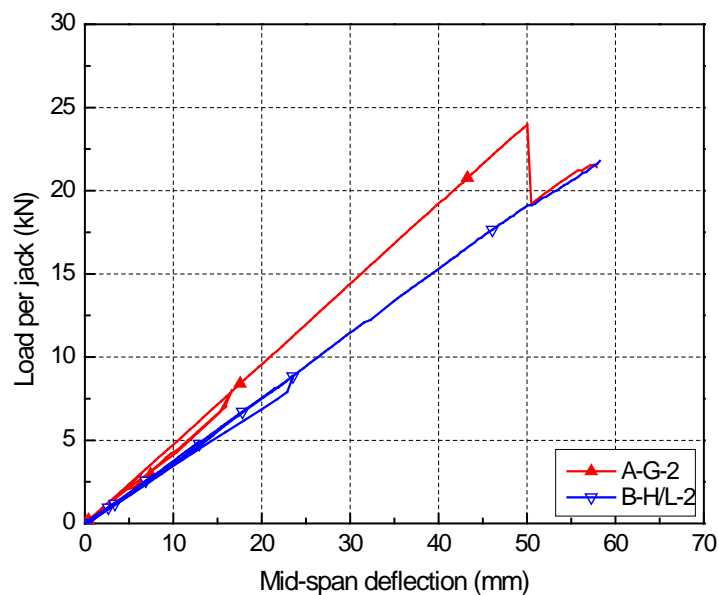
Figure 4.13: Load-deflection responses at mid-span of A-G-2 and B-H/L-2 beams under 4-point loading

The failure mode in the A-G beams is shown in Fig. 4.14 and developed in two stages. In the first stage, two cracks formed through the thickness of the lower low-density layer at 1450 and 1490 mm from the left support, see Fig. 4.14a for beam A-G-2. Crack development was accompanied by debonding of the low-density core from the lower face sheet and the GFRP arch. This resulted in a drop of the load from 24 kN to 19 kN per jack, as shown in Fig. 4.13, and a change in the structural system insofar as the arch was now activated and contributed to the shear transfer [24]. The load could thus be increased again, in the second

stage, while the crack between the low-density layer and the arch propagated towards the jack until failure also occurred in the upper high-density layer near the jack at 22 kN per jack, see Fig. 4.14b.
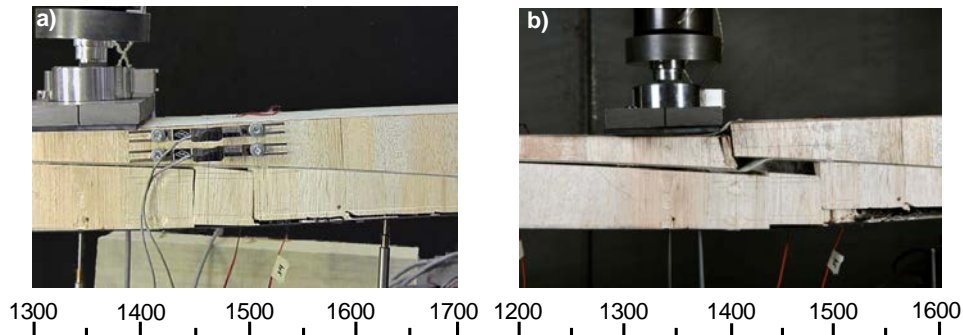
Figure 4.14: Failure mode of beam A-G-2, a) stage 1 at ultimate load, b) stage 2 at second peak

The lower low-density balsa layer was subjected to combined tensile and shear stresses in all beams. Crack propagation thus occurred in mixed-mode, Mode I combined with Mode II, while the latter was dominant (predominant shear contribution in the failure function, see previous section). In the upper high-density layer, subjected to compression and shear, Mode II fracture occurred. Both modes caused crack propagation along the fibers in the RL and TL planes in both balsa layers, as discussed in the following section.

4.4 Post-failure analysis

4.4.1 Analysis of crack propagation in B-H/L beams

The crack paths on the bottom surface of the lower low-density balsa layer, across the width of B-H/L-2 beam, are shown in Fig. 4.15a (picture taken after removal of face sheet). Due to the small Mode I portion in the mixed-mode fracture, crack propagation in the RL plane exhibited a slightly higher probability than propagation in the TL plane since in the predominant Mode II toughness in RL and TL fracture is similar (see Section 4.2). Accordingly, about 82% of the primary crack and 50% of the secondary crack developed in the RL plane. Both cracks remained in the band between the two adjacent adhesive layers, whose fracture toughness was much higher (see Section 4.2).

Figure 4.15b shows the crack paths on the top surface of the upper high-density balsa layer (after removal of the face sheet). Since Mode II fracture was dominant, toughness in RL and TL fracture was similar. Accordingly, a similar total length of the crack propagated in the

RL plane (58%) and TL plane (42%). Again, the crack was not able to propagate through the adjacent adhesive layers and therefore remained within the narrow band of this block row.
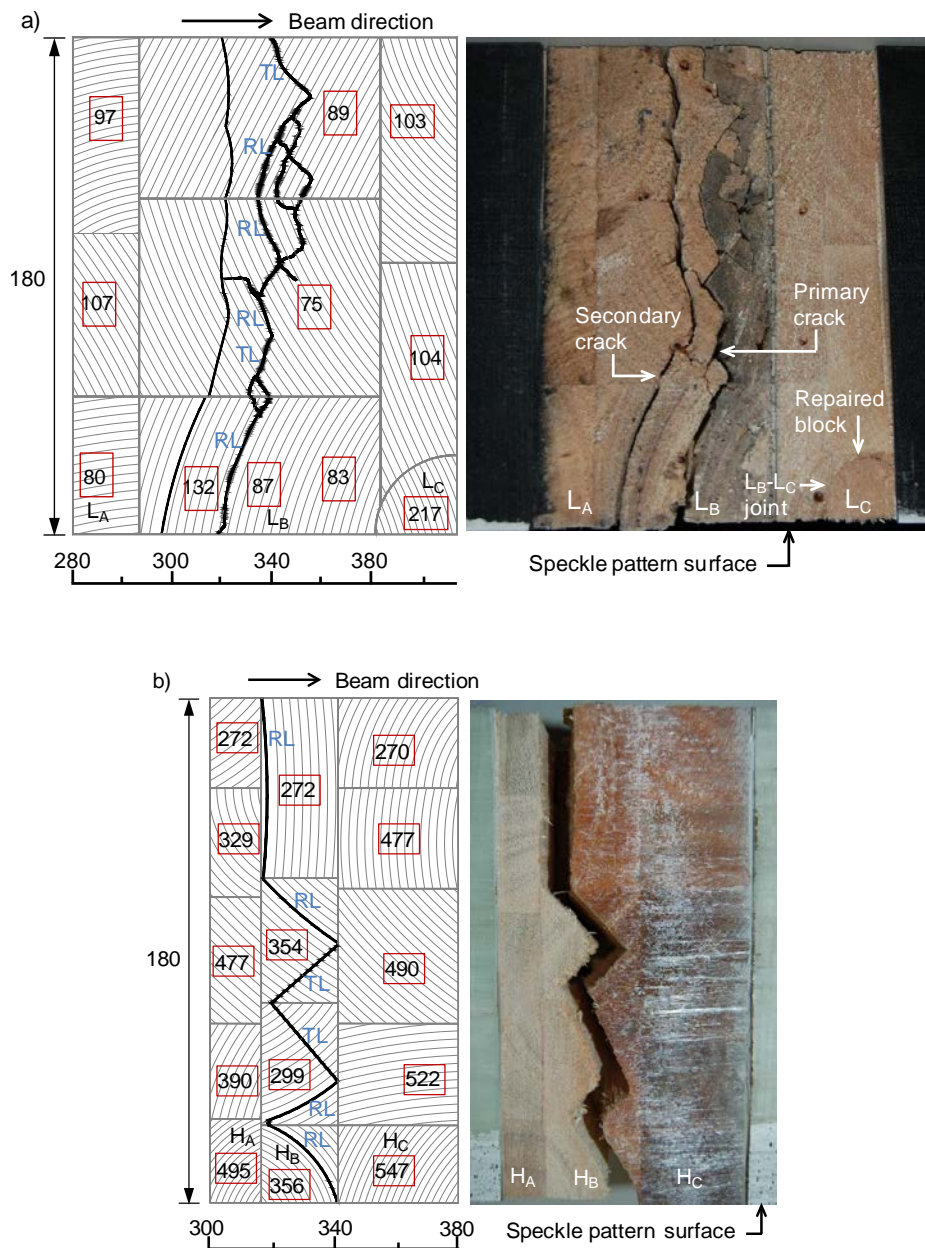
Figure 4.15: Crack patterns in B-H/L-2 beam and prism locations and densities (kg/m³), a) bottom view of lower low-density balsa layer, b) top view of upper high-density balsa layer

4.4.2 Analysis of crack propagation in A-G beams

The crack paths at 1450 and 1490 mm from the left support, on the bottom surface of the low-density layer of beam A-G-2, are shown in Fig. 4.16a. More than 50% of the crack propagated in the interface (IF) layer of the block joints, indicating poor bond quality. In the remaining part, the crack propagated on the lower density side, either in the RL or TL plane. Excluding

the IF paths, 68% of the crack propagated in the RL plane and 32% in the TL plane. Similarly to beam B-H/L-2, the RL portion was slightly higher, which can be explained by the small Mode I presence.
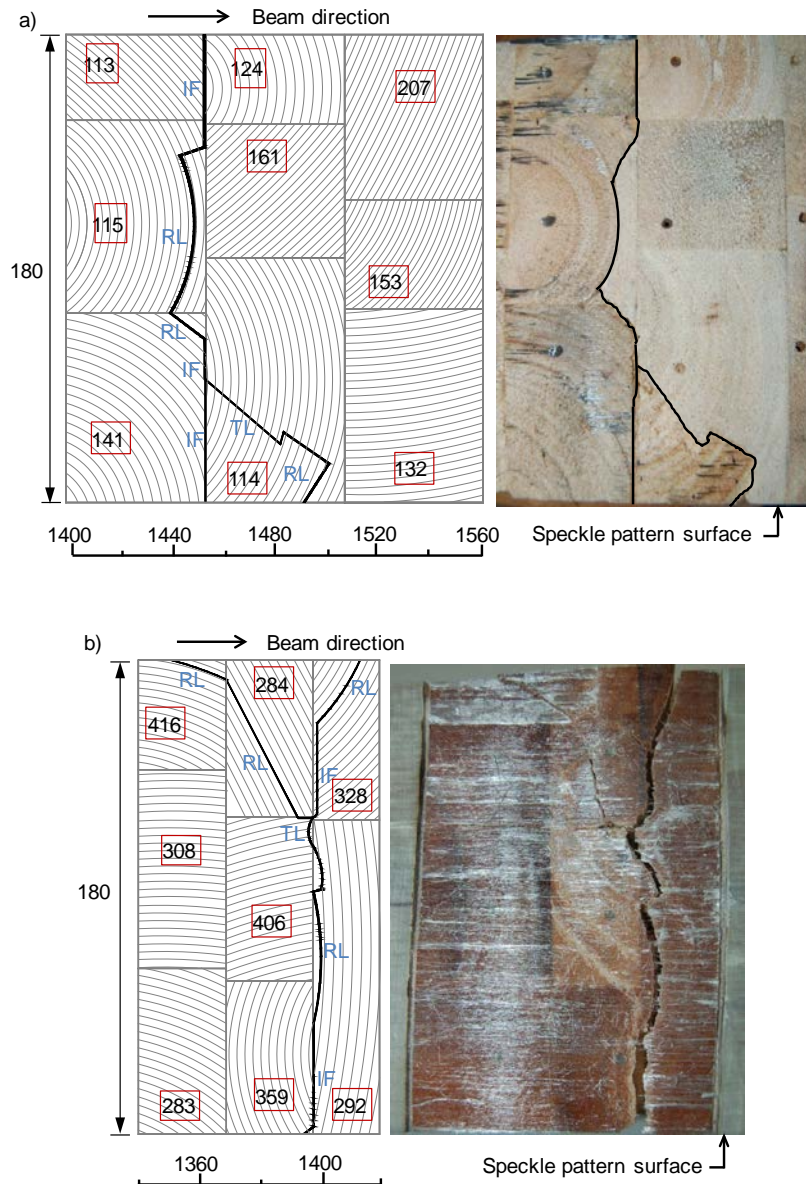
Figure 4.16: Crack patterns in A-G-2 beam and prism locations and densities (kg/m^3), a) bottom view of lower low-density balsa layer, b) top view of upper high-density balsa layer

Crack propagation in the upper high-density layer was similar, see Fig. 4.16b. Approximately 30% of the main crack propagated in the IF layer. In the remaining part, the crack developed either on the clearly lower density side (292 kg/m^3) or, in the case of similar density on both sides of the joint (284 and 328 kg/m^3), the main crack propagated in the block of slightly higher density while a secondary crack formed in the slightly lower density block.

It must be emphasized that the indicated densities were measured on small prisms and were not necessarily representative for the whole blocks; corresponding prism locations are indicated in Figs. 4.15 and 4.16.

4.5 Conclusions

Failure in the complex balsa cores of FRP sandwich beams was analyzed. The cores were composed of high- and low-density balsa layers separated by a circular adhesive interface or GFRP arch. The balsa layers were cut from panels which consisted of balsa blocks adhesively bonded together. The effects of varying block densities and orientations and adhesive bonding between the blocks on the crack propagation and failure mode were investigated. The following conclusions have been drawn:

1) Although commercially available low- and high-density balsa panels were used, the density and thus mechanical properties of the panels and individual balsa blocks varied significantly, in the latter case due to varying early and late wood portions in the same block.

2) Failure in the beams was initiated by cracks through the balsa core thickness. The crack locations could be predicted using the Tsai-Wu failure criterion.

3) Cracks initiated and propagated in the low-density blocks due to their low fracture toughness. Propagation occurred either in the RL or TL planes. In mixed-mode fracture, propagation in the RL plane prevailed due to the lower fracture toughness compared to TL fracture in Mode I. In Mode II no propagation tendency could be observed since the toughness in RL and TL fracture was similar.

4) Cracks were not able to propagate through the transverse adhesive joints between blocks if the bonding was perfect and thus the fracture toughness was high. Cracks initiated at the locations of lowest density and then remained in the corresponding transverse block band limited by the two adhesive layers. If however the bonding was poor, interface failure occurred and cracks could penetrate the adhesive layer.

References

[1] Zenkert D. An introduction to sandwich construction. London: First ed. EMAS Publishing; 1995.

[2] Steeves CA, Fleck NA. Collapse mechanisms of sandwich beams with composite faces and a foam core, loaded in three-point bending. Part I: analytical models and minimum weight design. Int J Mech Sci 2004; 46: 561-583.

[3] Dai J, Hahn T. H. Flexural behavior of sandwich beams fabricated by vacuum-assisted resin transfer molding, Compos Struct 2003; 61: 247-253.

[4] Triantafillou TC, Gibson LJ. Failure mode maps for foam core sandwich beams. Mater Sci Eng 1987; 95:37-53.

[5] Petras A, Sutcliffe MPF. Failure mode maps for honeycomb sandwich panels. Compos Struct 1999; 44: 237-252.

[6] Keller T, Rothe J, de Castro J, Osei-Antwi M. GFRP-balsa sandwich bridge deck-concept, design and experimental validation. J Compos Constr. http://dx.doi.org/10.1061/(ASCE)CC.1943-5614.0000423.

[7] 3A Composites. Baltek SB data sheet. 2011. http://www.corematerials.3acomposites.com/baltek-sb-us.html

[8] Panshin AJ, de Zeeuw C. Textbook of wood technology. New York. 3rd ed. Oxford: McGraw-Hill Book Company; 1970.

[9] Roberts JC, Boyle MP, Wienhold GJ, White G.J. Buckling, collapse and failure analysis of FRP sandwich panels. Composites: Part B 2002; 33: 315-324.

[10] Daniel IM. Influence of core properties on the failure of composite sandwich beams. J Mech Mater Struct 2009; 4: 7-8.

[11] Bare S, Benezeggah ML, Matthieh P. Fatigue evaluation of structural phenolic sandwiches. In: Proceedings: ICCM-10 Conference. Whistler; 1995; 1: 633-640.

[12] Whistler D, Chen A, Kim H, Huson P, Asaro R. Methodoly for exciting dynamic and shear moment failure in composite sandwich beams. J Sandw Struct Mater 2012; 14(4): 365-396.

[13] Shivakumar KN, Smith SA. In situ fracture toughness testing of core materials in sandwich panels. J Compos Mater 2004; 38: 655-668.

[14] Mohammadi M.S. Fracture properties of balsa wood and balsa core sandwich composites. MSc-Thesis. Oregon State University; 2012.

[15] Fruhmann K, Reiterer A, Tschegg EK, Stanzl-Tschegg SS. Fracture characteristics of wood under mode I, mode II and mode III loading. Philos Mag A. 2002; 82 (17-18): 3289-3298.

[16] River B.H. Fracture of adhesive-bonded wood joints. Handb Adhes Technol 1994; chapt 9: 151-177.

[17] Johansson CJ, Pizzi T, Leemput MV. State of the art-report: wood adhesion and glued products. COST Action E13, Working Group 2: Glued Wood Products. 2nd ed. 2002.

[18] Wu EM. Applications of fracture mechanics to orthotropic plates. J Appl Mech 1967; 67: 966-974.

[19] Jeronimidis G. The fracture behavior of wood and the relations between toughness and morphology. Proc R Soc London Ser B, Bio Sci 1980; 1173: 447-460.

[20] Ashby MF, Easterling KE, Harrysson R, Maiti SK. The fracture and toughness of woods. Proc R Soc London Ser A, Math Phys Sci 1985; 398: 261-280.

[21] Smith I, Landis E, M Gong. Fracture and fatigue in wood. Sussex. 2nd ed. Sussex: John Wiley and Sons; 2003.

[22] Willliams JG, Birch MW. Mixed mode fracture in anisotropic media. ASTM Cracks and Fracture ASTM STP 601 1976; 125-127.

[23] Nairn JA, Matsumoto N. Fracture toughness of medium density fiber wood including effects of fiber bridging modeling and crack plane interference. Eng Fract Mech 2009; 76: 2748-2757.

[24] Osei-Antwi M, de Castro J, Vassilopoulos AP, Keller T. FRP-balsa composite sandwich bridge deck with complex core assembly. J Compos Constr; 17(6): 04013011. http://dx.doi.org/10.1061/(ASCE)CC.1943-5614.0000435.

[25] Gibson LJ, Ashby MF. Cellular solids. Oxford. 1st ed. Oxford: Pergamon Press Ltd.; 1988.

[26] Baltek Alcan Composite. Data sheet, summary of the mechanical properties of balsa wood for use in FEA. 2008. Baltek Inc, Northvale, NJ, USA. http://www.corematerials.3acomposites.com

[27] Cabrero JM, Gebremedhin KG. Evaluation of failure criteria in wood members. In: Proceedings: World Conference on Timber Engineering, WCTE. Trentino, Italy; 2010; 1274-1281.

5.

Complex core system 1: Analytical multilayer modeling
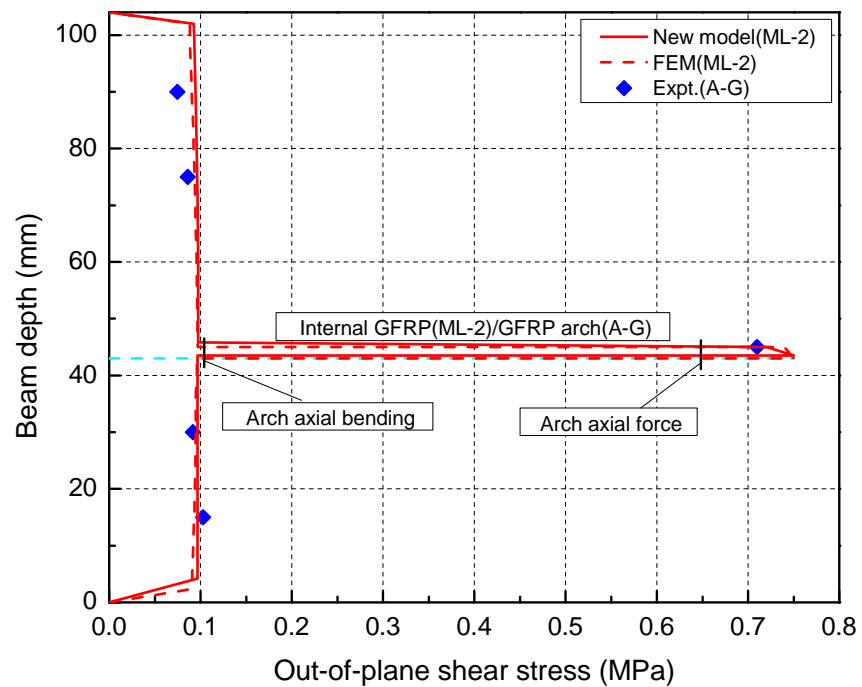
Out-of-plane shear stress distribution in upper high-density balsa core, GFRP arch and lower low-density balsa core of complex core system successfully predicted by new analytical model (ML-2)

5.1 Overview

Sandwich structures are efficient load-bearing components normally composed of a lightweight core made of structural foam or balsa, which separates two thin face sheets, usually made of metals or fiber-reinforced polymer (FRP) laminates. In order to further optimize these structures and provide tailored designs for specific applications, multilayer sandwiches are developed, which involve variation of the core materials and properties in different layers through the thickness of the sandwich.

Multilayer sandwich structures were developed to increase peeling, impact and wrinkling strengths [1-2] for example. Complex core assemblies were also used to improve the performance of FRP-balsa sandwich bridge decks [3]. The complex core comprised high-density and low-density balsa layers, separated by an FRP arch inserted into the high-/low-density core interface. The upper high-density core was also intended to prevent indentation caused by wheel loads. Furthermore, multilayer sandwich structures have also been successfully applied in the aerospace industry [4].

Analytical models exist to predict the mechanical behavior of multilayer sandwich structures. They are based on Reissner-Hoff's models developed for single-layer core sandwich beams, which assume a plane strain distribution through the thickness. The face sheets resist the bending moments that cause axial in-plane stresses, while the core bears the shear forces that cause out-of-plane shear stresses [5-6]. The first analytical model for multilayer sandwich beams was developed by Little and Liaw using an energy method [4]. The face sheets were modeled as isotropic membrane layers without any bending rigidity while the core layers were assumed to be orthotropic and to only resist out-of-plane shear stresses but not axial stresses. A further assumption was that the core layers exhibited the same shear strain through the core thickness. Using the same energy method and similar assumptions, Little and Liaw's model was extended by Azar [7] to include orthotropic face sheets.

Again based on a similar energy method, Kao and Ross [8] established a model that is able to attribute, depending on the shear moduli, different shear strains to the individual core layers. Furthermore, the model can also take the bending rigidity of the face sheets into account. They showed that, compared to their model, Little and Liaw's model resulted in a 79% underestimation of the shear strain of the weak core of a sandwich with two core layers with a shear stiffness ratio of 10. Kao and Ross' model was then extended by Khatua and Cheung [9] to include the influence of face sheet thickness on the shear strains of the core

layers. This new model was validated by FEM for arbitrary isotropic and orthotropic face sheets and core properties.

Frostig and Rabinovitch [10] used a different approach and developed two new multilayer models based on the high-order sandwich panel theory (HSAPT), one that takes into account only core layers and a second one that enables intermediate ″skin″ or laminate layers to be placed in between core layers. The models involve the solution of 13 differential equations and were not validated by any other method. The models also take only soft cores into account (assuming a constant shear stress distribution through the thickness) and thus disregard axial deformations and stresses in the cores.

Meanwhile, stiff cores such as balsa and timber are being increasingly used in sandwich structures due to their favorable shear properties and significant contributions to bending stiffness and resistance [11-12]. The balsa core of a glass-FRP (GFRP) sandwich beam bore 18% of the axial force resulting from the bending moment [11]. Furthermore, the maximum shear stress resulting from the correct parabolic distribution exceeded that resulting from a constant distribution by 14%.

None of the existing models for multilayer sandwich structures is able to accurately predict axial and shear stresses in the case of stiff cores. The HSAPT model is also complex, involves considerable computational times and has not yet been validated. This chapter thus proposes new analytical models for predicting axial and shear strains and stresses in multilayer sandwich structures composed of stiff cores and intermediate laminates. The models have been validated by both FEM and results from 4-point bending experiments on the GFRP-balsa sandwich beams with complex core assembly described above [3].

5.2 Experimental work and FEM

A short description of the experimental investigations is given in the following; details can be found in [3]. Furthermore, the finite element modeling (FEM) of multilayer sandwich beams similar to those used in the experiments is described. Both experimental and FEM results are used to validate the new models subsequently presented.

5.2.1 Experimental beam and material description

Two types of sandwich beams with complex core assemblies were experimentally investigated: 1) beams where an upper, high-density balsa (SB150) core was separated from a lower, low-density balsa (SB50) core by a circular adhesive interface (denominated B-H/L

beams), and 2) beams with the same balsa core configuration but with a GFRP arch laminate in the circular high-/low-density balsa core interface (denominated A-G beams), as shown in Fig. 5.1. In both configurations, the lower face sheets were a 2-mm-thick CFRP layer, while a 2-mm-thick GFRP layer was applied as the upper face sheets. For the arch laminate, a 2-mm-thick GFRP layer was used. The balsa cores were oriented with fibers perpendicular to the face sheets to prevent indentation. The properties of the FRP laminates and balsa materials are given in Tables 5.1 and 5.2. Beam length, span and width were 2400 mm, 2000 mm and 180 mm respectively and the total core height was 100 mm.
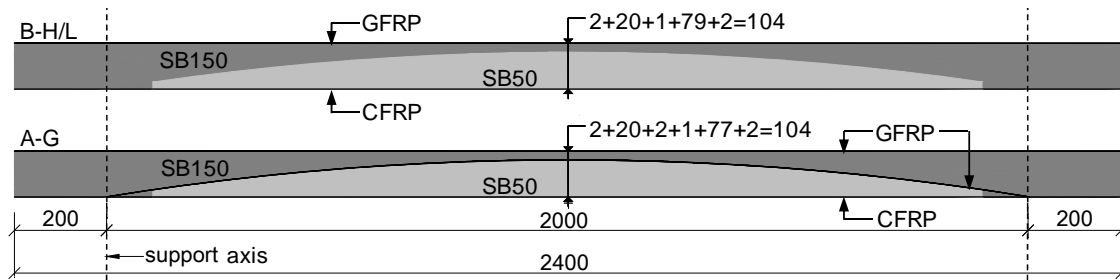
Figure 5.1: Composition/description of B-H/L and A-G beams (dimensions in mm).

Table 5.1: Density and stiffness properties of balsa core and FRP laminates (x=longitudinal, y=vertical, z=transverse beam axis) [3]

Properties	[a]Balsa SB150	[a]Balsa SB50	[b]Douglas fir	[c]UD GFRP	[c]UD CFRP
Density (kg/m^3)	250	95	590	2500	1800
Longitudinal elastic modulus, E_x(MPa)	200	75	16396	39000	120000
Out-of-plane elastic modulus, E_y (MPa)	4320	1993	1061	10000	10800
Transverse elastic modulus, E_z (MPa)	200	75	772	10000	10800
Out-of-plane shear modulus, G_{xy} (MPa)	354	221	910	2400	7400
In-plane shear modulus, G_{xz} (MPa)	64	35	882	-	-
In-plane shear modulus, G_{yz} (MPa)	309	106	76	-	-

[a]mean values according to [13]

[a]values according to [14]

[c]values estimated by rule of mixtures using data sheets from [15]

Table 5.2: Strength properties of balsa core and FRP laminates (x=longitudinal, y=vertical, z= transverse beam axis) [3]

Properties (MPa)	Balsa SB150	Balsa SB50	Douglas fir	UD GFRP	UD CFRP
Longitudinal compressive strength, σ_{cx}	18.9[a]	6.3[a]	49.9[c]	290[d]	900[d]
Transverse compressive strength, σ_{cy}	0.7[a]	0.4[a]	5.5[c]	141[e]	141[e]
Longitudinal tensile strength, σ_{tx}	18.5[a]	7.4[a]	107.6[c]	890[d]	1420[d]
Transverse tensile strength, σ_{ty}	-	-	2.3[c]	35[e]	42[e]
Out-of-plane shear strength, τ_{xy}	2.3[b]	1.5[a]	7.8[c]	-	-
In-plane shear strength, τ_{xz}	1.7[b]	0.4[a]	-	-	-
In-plane shear strength, τ_{yz}	5.1[b]	1.8[a]	-	-	-

[a]mean values according to [13]

[b]values according to [16]

[c]values according to [14]

[d]estimated values from [17] and [18]

[e]values according to [18]

5.2.2 Experimental set-up, instrumentation and measurements

The beams were loaded in a 4-point bending configuration, at the third points of the span, in different loading cycles up to failure; the beam set-up is shown in Fig. 5.2. Deflections were monitored with linear voltage displacement transducers and axial strains on the face sheets and arch laminates were measured with strain gages. Axial deformations of the core were measured in one section close to the right-hand load, see Fig. 5.2, using four Omega gages, one in the compression zone, one on each side of the arch or the adhesive interface and another in the tension zone.
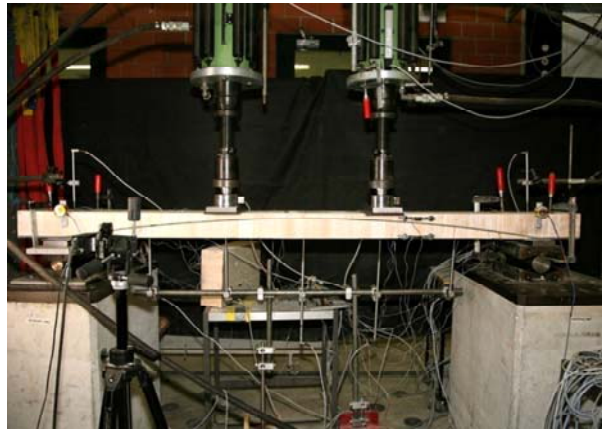
Figure 5.2: Experimental set-up for A-G beam with GFRP arch integrated in balsa core.

Shear deformations through the core thickness, including the arch laminate, were measured by five shear strain gages placed 334 mm from the left support. Two beams per configuration were examined.

5.2.3   Finite element modeling of two beam configurations

Two multilayer sandwich beam configurations were modeled: 1) a sandwich beam with two core layers (denominated ML-1) and 2) the same sandwich beam with an intermediate laminate between the two cores (ML-2). The beams were modeled as simply supported and subjected to the same symmetric four-point bending as the experimental beams, see Fig. 5.3.
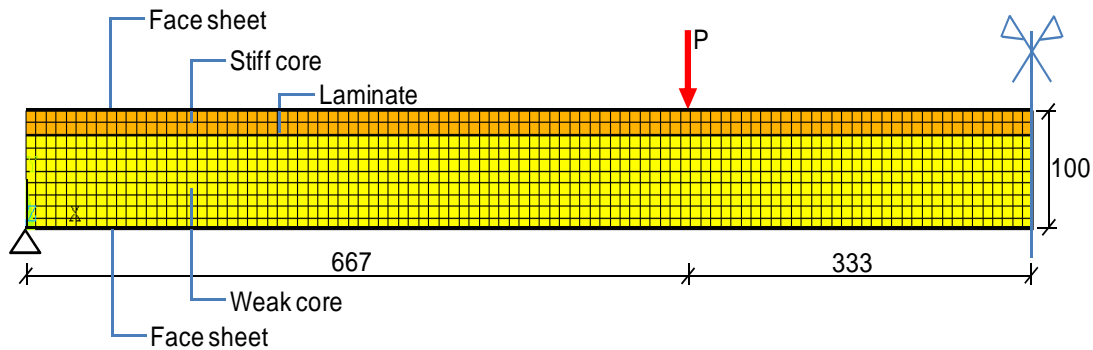
Figure 5.3: Finite element model for multilayer sandwich beam (dimensions in mm)

Both sandwich beams had the same dimensions and material configurations as the experimental beams. The only difference concerned the intermediate laminate layer or core interface, which was modeled parallel to the face sheets and not as an arch. To simulate the beam deflections and axial stresses at the mid-span of the B-H/L and A-G beams, the interface of the two cores was placed at 80% of the total core thickness (100 mm) while the prediction of the shear stresses was done at 334 mm from the left support, selecting the interface at 43% of the total core thickness (corresponding to the height of the arch interface/laminate at this location). In a variant of beam ML-1, the upper SB150 balsa core was subsequently replaced by Douglas fir (Df) to demonstrate the effect of increased core bending stiffness. The mechanical properties of Douglas fir are also listed in Tables 5.1 and 5.2.

The two sandwich beams were modeled in 3D by ANSYS v-13 software, using an 8-node layered shell element (shell 99) for the face sheets and intermediate laminate and a 20-

node structural solid element (solid 95) for the cores. The face sheets and intermediate laminate were modeled in 8 layers of 0.25-mm thickness each and 100 layers of 1-mm thickness were used for the cores. For the Douglas fir, the fibers were oriented in the beam direction to simulate its orientation as the upper core layer in a GFRP-balsa sandwich bridge deck with complex core assembly, whose fibers are oriented in the bridge direction to increase bending rigidity and shear capacity. Perfect bonding conditions were assumed at the face sheet/core joints as well as at the dissimilar core joints, and hence the adhesive bonds applied at these joints in manufacture were not modeled. The beams were meshed using 11,081face sheet/laminate and 54,043 core elements. Due to symmetry of the beam structure and loading, only half of the beams were modeled (see Fig. 5.3) and symmetry boundary conditions were applied at the mid-span cross sections.

Linear elastic simulations were performed for serviceability limit state (SLS) loads at 2x0.95 and 2x1.05 kN for beams ML-1 and ML-2 respectively. The SLS loads were defined at maximum beam deflections of span/500, according to Eurocode-2 part 2[19].

5.3 New analytical models

New analytical bending and shear stiffness models have been developed for a multilayer sandwich beam used to predict its deflection, axial and shear stresses in the face sheets, cores and laminate layers. The models are based on the single-core classical sandwich theory.

5.3.1 New bending stiffness model

The bending stiffness, D, of a single-core sandwich beam, as shown in Fig. 5.4a, is the summation of the individual rigidities of the face sheets and the core, obtained about the neutral axis of the entire sandwich beam [20]. This model can be extended, in a first step, to multilayer sandwich beams with two cores as shown in Fig. 5.4b, by splitting the rigidity of the single core into two core layers as follows:

$$D_{ml} = E_{f1}I_{f1} + E_{c1}I_{c1} + E_{c2}I_{c2} + E_{f2}I_{f2} \tag{1}$$

where subscripts ml, f and c denote multilayer sandwich beam, face sheet and core respectively, and $E_{f1}, I_{f1}, E_{f2}, I_{f2}, E_{c1}, I_{c1}, E_{c2}, I_{c2}$ are the Young's moduli and moments of inertia of the top face sheet, bottom face sheet, and core layers 1 and 2 about the neutral axis of the entire multilayer sandwich beam respectively.

Equation (1) can then be generalized for n layers between the top and bottom face sheets, which could either be cores or laminates as:

$$D_{ml} = \sum_{i=1}^{2} E_{f_i} I_{f_i} + \sum_{k=1}^{n} E_{c/l_k} I_{c/l_k} \qquad (2)$$

where i is the top or bottom face sheet, subscript c/l denotes any core/laminate layer in between the top and bottom face sheets and k is the kth core/laminate layer.
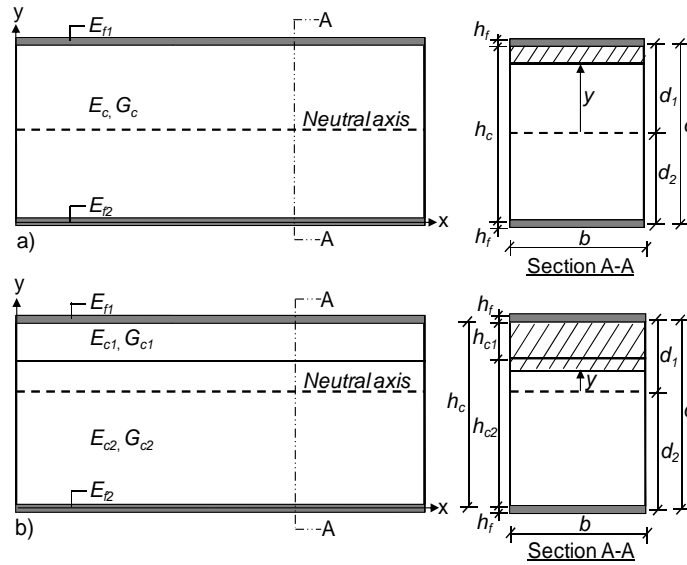
Figure 5.4: Schematic for a) single-core sandwich model and b) multilayer sandwich beam

5.3.2 New shear stiffness model

The shear stiffness, S, of a sandwich beam with a single core is simply a product of the core shear modulus, G_c, and the cross sectional area, A_c, of the core [21]. This model can be extended again to a multilayer sandwich beam with two cores in a first step using the energy method. Figure 5.5 shows a deformed multilayer sandwich beam element subjected to an arbitrary shear force, V_y.
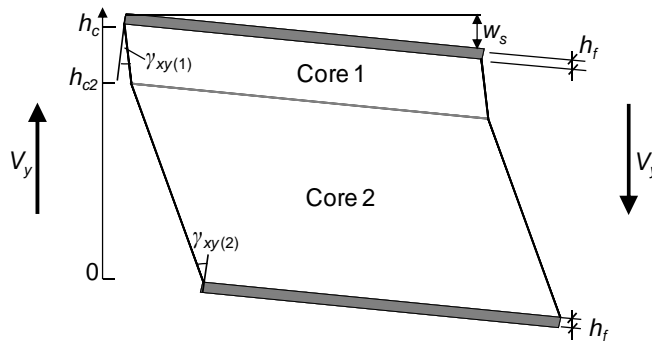
Figure 5.5: Deformed multilayer sandwich element illustrating shear deformation

The potential energy, U_p, of the load, which causes a vertical shear deflection, w_s, is:

$$U_p = \frac{1}{2} V_y \frac{dw_s}{dx} \tag{3}$$

The strain energy in the multilayer sandwich element due to the shearing of core layers 1 and 2 is the summation of the individual strain energies in each core as follows:

$$U_s = \frac{1}{2}\left[\int_0^{h_{c2}} \left(\tau_{xy}\gamma_{xy(2)}\right)dy + \int_{h_{c2}}^{h_c} \left(\tau_{xy}\gamma_{xy(1)}\right)dy\right] \tag{4}$$

where τ_{xy} is the average out-of-plane shear stress in both cores, and $\gamma_{xy(1)}$ and $\gamma_{xy(2)}$ are the shear strains in core layers 1 and 2 respectively. Substituting shear stress, $\tau_{xy} = V_y/bd$, where b is the beam width (assumed as being 1.0 m), d is the distance between the face sheet axis, and shear strain, $\gamma_{xy} = \tau_{xy}/G_{xy}$, into Eq. 4, and integrating over the entire core thickness gives:

$$U_s = \frac{1}{2}\left[\left(\frac{V_y}{d}\right)^2 \frac{h_{c_2}}{G_{c_2}} + \left(\frac{V_y}{d}\right)^2 \frac{\left(h_{c_1}\right)}{G_{c_1}}\right] \tag{5}$$

where h_{c1}, G_{c1}, h_{c2}, and G_{c2} are the core thicknesses and out-of-plane shear moduli of core layers 1 and 2 respectively, and h_c is the total core thickness of the multilayer sandwich beam. The energy balance equation $U_p = U_s$, results in:

$$\frac{dw_s}{dx} = \frac{V_y}{d^2}\left[\frac{h_{c_2}}{G_{c_2}} + \frac{h_{c_1}}{G_{c_1}}\right] \tag{6}$$

Taking into account that the derivative of the vertical shear deflection with respect to the beam direction denotes the average shear strain, $dw_s/d_x = \gamma_{xy}$, the shear stiffness of a multilayer sandwich beam with two core layers can be expressed for a beam width, b, as:

$$S_{ml} = bd^2\left[\frac{G_{c_1}G_{c_2}}{G_{c_1}h_{c_2} + G_{c_2}h_{c_1}}\right] \tag{7}$$

Equation (7) can then be extended for the general case of n core/laminate layers to:

$$S_{ml} = bd^2\left[\frac{\prod\limits_{i=1}^{n} G_{c/l_i}}{\sum\limits_{i=1}^{n}\frac{h_{c/l_i}}{G_{c/l_i}}\left[\left(\prod\limits_{j=1}^{n} G_{c/lj}\right)\right]}\right] \tag{8}$$

5.3.3   Deflections, axial and shear stresses in multilayer sandwich beam

The total beam deflection, w_t, of a sandwich beam is, according to the classical sandwich theory [21], the sum of the bending deflection, w_b, and shear deflection, w_s, as follows:

$$w_t = w_b + w_s \tag{9}$$

The bending deflection is analytically obtained based on a shape function, magnified by a coefficient A, which is the maximum bending deflection at mid-span, as follows:

$$w_b = A\left[\left(\frac{x}{L}\right)^4 - 2\left(\frac{x}{L}\right)^3 + \left(\frac{x}{L}\right)\right] \tag{10}$$

where L is the beam span and A depends on the type of applied load, such as, $A=qL^4/24D_{ml}$ for a uniformly distributed load, q, and $A=23PL^3/648D_{ml}$ for a four-point bending load configuration with loads, P, applied at the third points of the span. The shear deflection is related to the bending deflection according to [21] as follows:

$$\frac{dw_s}{dx} = -\frac{D_{ml}}{S_{ml}}\frac{d^3w_b}{dx^3} \tag{11}$$

For the case of the four-point bending load configuration described above, the shear deflection results as:

$$x \le L/3 : w_s = \frac{Px}{S_{ml}}, \; L/3 \le x \le 2L/3 : w_s = 0, \; x \ge 2L/3 : w_s = \frac{P(L-x)}{S_{ml}} \tag{12}$$

The axial stresses in the face sheets and core of a single-core sandwich beam, according to the classical sandwich theory, which assumes a plane strain distribution through the beam thickness, are obtained from:

$$\sigma_{f,x} = \frac{M_z E_f y}{D}, \; \sigma_{c,x} = \frac{M_z E_c y}{D} \tag{13}$$

where M_z is the bending moment at a distance, x, from the support and y is the depth at the stress location with reference to the neutral axis (see section A-A of Fig. 5.4a). Again assuming plane strain distribution, these equations can be extended for a multilayer sandwich beam and the axial stresses in the top or bottom face sheets and in the kth of n core/laminate layers result in:

$$\sigma_{f_i,x} = \frac{M_z E_{f_i} y}{D_{ml}} \; , \; \sigma_{c/l_k,x} = \frac{M_z E_{c/l_k} y}{D_{ml}} \tag{14}$$

The axial stresses at any depth, y, therefore vary linearly in each individual core/laminate layer depending on the Young's modulus of the core/laminate layers. The axial stress is zero at the neutral axis of the entire multilayer system.

The out-of-plane shear stresses in a single-core sandwich beam exhibit a parabolic distribution in the core, which decreases to zero in the top and bottom face sheets according to the classical sandwich theory. The magnitude of the shear stress at any beam section depends on the shear force at that section and the bending stiffness of the sandwich beam. The variation of the shear stress through the thickness depends on the first moments of area of the face sheets (top and bottom), S_f, and the core, S_c, about the neutral axis of the entire section. The shear stresses in the face sheet, τ_f, and the core, τ_c, are thus:

$$\tau_f = \frac{V_y S_f E_f}{D} \tag{15}$$

$$\tau_c = \frac{V_y \sum (S_c E_c)}{D} \tag{16}$$

where $\sum S_c E_c$ for the core, for instance, is the sum of the product of S_c and E_c of the shaded part of the cross section above y in section A-A of Fig. 5.4a. For a single core, this product is expressed as:

$$S_f E_f = \frac{E_f b}{2} \left(d_1 + \frac{h_f}{2} - y \right) \left(d_1 + \frac{h_f}{2} + y \right) \tag{17}$$

$$\sum (S_c E_c) = E_f b h_f d_1 + \frac{E_c b}{2} \left(d_1 - \frac{h_f}{2} - y \right) \left(d_1 - \frac{h_f}{2} + y \right) \tag{18}$$

where d_1 is the distance between the neutral axis of the entire sandwich beam and the top face sheet axis and h_f is the face sheet thickness (see Fig. 5.4a). The shear stress model for the single core can be modified for a sandwich beam with two cores by considering two separate shear stress distributions, τ_{c1} and τ_{c2}, in the core layers 1 and 2, which depend on their individual Young's moduli and first moments of area, represented by the shaded areas in section A-A of Fig. 5.4b. Extending to the general case, the shear stress in the kth of n core/laminate layers results in:

$$\tau_{c/l_k} = \frac{V_y \sum (S_{c/l_k} E_{c/l_k})}{D_{ml}} \tag{19}$$

where

$$\sum (S_{c/l_k} E_{c/l_k}) = E_{f1} b h_f d_1 + \sum_{m=1}^{k-1} \left[E_{c/l_m} b h_{c/l_m} \left(d_1 - \frac{h_f}{2} - \left(\sum_{r=1}^{m-1} h_{c/l_m} + \frac{h_{c/l_m}}{2} \right) \right) \right] +$$
$$E_{c/l_k} \frac{b}{2} \left(d_1 - \frac{h_f}{2} - \sum_{m=1}^{k-1} h_{c/l_m} - y \right) \left(d_1 - \frac{h_f}{2} - \sum_{m=1}^{k-1} h_{c/l_m} + y \right) \tag{20}$$

90

5.4   Experimental and numerical validation of new models

A comparison between the experimental results obtained from multilayer beams B/H-L and A-G (deflections and axial and shear stresses in the face sheets and core/laminate layers) and both FEM (models ML-1 and ML-2) and the new analytical models is presented and discussed in the following.

5.4.1   Beam deflections

Figure 5.4 shows the deflection curves obtained from the total deflection model (Eq. 9, thus applying the new bending stiffness and shear stiffness models, Eqs. 2 and 8), FEM (models ML-1 and ML-2) and measured beam deflections for the multilayer B-H/L and A-G beams at their SLS loads. The deflection predictions obtained from both the new analytical model and FEM are almost identical. Both models also agree well with the measured deflections of the B-H/L beam. However, both slightly overestimate the deflections of the A-G beam because of the arch effect, which is not taken into account in the models.
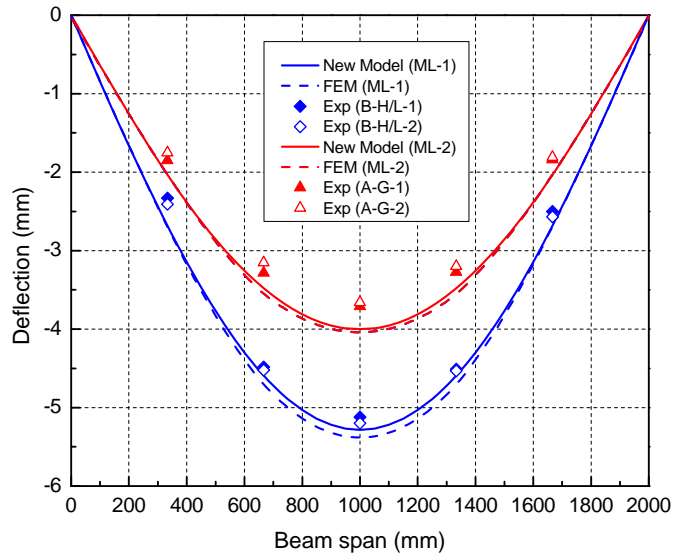
Figure 5.6: Comparison of multilayer beam deflections obtained from new analytical model and FEM, and measured deflections of B-H/L and A-G beams at SLS loads

The arch action reduces the axial deformations of the upper face sheet and shear deformations in the core. It is also apparent from Fig. 5.6 that the ML-2 and A-G beams show 14% lower beam deflection than the ML-1 and B-H/L beams. This deflection reduction is attributed to

the increase in bending stiffness of the ML-2 and A-G beams due to their internal GFRP layer and GFRP arch respectively.

5.4.2   Axial strain and stress distributions

Figure 5.7a shows the mid-span axial strain distributions through the sandwich beams, measured for the B-H/L beam and predicted by the new analytical model and FEM for the ML-1 beam at the SLS load. The same comparison is shown in Fig. 5.7b for the A-G beam and ML-2 model. The axial strain of the new analytical model is computed by dividing the axial stresses from Eq. (14) by the respective Young's moduli of the FRP laminates and balsa cores. The analytical predictions concur with those of the FEM and both agree well with the experimental results. The measured data shows plane strain distributions with slight scatter in both the B-H/L and A-G beams (caused by the different measurement devices: Omega-gages on the core and strain gages on the laminates and variability of balsa core properties). This result validates the plane strain assumption in the new analytical models for the multilayer sandwich beams.
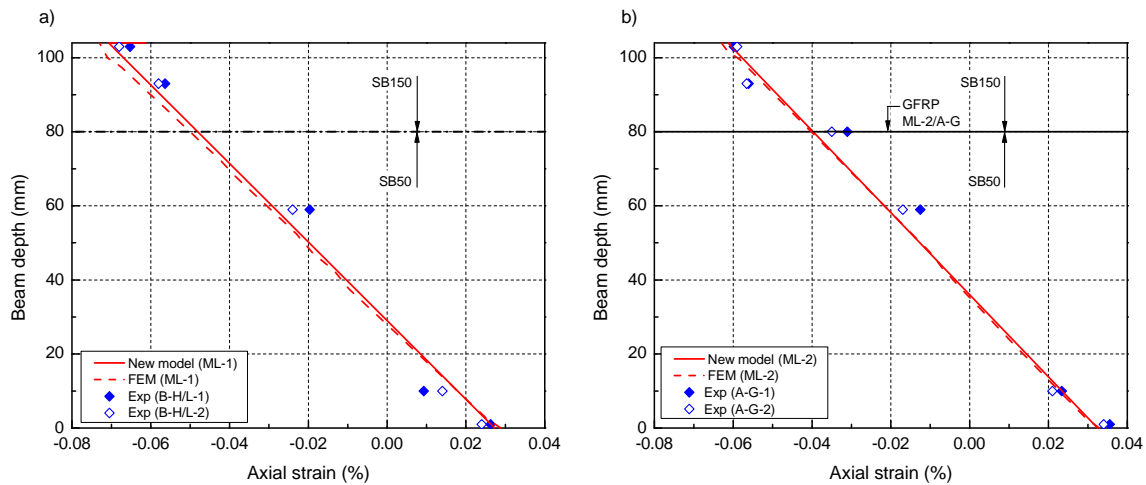
Figure 5.7: Comparison of axial strain distributions obtained from new analytical model and FEM and measured strains at SLS loads for a) ML-1 and B-H/L beams and b) ML-2 and A-G beams
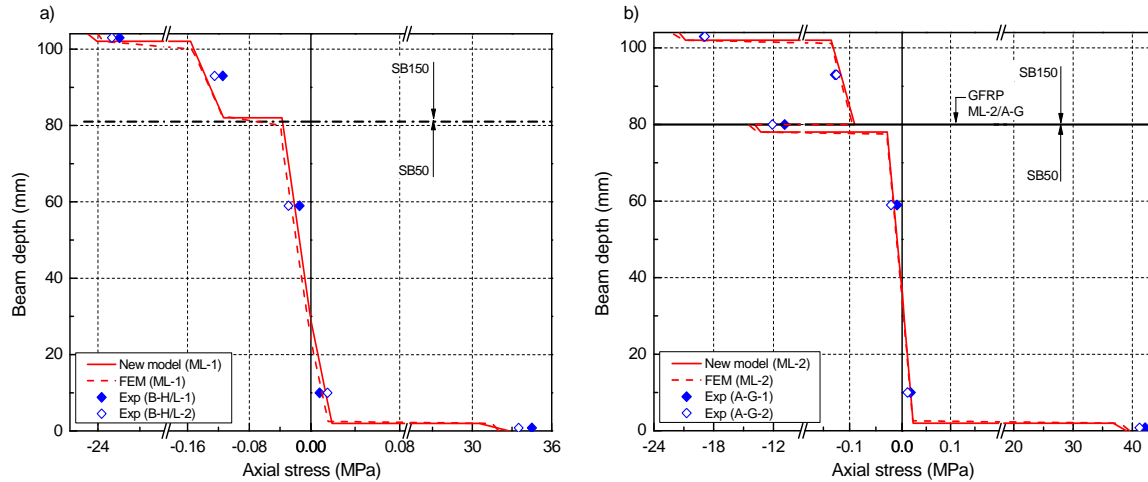
Figure 5.8: Comparison of axial stress distributions obtained from new analytical model and FEM and axial stresses at SLS loads for a) ML-1 and B-H/L beams and b) ML-2 and A-G beams

The corresponding axial stresses are shown in Fig. 5.8. The axial stresses for the B-H/L and A-G beams were obtained by multiplying the measured axial strains with the Young's moduli of the FRP laminates and balsa cores. The axial stress distributions predicted by the analytical models and FEM are almost identical to the experimental results. The maximum axial stresses in the cores always occur in the upper high-density balsa core. The core contributes about 7% of the total compression in the ML-1 beam. Furthermore, Figure 5.9 compares the axial stresses in the case of replacement of the upper high-density balsa core by an even stiffer Douglas fir core.
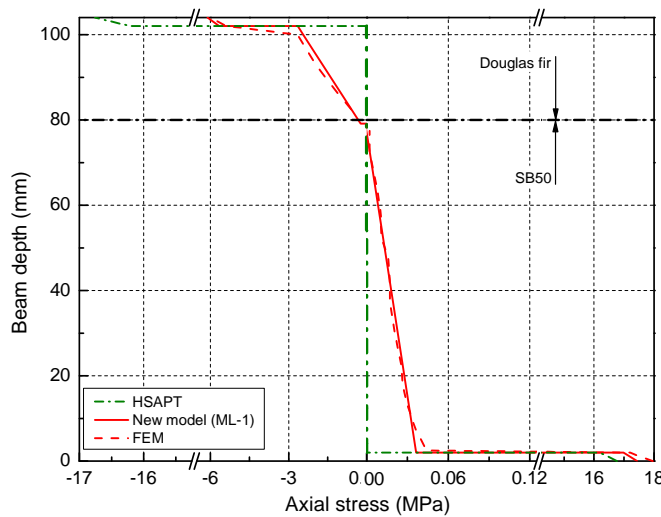
Figure 5.9: Comparison of axial stress distributions obtained from new analytical model, FEM and high-order sandwich panel theory (HSAPT) at SLS loads for ML-1 beam with Douglas fir upper core

The results from the new analytical model, FEM for the ML-1 beam and high-order sandwich panel theory (HSAPT, applied according to [11]) are shown. The Douglas fir contributes about 69% of the total compression force (resulting from the bending moment) in the ML-1 beam. This significant axial stress contribution by the core is, however, neglected in the high-order sandwich panel theory. Therefore the axial stresses in the top face sheet are largely overestimated, while all the values agree for the bottom face sheet.

5.4.3 Shear strain and stress distributions

The out-of-plane shear strain measurements at 334 mm from the left support of the B-H/L beam and the shear strain distribution prediction by the new analytical model and FEM for the ML-1 beam are shown in Fig. 5.10a. Figure 5.10b shows the same comparison for the A-G and ML-2 beams. The analytically predicted shear strains are computed by dividing the shear stresses obtained from Eq. (19) by the shear moduli of the GFRP laminate and balsa cores. The shear strain predictions by the analytical model concur with those from FEM and both were corroborated by the experimental results. Higher shear strains were obtained for the low-density than the high-density balsa core, at a ratio (0.037/0.024=1.5) approximately comparable to the inverse of their shear moduli ratio (1/ (221/354) =1.6).
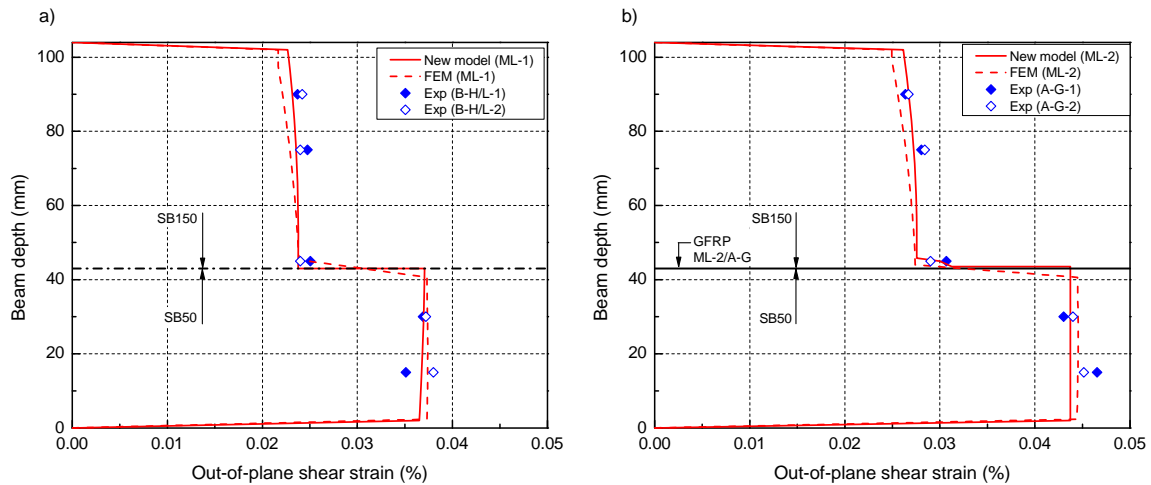
Figure 5.10: Comparison of shear strain distributions obtained from new analytical model and FEM and measured strains at SLS loads for a) ML-1 and B-H/L beams and b) ML-2 and A-G beams
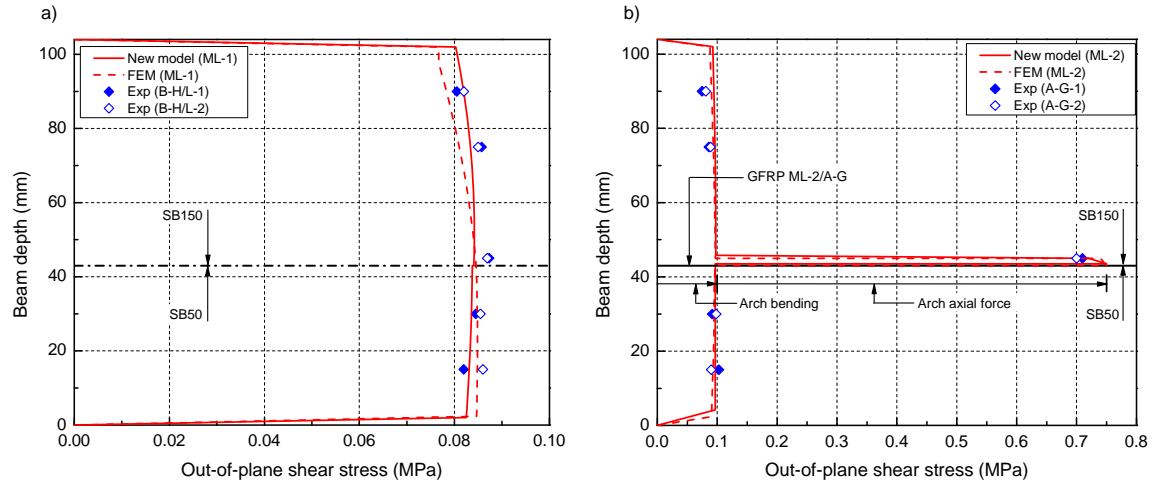
Figure 5.11: Comparison of shear stress distributions obtained from new analytical model and FEM and measured shear stresses at SLS loads for a) ML-1 and B-H/L beams and b) ML-2 and A-G beams

The corresponding out-of-plane shear stresses are shown in Fig. 5.11. Shear stresses in the B-H/L and A-G beams were determined from the shear moduli of the balsa cores and GFRP arch and their shear strain measurements. The shear stresses in the GFRP arch of the A-G beam are composed of the contributions from the bending of the arch laminate and from the vertical component of the arch thrust (for details see [3]). The shear stresses from arch bending were obtained from the analytical model. The vertical component of the arch thrust was calculated from the axial stresses in the arch laminate (obtained from the analytical model) and the arch inclination angle at the analyzed position. An almost constant shear stress distribution occurs in the balsa cores in the B-H/L beam, which agrees with the predictions by the new analytical model and FEM for the ML-1 beam. For the A-G beam, similar and almost constant shear stresses occur in the balsa cores while the GFRP arch exhibits high shear stresses due to the arch thrust contribution. Shear stresses in both the cores and the arch are well predicted by the new analytical model. Figure 5.12 shows shear stress distributions predicted by the new analytical model, FEM for the ML-1 beam and high-order sandwich theory (HSAPT) in the case of Douglas fir as upper core. Near the joint between the Douglas fir and low-density balsa, the high-order sandwich panel theory underestimates the shear stress by about 16% compared to estimations from the new analytical model and FEM, which agree well.
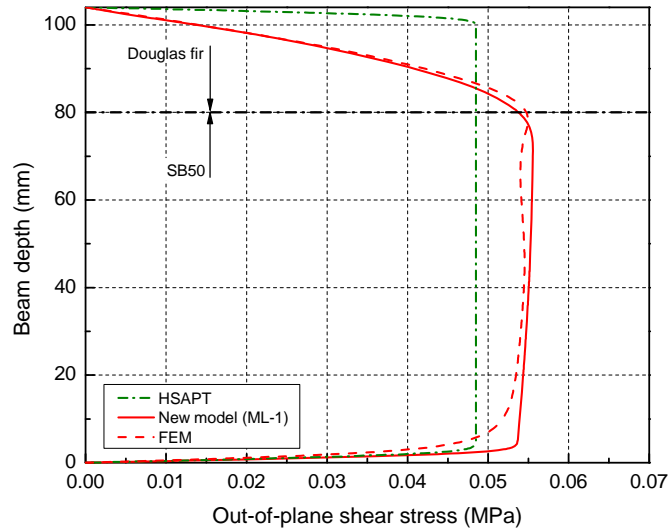
Figure 5.12: Comparison of shear stress predictions obtained from new analytical model, FEM and high-order sandwich panel theory (HSAPT) at SLS loads for ML-1 beam with Douglas fir upper core

5.5 Conclusions

New analytical models for predicting axial and shear strains and stresses in multilayer sandwich structures composed of stiff cores and intermediate laminates have been developed. The models are based on new formulations for calculating the bending and shear stiffness of multilayer sandwich structures. They have been validated by FEM and results from four-point bending experiments on GFRP-balsa sandwich beams with complex core assembly. The following conclusions can be drawn:

1) The beam deflections, axial and shear stresses determined from the experimental work and FEM correlate well with the results from the new models. The models are able to accurately predict axial and shear stresses in stiff cores and intermediate laminate layers.

2) The results from the models demonstrate that a stiff core can significantly contribute to the bending resistance of a sandwich structure. A stiff Douglas fir core layer is able to bear about 69% of the axial compression force in a multilayer sandwich beam with FRP face sheets. This contribution is disregarded by the existing high-order sandwich panel theory (HSAPT) and the compression stresses in the face sheet are thus largely overestimated.

3) The high-order sandwich panel theory (HSAPT) also underestimates the shear stresses in the Douglas fir layer by about 16% compared to the accurate prediction obtained from the new multilayer model.

References

[1] Danielsson M, Grenestedt JL. Gradient foam core materials for sandwich structures: preparation and characterisation. Composites Part A. 1998; 29: 981-988.

[2] Weeks CA, Sun CT. Mulit-core composite laminates. J. Adv. Mater 1994; 28-37.

[3] Osei-Antwi M, de Castro J, Vassilopoulos AP, Keller T. FRP-balsa composite sandwich bridge deck with complex core assembly. J Compos Constr; 17(6): 04013011. http://dx.doi.org/10.1061/(ASCE)CC.1943-5614.0000435.

[4] Liaw BD, Little RW. Theory of bending multilayer sandwich plates. Am Inst Aeronat Astronaut 1967; 5(2): 301-304.

[5] Reissner E. On bending of elastic plates. Quart Appl Math 1947; 5: 55-68.

[6] Hoff NJ. Bending and buckling of rectangular sandwich plates. NACA TN 1950; 2225.

[7] Azar JJ. Bending theory for multilayer orthotropic sandwich plates. Am Inst Aeronat Astronaut 1968; 6 (11): 2666-2169.

[8] Kao JS, Ross RJ. Bending of multilayer sandwich beams. Am Inst Aeronat Astronaut 1968; 6: 1583-1585.

[9] Khatua TP, Cheung YK. Bending and vibration of multilayer sandwich beams and plates. Int J Numer Met Eng 1973; 6: 11-24.

[10] Frostig Y, Rabinovitch O. Behavior of uni-directional sandwich panels with a multi-skin construction or a multi-layered core layout-high-order approach. J Sand Struct Mater 2000; 2:181-213.

[11] Phan CN, Frostig Y, Kardomateas GA. Analysis of sandwich beams with compliant core and with in-plane rigidity-extended high-order sandwich panel theory versus elasticity. J Appl Mech 2012; 79: 1-11.

[12] Keller T, Rothe J, de Castro J, Osei-Antwi M. GFRP-balsa sandwich bridge deck-concept, design and experimental validation. J Compos Constr. http://dx.doi.org/10.1061/(ASCE)CC.1943-5614.0000423.

[13] Alcan Baltek Corporation. Data sheet. Mechanical properties vs. density and grain orientation for balsa wood, Northvale, New Jersey, USA. 2001. http://www.corematerials.3acomposites.com/baltek-sb.html

[14] Kretschmann DE. Mechanical properties of wood.US Forest Prod Lab 2010; Chapter 5; 1-46.

[15] Swiss Composites Suter Kunststoffe AG. Data sheet for basalt, glass and carbon fibers and fabric, Fraubrunnen, Switzerland. 2010. http://www.swiss-composite.ch/

[16] Osei-Antwi M, de Castro J, Vassilopoulos AP, Keller T. Shear mechanical characterization of balsa wood as core for composite sandwich panels. Constr Build Mater 2013; 41: 231-238.

[17] Manshadi B, Mahmudi H, Abedian, A, Mahmudi R. A novel method for materials selection in mechanical design: combination of non-linear normalization and a modified digital logic method. Mater Des 2007; 28(1): 8-15.

[18] Gay D, Hoa SV. Composite materials: design and applications. CRC Press, Boca raton, Fl. 2007; 29-51.

[19] European Standard. Eurocode 2-Part 2: Design of concrete structures: concrete bridges. European Committee for Standardization. Brussels; 2002.

[20] Allen HG. Analysis and design of structural sandwich panels. Oxford: Pergamon Press 1969.

[21] Zenkert D. An introduction to sandwich construction. London: EMAS 1997.

6.

Complex core system 2: GFRP-balsa sandwich beam with timber inserts-analytical modeling
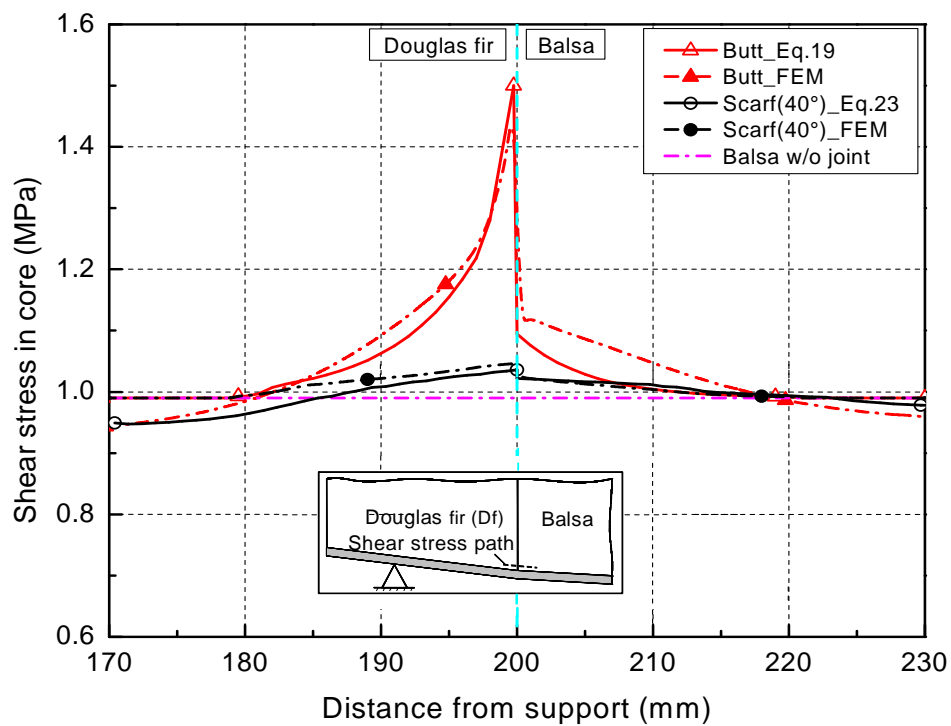
Shear stress concentration at Douglas fir/balsa core joint successfully predicted by new analytical models for butt joint (Eq. 19) and scarf joint (Eq. 23)

6.1 Overview

Sandwich structures consist of an assembly of lightweight honeycomb, foam or balsa cores which separate two thin, stiff and strong face sheets, usually composed of metal sheets or composite laminates. Due to their high stiffness-to-weight and strength-to-weight ratios, sandwich structures have been successfully applied in aircraft structures, ship and train hulls, and wind turbine rotor blades. Most of these structures require tailored designs of the individual sandwich components or sections at specific locations. For example, the fixation of rigs in hulls of marine structures requires the introduction of inserts in the sandwich core to facilitate attachment and efficient transfer of local loads [1]. It is also a common practice to assemble foams of different densities in the sandwich panels of hulls and fuselage structures [2-3]. The material discontinuities at such joints between dissimilar core materials cause abrupt changes of the shear angles and local bending of the face sheets at these locations [4]. The corresponding stress concentrations in the face sheets and surrounding cores may lead to local failures in the face sheets or core, which could subsequently trigger the overall collapse of the whole sandwich structure.

Several design concepts were developed with the aim of reducing the local stress concentrations at such core joints [5]. The use of face sheet doublers as one of the solutions involves the bonding of additional short plates onto the face sheets at the core joint [5]. This solution reduced the peak stresses in the face sheets significantly but caused additional stress concentrations at the geometric discontinuities between the face sheets and the doublers. The insertion of a core patch, which plays an intermediate role regarding location and mechanical properties between those of the stiff and weak cores, constitutes another design option. Although the stress concentrations in the face sheets are reduced significantly, integrating an intermediate core for each core joint did not seem practical in manufacture [5]. The use of scarf joints on the other hand eliminates almost completely this local phenomenon, with a slightly increased joint length however. A scarf joint, unlike a butt joint, has its interface between the dissimilar cores at angles of termination of other than 90° with respect to the face sheets.

Analytical models were developed to predict the local stress concentrations in the face sheets and core in the vicinity of the core joint. For butt joints, a closed-form model has been formulated to predict the intensity of this local effect and its expansion by Skvortsov et al. [6]. The model assumes the core to be soft such as a foam core, with no transfer of axial stresses and a constant through-thickness shear stress. The intensity and decay of the local

phenomenon are dependent on the level of disparity between the shear stiffnesses of the dissimilar cores, the face sheet thickness and the core height. The model was experimentally and numerically validated for a sandwich beam of aluminum face sheets bonded over a butt joint of Divinycell H-60 and H-200 foam cores, and loaded in three-point bending. Compared to a single H-60 foam core, a local compressive stress increase of ~100 % was accurately predicted in the outer layer of the top face sheet [5]. For the shear stress concentrations in the core, however, the model was inaccurate and predicted only ~24 % of the values obtained by the FEM. This was partly attributed to the unrealistic assumption of a constant shear stress in the core at the vicinity of the joint. A high-order theory was also formulated by Frostig and Thomsen [7] to predict the bending and shear stresses in the face sheets and cores respectively for butt and scarf joints. They showed that although the local axial stresses in the face sheets were reduced significantly in scarf joints compared to butt joints, the shear stress concentrations did not decrease in the cores even at a termination angle of 26°. The reason for this surprising result was not further investigated. The theory, involving the solution of fourteen differential equations in order to estimate the stress concentrations in the face sheets and cores at the core joint, however, was not validated by any experimental or FEM investigations.

In sandwich structures, since all the shear stresses occur in the core, any additional stress concentrations at a joint between two dissimilar core materials can make the shear stress in the weaker core the limiting factor in design. The closed-form model by Skvortsov et al. is however unable to accurately predict the shear stress concentrations at core joints and its application is limited to butt joints. The high-order theory-based solution that was developed for butt and scarf joints provides results that are not consistent and furthermore have not been validated. Moreover, the model involves considerable computational cost and time.

This chapter proposes two new analytical models for estimating the stress concentrations at both butt and scarf joints in sandwich structures. The first model is based on the closed-form model presented in [6] and estimates the axial stresses in the face sheets and cores in the case of scarf joints. The second model is able to predict the shear stress concentrations in the sandwich cores at both butt and scarf joints. Both new models were validated by FEM for a GFRP sandwich beam with balsa-Douglas fir core joints.

6.2   Joint configurations and finite element modeling

6.2.1   Investigated joint configurations

The common core joint in sandwich structures is the butt joint shown in Fig.6.1a, which is used mainly due to an ease of manufacture. Due to the abrupt material discontinuity and corresponding stress concentrations around this joint type, the scarf joint configuration, shown in Fig 6.1b, was developed to reduce these peak stresses, as discussed above. To analyze scarf joints, lap joint models, which comprise single-lap joints (SLJ) and angled-lap joints (ALJ), are studied in the following as intermediate design steps between butt and scarf joints. For the SLJ, the adjacent cores in the transition zone occupy half of the sandwich beam height and remain constant in this zone, as shown in Fig. 6.1c. Subsequently increasing the core height, h_{cs}, of the stiffer core in the transition zone of the SLJ results in the ALJ, as shown in Fig. 6.1d. A finite element model (FEM) analysis comparing the above designs is conducted in the following, which will serve to validate the analytical models subsequently developed.
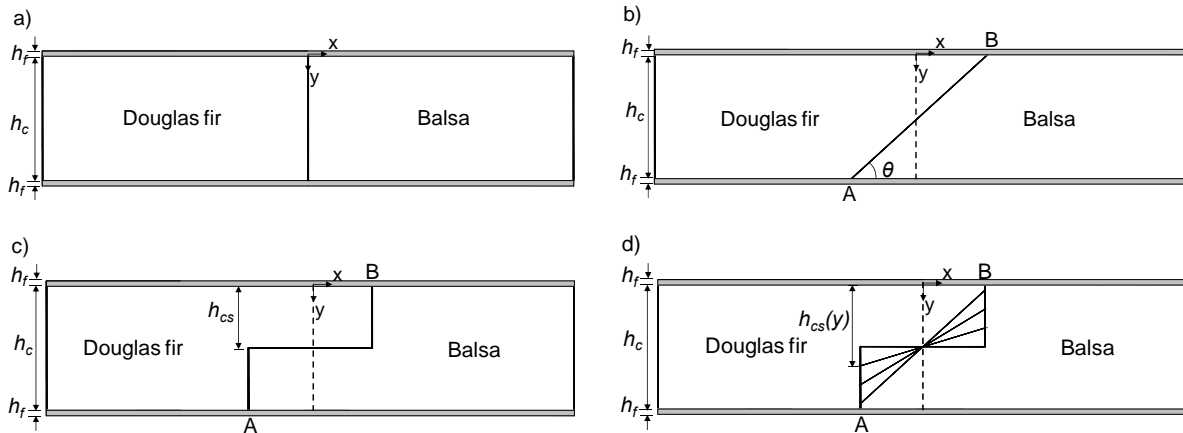
Figure 6.1: Configuration of core joints for; a) butt joint; b) scarf joint; c) single lap joint, SLJ; d) angled lap joint, ALJ

6.2.2   Finite element modeling

Two sandwich beam models were established; one for butt joints, which also simulates scarf joints and the other for SLJs, which also simulates ALJs. Both sandwich beams had a 2000-mm span, 180-mm width and 104-mm height (dimensions according to [8]). The beams were modeled as simply supported and loaded in a symmetric four-point bending configuration with two loads of 100 kN each. The face sheets consisted of unidirectional glass-fiber reinforced polymer (GFRP) laminates of 2-mm thickness, and the 100-mm-thick core

comprised Balsa and Douglas fir timber materials. The Douglas fir core parts with higher shear capacity were placed at the end supports. At a distance of 200 mm from these end supports, they were bonded in a butt joint or a scarf joint to the balsa part with a lower shear capacity, which was placed in the remaining 1600 mm of the beam span. For the scarf joint, the angle of termination, θ, at the bottom tri-material point, A, was varied, as shown in Fig. 6.2. To simulate the single-lap joint, the core was horizontally divided into two rectangular halves from points A to B over a length of 120 mm, according to Fig. 6.1c. For the angled-lap joint, the line dividing the two areas was rotated (see Fig. 6.21d). In all the cases, the Douglas fir timber was placed with the wood fibers transverse to the beam plane in order to simulate its orientation in a GFRP-balsa sandwich bridge deck, where the balsa core above the deck-girder joint is replaced with a much stiffer timber insert whose fibers are oriented in the bridge direction to increase composite action. The balsa, however, is placed with the fibers in the load direction to prevent indentation. The mechanical properties of the face sheets and Balsa and Douglas fir used in the FEM study are listed in Table 6.1.
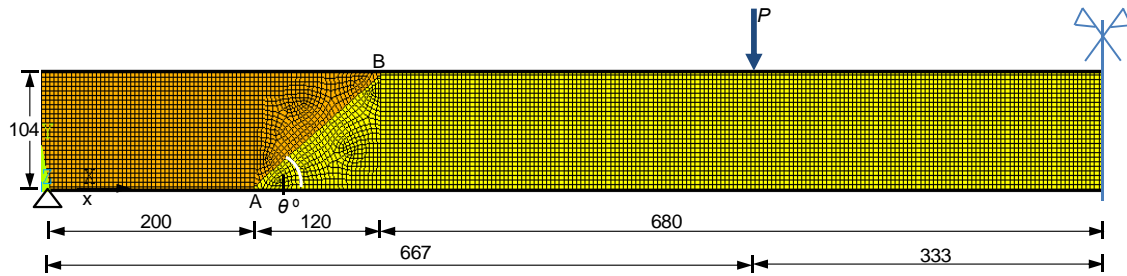
Figure 6.2: Finite element model of beam with scarf joint (θ=40°), applied load and boundary conditions (dimensions in (mm))

The linear elastic modeling of the sandwich beams was performed using the FEM analysis software, ANSYS v-13. Due to the constant beam width and linear elastic material properties, the beam was modeled in 2D, assuming plane strain conditions and linear elastic material behavior. Due to symmetry only half of the beams were modeled. Perfect bonding conditions were assumed between the face sheet and core joints, and hence the adhesive bonding applied at core joints in manufacture was not considered. Both the face sheets and cores were implemented using the 2D, 8-node parametric elements ″plane 182″. The mesh consisted of 8 layers of 0.25-mm thickness each for the face sheets and 100 layers of 1-mm thickness each for the cores. At the tri-material points, varying element size meshing was used. Smaller mesh sizes were implemented in the vicinity of the joint between the stiff and

weak cores. The beams were meshed using a total of 85,446 elements (13,247 face sheets and 72, 199 cores). The FEM mesh of the sandwich beam with a 40° scarf joint is shown in Fig. 6.2.

Table 6.1: Properties of GFRP face sheets, Balsa and Douglas fir timber cores (x=longitudinal, y=vertical, z=horizontal transverse axis)

	[a]UD-GFRP	[b]Balsa	[c]Douglas fir	[c]Beech
Density (kg/m^3)	2500	250	590	750
Longitudinal elastic modulus, E_x (MPa)	39000	200	772	2240
Out-of-plane elastic modulus, E_y (MPa)	10000	4320	1061	1137
Transverse elastic modulus, E_z (MPa)	10000	200	16396	13700
Out-of-plane shear modulus, G_{xy} (MPa)	2400	354	76	462
In-plane shear modulus, Gyz (MPa)	-	309	882	1062
In-plane shear modulus, Gxz (MPa)	-	64	910	1613
Out-of-plane Poisson ratio, v_{xy}	0.3	0.23	0.37	0.45
In-plane Poisson ratio, v_{yz}	-	0.49	0.43	0.51
In-plane Poisson ratio, v_{xz}	-	0.66	0.63	0.75
Weak/stiff core shear stiffness ratio, g (-)[d]	-	-	0.5	0.9
Core/face sheet stiffness ratio, μ (-)[d]	-	-	6.4	16.1

[a]values estimated from [1]

[b]values according to [9]

[c]values according to [10]

[d]values based on Balsa as the weak core

In these simulations, the core joints presented singularity points making the obtained core stresses mesh-dependent. Hence, the point stress failure criterion for brittle materials in linear elastic analysis was adopted [11]. In this theory, extreme, unreliable stress data at a joint caused by the inability of the finite elements to predict high deformations are replaced with approximate stress values at a characteristic distance away from the joint. The characteristic lengths according to [11] is $l_{ch}=1/2\pi(K_{IC}/\sigma_{cr})$, where K_{IC} is the Mode I fracture toughness of the core material (transverse to core fibers) and σ_{cr} is the critical stress, which in this case is the tensile strength transverse to fibers of the core materials. The characteristic lengths of Balsa and Douglas fir were therefore computed as being approx. 1 mm, see Table 6.2, and hence a 1- mm mesh size was used for the sandwich beam models. Stresses in the cores were therefore obtained from the nodes of the elements that were 1mm away from the joints.

Table 6.2: Description of different beam configuration

	Balsa	Douglas fir
Fracture toughness, K_{IC} (MPa)	[a]0.11	[b]0.24
Critical stress, σ_{cr} (MPa)	[c]1.30	[d]2.70
Characteristic length, l_c, (mm)	1.18	1.26

[a]values according to [12]

[b]values according to [13]

[c]values according to [9]

[d]values according to [14]

6.2.3   Numerical results

Figures 6.3 and 6.4 show the axial tensile stress distribution in the outer and inner layers of the bottom face sheets at the location of a balsa-Douglas fir butt, SLJ, ALJ and scarf joint, as well as for the case of no joint, i.e. a continuous balsa core. The height of the Douglas fir in the ALJ was 80% of the total core height, i.e. $h_{cs}(y) = 0.8h_c$ (see Fig. 6.1d for the ALJ configuration). It is apparent that outside the joint zone the stress distributions in the four joint types approached the linear distribution of the balsa without joint. However, the distributions were perturbed by the local stress concentrations at the core joints, whose extent, *l*, was about 20 mm on both sides. The local bending of the bottom face sheet at the core joint resulted in additional tension and compression stresses in the outer and inner layers of the bottom face sheet respectively. In the case of the butt joint, the tensile stresses increased by 24% in the outer layer (Fig. 6.3) and decreased by 21% in the inner layer (Fig. 6.4) compared to the case without a joint. In the case of the SLJ, ALJ and scarf joints, the increase in tensile stresses was reduced to 15%, 8% and 4% respectively. These reductions were attributed to the combined stiffness of the stiff and soft cores in the transition zones, which considerably reduced the stiffness disparity and hence the shear angle abruptness in the joint region.
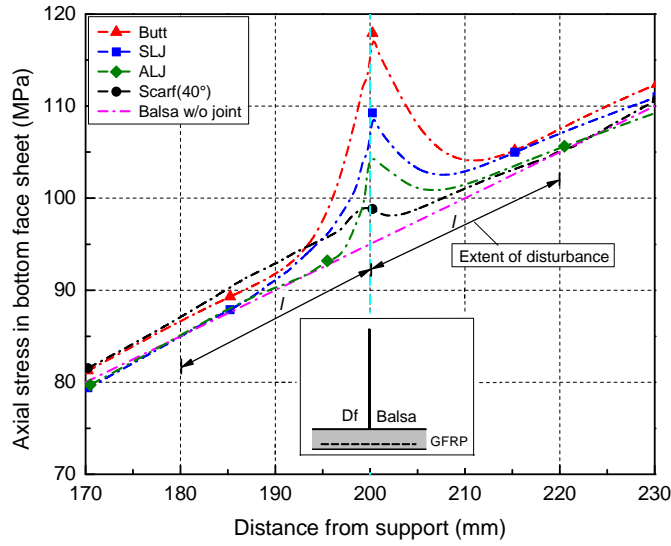
Figure 6.3: Axial stress in outer layer of bottom face sheet at balsa-Douglas fir joint predicted by FEM
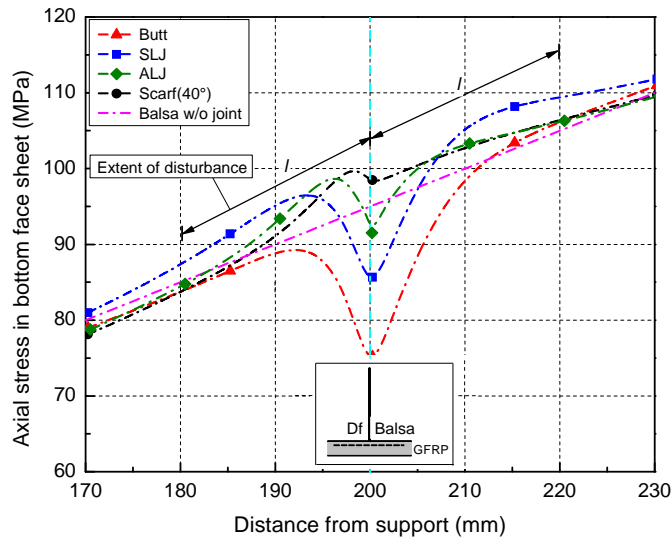
Figure 6.4: Axial stress in inner layer of bottom face sheet at balsa-Douglas fir joint predicted by FEM

The shear stress distributions across the balsa-Douglas fir butt, SLJ, ALJ and scarf joints, as well as for the case without a joint, are shown in Fig. 6.5. In the case of the butt joint, the shear stresses increased by 46% and 12% in the Douglas fir and balsa core respectively. The stress increases were only slightly reduced in the SLJ, but for the ALJ the increases were reduced to 15% and 11% and for the scarf joint to 7% and 6% respectively.
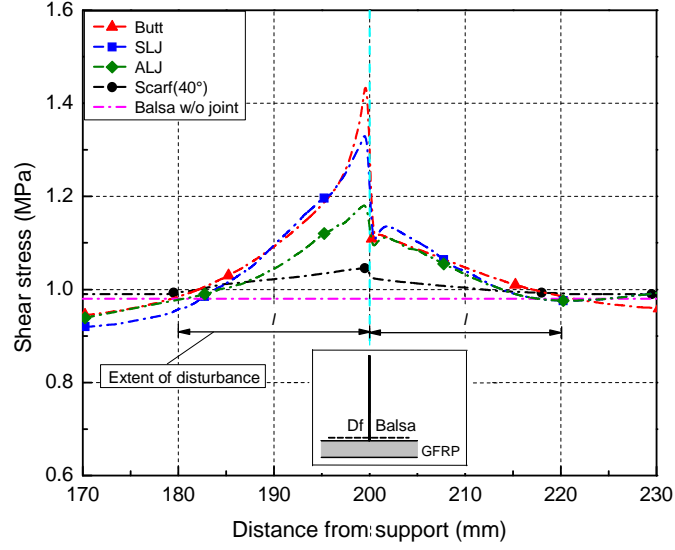
Figure 6.5: Shear stress across balsa-Douglas fir joint predicted by FEM

6.3 Existing analytical model

A closed-form estimation of the local stress changes in the face sheets and cores at a butt joint was developed by Skvortsov et al. using the elasticity theory [6]. The total axial stress, σ_{tot}, at the joint is composed of the normal axial stress in the face sheets (without joint effect), $\sigma_{f,x}$, and the local stress change, $\Delta\sigma_{f,x}^{loc}$, as follows:

$$\sigma_{tot} = \sigma_{f,x} + \Delta\sigma_{f,x}^{loc} \tag{1}$$

where the local axial stress change is expressed as:

$$\Delta\sigma_{f,x}^{loc} = \frac{P}{h_c}\sqrt{\frac{3E_f}{2G_{cw}h_f h_c}(1-g)\left(\frac{\sqrt{1+2\mu}}{1+\mu(1+g^{1/4})}\right)}f_a(x) \tag{2}$$

where G_{cw}, h_c, E_f, h_f, are the shear moduli of the weaker core, total height of the core, elastic modulus and thickness of face sheets respectively. P is the shear force at the joint, g is the weak/stiff core shear stiffness ratio (which defines the magnitude of the local effect) and μ is the core/face sheet bending stiffness ratio (which influences the extent of disturbance caused by the local effect), both defined as follows:

$$g = \sqrt{\frac{G_{cw}}{G_{cs}}} \tag{3}$$

$$\mu = \sqrt{k_a \frac{G_{cw}h_c(h_c+h_f)^2}{E_f h_f^{\;3}}} \tag{4}$$

109

where G_{cs}, v_f, are the shear moduli of the stiff core and Poisson ratio of the face sheet respectively and k_a is a parameter for the assumption of a plane strain condition of the sandwich beam, defined as:

$$k_a = \frac{1-2v_f}{4(1-v_f)} \tag{5}$$

In Eq. (2), $f_a(x)$ comprises a stress distribution function that describes the decay of the stress concentrations in the face sheets on both sides of the joint as follows:

$$f_a(x) = \begin{cases} \dfrac{c_1\alpha_1 e^{-\alpha_1 x} + c_2\beta_1 e^{-\beta_1 x}}{c_1\alpha_1 + c_2\beta_1}, & x > 0 \\[2ex] \dfrac{c_3\alpha_2 e^{-\alpha_2 x} + c_4\beta_2 e^{-\beta_2 x}}{c_3\alpha_2 + c_4\beta_2}, & x < 0 \end{cases} \tag{6}$$

with $x=0$ representing the location of the joint such that $x>0$ is the weak core, $x<0$ is the stiff core (see Fig. 6.1a), and c_1, c_2, c_3, c_4, are the coefficients of the distribution function obtained from the solution of linear algebraic equations, which are formulated by assuming continuity across the core joint for bending moments and rotations of the face sheets, shear force in the cores and relative out-of-plane displacement of the core mid-heights as follows:

$$\begin{pmatrix} 1 & 1 & -g^2 & -g^2 \\ \alpha_1 & \beta_1 & g^2\alpha_2 & g^2\beta_2 \\ \alpha^2_1 & \beta^2_1 & -g^2\alpha^2_2 & -g^2\beta^2_2 \\ \alpha^3_1 & \beta^3_1 & g^4\alpha^3_2 & g^4\beta^3_2 \end{pmatrix} \begin{pmatrix} c_1 \\ c_2 \\ c_3 \\ c_4 \end{pmatrix} = \begin{pmatrix} g^2-1 \\ 0 \\ 0 \\ 0 \end{pmatrix} \tag{7}$$

where α_1, β_1 and α_2, β_2 are decay rates of the distribution functions, and D_f and S represent the bending stiffness of face sheets and shear stiffness of the entire sandwich beam as follows:

$$\alpha_1 = \sqrt{\frac{6}{k_a}} \frac{\sqrt{1+2\mu}+\sqrt{1-2\mu}}{2} \frac{1}{h_c}, \quad \beta_1 = \sqrt{\frac{6}{k_a}} \frac{\sqrt{1+2\mu}-\sqrt{1-2\mu}}{2} \frac{1}{h_c} \tag{8}$$

$$\alpha_2 = \sqrt{\frac{6}{k_a}} \frac{\sqrt{1+2\mu/g}+\sqrt{1-2\mu/g}}{2} \frac{1}{h_c}, \quad \beta_2 = \sqrt{\frac{6}{k_a}} \frac{\sqrt{1+2\mu/g}-\sqrt{1-2\mu/g}}{2} \frac{1}{h_c} \tag{9}$$

$$D_f = \frac{E_f h_f^3}{6}, \quad S = \frac{G_{cw}(h_f+h_c)^3}{h_c}. \tag{10}$$

The local effect in the face sheet and cores is completely eliminated at $x=\pm l$ (see Figs. 6.3-6.5). The extent of disturbance can therefore be obtained when Eq. (2) is set to a small value close to zero (since $f_a(x)$ is an exponential function that approaches zero in infinity), for instance $a_0=0.01$, which is about 1% of $f_a(x)$ (at $x=0$, $f_a=1$). The extent of disturbance is then obtained as follows:

$$l = \left| \begin{array}{ll} \dfrac{ln\left(\dfrac{a_0(c_1\alpha_1 + c_2\beta_1)}{c_1\alpha_1}\right) - ln\left(\dfrac{c_1\beta_1}{c_2\alpha_1}\right)}{\beta_1}, & x > 0 \\[3ex] ln\left(\dfrac{a_0(c_3\alpha_2 + c_4\beta_2)}{c_3\alpha_2}\right) - ln\left(\dfrac{c_3\beta_2}{c_4\alpha_2}\right), & x < 0 \end{array} \right. \tag{11}$$

The extent of disturbance, predicted by Eq. (11) for various core/face sheet bending stiffness ratios, is shown in Fig. 6.6. For a high core/face sheet bending stiffness ratio such as that for balsa-Douglas fir/GFRP face sheets (μ=6.4, see Table 6.1), a high extent of disturbance of l=20 mm is obtained. However, if the Douglas fir is replaced with beech, the ratio increases to approx. 16, which results in a low extent of disturbance of 11 mm due to the low small disparity in shear stiffness between beech and balsa.
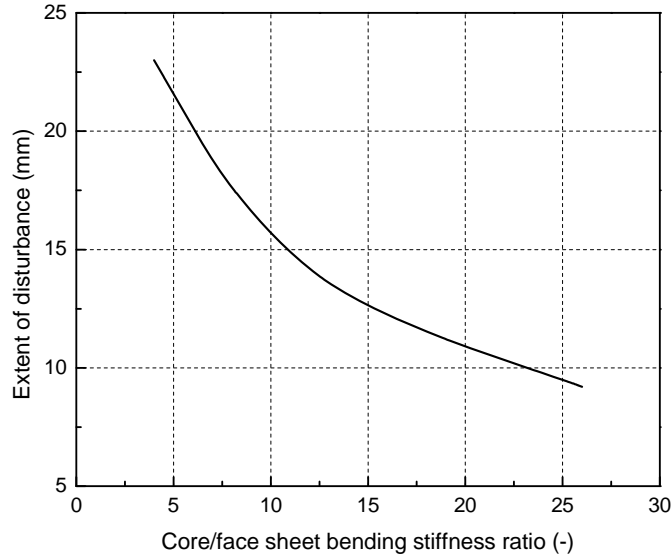
Figure 6.6: Extent of disturbance vs. core/face sheet bending stiffness ratio

6.4 New analytical models

6.4.1 Face sheet axial stress model for scarf joints

The stiff and weak cores in the SLJ present a layered multi-core sandwich in the transition zone between points A and B (see Fig. 6.1c). Therefore an equivalent shear modulus of the combined stiff and weak cores can be computed and applied at these joints according to [15]. This equivalent shear modulus will however vary in the transition zone for the ALJ due to the core height variation, as shown in Fig. 6.1d, until the scarf joint configuration is reached, i.e.

$h_{cs}(y) = h_c$. Applying the inverse rule of mixture according to [15], the variation of the equivalent shear modulus, G_{eq}, along the transition zone can be determined as follows:

$$G_{eq}(x) = \frac{G_{cw}G_{cs}h_c}{G_{cw}(h_c - h_{cs}(x)) + G_{cs}h_{cs}(x)} \tag{12}$$

A new shear stiffness ratio, g^*, can thus be obtained in the transition zone of the joint and the local axial stresses in the face sheets according to Eq. (2) can consequently be modified as follows:

$$\Delta\sigma_{f,x}^{loc^*} = \frac{P}{h_c}\sqrt{\frac{3E_f}{2G_{eq}h_f h_c}(1-g^*)\left(\frac{\sqrt{1+2\mu^*}}{1+\mu^*(1+g^{*\frac{1}{4}})}\right)}f_a(x) \tag{13}$$

$$g^* = \sqrt{\frac{G_{eq}}{G_{cs}}}, \quad \mu^* = \sqrt{k_a\frac{G_{eq}h_c(h_c + h_f)}{E_f h_f^3}} \tag{14}$$

where superscript (*) represents the new model equations.

6.4.2   Core axial and shear stress models for butt and scarf joints

The face sheet axial stress models, Eqs. (2, 13), are employed to model the axial and shear stresses in the core, first at the butt and subsequently at the scarf joint. It is assumed that the core at the butt point, just above the face sheet, as shown in Fig. 6.7, undergoes the same tensile strain deformation in the *x*-direction as the face sheet, as follows:

$$\varepsilon_{f,x} = \varepsilon_{c,x} \tag{15}$$

where $\varepsilon_{f,x}$ and $\varepsilon_{c,x}$ are the axial strains in the face sheets and cores respectively in *x*-direction. Accordingly, $\varepsilon_f = \Delta\sigma_f^{loc}/E_f$ and $\Delta\sigma_c^{loc} = \varepsilon_f \cdot E_c$ can be used to estimate the axial strains in the face sheets and axial stresses in the core respectively.
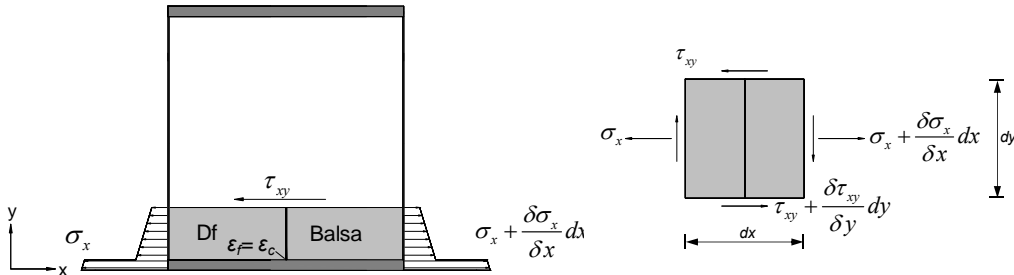
Figure 6.7: Beam section showing equilibrium for core element

The stress field across the core joint in x-direction is assumed to follow Eq. (2) but decays rapidly inside the thick core, which is assumed here as finite due to its interaction with the face sheets [16-17]. The axial stress distribution along and across the core can thus be expressed as follows:

$$\Delta\sigma_{c,x}^{loc}(x,y) = \Delta\sigma_c^{loc} f_a(x)e^{-ky} \tag{16}$$

where k is the parameter for stress decay across the core. An exponential function is selected since it has been successfully used to predict a similar case of stress decay in cores during face sheet wrinkling in [1, 16].

The shear stress can be obtained by considering the balance of forces in x-direction in an element of the core in the sandwich beam, shown in Fig. 6.7, as follows:

$$\frac{\delta\sigma_x}{\delta x} + \frac{\delta\tau_{xy}}{\delta y} = 0 \tag{17}$$

or:

$$\tau_{xy} = -\int \frac{\delta\sigma_x}{\delta x}dy \tag{18}$$

The integration of the shear stresses over the core height on both sides of the core joint results in:

$$x>0: \quad \Delta\tau_{c,xy}^{loc} = -\Delta\sigma_{c,x}^{loc}\left(\frac{c_1\alpha_1^2 e^{-\alpha_1 x} + c_2\beta_1^2 e^{-\beta_1 x}}{k(c_1\alpha_1 + c_2\beta_1)}\right)e^{-ky} + C$$

$$x<0: \quad \Delta\tau_{c,xy}^{loc} = -\Delta\sigma_{c,x}^{loc}\left(\frac{c_3\alpha_2^2 e^{-\alpha_2 x} + c_4\beta_2^2 e^{-\beta_2 x}}{k(c_3\alpha_2 + c_4\beta_2)}\right)e^{-ky} + C \tag{19}$$

where C is an integration constant, which can be set to zero for the local shear stress decay in the core, similar to the case of stress decay in the core during face sheet wrinkling according to [16]. Considering the extents of disturbance, l, along the joint and through the core thickness (both are similar, see FEM results of Fig. 6.5 and Fig. 6.11) as boundary conditions, i.e. the shear stress in the core, $\Delta\tau_{c,xy}^{loc}=0$ at $x=l$, $y=0$ and $x=0$, $y=l$, the decay parameter, k, in the core results in:

$$x>0:, k = -\frac{1}{l}ln\left(\frac{c_1\alpha_1^2 e^{-\alpha_1 l} + c_2\beta_1^2 e^{-\beta_1 l}}{c_1\alpha_1^2 + c_2\beta_1^2}\right)$$

$$x<0: k = -\frac{1}{l}ln\left(\frac{c_3\alpha_2^2 e^{-\alpha_2 l} + c_4\beta_2^2 e^{-\beta_2 l}}{c_3\alpha_2^2 + c_4\beta_2^2}\right) \tag{20}$$

Equation (19) can be extended to scarf joints by employing the equivalent stiffness model above. Inserting the equivalent shear stiffness ratio, g^*, of Eq. (14) into Eq. (16), the local axial stress in the core of the scarf joint results in:

$$\Delta\sigma_{c,x}^{loc*}(x,y) = \Delta\sigma_c^{loc*} f_a(x)e^{-ky} \tag{21}$$

where

$$\Delta\sigma_c^{loc*} = \frac{P}{h_c}\sqrt{\frac{3E_f}{2G_{eq}h_f h_c}(1-g^*)\left(\frac{\sqrt{1+2\mu^*}}{1+\mu^*(1+g^{*\frac{1}{4}})}\right)} \tag{22}$$

and similarly, the core shear stresses at the scarf joint are obtained from:

$$x>0: \; \Delta\tau_{c,xy}^{loc*} = -\Delta\sigma_{c,x}^{loc*}\left(\frac{c_1\alpha_1^2 e^{-\alpha_1 x} + c_2\beta_1^2 e^{-\beta_1 x}}{k(c_1\alpha_1 + c_2\beta_1)}\right)e^{-ky}, \; k = -\frac{1}{l}ln\left(\frac{c_1\alpha_1^2 e^{-\alpha_1 l} + c_2\beta_1^2 e^{-\beta_1 l}}{c_1\alpha_1^2 + c_2\beta_1^2}\right),$$

$$x<0: \; \Delta\tau_{c,x}^{loc*} = -\Delta\sigma_{c,x}^{loc*}\left(\frac{c_3\alpha_2^2 e^{-\alpha_2 x} + c_4\beta_2^2 e^{-\beta_2 x}}{k(c_3\alpha_2 + c_4\beta_2)}\right)e^{-ky}, \; k = -\frac{1}{l}ln\left(\frac{c_3\alpha_2^2 e^{-\alpha_2 l} + c_4\beta_2^2 e^{-\beta_2 l}}{c_3\alpha_2^2 + c_4\beta_2^2}\right) \tag{23}$$

6.4.3 Validation of new models

The two new models were validated by comparing their results to those of the numerical investigations. Figures 6.8 and 6.9 show axial stress estimates in the outer and inner layers of the bottom face sheet of the scarf joint at 40° using FEM and the new axial model, Eq. (13).
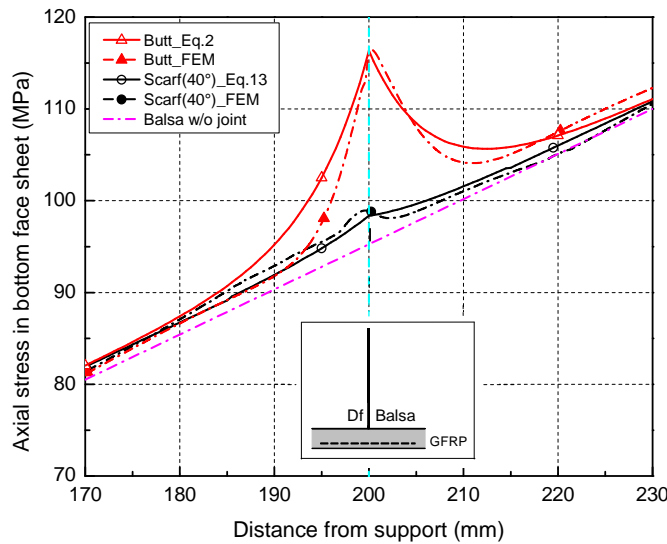
Figure 6.8: Axial stress in outer layer of bottom face sheet across core joint predicted by new axial model, Eq. (13), for scarf joint and existing axial model, Eq. (2), for butt joint, as well as FEM

114
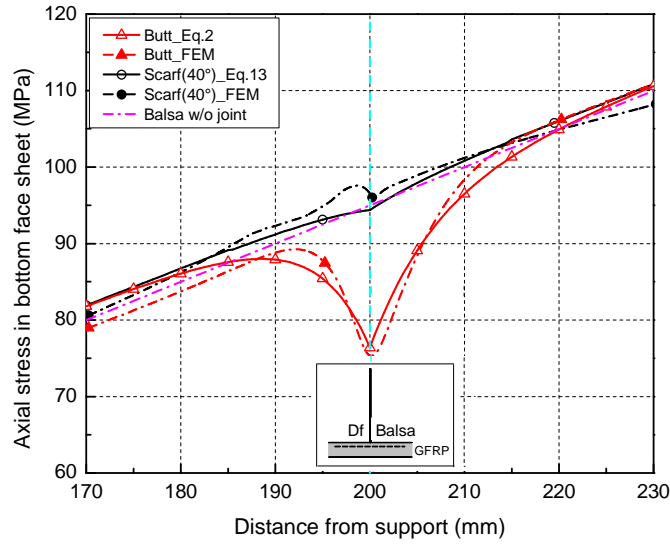
Figure 6.9: Local axial stress in inner layer of bottom face sheet across core joint predicted by new axial model, Eq. (13), for scarf joint and existing axial model, Eq. (2), for butt joint, as well as FEM

Also shown is the same comparison for the butt joint with the existing axial model, Eq. (2), as well as again the case without a joint. A good correlation between the FEM and both analytical models is obtained.

The application range of the new axial model, Eq. (13), is limited in terms of angle of termination, as shown in Fig. 6.10. The new model provides acceptable results for angles of termination of between 20° and 60°, which however also represents a reasonable range from the practical point of view.
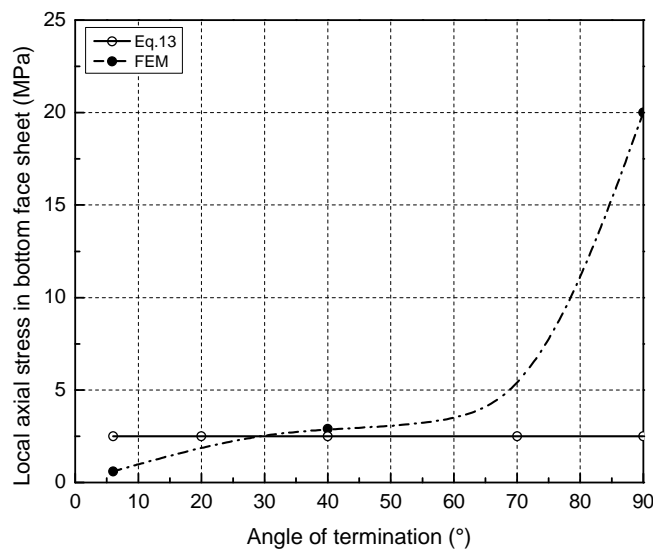
Figure 6.10: Local axial stress in outer layer of bottom face sheet at varying angles of termination of scarf joints predicted by new axial model, Eq. (13), and FEM

Figure 6.11 shows the decay of the shear stress through the core thickness at 1-mm distance on both sides of a balsa-Douglas fir butt joint, predicted by FEM and the new shear model, Eq. (19). The results again show good agreement, particularly for the peak value. Maximum shear stresses occurred in the Douglas fir just above the face sheet, which decayed rapidly into the core. For the balsa core, a lower shear stress, about one third of that in Douglas fir, was obtained just above the face sheet, which also decayed into the core. The decay of both stress distributions occurred across about 20-25% of the core height, a value that is similar to the extent of disturbance in the face sheets, as shown in Figs. 6.3-6.4.
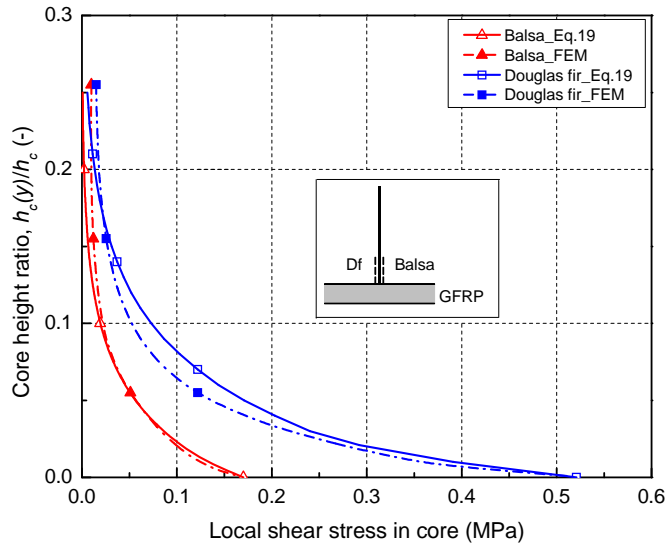
Figure 6.11: Through-thickness local shear stress in balsa and Douglas fir at butt joint predicted by new shear model, Eq. (19), and FEM

The shear stress distribution at 1mm above the bottom face sheet and across the Balsa -Douglas fir joint was also predicted for both butt and scarf joints using the new shear models, Eqs. (19, 23), and again correlates well with FEM results, see Fig. 6.12. A shear stress increase of 45% in the Douglas fir was obtained at the butt joint compared to the case without a joint in the balsa core, which was three times higher than the corresponding 15% increase in the balsa. In the scarf joint, the shear stresses increased by less than 5% however. This contradicts the predictions by the high-order model in [7], where the local shear stresses in the cores were unaffected by the scarf joint.
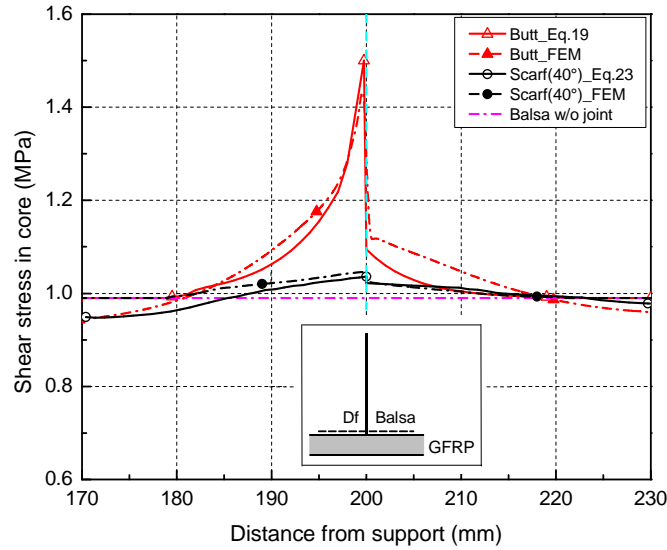
Figure 6.12: Local core shear stress across balsa-Douglas fir butt and scarf joint predicted by new shear model, Eqs. (19) and (23), and FEM

6.5 Conclusions

Two new analytical models have been developed to estimate local stress concentrations at joints between dissimilar sandwich cores. The first model predicts local axial stresses in the face sheets at scarf joints while the second model predicts local shear stresses in cores at both butt and scarf joints. The models are based on an existing closed-form model and have been validated by FEM for balsa-Douglas fir butt and scarf joints, both integrated into a sandwich with GFRP face sheets. The following conclusions can be drawn:

1) The effects of joints between dissimilar cores on axial and shear stress distributions in face sheets and cores were accurately predicted by the new models, when compared to corresponding FEM results. The models are applicable for scarf joints with angles of termination of between 20° and 60°.

2) The stress concentrations rapidly decay along the face sheets and through the core thickness. The decay rate depends on the core/face sheet bending stiffness ratio.

3) The positive effect of scarf joints compared to butt joints could be demonstrated: the axial stress concentrations in the face sheets and shear stress concentrations in the cores almost disappear if a butt joint is changed to a scarf joint configuration.

4) Particularly the local shear stress increases at the balsa-Douglas fir butt joint decreased significantly from 46% to 7% when the latter was replaced with a scarf joint. This contradicts the results from the existing high-order model, which predicts the same local shear stresses for butt and scarf joints.

117

References

[1] Gay D, Hoa SV. Composite materials. Boca Raton, Florida: CRC Press: 2007.

[2] Zenkert D, editor. The handbook of sandwich construction. London: EMAS: 1997.

[3] Danielsson M, Grenestedt JL. Gradient foam core materials for sandwich structures: preparation and characterization. Composites, Part A 1998; 29(8): 981-988.

[4] Allen GA, Zhengnong F. Classification of structural sandwich panel behavior. Mech Sandw Struct 1998; 1-12.

[5] Bozhevolnaya E, Kildegaard A, Thomsen OT, Skvortsov V. Local effects in the vicinity of inserts in sandwich panels. Compos Part B: Eng 2004; 35: 619-627.

[6] Skvortsov V, Thomsen OT. Analytical estimates for stresses in face sheets of sandwich panel at the junctions of two core materials. Inst Mech Eng, Aalborg Univ.; 2002: Report No. 113.

[7] Frostig Y, Thomsen OT. Localized effects near non-vertical core junctions in sandwich panels - A high-order approach. Journal of sandwich structures and materials 2006; 8: 125-156.

[8] Osei-Antwi M, de Castro J, Vassilopoulos AP, Keller T. FRP-Balsa composite sandwich bridge deck with complex core assembly. J Compos Constr 2013; 17(6): http://dx.doi.org/10.1061/(ASCE)CC.1943-5614.0000435

[9] Baltek Alcan Composite. Data sheet, mechanical properties versus density and grain orientation for Balsa wood. 2001. http://www.corematerials.3acomposites.com/baltek-sb.html.

[10] Bodig J, Goodman JR. Prediction of elastic properties of parameters for wood. Wood Sci 1973; 5(4): 249-264.

[11] Ribeiro-Ayeh S, Hallstrom S. Strength prediction of beams with bi-material butt-junctions. Eng Fract Mech 2003; 70: 1491-1507.

[12] Wu EM. Applications of fracture mechanics to orthotropic plates. J Appl Mech 1967; 67: 966-974.

[13] Gibson LJ, Ashby MF. Cellular solids. Oxford. 1st ed. Oxford: Pergamon Press Ltd.; 1988.

[14] Kretschmann DE. Mechanical properties of wood.US Forest Prod Lab 2010; Chapter 5; 1-46.

[15] Bareisis J. Stiffness and strength of multilayer beams. J Compos Mater 2006; 40: 515-530.

[16] Vonach WK, Rammerstorfer FG. The effects of in-plane core stiffness on the wrinkling behavior of thick sandwiches. Acta Mech 2000; 141: 1-10.

[17] Plantema FG. Sandwich construction. New York: Wiley: 1966.

7.

Application of complex core systems in bridge construction
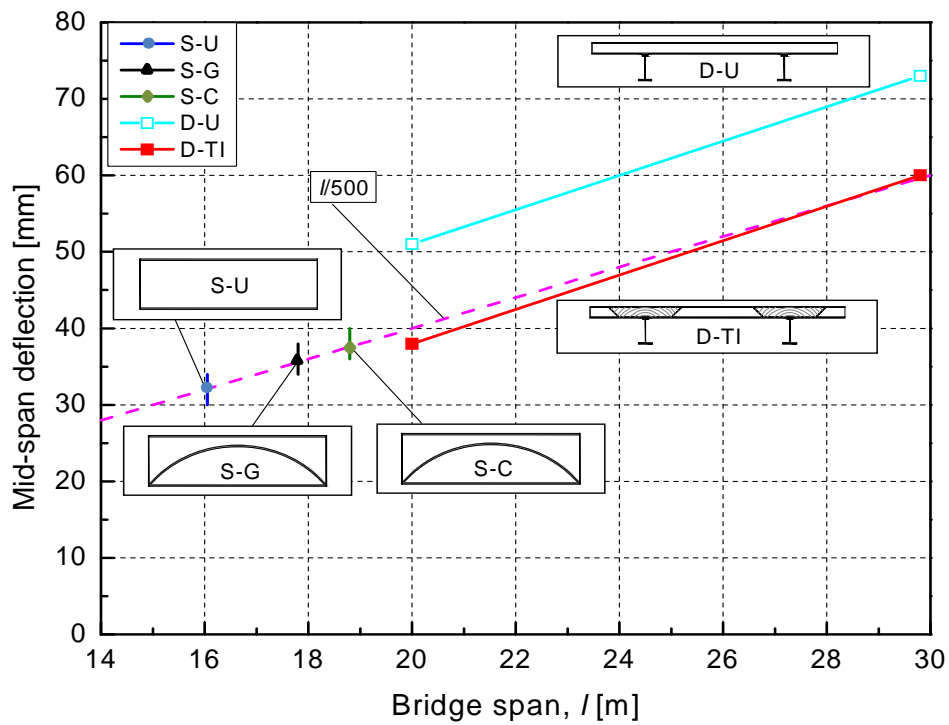
Bridge span limits at SLS for sandwich slabs with uniform high-density balsa core (S-U), sandwich slabs with balsa cores reinforced with GFRP arch (S-G), sandwich slabs with balsa cores reinforced with CFRP arch (S-C), sandwich decks with high-density balsa core bonded on steel girders (D-H) and sandwich decks with timber inserts bonded on steel girders (D-TI)

7.1 Overview

Glass fiber-reinforced polymer (GFRP) composite bridge systems offer favorable characteristics such as high strength per unit weight, resistance to corrosion, excellent fatigue performance, increased live load ratings in the case of bridge replacement and rapid field installation with minimized traffic disruptions [1-2]. Two basic concepts of GFRP bridge systems exist: orthotropic systems composed of adhesively-bonded pultruded shapes and sandwich constructions. Both are used either as bridge decks in deck-girder bridges or as slabs in the case of slab bridges. Sandwich decks or slabs have the advantage, amongst others, of variable thickness unlike pultruded decks or slabs and can thus be used for much larger spans. They are currently composed of GFRP face sheets and honeycomb or foam cores. In the latter case, additional GFRP webs are normally required to provide sufficient core shear capacity [3]. However, the honeycomb walls and internal GFRP webs in the foam core provide a non-uniform stiffness support for the upper face sheet, which – under frequent wheel loads – may lead to the debonding of the upper face sheet from the core [4]. To overcome this drawback, i.e. provide a core with sufficient shear capacity and uniform support for the upper face sheet, balsa wood was used as core material in the new Avançon Bridge, in Bex, Switzerland [5]. The use of balsa with fibers transverse to the upper face sheet and thus in line with the wheel load direction eliminated the need for reinforcements by internal webs and provided high indentation resistance against concentrated wheel loads. The new 11.45-m span and two-lane Avançon Bridge, composed of a GFRP-balsa sandwich deck adhesively bonded onto two steel girders, replaced an old one-lane reinforced concrete (RC) bridge.

A further disadvantage of pultruded decks is demonstrated in the case of RC deck replacement. RC decks normally act as top chord of hybrid RC-steel girders in the bridge's longitudinal direction. Pultruded GFRP decks, however, exhibit low stiffness in this direction (which is transverse to the pultrusion direction) and are thus not able to transfer significant longitudinal forces in the RC chord. Furthermore, depending on the cell geometry, composite action between the upper and lower face sheets may be reduced, which further decreases the possible contribution of the deck as top chord [6]. The effects of these drawbacks are increased deflections in the longitudinal bridge direction and significant longitudinal stress increases in the upper flanges of the steel girders, which may require additional strengthening of the bridge. This was shown in the study by Harries [7], where the compressive and tensile stresses in the upper and lower steel girder flanges increased by 109% and 12% respectively if the RC deck of a 17.5-m span bridge had been replaced by a pultruded GFRP bridge deck.

The increased compressive stresses would have exceeded the compressive strength of the steel flanges and the deflection limit would no longer have been met.

GFRP sandwich slabs, however, have demonstrated their capacity to replace RC slab bridges because high slab thickness can be manufactured to provide the required bending stiffness. An example is the 7.6-m-span Bennetts' Creek Bridge, in Rexville (NY, USA), where the RC slab was replaced by a GFRP-foam sandwich deck composed of 12.8-mm GFRP face sheets and 621-mm foam core [8].

In parallel to the above-mentioned Avançon Bridge project, structural concepts for GFRP-balsa slab bridges with thick balsa cores have also been developed. It has been shown that the balsa core thickness can be reduced by a complex core assembly composed of an upper high-density and lower low-density balsa core layer, separated by a circular FRP arch to improve the shear and bending capacity [9]. Furthermore, composite action of the GFRP-balsa sandwich in the case of RC deck replacement can be improved by replacing the softer balsa wood above the steel girders by timber with fibers oriented in the bridge direction. In cases of even higher deck stiffness requirements, additional thin steel plates can be inserted between the timber inserts and upper face sheet.

This chapter investigates the span limits of new GFRP-balsa sandwich slab and deck bridges. The potential of replacing RC decks with GFRP-balsa sandwich decks is further explored. Also discussed are structural effects arising from timber inserts, such as local stress concentrations at the balsa/timber joints in the core and face sheets.

7.2 Structural concepts and materials

7.2.1 GFRP-balsa sandwich slab bridge

The span limits of three types of slab bridges were evaluated: 1) sandwich slabs with a uniform high-density balsa core (designated S-U concept), 2) sandwich slabs with a complex core composed of high- and low-density balsa and an GFRP arch in the interface, as shown in Fig. 7.1 (S-G concept), 3) the same case as S-G but with a carbon-FRP (CFRP) arch instead (S-C concept). The S-G and S-C cases correspond to the concept shown in Ref. [9]. Here, the high-density balsa is required to prevent indentation and wrinkling of the upper face sheet and provide sufficient shear strength and stiffness in the support region of the slab. In the less stressed lower zone between the supports, low-density balsa can be used to minimize deck weight. The vertical components of the FRP arch forces reduce the shear load borne by the balsa core.

A two-lane bridge of 7.50-m width was investigated; the span was varied up to the limit span. The GFRP face sheets and GFRP/CFRP arch laminates were 30 mm thick and the upper and lower balsa cores had a combined thickness of 710 mm, resulting in a total sandwich slab thickness of 800 mm. From the experiences gained with the Avançon Bridge construction, these thicknesses were considered as the limits imposed by the manufacturing process (vacuum infusion). The GFRP face sheets were composed of E-glass fibers and vinylester resin. The E-glass architecture was orthotropic with the same number of unidirectional (UD)-layers in the bridge's longitudinal (0°) and transverse directions (90°). The same resin was used for the arch laminates but the UD E-glass and carbon (T-700) fiber layers were arranged only in the longitudinal direction. The fiber volume fraction was 49% for both laminates. The fibers of the balsa cores were oriented perpendicular to the faces sheets, thus providing the required indentation and shear resistances. The lowest possible thickness of the upper high-density balsa layer at mid-span was 50 mm, resulting in a maximum arch rise of 690 mm. The properties of the high-density (SB150) and low-density (SB50) balsa cores and the GFRP/CFRP UD-layers are listed in Table 7.1. The bridge slab was covered by an asphalt layer of h_a=60 mm thickness (similar to the Avançon Bridge).
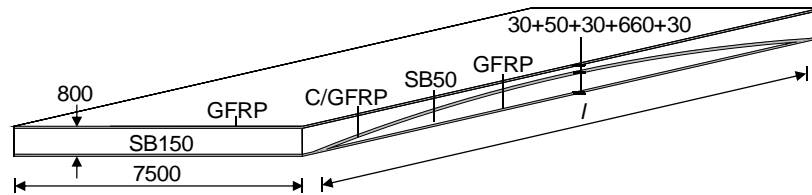
Figure 7.1: Sandwich bridge concepts for S-C/S-G slabs (dimensions in mm)

Table 7.1: Properties of balsa core and FRP laminates: characteristic (5% fractile) values for strength, mean values for other properties (x=longitudinal, y=vertical, z= transverse bridge direction)

Properties	[a]Balsa SB150	[a]Balsa SB50	[b]UD GFRP	[b]UD CFRP
Density (kg/m^3)	250	95	2080	1530
Longitudinal elastic modulus, E_x (MPa)	200	75	40000	120000
Out-of-plane elastic modulus, E_y (MPa)	4320	1993	12000	7000
Transverse elastic modulus, E_z (MPa)	200	75	12000	7000
In-plane shear modulus, G_{yx} (MPa)	309	106	-	-
Out-of-plane shear modulus, G_{xy} (MPa)	290	106	2400	4200
Out-of-plane shear modulus, G_{zy} (MPa)	290	106	-	-
Longitudinal compressive strength, σ_{cx} (MPa)	0.7	0.3	300	1130
Out-of-plane compressive strength, σ_{cy} (MPa)	18.9	7.4	141	141
Transverse compressive strength, σ_{cz} (MPa)	0.7	0.3	141	141
Longitudinal tensile strength, σ_{tx} (MPa)	0.7	0.3	1250	1270
Transverse tensile strength, σ_{ty} (MPa)	0.7	0.3	35	42
Out-of-plane shear strength, τ_{xy} (MPa)	2.3	1.5	80	90
Out-of-plane shear strength, τ_{zy} (MPa)	2.3	1.5	-	-

[a]Values according to Ref. [11]

[b]Values according to Ref. [12]

7.2.2 GFRP-balsa sandwich deck bridges

Three types of GFRP-balsa sandwich deck bridges were investigated, all with the same width of 7.50 m (for two lanes) as the slab bridges. The deck, however, was adhesively bonded onto two steel girders, which were identical in all three cases, see Figs. 7.2 and 7.3. The differences were only in the core composition above the steel girders where: 1) the bridges designated D-U had a uniform high-density balsa core over the whole width, 2) the balsa in bridges D-TI was replaced by timber inserts above the steel girders, 3) additional steel plates were placed in bridges D-T/SI between the timber inserts and the upper GFRP face sheets.

The timber and steel plate inserts were arranged to increase the longitudinal stiffness and thus contribute to the top chord of the hybrid sandwich-steel girders. The fibers of the timber inserts were oriented in the longitudinal bridge direction accordingly. A timber width of 1500 mm was selected as a compromise between efficiency, deck weight and cost. The adhesively-bonded balsa-timber joints were designed as scarf joints with 40° angles of termination to reduce stress concentrations, see Fig. 7.3. The steel plate insert had a width of

1500 mm and the thickness was h_{SI}=10 mm. Steel grade S355 was selected, according to Ref. [10]; the properties are listed in Table 7.2. The total deck thickness was h_D=300 mm and was kept constant across the deck width. The face sheets had the same thicknesses (30 mm) and GFRP composition as in the slab bridges. High-density balsa (SB150) and different types of timber inserts (spruce, Douglas fir (Df), birch, ash and cedar) were evaluated; their properties are listed in Table 7.3. The edges of the 1.90-m overhangs were reinforced by longitudinal 100 x 20-mm² CFRP strips, adhesively bonded onto the outer layers of the upper and lower face sheets, to reduce edge deflections due to concentrated wheel loads.
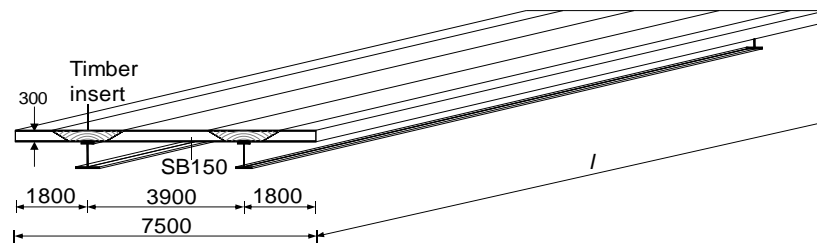
Figure 7.2: Sandwich bridge concepts for D-TI deck on steel girders (dimensions in mm)
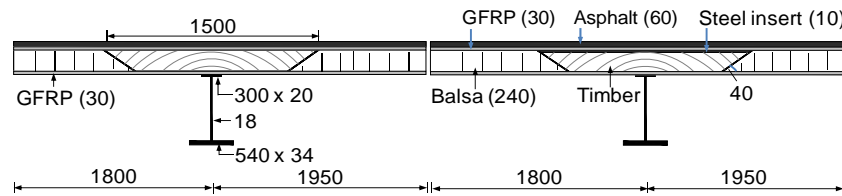
Figure 7.3: Cross sections of D-TI (deck on left girder) and D-T/SI deck (deck on right girder) bridges (dimensions in mm)

The welded steel girders had upper/lower flange widths of 300/540 mm and thicknesses of 20/34 mm and a web thickness of 18 mm. The height of the webs was varied in order to obtain a slenderness ratio of $h/l = 1/20$, where h is the total girder height (including the deck) and l is the longitudinal span of the bridge. The steel grade was the same as that used for the steel inserts. Again, a 60-mm asphalt layer was taken into account.

Table 7.2: Properties of concrete, steel reinforcement and steel girders: 5% fractile values for strength, mean values for other properties (x=longitudinal, y=vertical, z= transverse bridge direction)

Properties	[a]Concrete	[a]Steel reinforcement	[b]Steel girder
Density (kg/m^3)	2500	7850	7850
Elastic modulus, E_x=E_z (MPa)	32000	200000	210000
Out-of-plane shear modulus, G_{xy}=G_{yz} (MPa)	12000	81000	81000
Compressive strength, σ_{cx}= σ_{cz} (MPa)	30	500	355
Tensile strength, σ_{tx}= σ_{tz} (MPa)	2	500	355
Out-of-plane shear strength, $\tau_{xy =} \tau_{yz}$ (MPa)	1.4	288	204

[a]Values according to Ref. [13]

[b]Values according to Ref. [10]

Table 7.3: Properties of timber: characteristic (5% fractile) values for strength, mean values for other properties (x=longitudinal, y=vertical, z= transverse bridge direction)

Properties	Spruce	Douglas Fir	Birch	Ash	Cedar
[a]Density (kg/m^3)	500	590	620	800	300
[a]Longitudinal elastic modulus, E_x (MPa)	16589	16396	16285	14996	6500
[a]Out-of-plane elastic modulus, E_y (MPa)	848	1061	1110	1509	527
[a]Transverse elastic modulus, E_z (MPa)	689	772	621	800	358
[a]In-of-plane shear modulus, G_{yx} (MPa)	751	910	1179	861	559
[a]Out-of-plane shear modulus, G_{xy} (MPa)	841	882	910	889	566
[a]Out-of-plane shear modulus, G_{zy} (MPa)	38	76	193	269	33
[b]Longitudinal compressive strength, σ_{cx} (MPa)	41.1	49.9	39.2	41.2	32.4
[b]Compressive strength, σ_{cy} = σ_{cz} (MPa)	3.8	5.5	4.1	5.2	2.8
[b]Longitudinal tensile strength, σ_{tx} (MPa)	84.8	107.6	86.2	85.3	78.6
[b]Transverse tensile strength, σ_{tz} (MPa)	2.4	2.3	6.6	4.8	1.5
[b]Out-of-plane shear strength, τ_{xy} (MPa)	8.5	7.8	8.3	10.8	5.5
Out-of-plane shear strength, τ_{zy} (MPa)	1.6[c]	1.4[c]	2.5[b]	3.2[b]	0.5[c]
Out-of-plane shear stiffness ratio, g(-)	0.36	0.51	0.82	0.96	0.34

[a]Values according to Ref. [14]

[b]Values according to Ref. [15]

[c]Characteristic values obtained using data (35 test data each) from Ref. [16]

7.2.3 RC bridge deck replacement

The RC bridge was composed of an RC deck joined by shear studs to two welded steel girders, as shown in Fig. 7.4. The deck width and position of the steel girders were the same as in the D-bridges. The RC deck had a constant deck thickness of h_{RC}=250 mm; a concrete of class C30/37 was selected according to Ref. [13]. The steel girders had the same dimensions and grade as the D-bridges. The deck replacement case, however, was investigated at one specific span only, i.e. l=25.0 m, and the corresponding steel girder height was 1000 mm. The properties of the concrete, concrete steel reinforcement and steel girders are listed in Table 7.2. An asphalt layer thickness of 100 mm was selected, which is common for RC bridges in Switzerland.
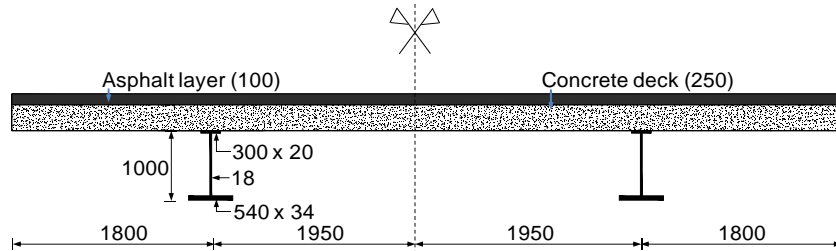
Figure 7.4: Cross section of a 25 m RC bridge (dimensions in mm)

7.3 Structural design

7.3.1 Limit state design

All bridges were designed according to the limit state design specified in Ref. [10, 13, 17], by verifying the ultimate limit state (ULS) and serviceability limit state (SLS). Load factors were applied to the actions and material factors to the characteristic (5% fractile) values of the material properties to obtain the design values of actions and properties. The load combinations and load factors were obtained from Ref. [18]. Material factors for concrete, steel reinforcements, steel girders and balsa/timber were selected from Ref. [10, 13, 17] respectively. For the FRP materials, the same material factors were adopted as in the Avançon Bridge design [5], which were based on the Refs. [19] and [20]. The material factors applied at ULS and SLS are summarized in Table 7.4. At SLS, the deck deflections were limited to span/500 in the short term, according to Ref. [13].

Table 7.4: Material factors used in design

Component and action	Factor	
	ULS	SLS
[a]FRP laminates, traffic load	2.64	1.50
[a]FRP laminates, permanent load	2.88	1.50
[b]Balsa/timber	1.50	1.60
[c]Concrete	1.50	1.00
[c]Steel reinforcement	1.15	1.00
[d]Steel girder	1.10	1.00

[a]Data from Ref. [19]
[b]Data from Ref.[17]
[c]Data from Ref. [13]
[c]Data from Ref. [21]

7.3.2 Design of GFRP-balsa sandwich slab and deck

The design procedure and criteria for the GFRP-balsa sandwich slab and deck were the same as for the Avançon Bridge, see [5]. The bridges were modeled in 3D by the Ansys finite element software (version 13) for both ULS and SLS verifications. The face sheets and arch laminates were modeled with multilayered shell 91 elements while solid 95 elements were used for the sandwich core, RC deck and steel girders. The critical design criterion was the deflection at SLS and not the ULS strength limit. Maximum deflections were obtained for the S- and D-bridges at the traffic load positions shown in Fig. 7.5a.
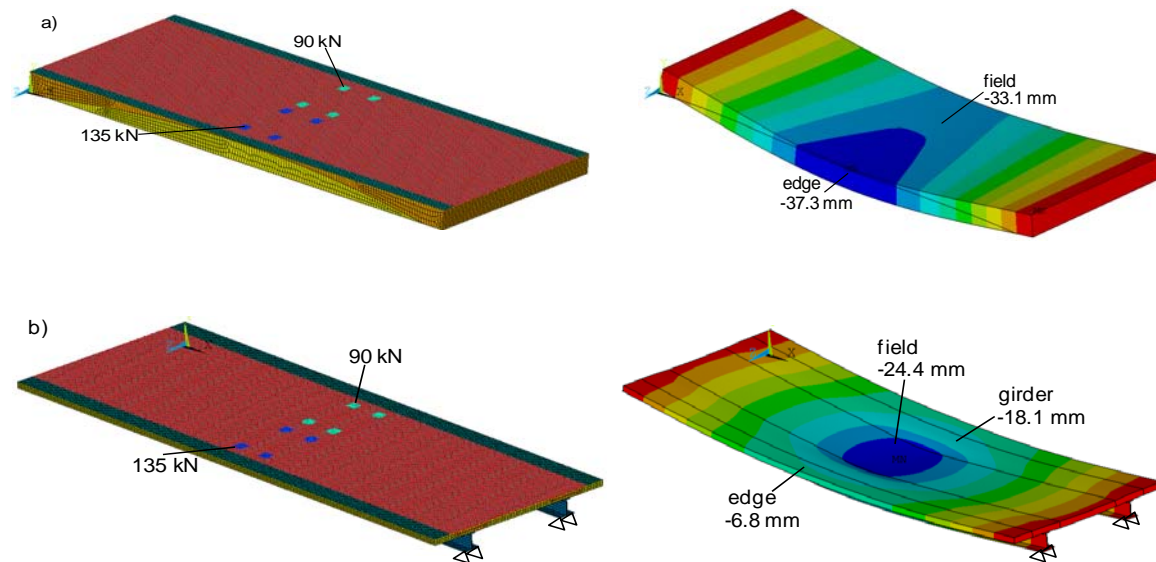
Figure: 7.5. Critical load positions according to Ref. [22] and corresponding SLS deck deflections for a) S-C slab of 19 m span b) D-TI deck-girder bridge of 25 m span

The traffic loads were composed of two groups of two-axle loads, in total, 4x135 kN (1st lane) and 4x90 kN (2nd lane, characteristic values for both lanes). Additionally, uniformly distributed loads of 8.1 kN/m^2 and 2.25 kN/m^2 were applied on the first and second lanes. The corresponding deflections, calculated at 75% of the characteristic loads [22], are shown in Fig. 7.5b. The limits of span/500 were met in both the longitudinal and transverse directions.

7.4 Results and discussion

7.4.1 Bridge span design limits

The bridge span limits obtained according to the SLS deflection requirement are shown in Fig. 7.6. The S-G and S-C slabs were able to reach maximum spans of 17.7 m and 18.9 m respectively. In comparison to the 16.0-m maximum span of the S-U slabs, they exhibited a possible span increase of 11% and 18% respectively due to the additional bending and shear stiffness provided by the GFRP and CFRP arches. The D-U deck-girder bridges exhibited high deflections of more than 20% above the limit in the 20-30 m span range. The D-TI (Douglas fir) deck-girder bridges, however, satisfied the deflection limit up to 30 m span due to the additional contribution of the timber inserts to the bending stiffness of the hybrid sandwich-steel girders.
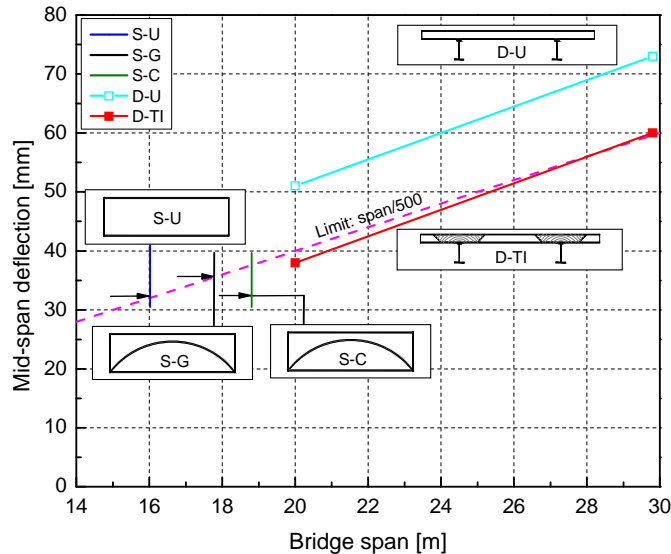
Figure 7.6: Bridge span limits at SLS for S-U, S-G, S-C slabs, and D-H, D-TI deck-girder bridges

7.4.2 Bending stiffness and composite action

The contribution of an FRP deck to the bending stiffness of a hybrid deck-steel girder depends not only on the deck stiffness (in the longitudinal bridge direction) but also on the composite action between the deck and steel girders (provided by the adhesive connections) and the composite action inside the deck between upper and lower face sheets, which is related to the in-plane shear stiffness of the core. Keller and Gürtler [6] demonstrated that adhesive connections in most cases provide full composite action. They also showed that composite action within pultruded decks largely depends on the cell geometry. Triangular decks provide high composite action between upper and lower face sheets, while decks with trapezoidal or rectangular cell shapes exhibit very limited composite action since the upper face sheet in most cases cannot be fully activated. In the following, the composite action within GFRP-balsa/timber sandwich decks is investigated and compared to that of pultruded and RC decks. The DuraSpan [23] and Asset [24] pultruded decks with trapezoidal and triangular cell geometries respectively were selected.

The degree of composite action, γ, according to Ref. [6] is calculated as follows:

$$\gamma = \frac{1}{1 + \dfrac{\pi^2 E_x A_x}{K b_{eff} l^2}}$$

(1)

where E_x and A_x are the elastic modulus and equivalent cross-section area of the upper facesheet and core of the deck in the longitudinal direction respectively, K is the in-plane shear stiffness of the deck system according to Ref. [25] (2005) and b_{eff} is the effective deck width.

A deck-girder bridge of 20-m span was selected for the comparative analysis. The deck of the D-U and D-TI bridges had a thickness of 250 mm while inserts of five different timber species were selected for the D-TI bridges (spruce, Douglas fir, birch, ash and cedar). The RC deck also had a 250-mm thickness. The steel girders had a 750-mm height in all bridges.

The effective deck width was obtained from the longitudinal stress distribution in the upper face sheet at mid-span, under SLS loads, using the shear lag model according to Ref. [26]:

$$b_{eff} = \frac{\int_{-b_1}^{b_2} \sigma_x}{\sigma_{max}}$$

(2)

where σ_x is the longitudinal stress in the upper face sheet across the deck width, b_1 and b_2 are the distance between minimum longitudinal stresses on the left and right sides and the steel girder axis and σ_{max} is the maximum longitudinal stress above the steel girder axis. The result for the D-U deck is b_{eff}=3550 mm, as shown in Fig. 7.7. Almost the whole deck width thus contributed as top chord. Accordingly, an effective width, twice the overhang width, i.e. b_{eff}=3600 mm, was assumed for all the decks, including RC and pultruded decks. In the latter case, the in-plane shear stiffness of the face sheets was similar to that of the face sheets of the sandwich deck and the assumption was thus justified.
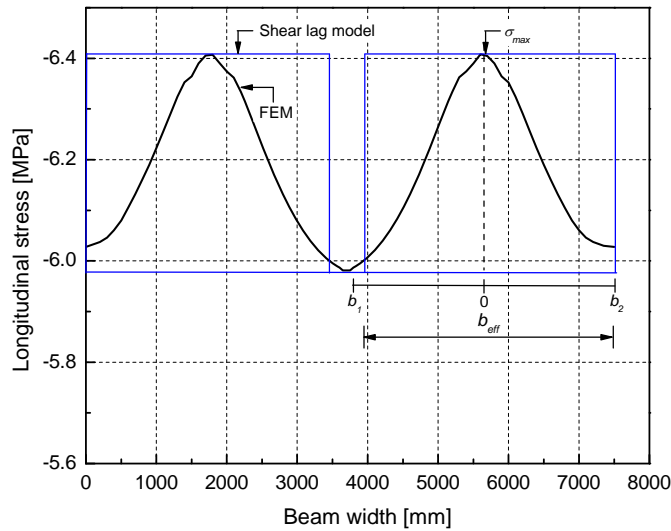
Figure 7.7: Longitudinal stress distribution in upper face sheet of D-U deck and effective width at SLS load (l=20 m, h_D=250 mm).

The degrees of composite action within the decks and the corresponding bending stiffnesses of the hybrid deck-steel girders, E_xI_z, in the longitudinal bridge direction are compared in Fig. 7.8. Full composite action in the adhesive bond between decks and steel girders was assumed. The bending stiffness was computed using the transformed-section method, taking into account the effective deck widths obtained above. The *K*-values were computed as the deck's in-plane shear modulus divided by the deck thickness. *K*-values for D-U decks (1.16 N/mm^3) and D-TI decks (2.24 - 4.72 N/mm^3) were computed from FEM results and those for the DuraSpan (0.03 N/mm^3) and Asset decks (0.21 N/mm^3) were selected from Ref. [25]. The DuraSpan deck exhibited low partial composite action and the corresponding girder also exhibited the lowest bending stiffness mainly due to the deck's low in-plane shear stiffness. The RC deck exhibited the highest (full) composite action and bending stiffness. The composite action in the D-U and Asset decks was similar, while the bending stiffness of

the former was much higher. Amongst the D-TI bridges, the decks comprising spruce, Douglas fir and birch showed almost full composite action and highest bending stiffness, and both values approached those of the RC deck. Compared to the D-U bridge with uniform balsa core, composite action and bending stiffness could be improved thanks to the timber inserts by approximately 6 and 33% respectively.
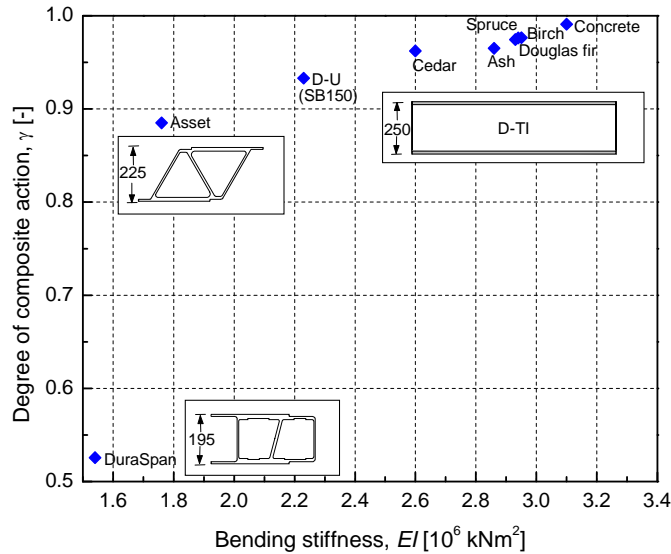
Figure 7.8: Degree of composite action in sandwich decks vs. bending stiffness of pultruded decks (Asset, DuraSpan) on steel girders, and D-U, D-TI and RC decks-girder bridges (thickness in mm), at 20 m span

7.4.3   Local stress at Balsa/timber joints

Local stress concentrations occur in the D-TI deck at the balsa/timber joints in the transverse bridge direction due to a change in the shear strain from the weaker balsa to the stiffer timber core [27]. The intensity of the local stress increases depends on the out-of-plane shear stiffness ratio, $g = \sqrt{G_{zy}(timber)\big/G_{zy}(balsa)}$, whose corresponding values are given in Table 7.3.

The increases of the transverse stresses in the bottom face sheet and of the out-of-plane shear stresses in the timber at the balsa/timber joints are shown in Fig. 7.9 for the five timber species and for the cases of butt and scarf joints (values at ULS design load). The critical stress locations are indicated in Fig. 7.9; the values were normalized by the corresponding design strength values. The stress increases in the balsa were less critical than in the timber due to the different fiber orientations. The timber was exposed to rolling shear with a design shear strength of 1.4 MPa, which was much lower than that of 2.3 MPa along

133

the balsa fibers. Figure 7.9 shows that the stress increases in the face sheets were not critical. However, depending on the timber species, shear stress increases in the timber of up to 60% of the design strength could occur for butt joints, based on the disparity between of the shear moduli between the two cores. These stresses could be reduced by a factor of approximately five if scarf joints were used instead, with angles of termination of 40°. In this case, stress increases remained below 5% of the design strength at ULS and were thus no longer critical.
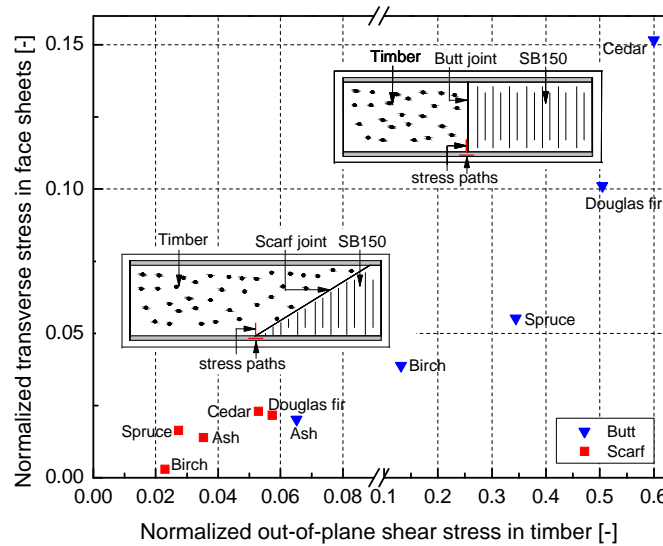
Figure 7.9: Increase of transverse stress vs. out-of-plane shear stress in face sheets and core respectively at balsa/timber butt and scarf joints of D-TI deck at ULS load (values normalized by design strength)

7.4.4   RC deck replacement

Contrary to the S- and D-bridges, material strength was the critical design criterion for the RC-bridge and not the deflection, as shown in Fig. 7.10. At 25-m span, the longitudinal hybrid girder deflections were about 34% below the span/500 limit. This was advantageous for RC-deck replacement by a less stiff D-TI deck (of the same thickness) with Douglas fir inserts. Nevertheless, the deflections of the latter deck still exceeded the 50-mm limit by 20%. The limit could only be met by a further introduction of steel plate inserts of 10-mm thickness as described above; the D-T/SI deck met the deflection limit.

Furthermore, changing the 100-mm-thick asphalt layer to thinner polymer concrete (40-mm) or epoxy layers (10-mm) allowed an increase of the deck thickness since, in deck replacement, only the total deck thickness plus surfacing layer has to be maintained.

Accordingly, D-TI decks (without steel inserts) of 310- or 340-mm thicknesses were also able to satisfy the deflection limit requirement.
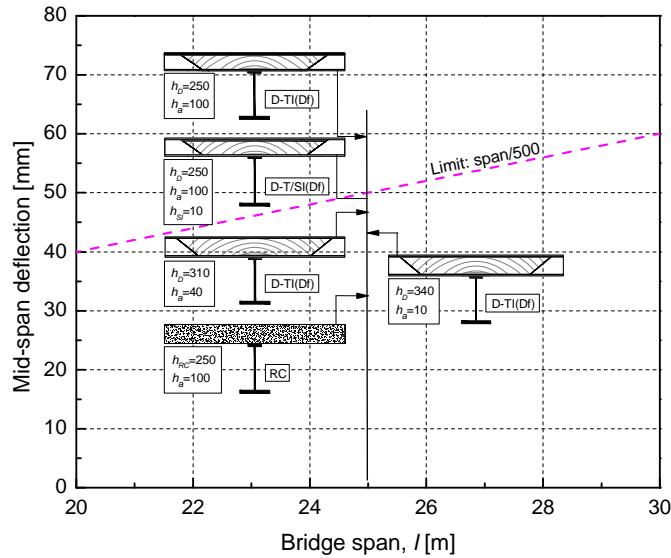
Figure 7.10: Mid-span deflections in deck replacement case for RC, D-TI (Douglas fir) and D-T/SI deck-girder bridges and comparison to SLS limit

Table 7.5: Sectional properties of RC, D-TI and D-T/SI decks and design moments at 25m span.

	RC	D-TI	D-T/SI
Deck thickness (mm)	250	250	250
Deck weight (kN/m^2)	6.25	1.92	2.24
[a]Moment of inertia, I_z (m^4)	0.18	0.16	0.17
Stiffness, $E_x I_z$ (10^6 kNm^2)	5.51	4.83	5.15
[b]Location of neutral axis (mm)	320	580	450
Girder design moment, $E_{Mx,d}$, due to dead load (kNm)	2858	959	998
Girder design moment, $E_{Mx,d}$, due to live load (kNm)	8372	8372	8372
Girder design moment, $E_{Mx,d}$, total (kNm)	11230	9331	9370
Girder resistance moment, $R_{Mx,d}$, (kNm)	11306	9765	10450
Additional safety factor $R_{Mx,d}/E_{Mx,d}$	1.00	1.05	1.12

[a] with reference to RC
[b] measured from top of upper face sheet or RC

Further details of the designs are shown in Table 7.5. The D-TI and D-T/SI decks were approximately 2.8-3.3 times lighter than the RC deck. Consequently, the hybrid girder design moments of the D-bridges due to dead load were only 35-40% and those due to the total load (dead plus live loads) were still only 83% of the hybrid girder design moments of the RC-bridge. This led to additional safety factors of 1.05 and 1.12 for the D-bridges compared to the

RC-bridge. On the other hand, the stiffnesses, E_xI_z, of the D-bridges were 14% and 7% lower than those of the RC-bridge, which could be attributed to the lower position of the neutral axes, see Fig. 7.11 (at SLS loads). The full composite action of all elements was confirmed by the plane strain distribution. The corresponding stresses are shown in Fig. 7.12 and confirm the effectiveness of the steel inserts, which exhibit a significant longitudinal stress. The stresses in the timber and concrete were similar. With regard to the steel girder, which is maintained in the deck replacement case, the stresses in the upper flange increased significantly; however, they were still low in the D-T/SI bridge (of the same deck thickness as the RC deck), even if multiplied by the load factor (1.5) to obtain the ULS design value.
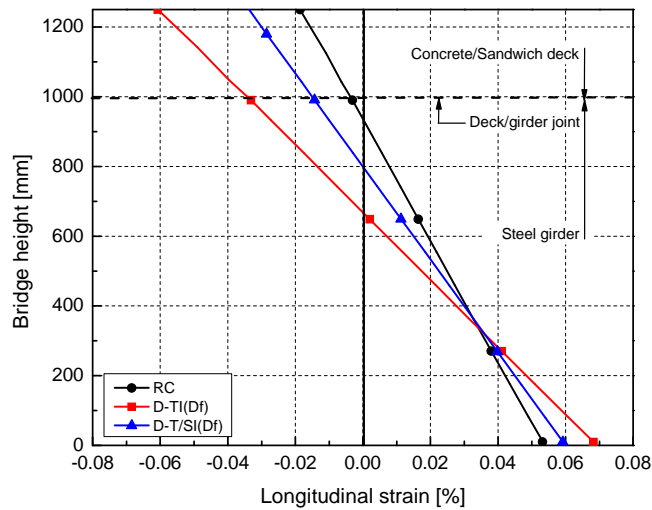
Figure 7.11: Longitudinal strain distributions in D-TI, D-T/SI and RC deck-girder bridges at SLS load
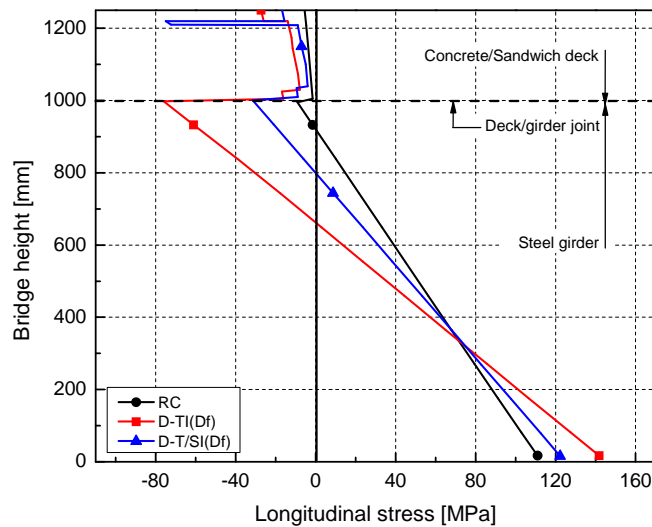
Figure 7.12: Longitudinal stress distributions in D-TI, D-T/SI and RC deck-girder bridges at SLS load

7.5 Conclusions

The span limits of two GFRP bridge concepts comprising GFRP-balsa sandwich plates have been investigated. In the first concept, the sandwich plate was directly used as a slab bridge, while in the second the plate was used as the deck of a hybrid sandwich-steel girder bridge. Furthermore, in the latter case, the potential of GFRP-balsa sandwich decks to replace RC decks of hybrid RC deck-steel girder brides was evaluated. The following conclusions were drawn:

1) Taking manufacturing limits into account (800-mm slab thickness), maximum spans of approximately 19 m can be reached with FRP-balsa sandwich slab bridges if a CFRP arch is integrated into the balsa core. This corresponds to a slenderness of span/24, similar to that of RC slab bridges. The sandwich slab, however, is approximately seven times lighter than the RC slab. The maximum span and slenderness without FRP arch are 16 m and span/20 respectively.

2) In the case of hybrid sandwich deck-steel girder bridges and assuming a reasonable slenderness of span/20 (concerning total height), the replacement of the balsa core by timber inserts above the steel girders is necessary to satisfy deflection limits. When the required span exceeds the limit for sandwich slab bridges (19 m), hybrid sandwich-steel girder bridges can thus be used up to spans of 30 m. To exceed this span, the slenderness must be reduced and additional steel inserts have to be inserted between the timber and upper face sheet.

3) RC deck replacement within the same span range (up to 30 m) is possible if either steel inserts are added between the timber inserts and the upper face sheet or if deck thickness can be increased by reducing the thickness of the asphalt layer (but maintaining the total thickness).

4) In contrast to some pultruded decks, GFRP-balsa sandwich slabs or decks exhibit full composite action between lower and upper face sheets.

5) Stress concentrations at the joints between balsa core and timber inserts can be effectively reduced by using scarf joints instead of butt joints.

References

[1] Zureick A. Fiber reinforced polymer bridge decks. Proc National Seminar on Advanced Composite Material Bridges, FHWA 1997.

[2] Keller T. Recent all-composite and hybrid fibre-reinforced polymer bridges and buildings. Prog Struct Eng and Mater 2001; 3(2): 132-140.

[3] Robinson MJ, Kosmatka JB. Lightweight fiber-reinforced polymer composite deck panels for extreme applications. J Compos Constr 2008;12(3): 344-354.

[4] Reising RMW, Shahrooz BM, Hunt VJ, Newmann AR, Helmicki AJ, Hastak M. Close look at construction issues and performance of four fiber-reinforced polymer composites bridge decks. J Compos Constr 2004; 8(1): 33-42.

[5] Keller T, Rothe J, de Castro J, Osei-Antwi M. GFRP-balsa sandwich bridge deck: Concept, design and experimental validation. J Compos Constr 2013. http://dx.doi.org/10.1061/(ASCE)CC.1943-5614.0000423.

[6] Keller T, Gürtler H. Design of hybrid bridge girders with adhesively bonded and compositely acting FRP deck. Compos Struct 2006; 74/2: 202-212.

[7] Harries A, Moses J. Replacing a composite RC bridge deck with an FRP deck-the effect on superstructure stresses. Proc Asia-Pacific Conference on FRP in Structures, APFIS 2007.

[8] Allampalli S, O'Connor J, Yannotti AP. Fiber reinforced polymer composites for the superstructure of a short-span rural bridge. Compos Struct 2002; 58/1: 21-27.

[9] Osei-Antwi M, de Castro J, Vassilopoulos AP, Keller T. FRP-balsa composite sandwich bridge deck with complex core assembly. J Comps Constr 2013; 17(6): 04013011. http://dx.doi.org/10.1061/(ASCE)CC.1943-5614.0000435

[10] European Standard. Eurocode 3-Part 1: Design of steel structures: general rules and rules for buildings. European Committee for Standardization, Brussels; 2005.

[11] Alcan Baltek Corporation. Mechanical properties vs. density and grain orientation for balsa wood. Data sheet . Northvale, NJ, 2001 http://www.corematerials.3acomposites.com/baltek-sb-us.html.

[12] Gay D, Hoa, SV. Composite materials: design and applications. CRC Press, Boca raton, Fl; 2007.

[13] European Standard. Eurocode 2-Part 2: Design of concrete structure- concrete bridges: design and detailing rules. European Committee for Standardization, Brussels; 2005.

[14] Bodig J, Goodman JR. Prediction of elastic parameters of wood. Wood Sci 1973; 5/4: 249-264.

[15] Forest Products Laboratory. Wood as an engineering material Wood Handbook, general technical report FPL-GTR-190. Madison, WI; 2010.

[16] Bendtsen BA. Rolling shear characteristics of nine structural softwoods. Forest Prod J 1976; 26/11: 51-56.

[17] European Standard. Eurocode 5-Part 1: Design of timber structures: general- common rules and rules for building. European Committee for Standardization, Brussels; 2005.

[18] European Standard . Eurocode 0: Basis of structural design. European Committee for Standardization, Brussels; 2002.

[19] BÜV. Empfehlung: Tragende Kuststoffbauteile im Bauwesen – Entwurf, Bemessung und Konstruktion. Stand 08/2010, Bau-Überwachungsverein (BÜV e.V.), Berlin; 2010.

[20] Clarke JL. Structural design of polymer composites - Eurocomp Design Code and Handbook. E & FN Spon, London; 1996.

[21] European Standard. Eurocode 3-Part 2: Design of steel structures: steel bridges. European Committee for Standardization, Brussels; 2006.

[22] European Standard. Eurocode 1-Part 2: Actions on structures: traffic loads on bridges. European Committee for Standardization, Brussels; 2003.

[23] Cassity P. Advanced composites for bridge infrastructure Renewal-Phase II DARPA. Adv Compos Tech, Transfer/Bridge Infrastructure Renewal Consortium, Vol. IV, Task 16; 2000.

[24] Luke S, Canning L, Collins S, Knudsen E, Brown P, Taljstern B, Olofsson I. Advanced composite bridge decking system. In: Struct Eng Int 2 , Adv Mater 2002; 76-79.

[25] Gürtler H. Composite action of FRP bridge decks adhesively bonded to steel main girders. PhD thesis, EPFL, Lausanne 2005.

[26] Zou B, Chen A, Davalos JF, Salim HA. Evaluation of effective width by shear lag model for orthotropic FRP bridge decks. Compos Struct 2011; 93/2: 474-482.

[27] Skvortsov V, Thomsen OT. Analytical estimates for stresses in face sheets of sandwich panel at the junctions of two core materials. Report No. 113, Inst Mech Eng, Aalborg Univ; 2002.

8.

Conclusions and future work

8.1 Summary of conclusions

This chapter presents the main conclusions and recommendations for future work. The conclusions are based on the objectives of this thesis explained in Section 1.2.

8.1.1 Shear characterization of balsa core

Balsa panels are selected as the core material in sandwich deck applications where the main loading case is shear. Due to the anisotropic nature of the material, the shear response depends on the shear plane. Shear experiments were performed to evaluate the effects of the shear plane, density and adhesive joints on the shear stiffness and strength as well as the shear ductility of the balsa panels. The main conclusions drawn are as follows:

- The shear planes significantly influenced the shear stiffness and strength. Highest values were obtained for the Eg shear plane (parallel to end grain), intermediate values for the Fg/P plane (parallel to flat grain) and lowest values for the Fg/T plane (transverse to flat grain). Shear stiffness and strength increased with increasing density, which was attributed to the cell wall thickness of tracheids in the wood microstructure.

- The thin adhesive joints between the balsa blocks, which together constitute the balsa panels, slightly increased the shear stiffness and strength with the exception of the strength of Fg/T specimens, which was reduced due to a change in the failure mode.

- The Eg and Fg/T specimens exhibited significant shear ductility due to plastic deformations in the balsa tracheids while the Fg/P exhibited low ductility due to the relatively brittle middle lamella, which joins adjacent..

8.1.2 Complex core system 1: GFRP-balsa sandwich beam with complex core assembly

Sandwich beams, with a complex core assembly consisting of upper high-density and lower low-density balsa and an FRP arch bonded in thecore interface, were investigated in four-point and asymmetric three-point bending experiments and compared to a reference case of uniform high-density balsa sandwich beams. The resulting mode of failure in the complex balsa core was analyzed to evaluate the effects of block arrangement, block density and adhesive joints between the blocks on crack initiation and propagation. The deflections and axial strain and stress distributions of the new sandwich beams were predicted by a new analytical multilayer model. The main conclusions drawn are as follows:

- The FRP arch prevented compression failure of the upper face sheet by reducing compressive forces in the latter, which led to a higher ultimate load. The arches also contributed up to 20% to the shear resistance for symmetric loading and increased the beam stiffness.

- The sandwich beam with complex core assembly showed the overall best performance in terms of stiffness, strength and weight, which was much better than that of the beams with uniform high-density core.

- The failure analysis showed that cracks initiated and propagated in the lowest density blocks due to their low fracture toughness. Cracks were not able to propagate across the adhesive joints between blocks if the bonding was perfect, but in the case of poor bonding, interface failure occurred and cracks could penetrate the adhesive layers.

- The new multilayer models successfully predicted the beam deflections, axial and shear strains and stress distributions in the complex core assembly.

8.1.3   Complex core system 2: GFRP-balsa sandwich beam with timber inserts

A balsa-sandwich beam with timber insert whose fibers are oriented transverse to the beam direction, to be extended to a GFRP-balsa sandwich bridge deck with timber inserts integrated into the balsa core above the girder, was numerically investigated. Axial and shear stress concentrations occurred in the face sheets and cores respectively at the balsa/timber joints due to material disparity. Two new analytical models were developed to estimate these stress concentrations at butt and scarf joints. The models were based on an existing closed-form model and have been validated by FEM for balsa-Douglas fir butt and scarf joints, both implemented in a sandwich with GFRP face sheets. The main conclusions drawn are as follows:

- The axial and shear stress concentrations in face sheets and cores due to the effect of joints were accurately predicted by the new models and validated by corresponding FEM results. The models for scarf joints are applicable for angles of termination of between 20° and 60°.

- Stress concentrations at dissimilar core joints almost disappear if a butt joint is changed to a scarf joint configuration. A scarf joint of 40° angle of termination was therefore recommended for the design of sandwich bridge decks.

8.1.4   Application of complex core systems in sandwich bridge construction

The two complex core systems have been applied to the design of two new GFRP-balsa sandwich plates. Based on the first concept (Section 9.1.2), the sandwich plate was used as a slab bridge while in the second concept (Section 9.1.3), the plate was used as a sandwich deck of a hybrid sandwich-steel girder bridge. Two critical subjects were investigated:

- structural limits of the two new GFRP-balsa bridges and
- potential of replacing long-span reinforced concrete decks by GFRP-balsa sandwich decks.

For the first subject, based on the limit of sandwich slab thickness of 800 mm due to manufacturing challenges, maximum bridge spans of approximately 19 m can be reached with FRP-balsa sandwich slab bridges. In the case of hybrid sandwich deck-steel girder bridges, bridge spans of up to 30 m can be reached. For the second subject, reinforced concrete decks of up to 30 m can be replaced by GFRP-balsa sandwich decks, if either steel plates are inserted between the timber inserts and upper face sheets or the sandwich deck thickness is increased by reducing the thickness of the asphalt layer.

8.2   Original contributions

The original contributions provided by the thesis with regard to experimental and analytical investigations as well as application in bridge construction are summarized as follows:

(a) Experimental investigations

- The shear properties database for balsa panels has been extended to include data at all three shear planes and an explanation for the different shear responses for each plane has been offered.
- The influence of adhesive joints in balsa panels has been quantified.
- The shear ductility of balsa at each of the three shear planes has been established and an explanation for the different behavior at each plane has been offered.
- The influence of beam length and thickness on the shear properties of balsa has been established.
- The possibility of integrating an FRP arch into sandwich cores has been explored and the shear contribution of the FRP arch in sandwich decks has been quantified.

(b) Analytical modeling

- A new analytical model has been developed to predict the bending behavior of multilayer sandwich beams. The model is superior to an existing high-order sandwich panel theory that is unable to accurately predict the axial and shear stresses in stiff cores such as balsa or timber.

- The existing analytical model that predicts axial stress concentrations in face sheets at butt core joints in sandwich beams has been extended to scarf joints.

- A new analytical model to predict shear stress concentrations in the cores at butt and scarf joints has been developed.

These new joint models have been numerically validated and offer simpler solutions than the complicated existing high-order sandwich panel theory that is yet to be validated.

(c) Bridge construction

- New sandwich beam concepts for solving debonding problems between the face sheet and the core, eliminating low bending stiffness and providing longer bridge spans for sandwich decks have been developed and successfully applied in GFRP-balsa sandwich bridge decks.

- Maximum bridge spans of GFRP-balsa sandwich bridge slabs and decks have been established.

- For the first time, the possibility of replacing a concrete deck with a GFRP-balsa sandwich deck has been explored.

8.3 Future work

This section introduces research topics concerning the future prospects of the present work. The first four topics are dedicated to further research work to improve on the structural performance of the proposed sandwich bridge decks while in service. The last topic deals with a wider scope of sandwich deck application in bridge construction in the future.

8.3.1   Wide variation in shear properties of balsa

The results of the shear experiments on balsa panels exhibited relatively large variations due to the natural and anisotropic characteristics of the material. Specifically, adhesive joints, dissimilar balsa blocks and variation of early and late woods even within the same block,

accounted for these large variations. In order to obtain reliable fractile values as a basis for design, the database has to be significantly extended.

8.3.2 Fire safety of FRP-balsa sandwich decks

Exposure of GFRP-balsa sandwich decks to fire loads causes complete deterioration of the fibers and resin in the face sheets as well as the adhesive layers between the balsa blocks and at the deck-girder joints. Fire resistance of up to 30 minutes has been achieved in GFRP-honeycomb panels by the use of Structo-Gard and Intumescent Mat protective layers [1]. These protective layers are composed of flame retardant adhesives, which create a fire zone boundary at the exposed surface and retard the fire from passing onto the other side (unexposed side). An investigation into the fire resistance of GFRP-balsa panels in order to establish the fire rating of GFRP-balsa sandwich decks should be considered in the near future.

8.3.3 Fatigue performance of sandwich beams with complex core systems

Joint failures are common in structures subjected to fatigue loads and this has been attributed to poor bonding and adhesion quality and technique. In sandwich decks, two primary interfaces exist between the core and the upper and lower face sheets. Inserting an arch into the balsa core in the proposed complex core system introduces additional interface and an adhesive joint between the arch and the lower balsa core and adhesive joint and upper and lower balsa cores. Additional joints are also introduced at balsa/timber joints in sandwich decks with timber inserts. These new joints add to the critical parts of the proposed sandwich bridge decks and therefore an experimental investigation to evaluate their fatigue performance is necessary.

8.3.4 Dynamic behavior of sandwich deck

The mass of a bridge has a direct influence on its natural frequency: the lower the mass, the higher the natural frequency. Stiffer materials also exhibit high natural frequency. GFRP-balsa sandwich decks are stiff and lightweight and therefore have high natural frequency. High deck vibrations adversely affect the comfort of users, result in fatigue phenomena and can cause resonance. To avoid these problems in sandwich decks, the deck weight can be enhanced by using steel material for the guard rails. Dampers can also be attached to the lower face sheets of the decks at the mid-span to dampen the deck's vibration [2]. A

comprehensive evaluation of the dynamic behavior of GFRP-balsa decks is required and further investigation of the applicability of the suggested solutions is necessary for robust bridge deck design.

8.3.5   Bridge widening

The widening of existing concrete bridges is in demand due to a recent increase in traffic as a result of growing world economies and free movement of people in the EU and between the EU and Switzerland. One way of achieving this is by bonding lightweight GFRP-balsa sandwich decks to the existing concrete decks as shown in Fig. 8.1. In such a case, the resulting deck weight remains virtually unchanged and in some cases the substructure will no longer require reconstruction. The critical parts, however, are the joints between the upper face sheet and concrete (see Fig. 8.1), which under bending loads can trigger fiber tear failure. Investigation into this failure mode will establish optimum joint concepts to improve the structural performance.
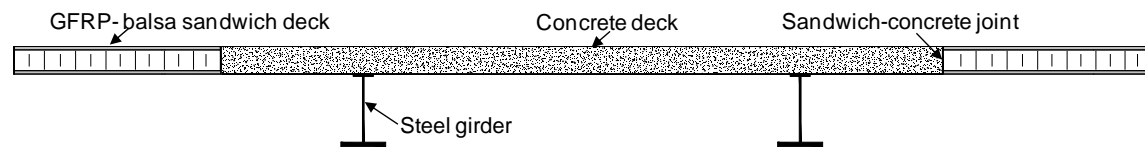
Figure 8.1: Concrete bridge widened with GFRP-balsa sandwich deck

References

[1] Sorathia U, Gracik T, Ness MB, Le A, Scholl B, Long G. Fire safety of marine composites. 45th International SAMPE Symposium, Long Beach, CA 2000; 1191-1203.

[2] Lebet JP, Hirt MA. Steel bridges: conceptual and structural design of steel and steel-concrete composite bridges. 1st ed. Siwtzerland: EPFL press; 2013.

ANNEX A.

Detailed shear experimental data on balsa panels

A.1 Shear planes of balsa panels tested and experimental set-up
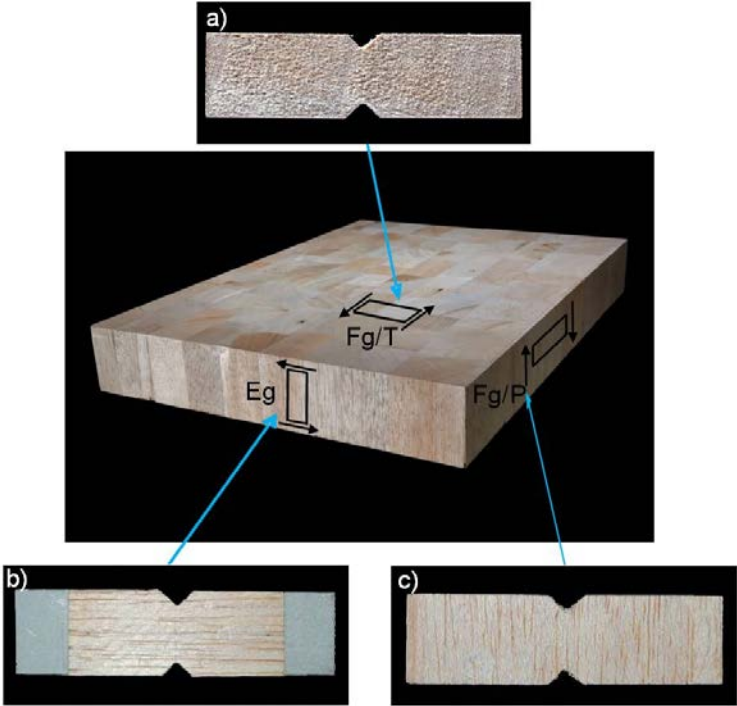
Figure A.1: Balsa panel showing: a)shear plane transverse to flat grain (Fg/T), b) shear plane parallel to end grain (Eg specimen with tabs), and c) shear plane parallel to flat grain (Fg/P)
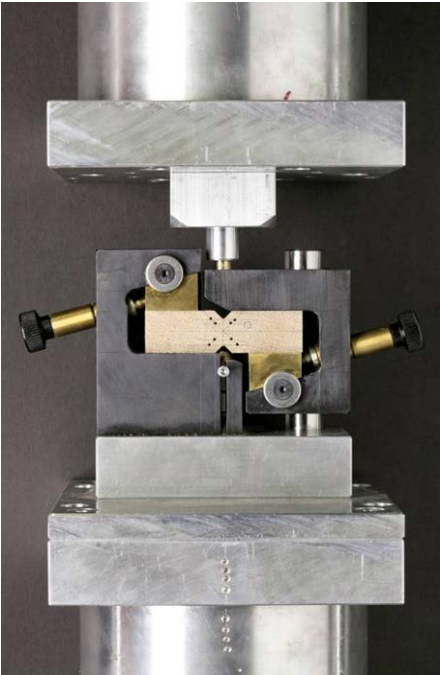
Figure A.2: Experimental set-up, specimen with black dots for video extensometer measurements

A.2   Shear stress and strain curves

A.2.1   Eg specimens
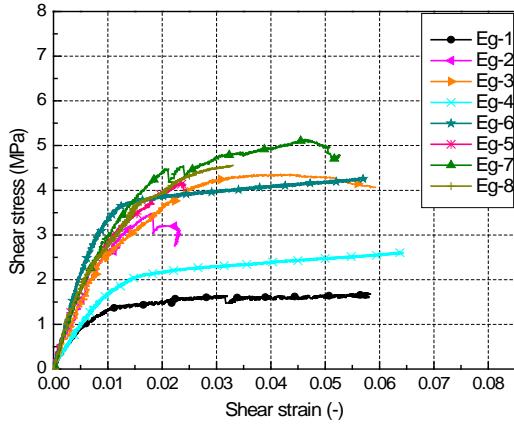
Figure A.3: Shear stress - strain responses for Eg specimens
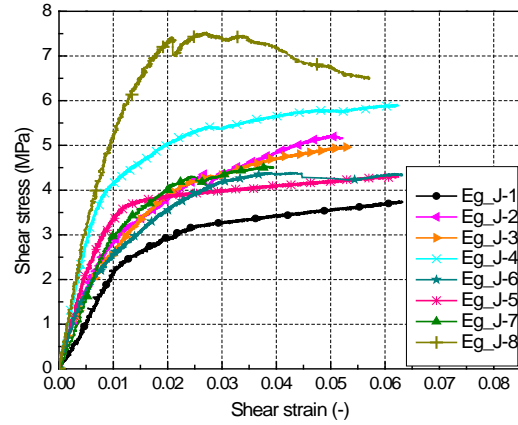
Figure A.4: Shear stress - strain responses for Eg_J specimens

A.2.2   Fg/P specimens
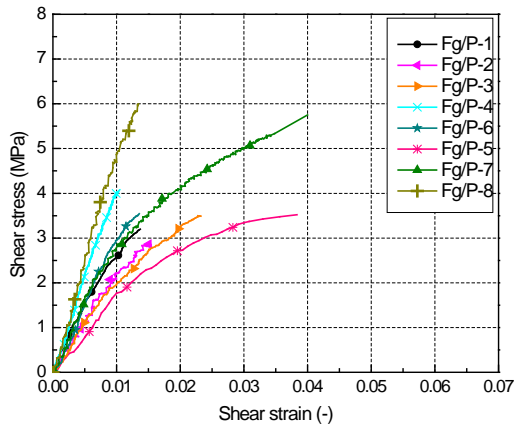
Figure A.5: Shear stress - strain responses for Fg/P specimens
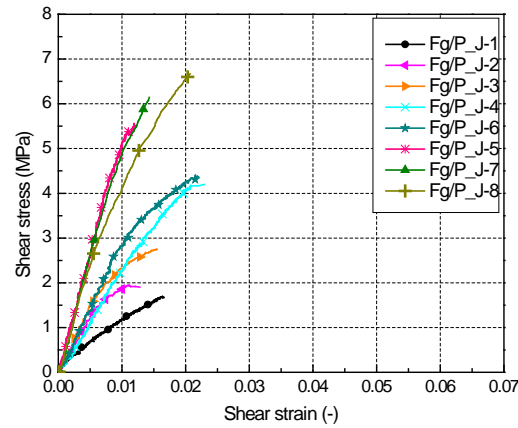
Figure A.6: Shear stress - strain responses for Fg_J specimens

A.2.3   Fg/T specimens
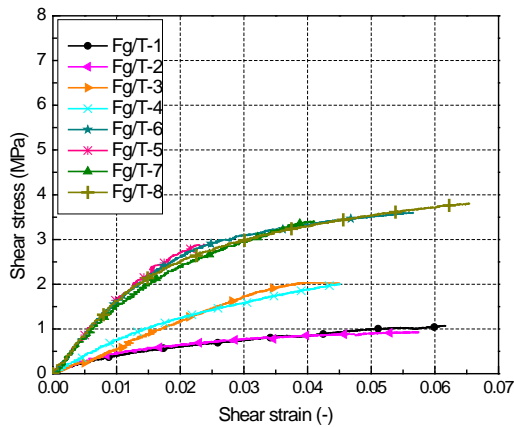
Figure A.7: Shear stress - strain responses for Fg/T specimens
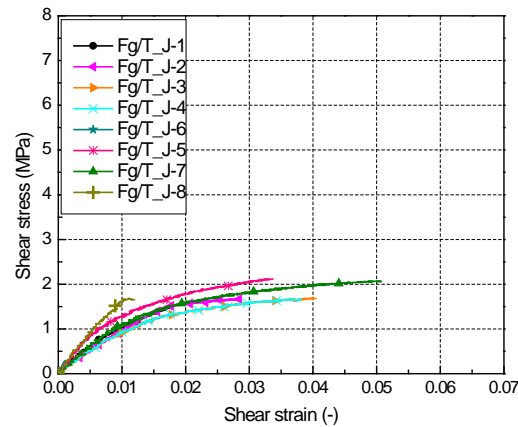
Figure A.8: Shear stress - strain responses for Fg/T_J specimens

151

A.3 Failure modes

A.3.1 Eg specimens
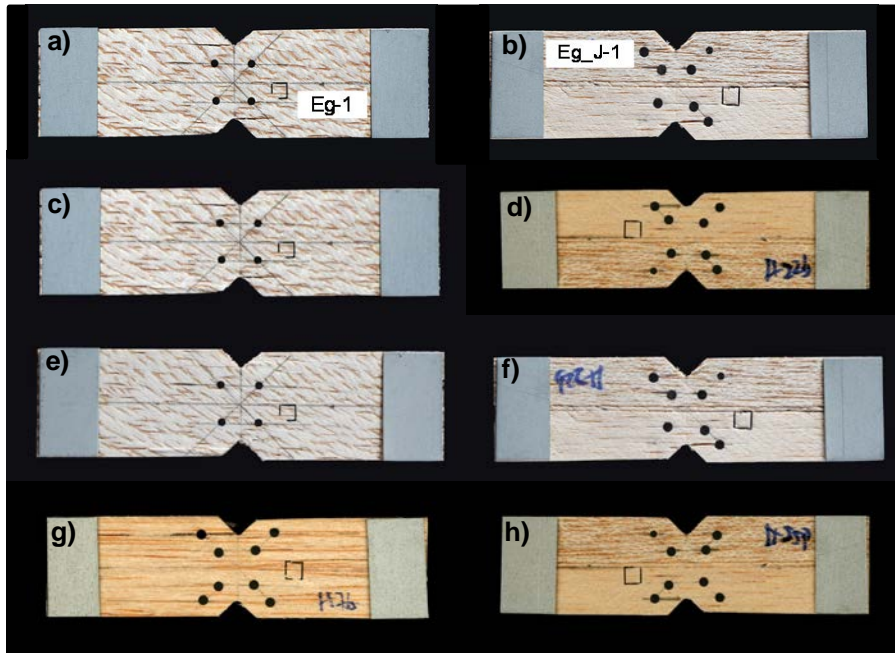
*Figure A.9: Failure mode for specimens (a) Eg-1, (b) Eg_J-1, (c) Eg-2, (d) Eg_J-2, (e) Eg-3,
(f) Eg_J-3, (g) Eg-4, (h) Eg_J-4*

A.3.2 Fg/P specimens
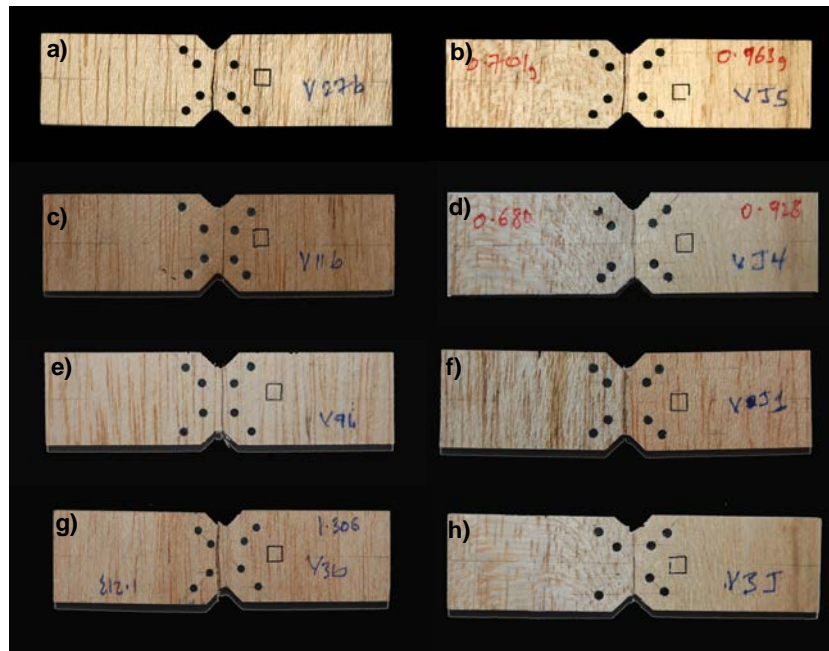
*Figure A.10: Failure mode for specimens (a) Fg/P-1, (b) Fg/P_J-1, (c) Fg/P-2, (d) Fg/P_J-2,
(e) Fg/P-3, (f) Fg/P_J-3, (g) Fg/P-4, (h) Fg/P_J-4*

A.3.3 Fg/T specimens
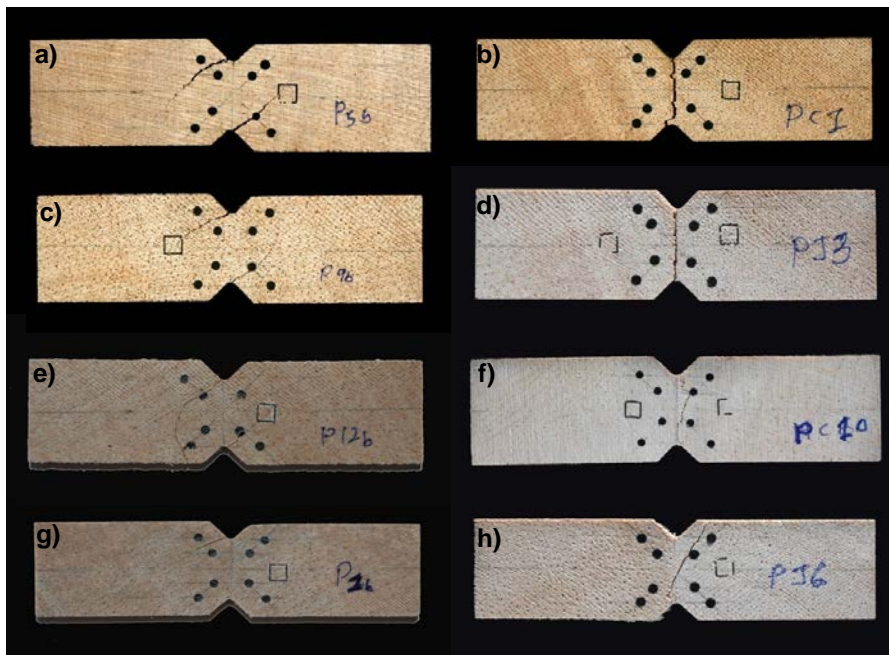
Figure A.11: Failure mode for specimens (a) Fg/T-1, (b) Fg/T_J-1, (c) Fg/T-2, (d) Fg/T_J-2, (e) Fg/T-3, (f) Fg/T_J-3, (g) Fg/T-4, (h) Fg/T_J-4

A.4   Shear ductility

A.4.1   Eg specimens
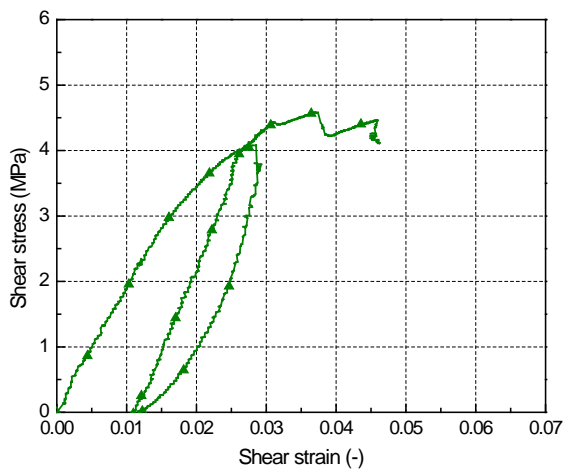
Figure A.12: Shear stress vs. strain loading and unloading cycles for Eg-10 specimen
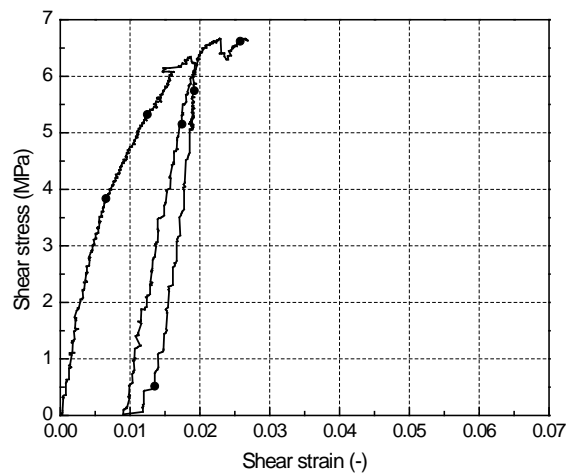
Figure A.13: Shear stress vs. strain loading and unloading cycles for Eg-11 specimen
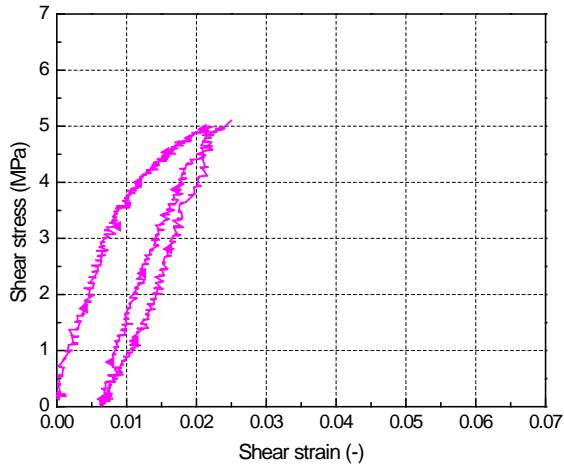
Figure A.14: Shear stress vs. strain loading and unloading cycles for Eg-12 specimen
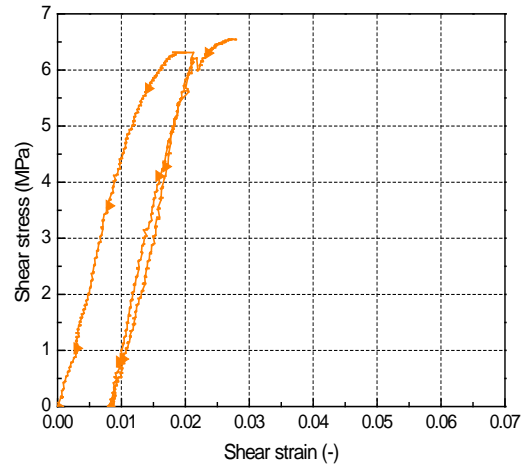
Figure A.15: Shear stress vs. strain loading and unloading cycles for Eg-12 specimen
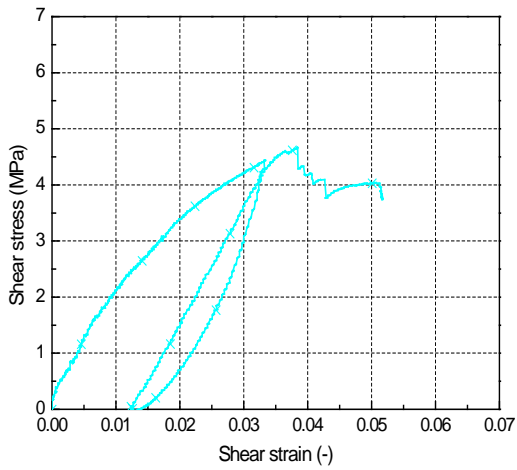
Figure A.16: Shear stress vs. strain loading and unloading cycles for Eg-14 specimen
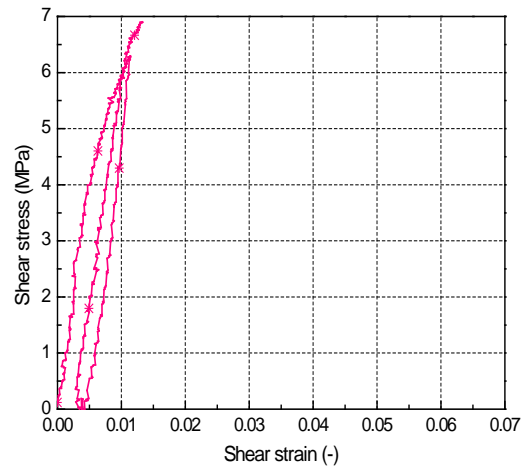
Figure A.17: Shear stress vs. strain loading and unloading cycles for Eg-15 specimen
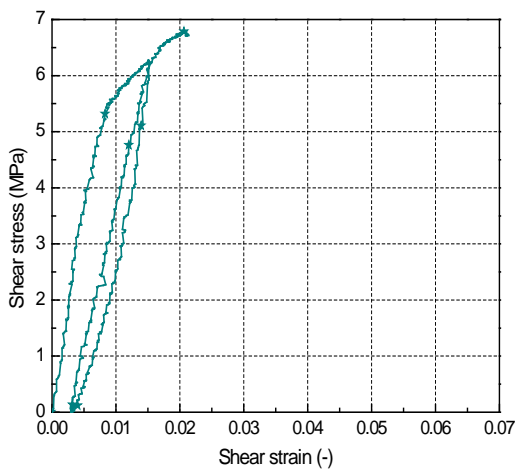
Figure A.18: Shear stress vs. strain loading and unloading cycles for Eg-16 specimen
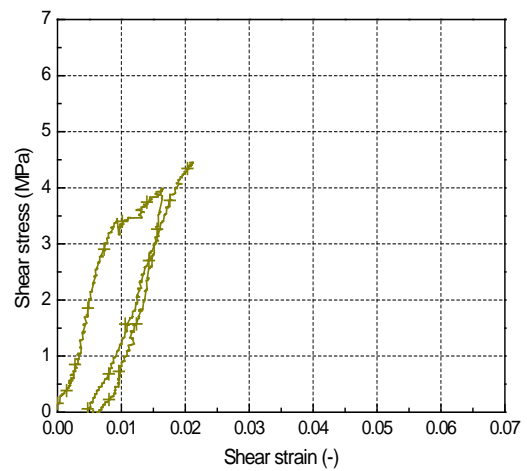
Figure A.19: Shear stress vs. strain loading and unloading cycles for Eg-17 specimen

A.4.2 Fg/P specimens
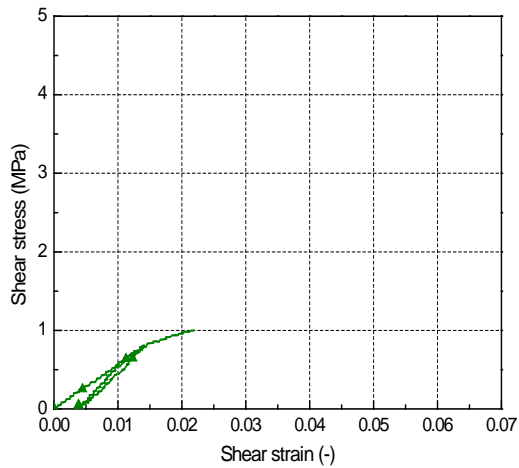
Figure A.20: Shear stress vs. strain loading and unloading cycles for Fg/P-10 specimen
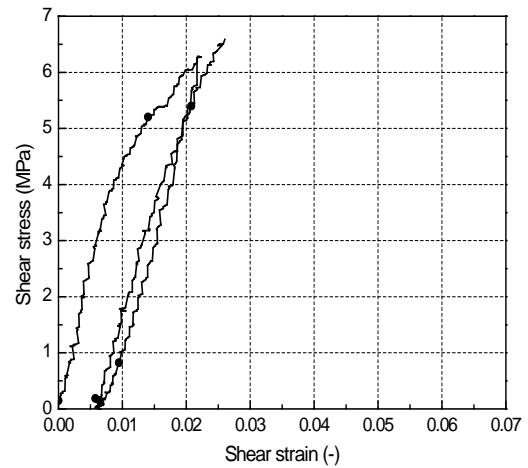
Figure A.21: Shear stress vs. strain loading and unloading cycles for Fg/P-10 specimen
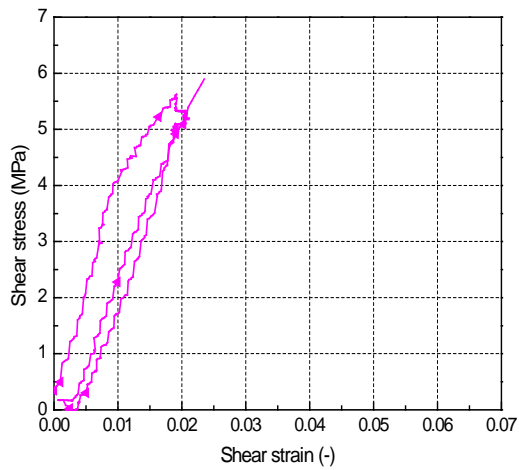
Figure A.22: Shear stress vs. strain loading and unloading cycles for Fg/P-12 specimen
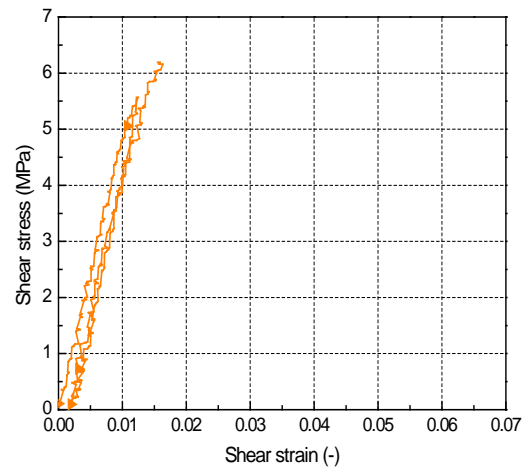
Figure A.23: Shear stress vs. strain loading and unloading cycles for Fg/P-13 specimen
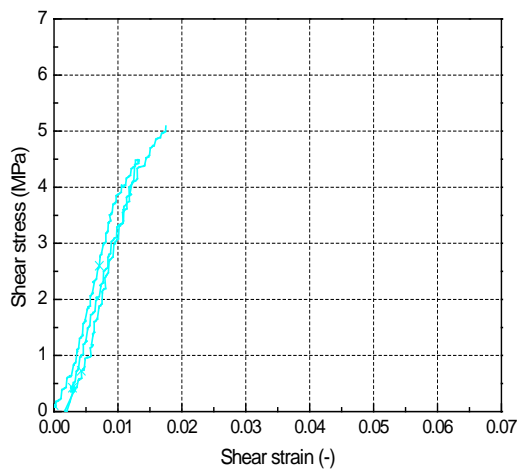
Figure A.24: Shear stress vs. strain loading and unloading cycles for Fg/P-14 specimen
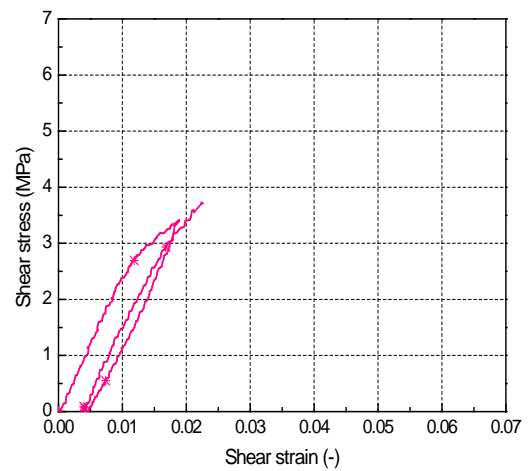
Figure A.25: Shear stress vs. strain loading and unloading cycles for Fg/P-15 specimen

155
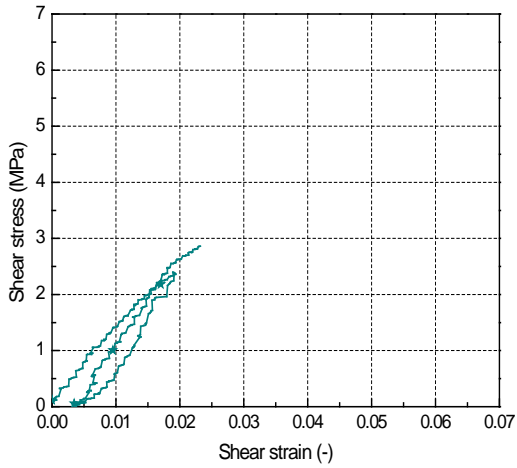
Figure A.26: Shear stress vs. strain loading and unloading cycles for Fg/P-16 specimen
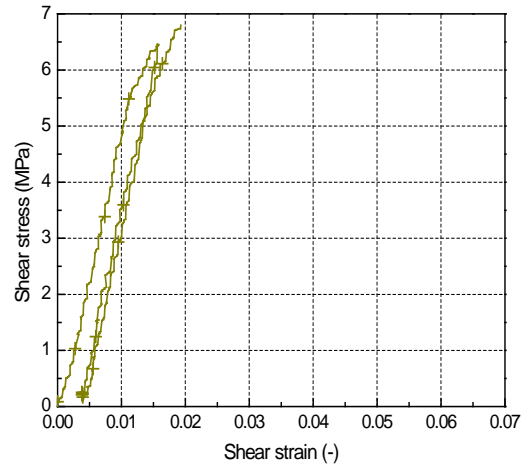
Figure A.27: Shear stress vs. strain loading and unloading cycles for Fg/P-17 specimen

A.4.3   Fg/T specimens
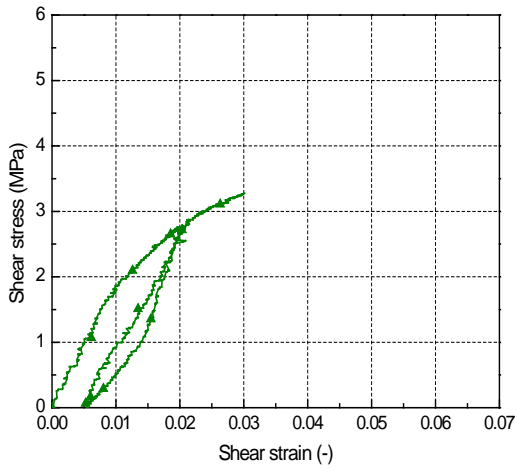
Figure A.28: Shear stress vs. strain loading and unloading cycles for Fg/T-10 specimen
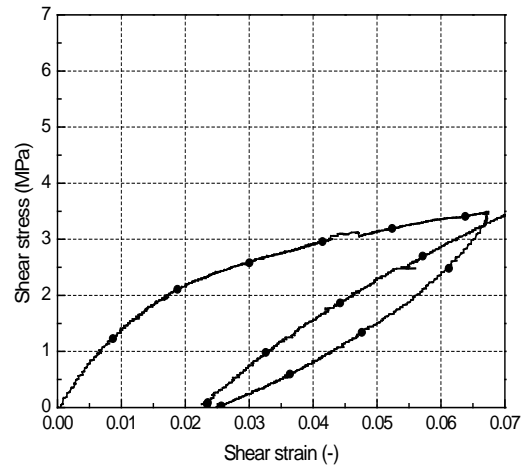
Figure A.29: Shear stress vs. strain loading and unloading cycles for Fg/T-11 specimen
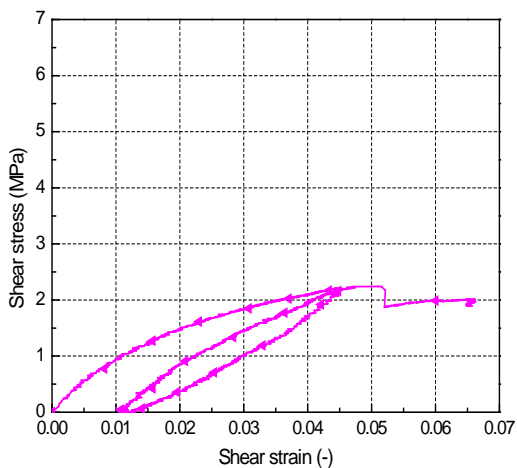
Figure A.30: Shear stress vs. strain loading and unloading cycles for Fg/T-12 specimen
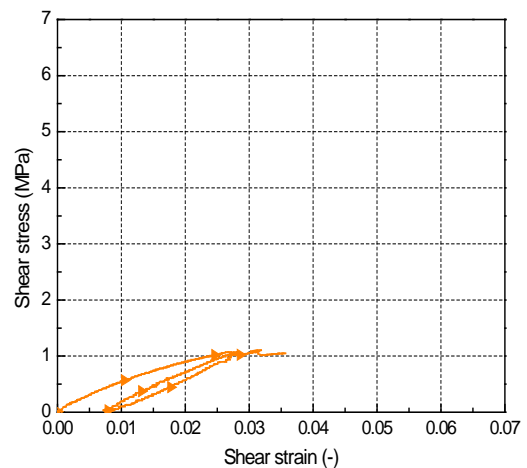
Figure A.31: Shear stress vs. strain loading and unloading cycles for Fg/T-13 specimen
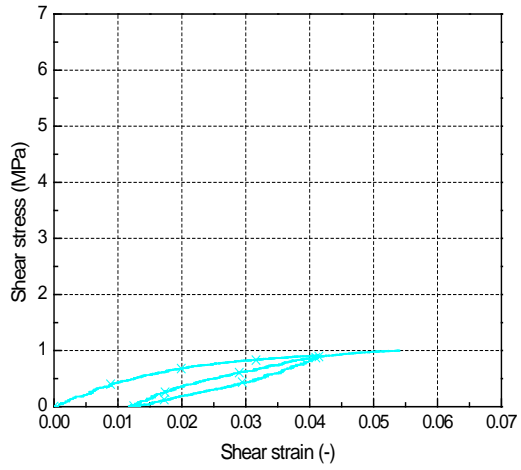
Figure A.32: Shear stress vs. strain loading and unloading cycles for Fg/T-14 specimen
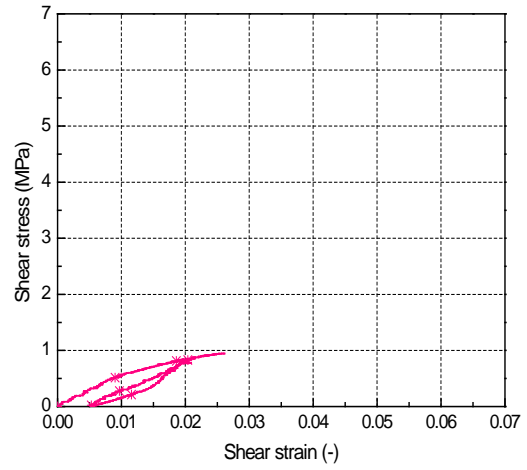
Figure A.33: Shear stress vs. strain loading and unloading cycles for Fg/T-15 specimen
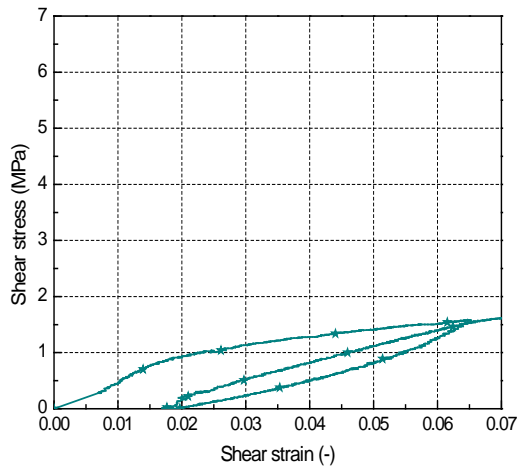
Figure A.34: Shear stress vs. strain loading and unloading cycles for Fg/T-16 specimen
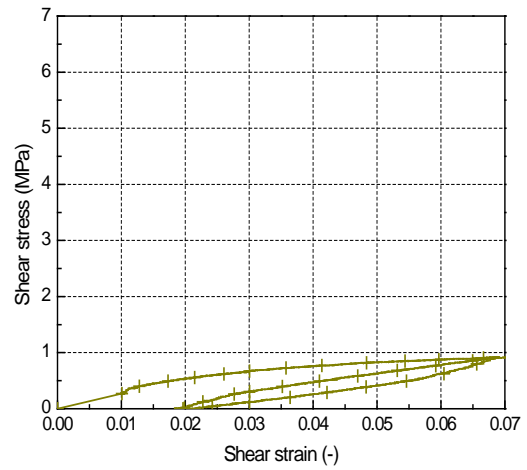
Figure A.35: Shear stress vs. strain loading and unloading cycles for Fg/T-17 specimen

ANNEX B.

Detailed four- and three-point bending experimental data on sandwich beams with complex core assembly

B.1 Sandwich beam manufacturing procedure
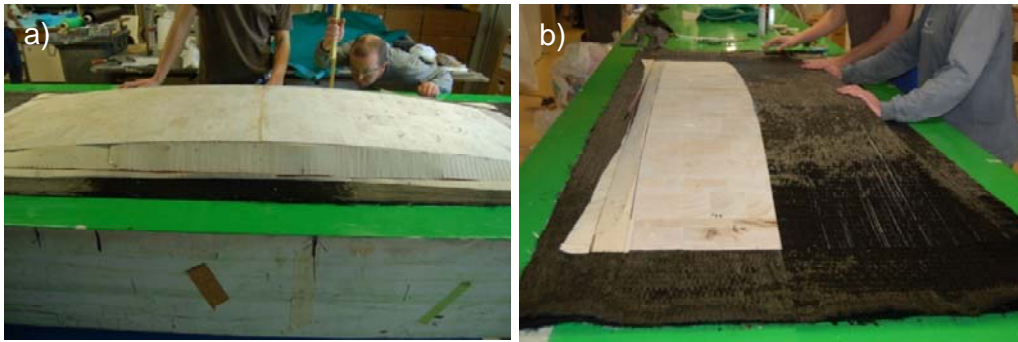
Figure B.1: (a) adhesive bonding of lower low-density balsa cores (SB50); (b) laying-up of CFRP fabric for lower face sheet and CFRP arch (A-C panel)

Figure B.2 (c) strain gauge installation and adhesive application on GFRP arch (A-G panel), (d) grooves for strain gauges in upper high-density balsa (SB150), (e) placing of upper high-density balsa and (f) laying-up of upper face sheet,

Figure B.3: (g) vacuum infusion, (h) fully infussed sandwich panel (i) cutting of panels with Sesto manual saw, (j) panels cut into three beams

B.2 Set-up for four-point bending experiment (same for three-point bending experiment)
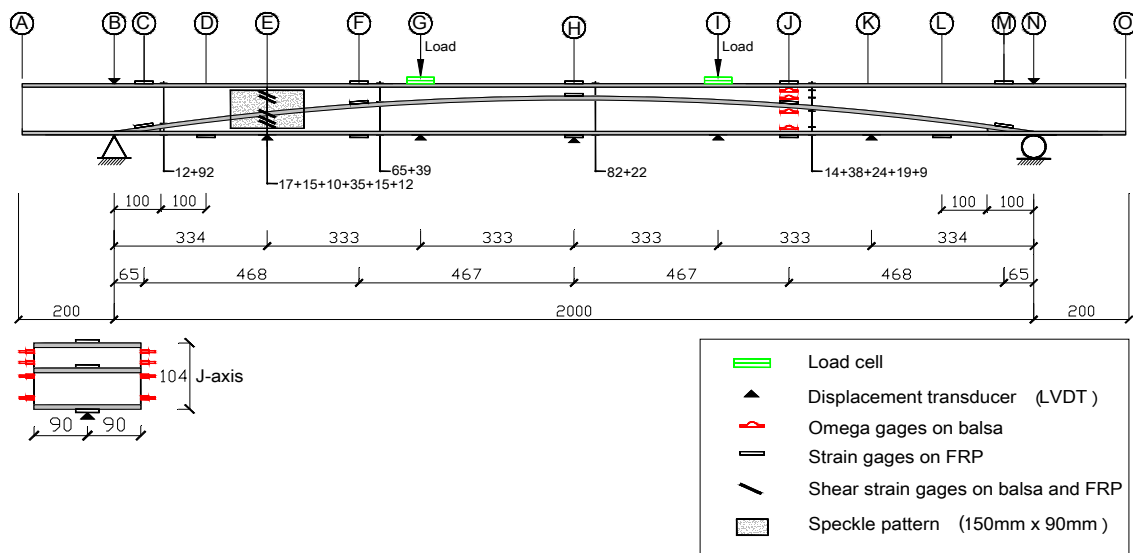
Figure B.4: Fully instrumented A-G-2 beam with cross section at J-axis

B.3   Load-displacement curves
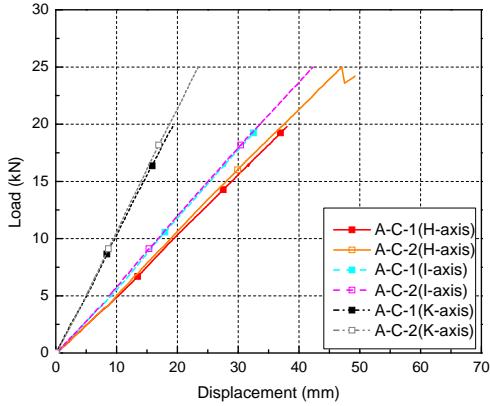
*Figure B.5: Load – deflection responses of **A-C beams** at H,I and K axes under 4-point bending load*
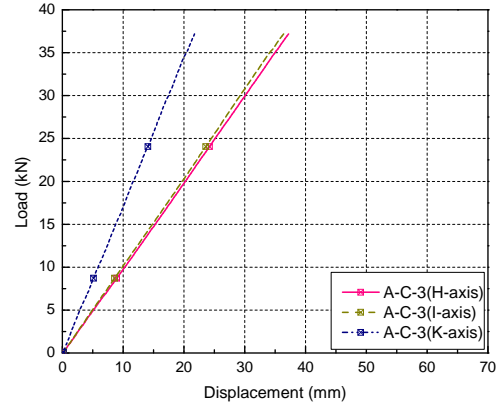
*Figure B.6: Load – deflection responses of **A-C beams** at H,I and K axes under 3-point bending load*
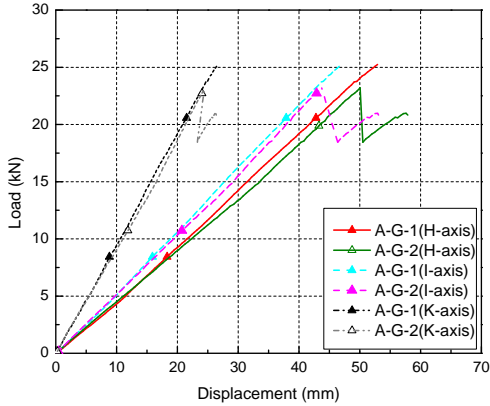
*Figure B.7: Load – deflection responses of **A-G beams** at H,I and K axes under 4-point bending load*
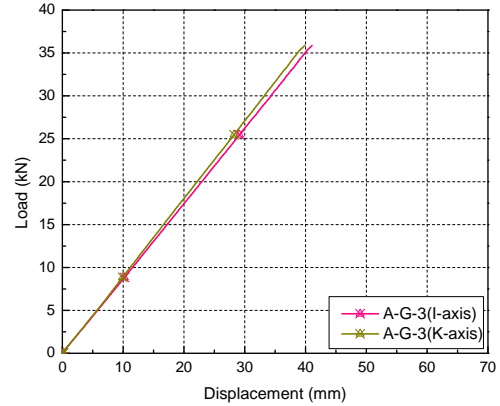
*Figure B.8: Load – deflection responses of **beam A-G-3** at H and K axes under 3-point bending load*
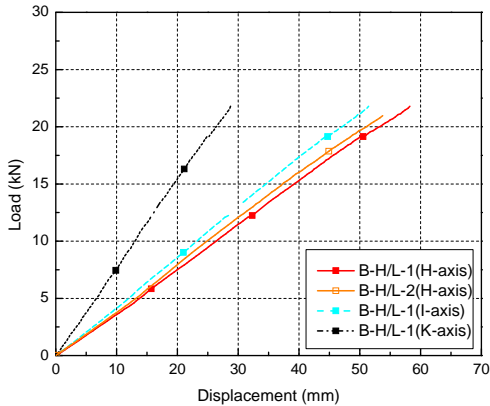
*Figure B.9: Load – deflection responses of **B-H/L beams** at H,I and K axes under 4-point bending load*
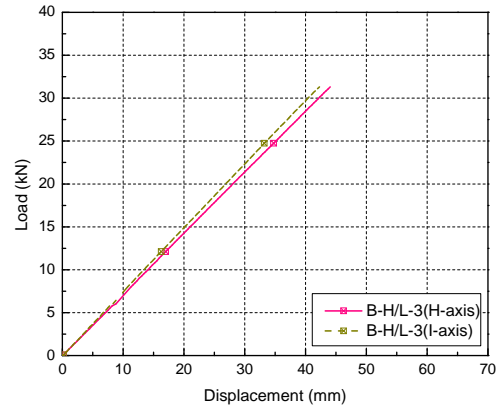
*Figure B.10: Load – deflection responses of **beam B-H/L-3** at H and K axes under 3-point bending load*
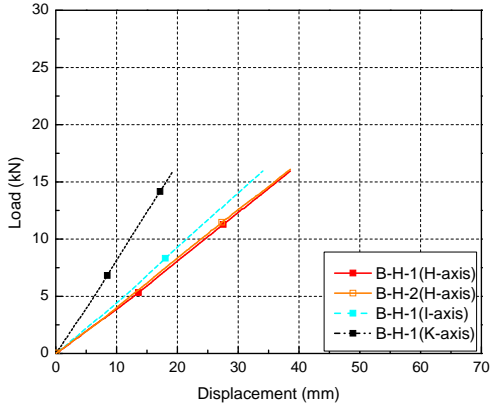
*Figure B.11: Load – deflection responses of **B-H beams** at H,I and K axes under 4-point bending load*
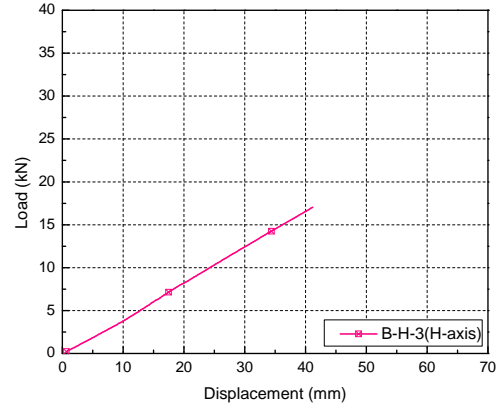
*Figure B.12: Load – deflection responses of **beam B-H-3** at H axis under 3-point bending load*
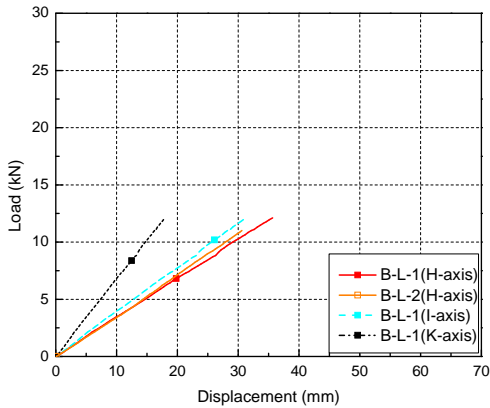
*Figure B.13: Load – deflection responses of **B-L beams** at H,I and K axes under 4-point bending load*
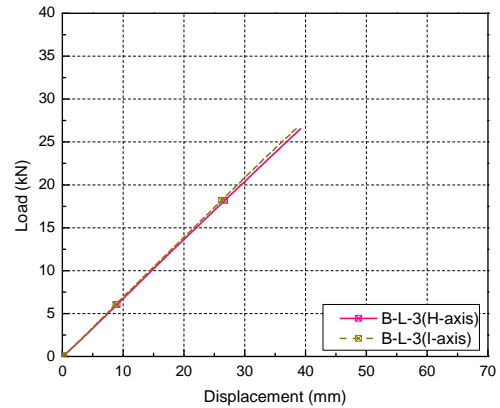
*Figure B.14: Load – deflection responses of **beam B-L-3** at H and I axes under 3-point bending load*

B.4 Axial strain in FRP face sheets, FRP arches and balsa cores

B.4.1 A-C beams
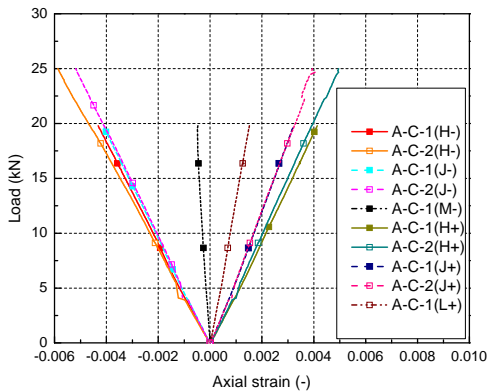
Figure B.15: Load – axial strain in upper (-) and lower (+) face sheets at axes H, J,L,M under 4-point bending load
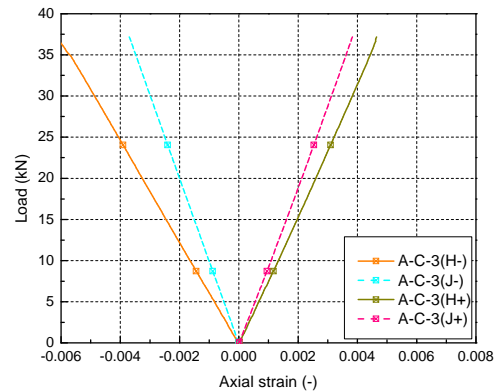
Figure B.16: Load – axial strain in upper (-) and lower (+) face sheets at axes H, J, L,M under 3-point bending load

163
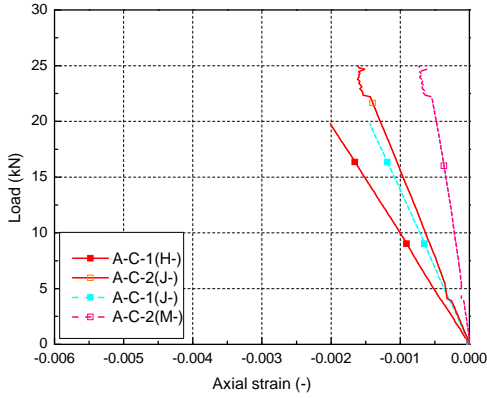
Figure B.17: Load – axial strain in FRP arches at axes H,J,M under 4-point bending load
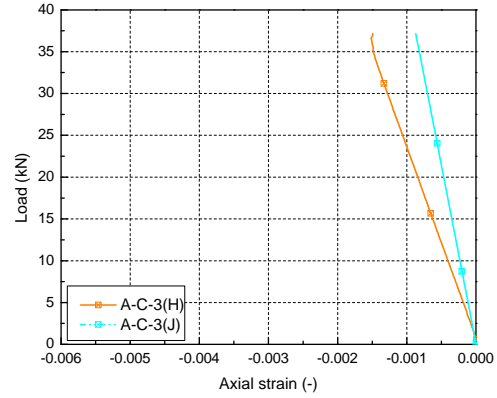
Figure B.18: Load – axial strain in FRP arch at axes H,J under 3-point bending load
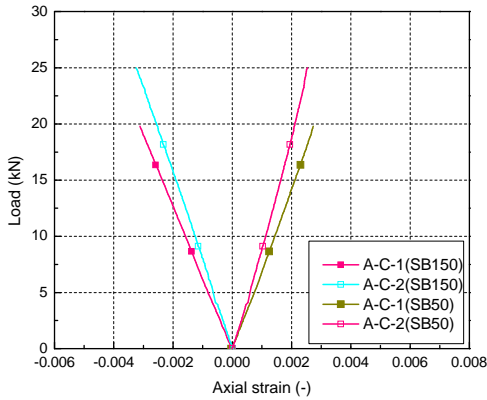
Figure B.19: Load – axial strain in balsa cores at under 4-point bending load (+ comp., - tension)
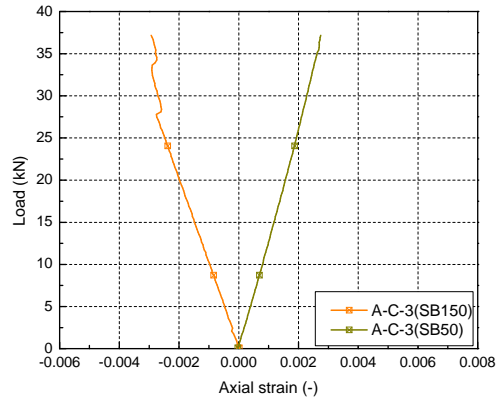
Figure B.20: Load – axial strain in balsa cores under 3-point bending load (+ comp., - tension)

B.4.2   A-G beams
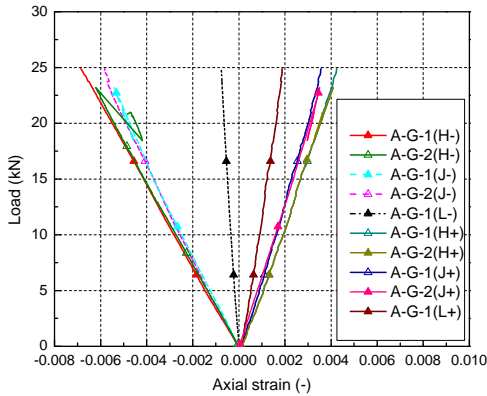
Figure B.21: Load – axial strain in top(-) and bottom(+) face sheets at axes H, J, L,M under 4-point bending load
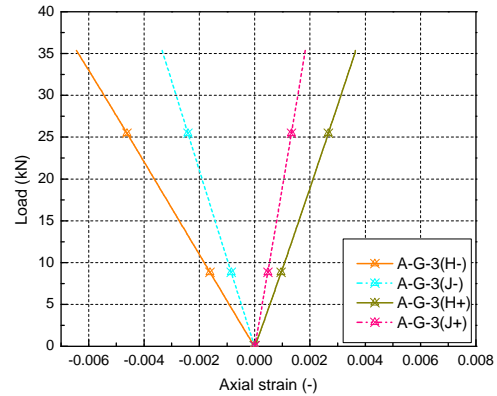
Figure B.22: Load – axial strain in top(-) and bottom(+) face sheets at axes H, J, L, M for under 3-point bending load

164
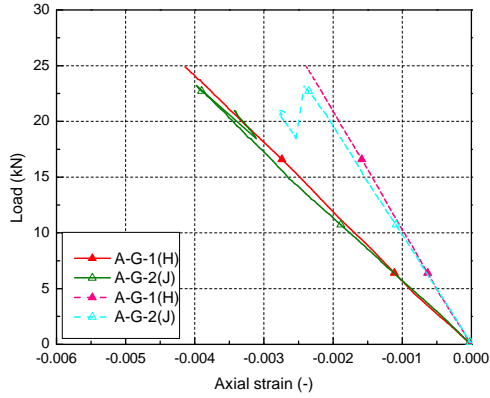
Figure B.23: Load – axial strain in FRP arches at axes H,J,M under 4-point bending load
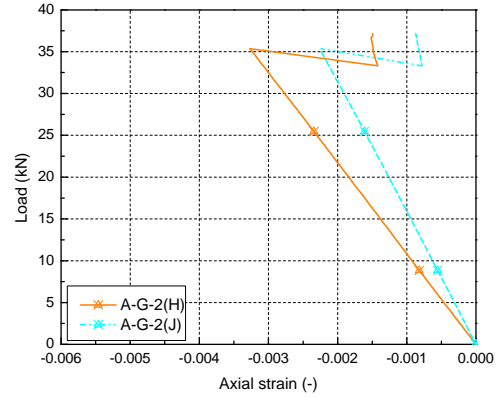
Figure B.24: Load – axial strain in FRP arches at axes H,J under 3-point bending load
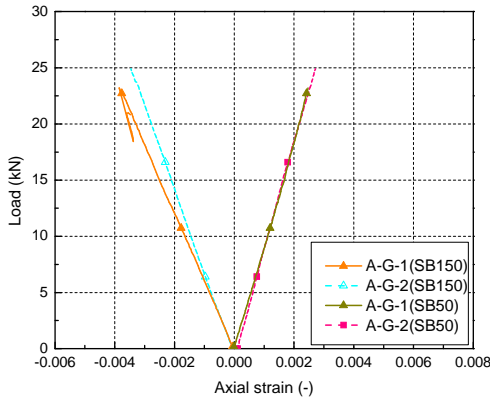
Figure B.25: Load – axial strain in balsa cores 4-point bending load (+ comp., - tension)
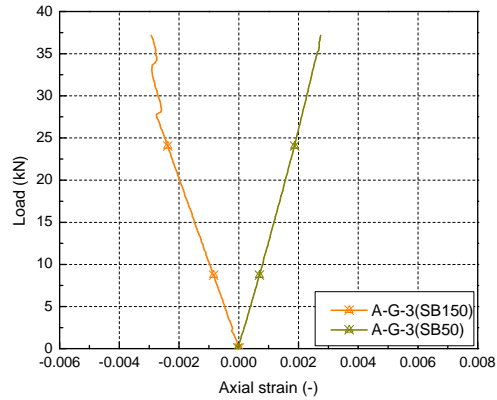
Figure B.26: Load – axial strain in balsa core under 3-point bending load (+ comp., - tension)

B.4.3   B-H/L beams
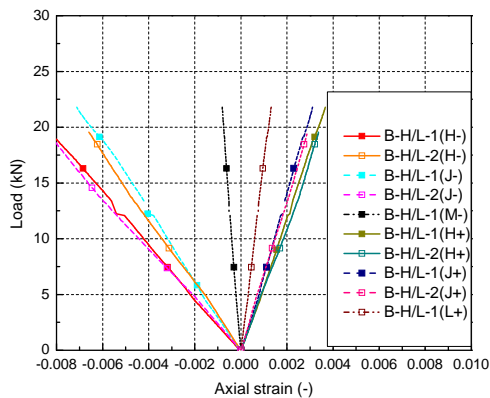
Figure B.27: Load – axial strain in top(-) and bottom(+) face sheets at axes H, J, L,M under 4-point bending load
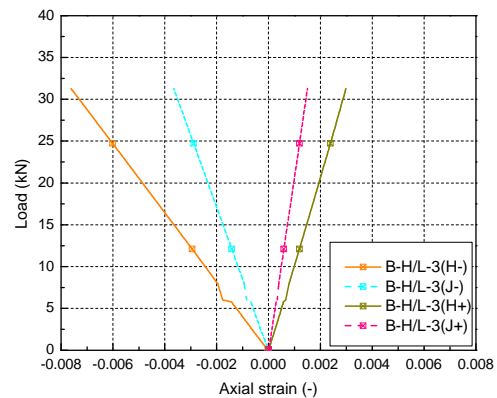
Figure B.28: Load – axial strain in top(-) and bottom(+) face sheets at axes H, J, L,M under 3-point bending load
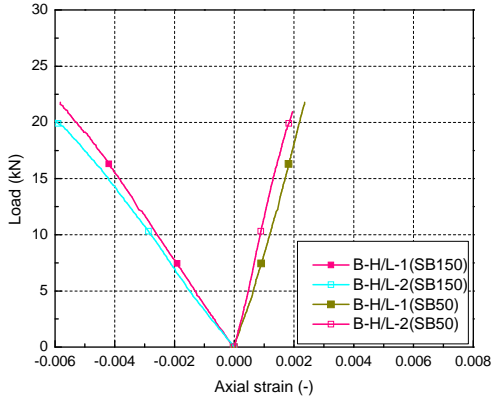
Figure B.29: Load – axial strain in balsa core under 4-point bending load (+ comp., - tension)
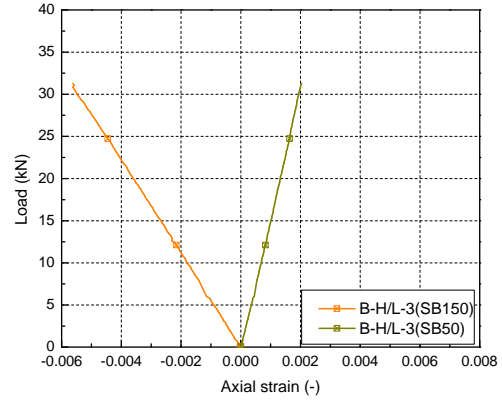
Figure B.30: Load – axial strain in balsa core under 3-point bending load (+ comp., - tension)

B.4.4 B-H beams
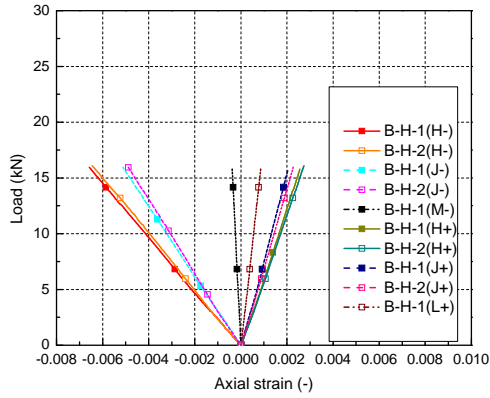
Figure B.31: Load – axial strain in top(-) and bottom(+) face sheets at axes H,J, L,M under 4-point bending load
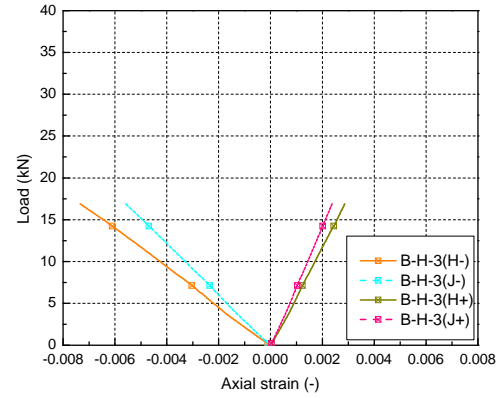
Figure B.32: Load – axial strain in top(-) and bottom(+) face sheets at axes H,J, L,M under 3-point bending load
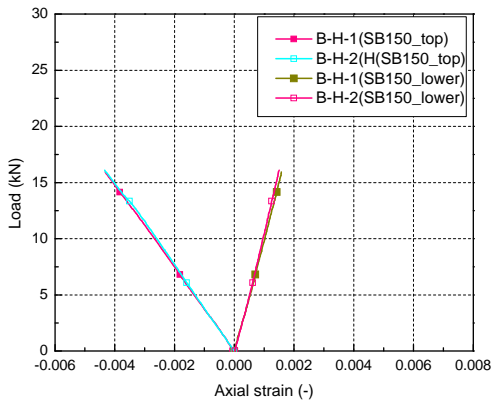
Figure B.33: Load – axial strain in balsa core under 4-point bending load (+ comp., - tension)
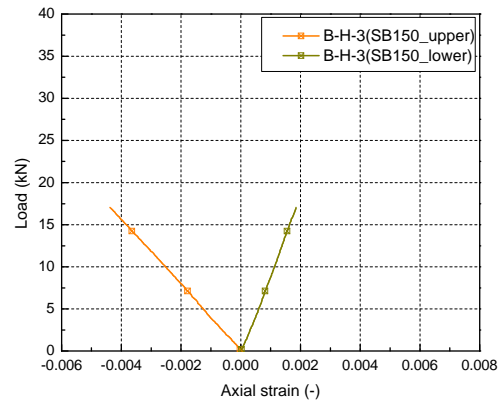
Figure B.34: Load – axial strain in balsa core 3-point bending load (+ comp., - tension)

166

B.4.5   B-L beams
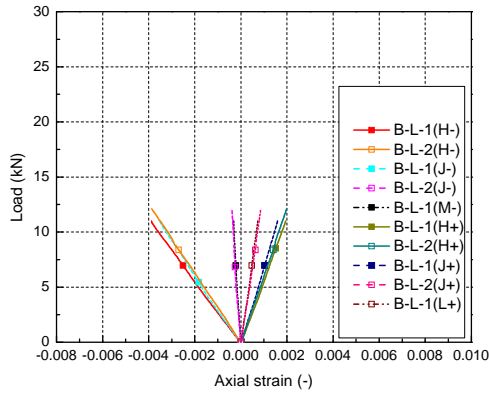
Figure B.35: Load – axial strain in top(-) and bottom(+) face sheets at axes H, J, L,M under 4-point bending load
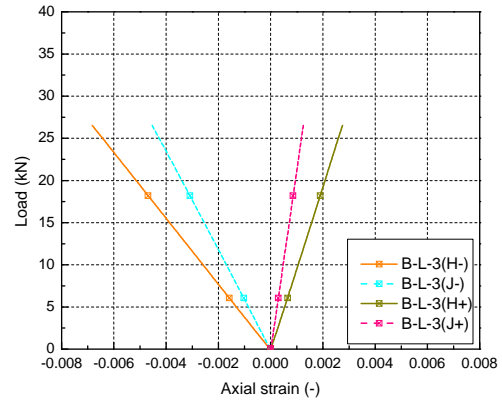
Figure B.36: Load – axial strain in top(-) and bottom(+) face sheets at axes H, J, L,M under 3-point bending load
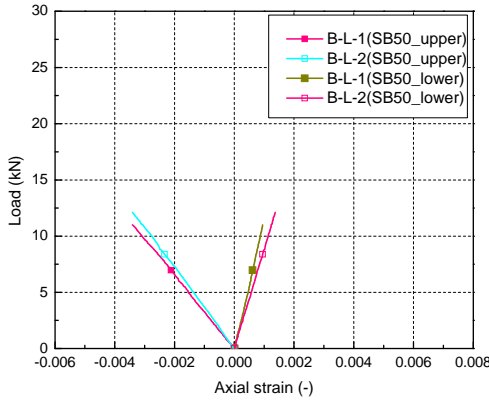
Figure B.37: Load – axial strain in balsa core under 4-point bending load (+ comp., - tension)
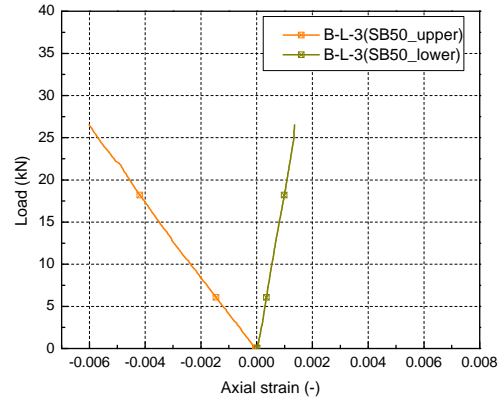
Figure B.38: Load – axial strain in balsa core under 3-point bending load (+ comp., - tension)

B.5   Out-of-plane axial strain distributions
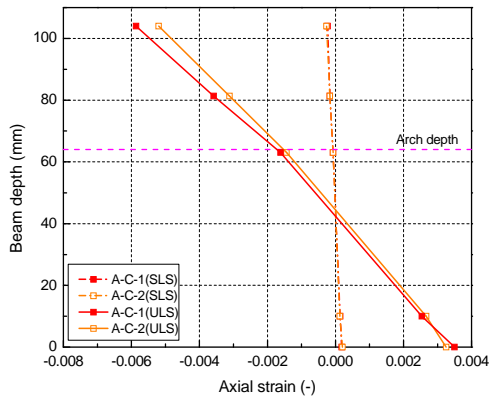
*Figure B.39: Axial strain distribution in **A-C beams** at J axis under 4-point bending load*
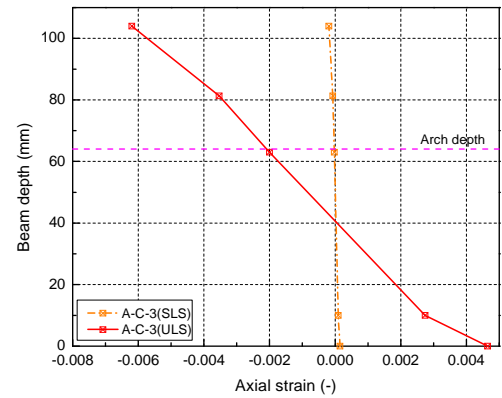
*Figure B.40: Axial strain distribution in **A-C beam** at J axis under 3-point bending load*

167
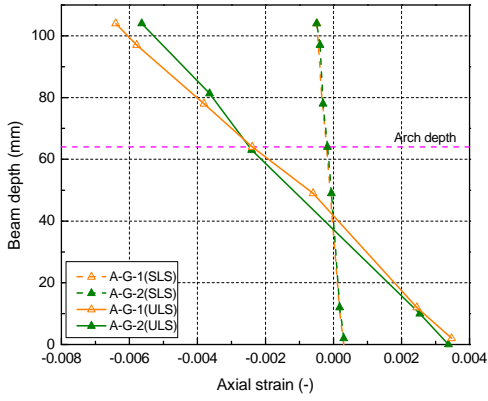
*Figure B.41: Axial strain distribution in **A-G beams** at J axis under 4-point bending load*
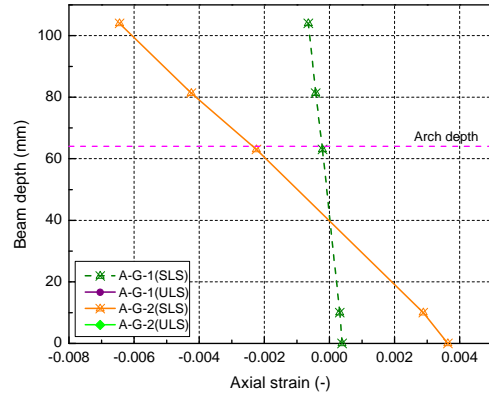
*Figure B.42: Axial strain distribution in **A-G beam** at J axis under 3-point bending load*
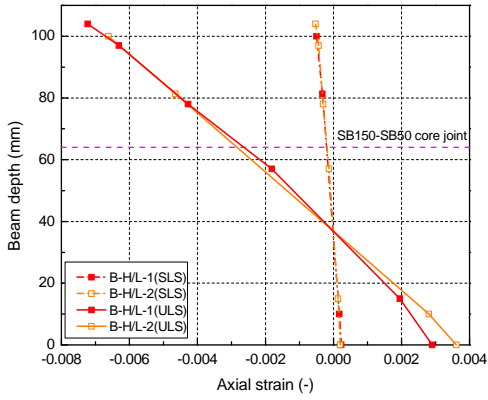
*Figure B.43: Axial strain distribution in **B-H/L beams** at J axis under 4-point bending load*
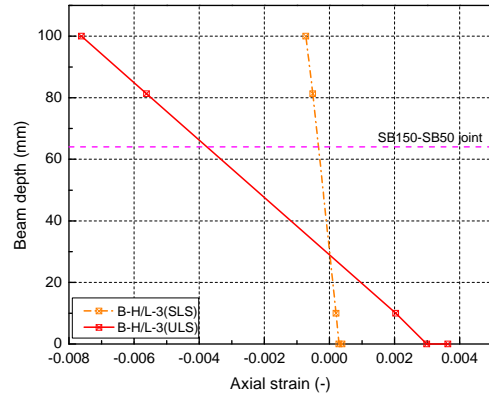
*Figure B.44: Axial strain distribution in **B-H/L beam** at J axis under 3-point bending load*
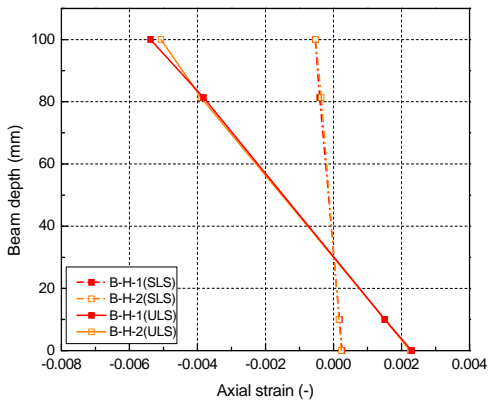
*Figure B.45: Axial strain distribution in **B-H beams** at J axis under 4-point bending load*
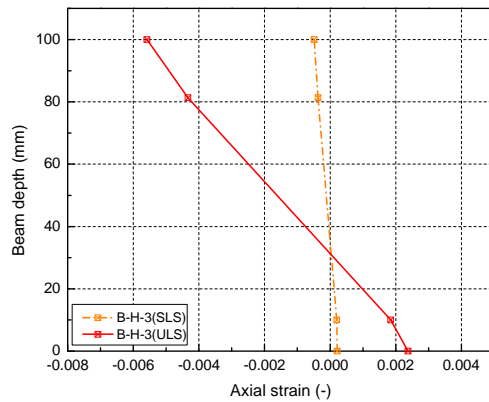
*Figure B.46: Axial strain distribution in **B-H beam** at J axis under 4-point bending load*
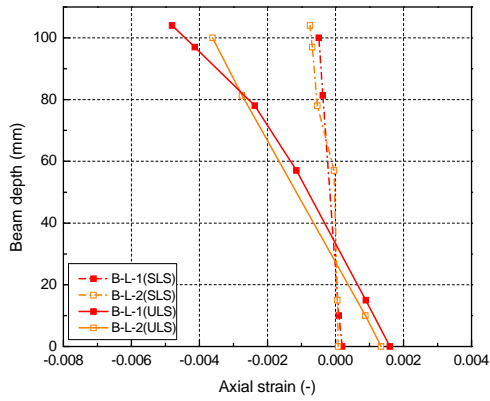
Figure B.47: Axial strain distribution in **B-L beams** at J axis under 4-point bending load
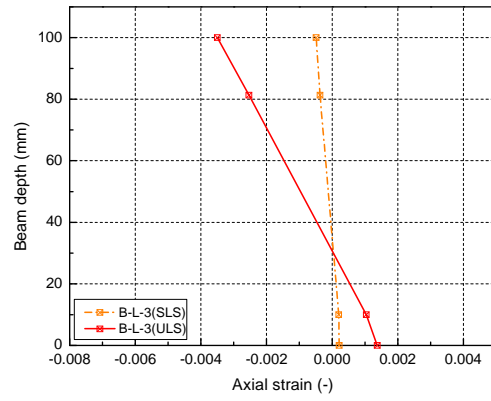
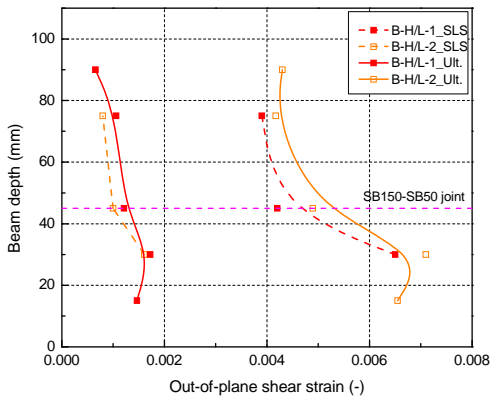Figure B.48: Axial strain distribution in **B-L beam** at J axis under 4-point bending load

B.6   Load versus shear strain curves
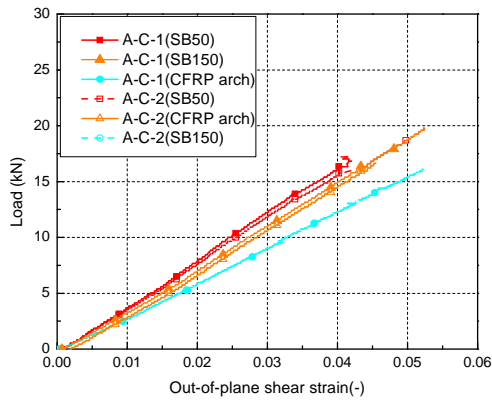
Figure B.49: Load – shear strain at E axis of **A-C beams** under 4-point bending load
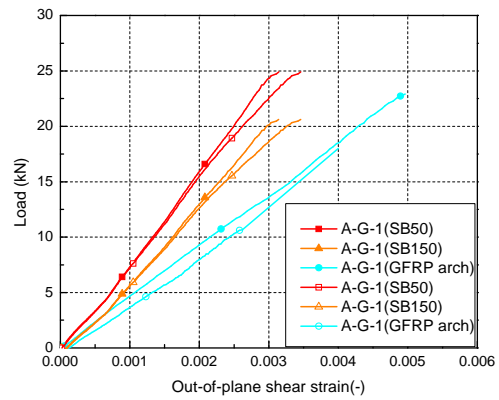
Figure B.50: Load – shear strain at E axis of **A-G beams** under 4-point bending load
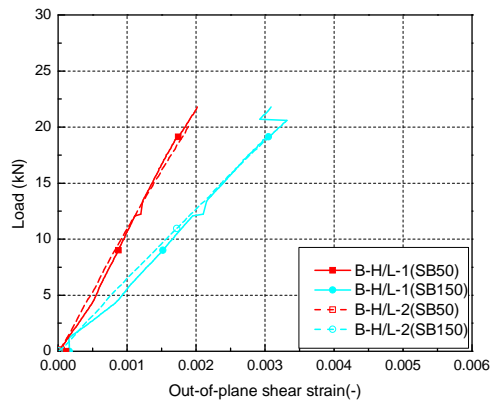
Figure B.51: Load – shear strain at E axis of **B-H/L beams** under 4-point bending load
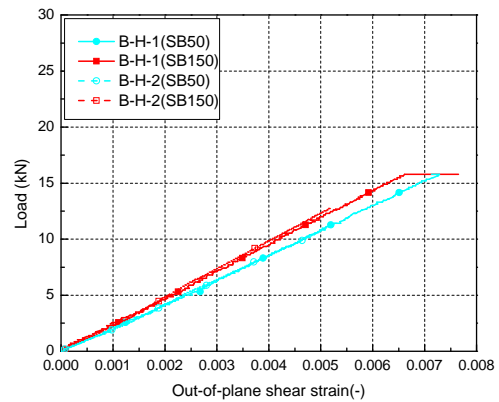
Figure B.52: Load – shear strain at E axis of **B-H beams** under 4-point bending load
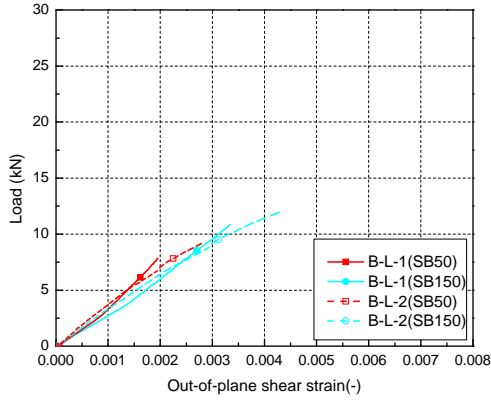
Figure B.53: Load – shear strain at E axis of
***B-L beams** under 4-point bending load*

B.7 Out-of-plane shear strain distribution
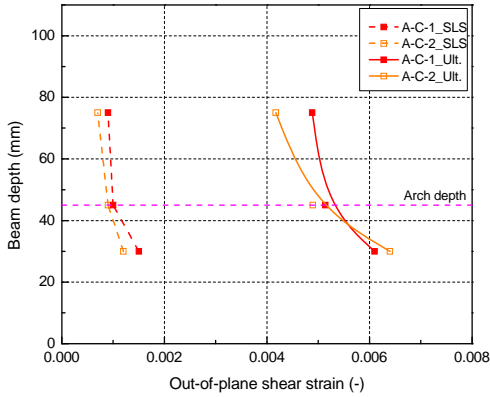
*Figure B.54: Shear strain distribution in **A-C beams** at E axis under 4-point bending load*
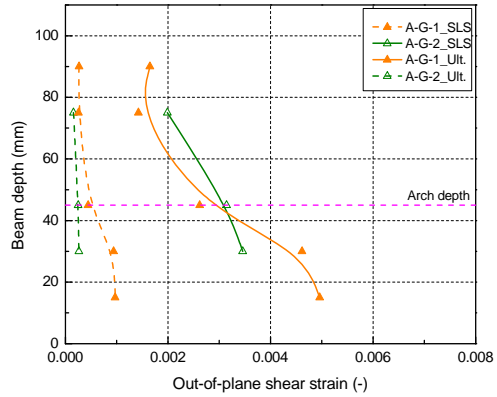
*Figure B.55: Shear strain distribution in **A-G beams** at E axis under 4-point bending load*

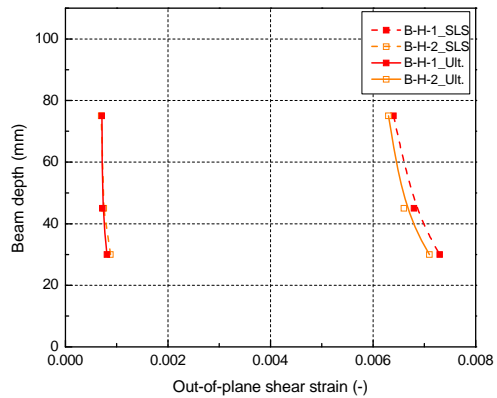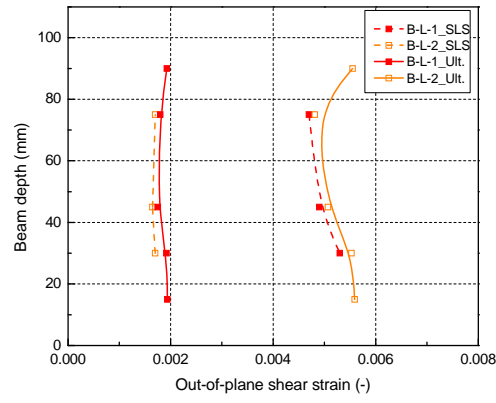*Figure B.56: Shear strain distribution in **B-H/L beams** at E axis under 4-point bending load*

*Figure B.57: Shear strain distribution in **B-H beams** at E axis under 4-point bending load*

*Figure B.58: Shear strain distribution in **B-L Beams** at E axis under 4-point bending load*
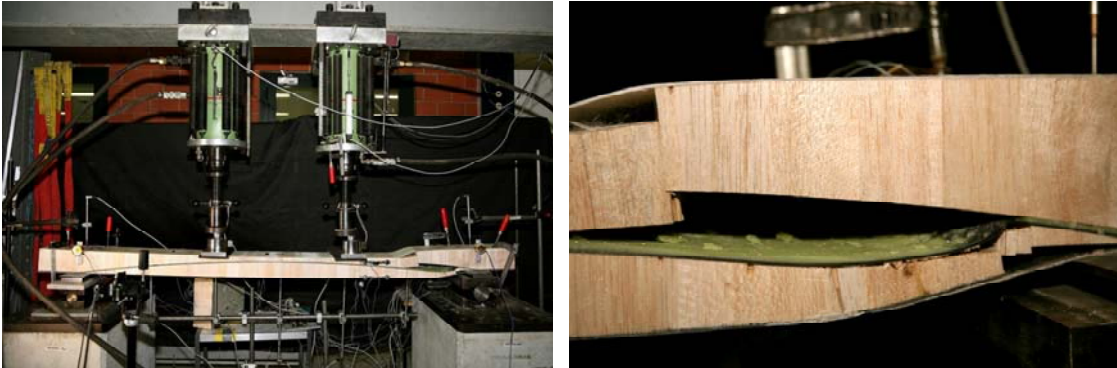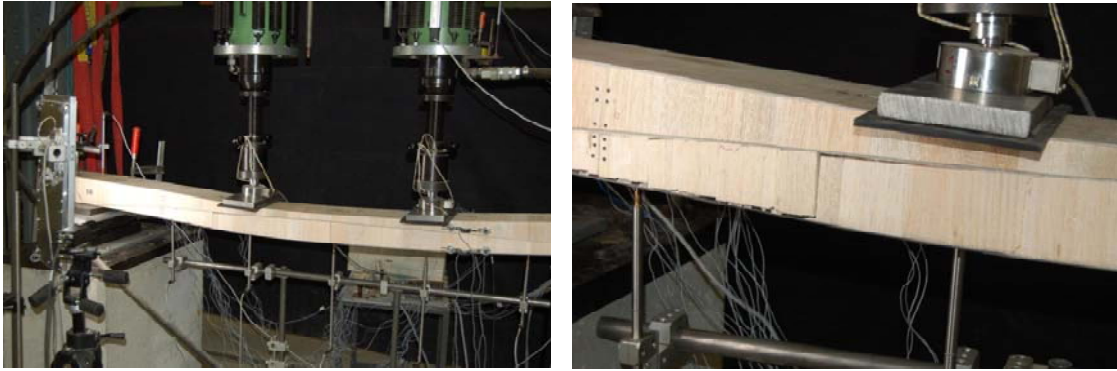
B.8 Failure modes

B.8.1 A-C beams

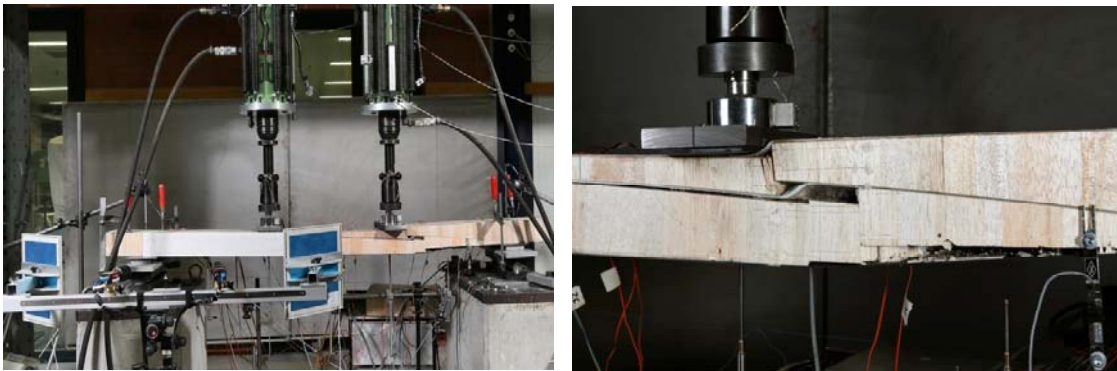*Figure B.59: Failure of beam A-C-1 (left), zoom of detailed failure mode (right)*

Figure B.60: Failure of beam A-C-2 (left), zoom of detailed failure mode (right)

Figure B.61: Failure of beam A-C-3 (left), zoom of detailed failure mode (right)

B.8.2 A-G beams

Figure B.62: Failure of beam A-G-1 (left), zoom of detailed failure mode (right)

Figure B.63: Failure of beam A-G-2 (left), zoom of detailed failure mode (right)

Figure B.64: Failure of beam A-G-3 (left), zoom of detailed failure mode (right)
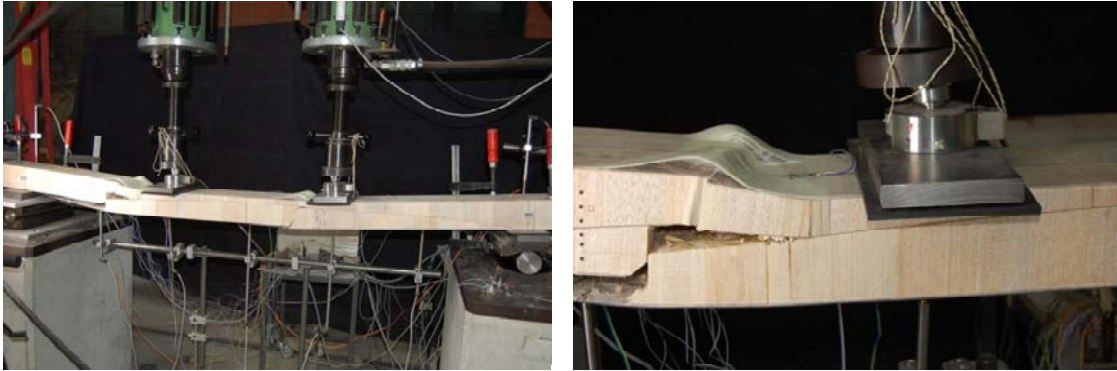
B.8.3 B-H/L beams

Figure B.65: Failure of beam B-H/L-1 (left), zoom of detailed failure mode (right)

Figure B.66: Failure of beam B-H/L-2 (left), zoom of detailed failure mode (right)

Figure B.67: Failure of beam B-H/L-3 (left), zoom of detailed failure mode (right)

B.8.4   B-H beams

Figure B.68: Failure of beam B-H-1 (left), zoom of detailed failure mode (right)

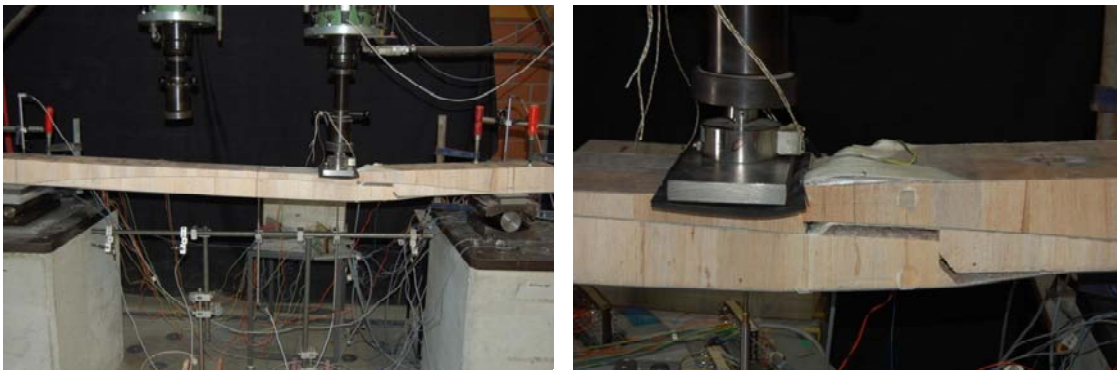*Figure B.69: Failure of beam B-H-2 (left), zoom of detailed failure mode (right)*

Figure B.70: Failure of beam B-H-3 (left), zoom of detailed failure mode (right)
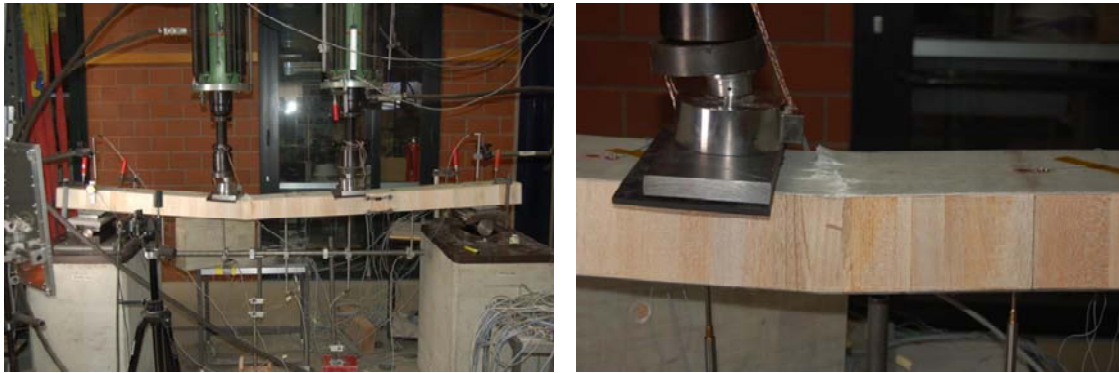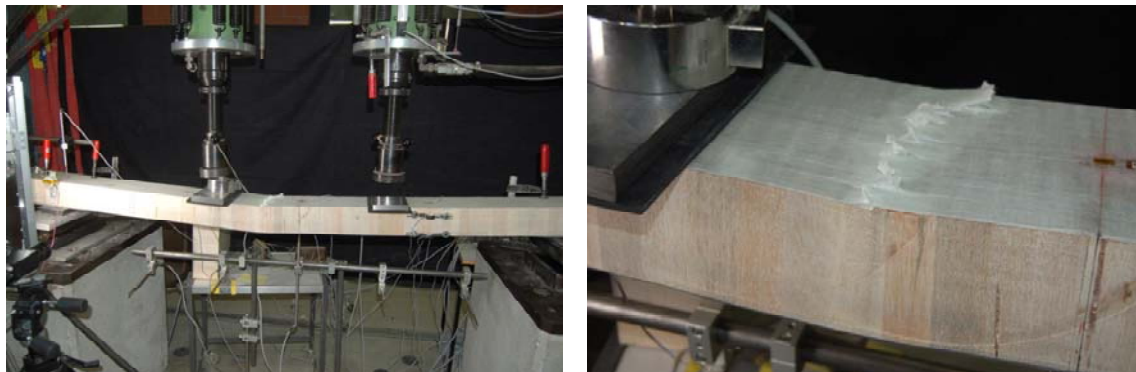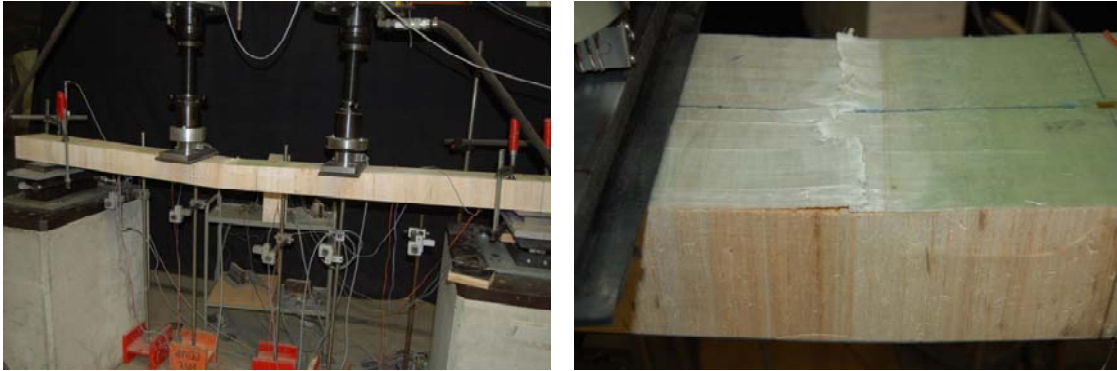
B.8.5 B-L beams

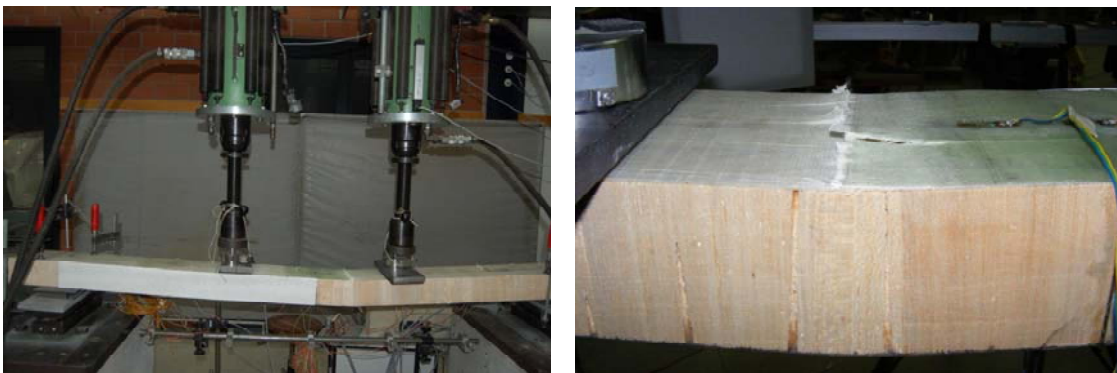*Figure B.71: Failure of beam B-L-1 (left), zoom of detailed failure mode (right)*

Figure B.72: Failure of beam B-L-2 (left), zoom of detailed failure mode (right)

Figure B.73: Failure of beam B-L-3 (left), zoom of detailed failure mode (right)

Michael Osei-Antwi

5200 Town and Country blvd, Apt# 1032
Frisco, TX 75034
(Phone) 469-685-7227
Email: m.oseiantwi@gmail.com

Structural / Civil/ Composite Engineering Professional

PROFILE

A mid-career engineer with over four years of engineering experience in design, research, construction and rehabilitation of bridges, commercial/residential/industrial infrastructure. Specialized in the use of composite materials in design and repair/retrofitting of civil engineering infrastructure.

TECHNICAL SKILLS

Numerical/Design/CAD Packages: ANSYS, STAAD, SAP2000, SolidWorks, AutoCAD, MATLAB, Mathematica, HECRAS, ARCGIS
Computer Skills: MS Office, MS Project.

EDUCATION

Ph.D., Structural Engineering, Swiss Federal Institute of Technology, Lausanne, Switzerland.	02/2010 - present
M.S., Civil Engineering, Politecnico di Milano, Milan, Italy.	10/2007-10/2009
B. S., Civil Engineering, Kwame Nkrumah Univ. of Science and Technology, Kumasi, Ghana.	09/2001-06/2005

PROFESSIONAL EXPERIENCE

Composite Construction Laboratory, Lausanne, Switzerland   **02/2010–Present**
Research Assistant
   Key Projects/Achievements:
- Part of engineering consultants that designed and experimentally tested the new Avancon Composite Bridge, Bex, Switzerland (10/2012), the first FRP-balsa composite sandwich bridge in Switzerland.
- Proposed and experimentally/numerically investigated new innovative complex core system to be used as a new model for sandwich bridge decks.

Conpro Limited, Kumasi, Ghana   **08/2006-10/2007**
Civil/Structural Engineer
   Key Projects/Achievements:
- Designed, supervised and managed construction of industrial and multi-storey residential complex.
- Structurally designed and supervised construction of large capacity assembly hall/theatre of 5000 capacity.

Kumasi Metropolitan Assembly, Kumasi, Ghana   **11/2005-08/2006**
Assistant Civil Engineer
   Key Projects/Achievements:
- Contributed to the development of a new solid waste collection system in the Kumasi metropolis, Ghana
- Contributed to the establishment of the user rate of public toilets in the Kumasi, Ghana.

PUBLICATIONS

Journal papers
- M. Osei-Antwi, J. de Castro, A. P. Vassilopoulos, T. Keller. Shear mechanical characterization of balsa wood as core material of composite sandwich panels. Journal of Construction and Building Materials, 2013; 41: 231-238. http://dx.doi.org/10.1016/j.conbuildmat.2012.11.009
- T. Keller, J. Rothe, J. de Castro, M. Osei-Antwi. FRP-balsa composite sandwich bridge deck with complex core assembly. ASCE Journal of Composite for Construction, 2013. http://dx.doi.org/10.1061/(ASCE)CC.1943-5614.0000435
- M. Osei-Antwi, J. de Castro, A. P. Vassilopoulos, T. Keller. GFRP-balsa sandwich bridge deck concept, design and experimental validation. ASCE Journal of Composite for Construction, 2013. http://dx.doi.org/10.1061/(ASCE)CC.1943-5614.0000423
- M. Osei-Antwi, J. de Castro, A. P. Vassilopoulos, T. Keller. Fracture in complex balsa cores of fiber-reinforced polymer sandwich structures sandwich. Submitted to ASCE Journal of Composite for Construction, in February, 2014
- M. Osei-Antwi, J. de Castro, A. P. Vassilopoulos, T. Keller. Modeling of axial and shear stresses in multilayer sandwich beams with stiff cores. Submitted to Composite Structures, in February 2014.

- M. Osei-Antwi, J. de Castro, A. P. Vassilopoulos, T. Keller. Analytical modeling of local stresses at balsa/timber core joints of FRP sandwich structures. Submitted to Composite Structures, in February 2014.
- M. Osei-Antwi, J. de Castro, A. P. Vassilopoulos, T. Keller. Structural limits of FRP-balsa sandwich decks in bridge construction. Submitted to Composites: B, in February 2014.
- M. Osei-Antwi, J. de Castro, A. P. Vassilopoulos, T. Keller. Micromechanical shear properties of balsa panels. Submitted to Journal of Construction and Building Materials, in February 2014.

Conference papers
- M. Osei-Antwi, J. de Castro, A. P. Vassilopoulos, T. Keller. Shear mechanical characterization of balsa wood as core material of composite sandwich bridge deck. ACUN6-Composites and nanocomposites in civil, offshore and mining infrastructure, Melbourne, Australia, November 14-16, 2012
- M. Osei-Antwi, J. de Castro, A. P. Vassilopoulos, T. Keller. FRP-balsa composite sandwich bridge deck with complex core configuration. The 7th International Conference on FRP Composites in Civil Engineering (CICE), International Institute for FRP in Construction, Vancouver, Canada, August 20-22, 2014
- M. Osei-Antwi, J. de Castro, A. P. Vassilopoulos, T. Keller. GFRP-balsa sandwich bridge deck: concept, design and experimental validation. The 7th International Conference on FRP Composites in Civil Engineering, International Institute for FRP in Construction (CICE), Vancouver, Canada, August 20-22, 2014
- M. Osei-Antwi, J. de Castro, A. P. Vassilopoulos, T. Keller. Structural limits of FRP-balsa sandwich decks in bridge construction. The 37th International Association for Bridge and Structural Engineering (IABSE). Engineering for progress nature and people, Madrid, Spain, September 3-5, 2014.

PROFESSIONAL REGISTRATION

Engineer in Training license (E.I.T.-Texas Professional Engineers) waived for PhD holders.
Ghana institution of Engineers No. 05823